博士論文

Search for Neutrinoless Double-Beta Decay in ^{136}Xe after Intensive Background Reduction with KamLAND-Zen

(徹底したバックグラウンド低減後の KamLAND-Zen における
^{136}Xe でのニュートリノを伴わない二重ベータ崩壊の探索)

松田さゆり

平成 28 年

Doctoral Dissertation

Search for Neutrinoless Double-Beta Decay in ^{136}Xe after Intensive Background Reduction with KamLAND-Zen

by Matsuda Sayuri

in Physics
in Graduate School of Science,
Tohoku University

2016

Abstract

This dissertation reports improved search for neutrinoless double-beta decay ($0\nu\beta\beta$) of ^{136}Xe with the KamLAND-Zen experiment. The extremely rare radioactive decay beyond the Standard Model gives knowledge for Majorana property of neutrino and its mass scale. It would also demonstrate the non-conservation of lepton number, which advances understanding for the baryon asymmetry of universe. The exploration requires large target mass and low background techniques. Most of current double-beta decay experiments uses 10 - 100 kg of mass towards achieving probe of quasi-degenerate neutrino mass region.

The KamLAND-Zen started data taking in 2011 with large liquid scintillation detector, "KamLAND" and maximum amount of Xe. Though it achieved the most stringent constraints on the $0\nu\beta\beta$ decay half-life $T^{0\nu}_{1/2} > 1.9\times10^{25}$ yr at 90 % C.L., unexpected impurity ^{110m}Ag distributing in Xe-loaded liquid scintillator (Xe-LS) and along inner-balloon (IB) holding Xe-LS, limited the sensitivity. Therefore, after completing the first data period (Phase-I), purification of Xe-LS by water extraction and distillation was implemented for 18 months. In this dissertation, data period after the purification (Phase-II) is analyzed, where 381 kg of enriched Xe is dissolved in LS.

The purification successfully reduced ^{110m}Ag background: 1/10 of the initial rate at least, and only upper limit is obtained in lower background period. By the reduction, contribution of other backgrounds namely ^{10}C spallation product and ^{214}Bi from natural impurities became unignorable. In this work, ^{10}C rejection using muon-neutron-^{10}C triple coincidence method is introduced for the first time, which achieves (64 $\pm$ 4) % of rejection efficiency. Huge amount of ^{214}Bi distributes along the IB film and its spatial distribution tail contributes to the innermost region being sensitive to $0\nu\beta\beta$ search. Therefore, accurate estimation of the tail is required. In order to satisfy it, decay-particle tracking, scintillation photon process and finite PMT timing resolution are introduced to MC simulation and additional tuning is implemented. It significantly improved the consistency of ^{214}Bi background tail with data.

Thus, intensive background reduction by purification and rejection enhanced the $0\nu\beta\beta$ constraint. Combining with the result in Phase-I, lower limit of $0\nu\beta\beta$ decay half-life $T^{0\nu}_{1/2} > 1.07\times10^{26}$ yr at 90 % C.L. is obtained, which corresponds to almost sixfold improvement compared to the Phase-I. Assuming exchange of light Majorana neutrinos, it is translated into the most stringent limit on the effective Majorana neutrino mass including uncertainty of the nuclear model: $\langle m_{\beta\beta}\rangle < (61-165)$ meV at 90 % C.L., which is the first constraint below $\sim$100 meV of all $\beta\beta$-decay nuclei. This result excludes most of allowed region for quasi-degenerate type of neutrino, and it reaches near the inverted mass hierarchy.

This result is summarized in the published article (A. Gando, Y Gando, et al., 2016 [1]).

Acknowledgement

First and foremost, I would like to express the deepest appreciation to the supervisor and the spokesperson of the KamLAND/KamLAND-Zen experiments, Prof. Kunio Inoue. He gave me the opportunity to work on such an exciting experiment. I would not be at this stage without his guidance and support. My heartfelt appreciation goes to my advisor, Assoc. Prof. Itaru Shimizu whose enormous support and insightful comments were invaluable during the course of my study.

Next, I want to thank the entire the KamLAND and KamLAND-Zen collaboration. This result could not have been accomplished without their great efforts mainly on the purification campaigns. Especially, I learned a lot of things from the RCNS members. Assoc. Prof. Junpei Shirai, Tadao Mitsui have taught me techniques in experimental particle physics. Assoc. Prof. Masayuki Koga and Drs. Kengo Nakamura, Yoshihito Gando and Kota Ueshima, contributed significantly to the success of purification works, and which became very educational to me. I always received enormous support from Dr. Haruo Ikeda when I faced difficulties. Dr. Koji Ishidoshiro gave me insightful comments and suggestions for my analysis. Kyoko Tamae, and Drs. Hiroko Watanabe and Azusa Gando have been wonderful role models as female researchers for me. And I want to thank all the postgraduate students in RCNS. I really had a fruitful and enjoyable time researching with them. There have been supports from the engineers, the clerks and other staffs in Sendai and Kamioka.

I also would like to thank the ex-RCNS members. Special thanks goes to Drs. Patrick Decowski, Brian Fujikawa, Yuri Efremenko and Jason Detwiler, whose meticulous comments refined this result. Dr. Tom Banks contributed to modification of MiniCAL calibration system. Dr. Andreas Piepke managed fabrication of the calibration source which played an important role in this result. Dr. Yasuhiro Takemoto spent much time in looking over my thesis. Drs. Daisuke Motoki and Hisataka Yoshida gave many advices concerning my analysis.

Finally, I would like to express my gratitude to my family for their moral support and warm encouragements.

Contents

List of Figures

List of Tables

1. Introduction

Why neutrinos have very small mass? This is the central issue of the neutrino physics. Majorana neutrinos introduce the most appealing answer via seesaw mechanism. An observation of $0\nu\beta\beta$ decay would directly prove lepton number violation, as well as Majorana nature of neutrinos, which are not predicted in the Standard Model. Exploration of the nuclear transition also provides information for the mass scale of neutrinos. Current double-beta decay experiments are constraining the quasi-degenerate neutrino mass region while improving low background techniques and increasing target mass.

KamLAND-Zen (KamLAND ZEro Neutrino double-beta decay) experiment is based on a modification of the existing KamLAND detector carried out in summer 2011 (Phase-I), where smaller balloon containing Xe-loaded liquid scintillator was installed into the detector center. This experiment provided impressive result such as exclusion of a positive claim for $0\nu\beta\beta$ decay measurement ((KLAPDOR-KLEINGROTHAUS and KRIVOSHEINA, 2006 [2])). However, dominant background ^{110m}Ag was found around the signal region, which suppressed the sensitivity for $0\nu\beta\beta$ decay. Therfore, Xe and liquid scintillator purification campaign aiming for ^{110m}Ag reduction by $\sim$2 orders of magnitude, was implemented after the completion of Phase-I.

In this thesis, further low background period after the purification (called Phase-II) is analyzed. It is dedicated to background reduction other than ^{110m}Ag, by improving event reconstruction procedure and background tagging method. Especially, spallation background rejection aiming for ^{10}C reduction is first applied owing to trigger development in new electronics. Such low radioactive condition requires more accurate background expectation. This work satisfies it by the improvement of MC simulation, and enables full volume analysis for the first time.

The contents of this thesis are organized as follows:
Physical backgrounds for massive neutrinos and double-beta decay, and current status of double-beta decay experiments are described in Chapter 2. Structure of KamLAND detector before KamLAND-Zen and purification systems are described in Chapter 3. History of KamLAND-Zen are described in Chapter 4. In the last section, motivation of this work and updates from the previous result are summarized. Event reconstruction and qualities are described in Chapters 5, 6. Event selection and detector related systematic uncertainties are described in Chapter 7. Backgrounds to be considered in double-beta decay analysis are described in Chapter 8. And reduction effect by Xe and LS purification are discussed. Analysis of $0\nu\beta\beta$ decay search and half-life measurement of $2\nu\beta\beta$ decay are described in Chapter 9. Chapter 10 is summary of this thesis.

2. Massive Neutrinos and Double-Beta Decay

Neutrinos are neutral leptons proposed by W.Pauli in 1930 to explain beta decay. It was proved to have mass by neutrino oscillation measurements, which implies incompleteness of the Standard Model (SM). Neutrinoless double-beta decay is one of the most promising interaction for extension of the SM. This occurs only if neutrinos are Majorana particles, i.e. particles and anti-particles are the same, which can naturally explain lightness of neutrino mass.

Besides, the decay is phenomenon beyond the SM, violating the lepton number. It is also appealing in order to explicate the cosmic baryon asymmetry. In a scenario "lepto-genesis", heavy sterile neutrinos have important role generating origin of the asymmetry. Thus, neutrinoless double-beta decay has potential to understand nature and properties of neutrinos, and baryon asymmetry in the universe.

2.1. Neutrino Masses

Absolute scale of neutrino mass is the main topic in the neutrino physics. It can be determined by the following observations:

- neutrinoless double-beta decay

$$\langle m_{\beta\beta} \rangle = \left| \sum_{i=1,2,3} |U_{ei}|^2 \mathrm{e}^{e\alpha_i} m_i \right| \tag{2.1}$$

- single-beta decay

$$\langle m_{\beta} \rangle^2 = \sum_{i=1,2,3} |U_{ei}^2| m_i^2 \tag{2.2}$$

- astrophysical and cosmological observations

$$\sum m_{\nu} = \sum_{i=1,2,3} m_i \leq m_{\mathrm{astro}} \tag{2.3}$$

They are correlated through the parameters obtained by the neutrino oscillation measurements. In this section, obtained limits by above measurements and future prospects are described, other than neutrinoless double-beta decay measurements.

2.1.1. Neutrino Oscillation

Neutrino Oscillation Probability

Neutrinos have flavors ($f = e, \mu, \tau$) which are expressed with mixing of mass eigenstates:

$$|\nu_f\rangle = \sum_{j=1}^{3} U_{fj}|\nu_j\rangle, \quad (f = e, \mu, \tau). \tag{2.4}$$

U_{fj} is the Unitary mixing matrix called "Pontecorvo-Maki-Nakagawa-Sakata matrix" (PMNS) written as,

$$\begin{aligned} U_{\mathrm{PMNS}} &= \begin{pmatrix} U_{e1} & U_{e2} & U_{e3} \\ U_{\mu 1} & U_{\mu 2} & U_{\mu 3} \\ U_{\tau 1} & U_{\tau 2} & U_{\tau 3} \end{pmatrix} \\ &= \begin{pmatrix} c_{12}c_{13} & s_{12}c_{13} & s_{13}\mathrm{e}^{-i\delta} \\ -s_{12}c_{23} - c_{12}s_{23}s_{13}\mathrm{e}^{i\delta} & c_{12}c_{23} - s_{12}s_{23}s_{13}\mathrm{e}^{i\delta} & s_{23}c_{13} \\ s_{12}s_{23} - c_{12}c_{23}s_{13}\mathrm{e}^{i\delta} & -c_{12}s_{23} - s_{12}c_{23}s_{13}\mathrm{e}^{i\delta} & c_{23}c_{13} \end{pmatrix} \end{aligned} \tag{2.5}$$

with notations $s_{ij} = \sin\theta_{ij}$, $c_{ij} = \cos\theta_{ij}$ and the CP-violating phase δ. Eq. 2.4 implies the flavor eigenstates may change into another kind while propagating through vacuum if neutrinos have mass, which is so called "neutrino oscillation".

A state for a neutrino of flavor α at time interval t is given by solving the Schrödinger equation as,

$$|\nu_\alpha(t)\rangle = \sum_j U_{\alpha j}|\nu_j\rangle \mathrm{e}^{-iE_j t} \tag{2.6}$$

for $p = |p|$ and the energy E_j of ν_j namely

$$E_j = \sqrt{p^2 + m_j^2} \simeq p + \frac{m_j^2}{2E}. \tag{2.7}$$

The transition probability to the flavor state $|\nu_\beta\rangle$ is

$$P(\nu_\alpha \to \nu_\beta) = |\langle\nu_\beta(0)|\nu_\alpha(t)\rangle|^2 = \left|\sum_j U_{\alpha j}U_{\beta j}^* \mathrm{e}^{-iE_j t}\right|^2 \tag{2.8}$$

With applying the Unitary condition

$$\delta_{\alpha\beta} = \left|\sum_j U_{\alpha j}U_{\beta j}^*\right|^2 = \sum_j |U_{\alpha j}|^2|U_{\beta j}|^2 + \sum_{j\neq k} U_{\alpha j}U_{\beta j}^* U_{\alpha k}^* U_{\beta k} \tag{2.9}$$

which is defined as the difference between $P(\nu_\alpha \to \nu_\beta)$ and $P(\bar{\nu}_\alpha \to \bar{\nu}_\beta)$, the Eq. 2.8 is written as

$$\begin{aligned} P(\nu_\alpha \to \nu_\beta) &= \delta_{\alpha\beta} + \sum_{j\neq k} U_{\alpha j} U^*_{\beta j} U^*_{\alpha k} U_{\beta k} (\mathrm{e}^{-i(E_j - E_k)t} - 1) \\ &= \delta_{\alpha\beta} - 4 \sum_{j>k} \mathrm{Re}(U_{\alpha j} U^*_{\beta j} U^*_{\alpha k} U_{\beta k}) \sin^2 \left(\frac{\Delta m^2_{jk}}{4E} L \right) \\ &\quad + 2 \sum_{j>k} \mathrm{Im}(U_{\alpha j} U^*_{\beta j} U^*_{\alpha k} U_{\beta k}) \sin \left(\frac{\Delta m^2_{jk}}{2E} L \right) \end{aligned} \tag{2.10}$$

where

$$\begin{aligned} \Delta m^2_{jk} &= m^2_j - m^2_k \\ L &= ct \\ \mathrm{Re}(\mathrm{e}^{-i(E_j - E_k)t} - 1) &\simeq -2 \sin^2 \left(\frac{\Delta m^2_{jk}}{4E} L \right) \\ \mathrm{Im}(\mathrm{e}^{-i(E_j - E_k)t} - 1) &\simeq \sin \left(\frac{\Delta m^2_{jk}}{2E} L \right). \end{aligned} \tag{2.11}$$

In the meanwhile, the survival probability of ν_α is obtained by setting $\alpha = \beta$ in Eq. 2.10 as

$$P(\nu_\alpha \to \nu_\alpha) = 1 - 4 \sum_{j>k} |U_{\alpha j}|^2 |U_{\alpha k}|^2 \sin^2 \left(\frac{\Delta m^2_{jk}}{4E} L \right) \tag{2.12}$$

These probabilities indicates the oscillation can occur only when massive neutrinos. The behavior of the neutrino oscillation is independent of the neutrino property i.e. Dirac particles or Majorana particle. If Majorana neutrinos, the mixing matrix is taken place as $U_{fj} \to U_{fj} \mathrm{e}^{i\alpha_j/2}$:

$$U_{\text{Majorana}} = U_{\text{PMNS}} \begin{pmatrix} \mathrm{e}^{i\alpha_1/2} & 0 & 0 \\ 0 & \mathrm{e}^{i\alpha_2/2} & 0 \\ 0 & 0 & 1 \end{pmatrix}. \tag{2.13}$$

The phase α_j causes CP violation. As described above, oscillation probability is proportional to $U_{\alpha j} U^*_{\beta j} U^*_{\alpha k} U_{\beta k}$, so the phase does not contribute it.

Global 3ν Analysis

The neutrino oscillation is measured by comparing the number of flavor neutrinos at multi-locations. One is categorized as "appearance" when counting the different flavor of neutrinos or as "disappearance" when counting common flavor. Searching parameter range is determined by choosing path length L and neutrino energy E: e.g. small L/E

enables to search small Δm^2_{ij}. Fig. 2.1 shows $\bar{\nu}_e$ disappearance of the nuclear reactor antineutrinos measured in the KamLAND experiment. As for supply source of neutrinos, natural neutrinos (solar, atmospheric) and artificial one (accelerator, reactor) are utilized. Measurement of squared mass gaps have constrained on the neutrino mass hierarchy: the normal hierarchy ($m_1 < m_2 < m_3$, NH) and inverted hierarchy ($m_3 < m_1 < m_2$, IH) types shown in Fig. 2.2 and quasi-degenerate type. Current oscillation experiments aim to distinguish the mass paterns.

Measurable oscillation parameters for the three generation mixing are listed as follows.

- known parameters :
  - $\delta m^2 \equiv m_2^2 - m_1^2$
  - $|\Delta m^2| \equiv |m_3^2 - (m_1^2 + m_2^2)/2|$
  - mixing angles : $\sin^2\theta_{12}$, $\sin^2\theta_{13}$, $\sin^2\theta_{23}$
- unknown parameters :
  - the mass ordering : sign($\pm\Delta m^2$) ($+\Delta m^2$ for NH, $-\Delta m^2$ for IH)
  - the θ_{23} octant : sign($\sin^2\theta_{23}$ - 1/2)
  - CP-violating phase δ

Compared to well-known parameters ($\delta m^2, \Delta m^2, \theta_{12}, \theta_{13}$), the θ_{23} is less precise including an octant ambiguity. For unknown parameters, presence of CP-violation is indicated by Tokai-to-Kamioka (T2K) experiment in Japan lately, in which δ is measured by comparing neutrino spectrum of $\nu_\mu \to \nu_e$ ($\bar{\nu}_\mu \to \bar{\nu}_e$) appearance with no-oscillation expectation. It favors negative value $\delta \sim \pi/2$. The allowed regions are δ =[-3.13, -0.39] rad (NH) and [-2.09, -0.74] rad (IH) at 90 % C.L. As for θ_{23}, maximal mixing ($\sin^2\theta_{23} \sim 1/2$) is weakly preferred (Iwamoto [3]).

According to the methodology in Ref. (Capozzi, Lisi, et al., 2016 [4]), the oscillation parameters of 3ν mass-mixing from the global fits are obtained by minimization of χ^2 as a function of (δm^2, $\pm\Delta m^2$, θ_{12}, θ_{13}, θ_{23}, δ), as shown in Fig. 2.3. Allowed parameter ranges at N_σ standard deviation are defined using $N_\sigma^2 = \chi^2 - \chi^2_{\rm min}$. The combination of various empirical results is implemented with the following order:

1. Solar + KamLAND + Long-baseline accelerator (LBL)
   Solar neutrino and KamLAND data has dominant constraints on δm^2 and θ_{12}. These combination provides lower/upper bounds of parameter ranges for δm^2, $|\Delta m^2|$, θ_{12}, θ_{13}, θ_{23}. But it is insensitive to the unknown parameters sign($\pm\Delta m^2$) and δ.

2. Short-baseline reactor (SBL)
   The disappearance events can strongly constrain θ_{13}. And from spectrum data, valuable bound for Δm^2 is obtained. The sensitivity to the δ increases significantly by synergetic effect of 1. and 2. combination.

3. Atmospheric neutrinos
   The atmospheric neutrinos dominantly constraints $(\Delta m^2, \theta_{23})$, and also contribute to constrain all the other oscillation parameters.

The best-fit values and errors of the oscillation parameters are listed in Table. 2.1. It provides allowed regions for the neutrino masses in Eqs. 2.1, 2.2 and 2.3, and these are translated each other through these parameters.

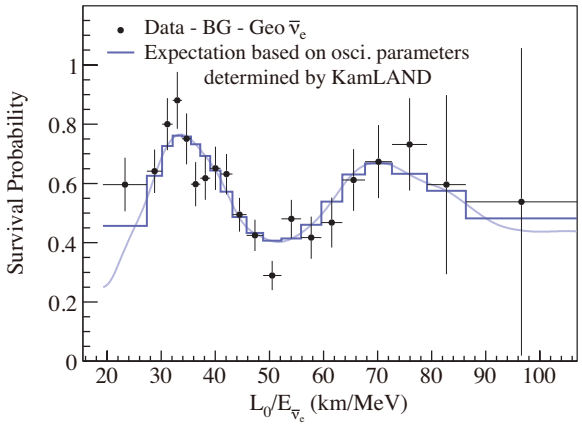

Figure 2.1.: Ratio of the $\bar{\nu}_e$ spectrum to the expectation for no-oscillation as a function of L_0/E, where background and geoneutrino events are subtracted. $L_0 =$ 180km indicates the effective path length weighted by $\bar{\nu}_e$ flux. (S. Abe, Ebihara, et al., 2008 [5]).

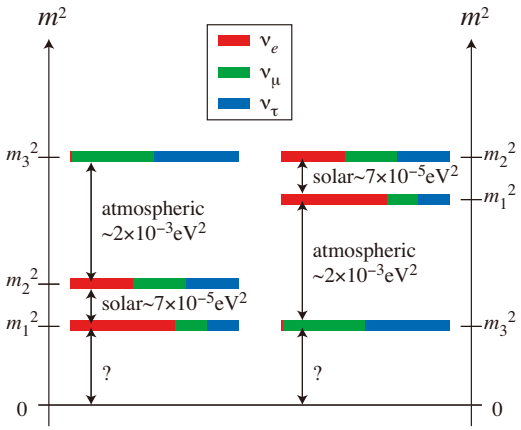

Figure 2.2.: Neutrino mass hierarchies constrained by the past neutrino oscillation measurements (King and Luhn, 2013 [6])

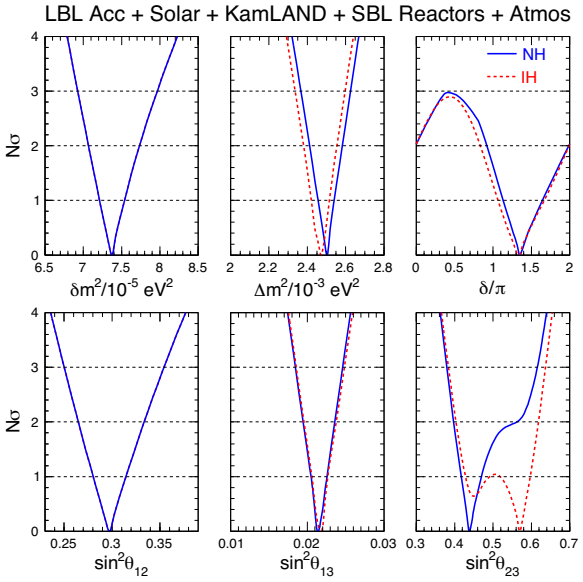

Figure 2.3.: Oscillation parameters obtained by the global analysis (Capozzi, Lisi, et al., 2016 [4]). The bounds on (δm^2, $\sin^2\theta_{12}$) are hierarchy-independent, whereas the other mass-mixing parameters are set for either NH (blue) and IH (red). The best-fit values and errors are summarized in Table. 2.1.

Table 2.1.: Neutrino mass-mixing parameters by the global 3ν oscillation analysis for two mass hierarchies (Capozzi, Lisi, et al., 2016 [4]). $\Delta m^2 = m_3^2 - (m_1^2 + m_2^2)/2$ is defined as $+\Delta m^2$ for NH and as $-\Delta m^2$ for IH herein.

parameter	NH		IH	
	best fit	3σ range	best fit	3σ range
$\delta m^2/10^{-5}\text{eV}^2$	7.37	6.93 - 7.97	7.37	6.93 - 7.97
$\Delta m^2/10^{-3}\text{eV}^2$	2.50	2.37 - 2.63	2.46	2.33 - 2.60
$\sin\theta_{12}/10^{-1}$	2.97	2.50 - 3.54	2.97	2.50 - 3.54
$\sin\theta_{13}/10^{-2}$	2.14	1.85 - 2.46	2.18	1.86 - 2.48
$\sin\theta_{23}/10^{-1}$	4.37	3.79 - 6.16	5.69	3.83 - 6.37
δ/π	1.35	0 - 2	1.32	0 - 2

2.1.2. Direct Mass Measurements

Measurement for highest energy of electron energy spectrum in β decay is attractive method to obtain absolute neutrino mass, along with search for neutrinoless double beta decay. It is independent of neutrino type; Dirac or Majorana. Electron energy spectrum in single β decay $N(E_e)$ is determined solely by phase-space volume factor. It leads with electron energy E_e and momentum p_e to:

$$S(E_e) \equiv \frac{N(E_e)}{E_e p_e F(E_e, Z)} \propto (E_0 - E_e)^2, \tag{2.14}$$

where $E_0 = Q - m_{\nu_e}$ is the maximum energy of the electron, and $F(E_e, Z)$ is the Fermi function. It indicates the shape factor $\sqrt{S(E_e)}$ as a function of E_e becomes linear. In the case of finite mass, the relation is modified to

$$S(E_e) \propto (Q - E_e)[(Q - E_e)^2 - m_\nu^2]^{1/2}(E_0 - E_e)^2, \tag{2.15}$$

Neutrino mass changes endpoint $Q \to Q - m_\nu$ and its gradient become infinite. Thus by measuring spectrum distortion, following "average electron neutrino mass" can be determined;

$$\langle m_\beta \rangle^2 = \sum_{i=1,2,3} |U_{ei}^2| m_i^2 \tag{2.16}$$

To measure extremely low mass, following tritium β-decay with minimum Q-value = 18.6 keV is usually selected.

$$^3\mathrm{H} \ \to \ ^3\mathrm{He}^+ + e^- + \bar{\nu}_e \tag{2.17}$$

The long half-life (∼12.3 yr) guarantees long stability during measurement. Fig. 2.4 shows β-spectrum distortion around its endpoint for $\langle m_\beta \rangle = 0$ and for an arbitrarily chosen $\langle m_\beta \rangle = 1$ eV. It requires to measure difference corresponding to a fraction of $2 \cdot 10^{-13}$ of all tritium β-decays. In Troitsk experiment consisting of windowless gaseous tritium source and an electrostatic electron spectrometer, the most stringent limit is obtained for Bayesian statistics (Aseev et al., 2011 [7]):

$$\langle m_\beta \rangle < 2.12 \text{ eV} \quad (95\%\text{C.L.}) \tag{2.18}$$

And Mainz experiment reports $\langle m_\beta \rangle < 2.3$ eV at 95 % C.L. (Kraus et al., 2005 [8]).

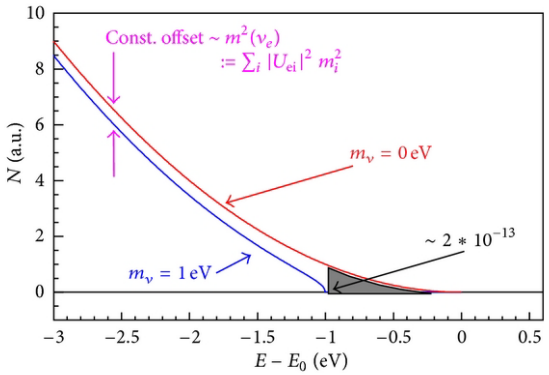

Figure 2.4.: β-spectrum focusing on its endpoint for massless neutrino (red) and for an arbitrarily chosen $m(\nu_e) = 1$ eV (blue) (Drexlin et al., 2013 [9]). In the case of tritium, gray-shaded region dominates only $2 \cdot 10^{-13}$ of all tritium β-decays.

2.1.3. Cosmological Surveys

Nonrelativistic massive neutrinos with density 113 cm^{-3} per neutrino species contribute to the density of the universe. By requiring that all masses of neutrinos does not exceed the critical value, one obtains,

$$\sum m_\nu = \sum_{i=1,2,3} m_i \leq m_{\mathrm{astro}} \tag{2.19}$$

The limit m_{astro} depends on the type of observation. Increasing of m_ν leads increase of energy density i.e. suppresses expansion rate. According to current observation, dominant effect by neutrino mass in the angular power spectra appears through gravitational lensing. Signature of 0.1 eV mass to power spectrum is only 0.1 % level without lensing. This contribution is only detectable through its influence on gravitational potential. Net effect is , when m_ν is 0.66 eV, around 10 % of suppression at multipole $l = 1000$.

In the recent result by the Planck satellite data (Planck Collaboration et al., 2016 [10]), following mass limit is obtained using Planck TT+lowP+lensing and external data of "Joint Light-curve Analysis", Baryon acoustic oscillation, and Hubble constant,

$$\sum m_\nu < 0.23 \text{ eV} \quad (95\%\text{C.L.}) \tag{2.20}$$

The result is based on standard spatially-flat ΛCDM cosmology in good agreement with Planck data. And three species of degenerated neutrinos are assumed, which is accurate approximation at the level of sensitivity in this measurement. Though model dependent, the result is already much stronger than direct mass measurement in Eq. 2.18. Using measurements of the Lyα flux power spectrum of high-redshift quasars is potential to improve the constraints. Combining with the Planck data in 2013, $\sum m_\nu < 0.15$ eV (95 % C.L.) is obtained (Palanque-Delabrouille et al., 2015 [11]).

2.2. Majorana Neutrino

In this section, Majorana neutrinos having potential to contribute neutrinoless double-beta decay, are introduced, with the Seesaw mechanism generating light neutrino mass.

2.2.1. Majorana Field

The Dirac equation,

$$(i\gamma^\mu \partial_\mu - m)\psi = 0 \tag{2.21}$$

is equivalent to the equations,

$$\begin{aligned} i\gamma^\mu \partial_\mu \psi_L &= m\psi_R \\ i\gamma^\mu \partial_\mu \psi_R &= m\psi_L \end{aligned} \tag{2.22}$$

for a fermion chiral field,

$$\psi = \psi_L + \psi_R. \tag{2.23}$$

Space-time evolution of ψ_L and ψ_R couples by the finite mass m. E. Majorana discovered that a massive particle can be described with only two independent components, i.e. Eq. 2.22 is expressed by one field, say ψ_L. This become possible by satisfying the Majorana condition,

$$\psi = \psi^C \tag{2.24}$$

ψ^C is the charge conjugated field. It implicates the equality of particle and antiparticle, that is Majorana particle. In such the Majorana field, Eq. 2.23 is rewritten as,

$$\psi = \psi_L + \psi_L^C \tag{2.25}$$

Among the known elementary fermions, only the neutrinos are neutral and can be Majorana particles. The Dirac field and the Majorana field are distinguishable only for massive particles.

2.2.2. Neutrino Mass Term

A Majorana neutrino mass is generated by a Lagrangian mass term of above the chiral-fields. Here the kinetic terms is omitted since kinematical effects of the Dirac or Majorana masses must be the same. The Dirac mass term for a Dirac neutrino field $\nu = \nu_L + \nu_R$ is written as,

$$\begin{aligned} \mathscr{L}^D_{\text{mass}} &= m_D \bar{\nu}\nu \\ &= -\frac{1}{2} m_D (\overline{\nu_R}\nu_L + \overline{\nu_L}\nu_R) \end{aligned} \tag{2.26}$$

The Majorana mass term can be written by left-handed chiral-field ν_L alone.

$$\mathscr{L}^L_{\text{mass}} = -\frac{1}{2} m_L (\overline{\nu_L^C}\nu_L + \overline{\nu_L}\nu_L^C) \tag{2.27}$$

Right-handed ν_L^C is used in place of ν_R. The neutrino Lagrangian contains only $\mathscr{L}^D_{\text{mass}}$ for a Dirac particle, and $\mathscr{L}^L_{\text{mass}}$ for ν_L existing in the SM. However, we do not know whether ν_R is present, where the Majorana mass term is,

$$\mathscr{L}^R_{\text{mass}} = -\frac{1}{2} m_R (\overline{\nu_R^C} \nu_R + \overline{\nu_R} \nu_R^C) \tag{2.28}$$

Therefore, If ν_R exists, it is possible to have the Dirac-Majorana neutrino mass term in general,

$$\mathscr{L}^{D+M}_{\text{mass}} = \mathscr{L}^D_{\text{mass}} + \mathscr{L}^L_{\text{mass}} + \mathscr{L}^R_{\text{mass}} \tag{2.29}$$

Among all known elementary particles, only neutrinos can have both of $\mathscr{L}^L_{\text{mass}}$ and $\mathscr{L}^R_{\text{mass}}$, which implies neutrinos are very special particles associating with new physics through the lepton number violating mass terms. The Dirac-Majorana mass term is only allowed for $m_L = 0$ in the framework of the SM.

The mass term is rewritten using left-handed chiral fields N_L,

$$\mathscr{L}^{D+M}_{\text{mass}} = \frac{1}{2} N_L^T C^\dagger M N_L + \text{h.c.} \tag{2.30}$$

with the symmetric mass matrix called "neutrino mass matrix",

$$M = \begin{pmatrix} m_L & m_D \\ m_D & m_R \end{pmatrix} \tag{2.31}$$

It implicates ν_L and ν_R do not have a definite mass. In order to find the fields of massive neutrinos, diagonalization of this mass matrix is needed. This can be done with a unitary transformation of the chiral fields,

$$N_L = U n_L \tag{2.32}$$

where,

$$n_L = \begin{pmatrix} \nu_{1L} \\ \nu_{2L} \end{pmatrix} \tag{2.33}$$

is the column matrix of chiral left-handed massive neutrino fields. The unitary matrix U satisfies

$$U^T M U = \begin{pmatrix} m_1 & 0 \\ 0 & m_2 \end{pmatrix}. \tag{2.34}$$

m_1 and m_2 are real and positive eigenvalues of the mass matrix M. With the transformation in Eq. 2.32, the Dirac-Majorana mass term is expressed as,

$$\mathscr{L}^{D+M}_{\text{mass}} = -\frac{1}{2} \sum_{k=1,2} m_k \overline{\nu_k} \nu_k \tag{2.35}$$

2.2.3. Seesaw Mechanism

Let us consider the interested case:

$$m_D \ll m_R, \quad m_L = 0. \tag{2.36}$$

This assumption is natural, since a Majorana mass term for the left-handed chiral field ν_L is forbidden by the symmetries and renormalizability of the SM. Eq. 2.36 provides neutrino masses,

$$\begin{aligned} m_1 &\simeq \frac{m_D^2}{m_R} \\ m_2 &\simeq m_R. \end{aligned} \tag{2.37}$$

The Dirac mass m_D is expected to be the scale of the electroweak symmetry breaking, in which Dirac fermion masses is generated through the Higgs mechanism. Hence, the order of magnitude of m_D cannot be much larger than the electroweak scale. On the other hand, the Majorana mass m_R is not subject to the restriction of the SM symmetries. m_R can be generated at the higher order, if the right-handed chiral field ν_R belongs to further high-energy symmetries. Therefore the ratio m_D/m_R become small, which gives light Majorana mass m_1 the mass from Eq. 2.37. ν_2 with heavy mass is responsible for the lightness of ν_1 like seesaw. This is the seesaw mechanism which can explain smallness of the neutrino mass naturally.

Thus far, the normal case $m_L = 0$ is considered, called "type-I seesaw". And the particular case contributed by the only high-energy scale Majorana mass, is described. Eq. 2.37 also implies the minimal mixing of the Majorana neutrinos: ν_1 is composed of active ν_L, and ν_1 is composed mainly of sterile ν_R. In general, other mechanism can contribute to the effective Lagrangian term.

It is possible to assume $m_L \neq 0$, so called "type-II seesaw", in which the mass m_L is generated by the vacuum expectation value of a Higgs triplet. There exists type-III and the combination of these models. In any case, the seesaw mechanism can provide a natural explanation of light neutrino mass, and the parameter space of these models can be constrained by the neutrinoless double-beta decay experiments.

2.3. Double-Beta Decay

Double-β decay is particular β-decay in which, two neutrons in a nucleus translates two protons. It occurs in "even-even" nucleus for the mass number A and the atomic number Z, where β-decay is strongly suppressed due to higher energy level of daughter nuclei or large spin difference, like Fig. 2.5. Therefore the double-β decay nucleus is extremely stable, exceeding 10^{18} yr of half-life. This rare decay elicits great interest for understanding neutrino properties and testing the lepton number conservation. Within the SM, it conserves lepton number and can occur with emission of two neutrinos in the final states (2ν mode). However, theories beyond SM predict the decay without emission of neutrinos, violating the lepton number conservation (0ν mode). Though it may have

various decay modes such as $2(0)\nu\beta^+\beta^+$, $2(0)\nu EC\beta^+$ and $2(0)\nu ECEC$, following modes are focused in this section:

$$\begin{aligned}(2\nu\beta\beta) &: (Z,A) \to (Z+2,A) + 2e^- + 2\bar{\nu}_e \\ (0\nu\beta\beta) &: (Z,A) \to (Z+2,A) + 2e^-\end{aligned}$$

The Feynman diagrams are shown in Fig. 2.6. In this section, basic information for each decay mode and motivation of $0\nu\beta\beta$ decay search are described.

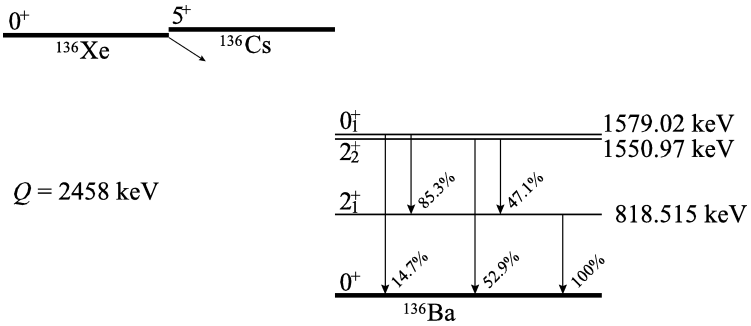

Figure 2.5.: Level diagram of double-β decay nuclide, ^{136}Xe.

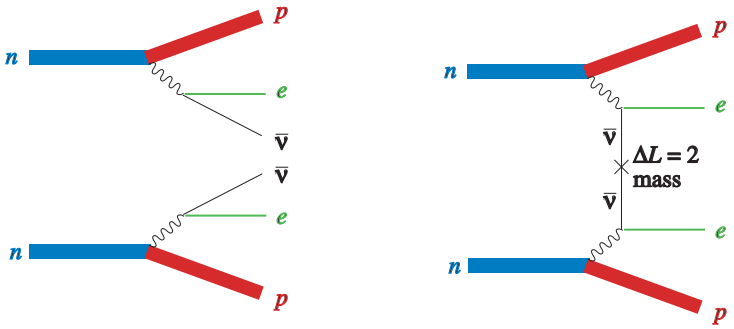

Figure 2.6.: Feynman diagrams for $2\nu\beta\beta$ (left) and $0\nu\beta\beta$ (right) decay (Strumia, 2007 [12]).

2.3.1. $2\nu\beta\beta$ Mode

$2\nu\beta\beta$ decay can be regarded as two single-β decay, except for the virtual intermediate state. The half-life with endpoint $Q_{\beta\beta}$ is expressed as follows.

$$(T^{2\nu}_{1/2})^{-1} = G^{2\nu}(Q_{\beta\beta}, Z)|M^{2\nu}|^2 \tag{2.38}$$

$G^{2\nu}$ is the phase-space factor (PSF) and $M^{2\nu}$ is the nuclear matrix element (NME), described later. Only Gamow-Teller (GT) type transition (momentum transition $\Delta J = 0, \pm 1$. $0 \to 0$ is forbidden) is taken into account as that contribution of Fermi-type (F)

Table 2.2.: Summary of recent $2\nu\beta\beta$ decay half-life (g.s.→g.s.) by the direct measurements.

	$T^{2\nu}_{1/2}$ [yr]	Experiment	Ref.
^{48}Ca	6.4×10^{19}	NEMO-3	(Arnold, Augier, Bakalyarov, et al., 2016 [15])
^{76}Ge	1.926×10^{21}	GERDA	(Agostini, Allardt, Bakalyarov, et al., 2015 [16])
^{82}Se	9.6×10^{19}	NEMO-3	(Arnold, Augier, J. Baker, A. Barabash, et al., 2005 [17])
^{96}Zr	2.35×10^{19}	NEMO-3	(Argyriades et al., 2010 [18])
^{100}Mo	6.93×10^{18}	NEMO-3	(Arnold, Augier, J. D. Baker, and A. S. Barabash, 2015 [19])
^{116}Cd	2.8×10^{19}	NEMO-3	(A. S. Barabash and V. B. Brudanin, 2011 [20])
^{130}Te	7.0×10^{20}	NEMO-3	(Arnold, Augier, J. Baker, A. S. Barabash, et al., 2011 [21])
^{136}Xe	2.165×10^{21}	EXO-200	(Albert, Auger, et al., 2014 [22])
^{150}Nd	6.4×10^{18}	NEMO-3	(Arnold, Augier, J. D. Baker, A. S. Barabash, Basharina-Freshville, Blondel, Blot, Bongrand, V. Brudanin, Busto, Caffrey, Calvez, Cascella, et al., 2016 [23])

transition ($\Delta J = 0$) is very small, i.e. the intermediate state is limited to 1^+. Fermi function for each electron is included in $G^{2\nu}$. As described above, the decay can occur regardless of neutrino properties.

$2\nu\beta\beta$ decay is already measured for more than 9 nuclei as summarized in Table. 2.2. Decay into the excited states is strongly suppressed (typically $\ll 1/100$), but it was measured in two nuclei, i.e. ^{100}Mo $\rightarrow^{100}$Ru (0^+_1) and ^{150}Nd $\rightarrow^{150}$Sm (0^+_1) with longer half-life by a factor of ∼100 (A. S. Barabash, 2010 [13]); (Kidd et al., 2014 [14]). Comparison of empirical NME with theoretical prediction gives the knowledge about nuclear structure, though it does not provide direct information to the NME of $0\nu\beta\beta$ decay which needs more complicated calculation.

2.3.2. $0\nu\beta\beta$ Mode

Search for $0\nu\beta\beta$ decay is the most effective method testing Majorana properties of neutrino, since it can occur only in a case of massive Majorana neutrino. It also violates the lepton number, which is not predicted within the SM. In various mechanisms of the violation described later, exchange of light majorana neutrino is the mainstream as the most natural. In this case, half-life of $0\nu\beta\beta$ decay $T^{0\nu}_{1/2}$ depends on the neutrino mass as follows:

$$(T^{0\nu}_{1/2})^{-1} = G^{0\nu}(Q_{\beta\beta}, Z)|M^{0\nu}|^2\langle m_{\beta\beta}\rangle^2 \tag{2.39}$$

$G^{0\nu}$ and $M^{0\nu}$ are PSF and NME for 0ν mode, described later. $\langle m_{\beta\beta}\rangle$ is called "effective Majorana mass" defined as,

$$\begin{aligned}\langle m_{\beta\beta}\rangle &= \left|\sum_{i=1,2,3}|U_{ei}|^2 \mathrm{e}^{i\alpha_i} m_i\right| \\ &= \left|c_{12}^2 c_{13}^2 \mathrm{e}^{i\alpha_1} m_1 + s_{12}^2 c_{13}^2 \mathrm{e}^{i\alpha_2} m_2 + s_{13}^2 m_3\right|\end{aligned} \tag{2.40}$$

where α_i are the unknown Majorana phases. The elements of the mixing matrix $|U_{ei}|^2$ and mass-squared difference Δm^2 are measured by the oscillation experiments. To derive $\langle m_{\beta\beta}\rangle$, only term violating the electronic number by two units is extracted from the Majorana mass terms in the Lagrangian density, as contributing to the amplitude of $0\nu\beta\beta$ decay. $\langle m_{\beta\beta}\rangle$ can be thought as the electron neutrino mass, though it is different from the "electron neutrino mass" ruling single-β decay.

From Eq. 2.39, one can determine the neutrino mass pattern from the degenerate, the normal hierarchy (NH) or the inverted hierarchy (IH), using known values and half-life limits. If existence of Majorana neutrinos is proved, absolute mass scale can be determined independently on the Majorana phases, though it needs dramatic decrease of uncertainties for the NMEs. Ref. (Šimkovic et al., 2013 [24]) reports that there is potential to measure α_i using very weak $\alpha_{21} = \alpha_2 - \alpha_1$ dependence on the lightest mass m_{lightest} (m_1 for the NH, m_3 for the IH) only for the case of the IH. (In this estimation, $m_{\mathrm{lightest}} = 0 - 10$ meV is assumed, which is expected by the strongest constraint from cosmological measurement. It requires within 50 % of determination accuracy for $\langle m_{\beta\beta}\rangle$ at least. Thus, the motivation of $0\nu\beta\beta$ decay search assuming exchange of light Majorana neutrino is summarized as follows,

- Whether the neutrinos are Majorana or Dirac particles
- Lepton number violation
- Neutrino mass hierarchy
- Scale of the neutrino masses

With the weak interaction Hamiltonian $H_W = G_F/\sqrt{2} J_\mu^\dagger J_\mu$ ($J_\mu = 2(\bar{\nu}_L \gamma_\mu e_L^- + \bar{u}_L \gamma_\mu d_L)$), the effective operator for $0\nu\beta\beta$ decay is expressed as,

$$H_{\mathrm{eff}} = (\sqrt{2} G_F \cos\theta_c)^2 (\bar{e}_L \gamma_\mu \nu_L)(-\overline{\nu_L^c} \gamma_\nu e_L^c) \times [\bar{p}\gamma^\mu (1 - g_A\gamma_5) n][\bar{p}\gamma^\nu (1 - g_A\gamma_5) n]. \tag{2.41}$$

Amplitude of 0ν mode configured by leptonic and hadronic parts, is calculated based on it. It requires summation over the intermediate excited states on the NME calculation, but the closure approximation commonly can be applied. Within this approximation, difference of nucleon energy between initial and intermediate states is replaced into average energy, and the sum over intermediate states is taken by closure approximation, $\sum_n |n\rangle\langle n| = 1$. It drastically simplifies numerical calculation. Decay rate of 0ν mode conducing to Eq. 2.39 is obtained.

Lepton Number Violating Mechanism

How ν and $\bar{\nu}$ transitions in $0\nu\beta\beta$ decay is of much interest to particle physics.

There are several proposed mechanism of lepton number violating processes, which includes one without intermediation of neutrinos as follows.

- light majorana-neutrino exchange
  The coupling strength depends on the light majorana neutrino mass. This is the most commonly discussed process, described later.

- heavy majorana-neutrino exchange
  If heavy neutrino which has a mass much larger than $0\nu\beta\beta$ decay energy mediates the transition, it basically follows the case of light neutrino exchange. The difference is that effective transition operators are local due to that the neutrino propagators can be constructed to points. The smaller the coupling strgenth become, the heavier the neutrino mass become, unlike light majorana-neutrino.

- majoron emission
  It is neutrino mass independent mechanism mediated by majorons, i.e. Nambu-Goldstone bosons which are only couple to neutrinos. Coupling with right handed neutrino is realistic theoretically, but the effective coupling is small due to the smallness of the mixing matrix. In this mechanism, the Majorana property of neutrino cannot be tested. Though difficulty of detection, extraction of limit is reported in various experiments.

- R-parity breaking SUSY mechanism
  R-parity is defined as $R = (-1)^{3B-L+2s}$ in SUSY (B: baryon number, L: lepton number, s: spin). It takes +1 for ordinary particles and -1 for their superpartners. R-parity violating superpotential can lead to majorana neutrino masses without introducing the right-handed neutrino and invoking the see-saw mechanism (Haug et al., 2000 [25]); (Hirsch and Valle, 2004 [26]).

2.3.3. Phase Space Factor

Phase space factor (PSF) is defined as densities of states available per unit energy, which can be calculated precisely by solving Dirac equation. It is specific to Q-value and atomic number Z of the target nucleus. The recent study accepts more exact electron wave function including electron screening effect and finite nuclear size, and more realistic proton density distribution in the daughter/parent nucleus. PSF for the $2\nu\beta\beta$ decay is expressed using electron ($\epsilon_{1,2}$) and neutrino ($\omega_{1,2}$) energies as:

$$\begin{aligned} G^{2\nu}(0^+ \to 0^+) = \frac{2\tilde{A}^2}{3\ln\, 2g_A^4(m_ec^2)^2} & \int_{m_ec^2}^{Q^{\beta\beta}+m_ec^2} d\epsilon_1 \\ \times & \int_{m_ec^2}^{Q^{\beta\beta}+2m_ec^2-\epsilon_1} d\epsilon_2 \int_0^{Q^{\beta\beta}+2m_ec^2-\epsilon_1-\epsilon_2} d\omega_1 \\ \times & f_{11}^0 w_{2\nu}(\langle K_N\rangle^2 + \langle L_N\rangle^2 + \langle K_N\rangle\langle L_N\rangle) \end{aligned} \tag{2.42}$$

where $Q^{\beta\beta} = M(A, Z_0) - M(A, Z_0 - 2) - 4m_e c^2$ is the Q-value of the decay (electron mass m_e). Expressions of electron phase factor f_{11}^0, $\langle K_N \rangle$, $\langle L_N \rangle$ and excitation energy $\tilde{A}$ are introduced in (Mirea, Pahomi, and Stoica, 2014 [27]). The differential rate of the decay is expressed as:

$$w_{2\nu} = \frac{g_A^4 (G\cos\theta_C)^4}{64\pi^7\hbar} \omega_1^2 \omega_2^2 (p_1 c)(p_2 c)\epsilon_1 \epsilon_2 \tag{2.43}$$

As to $0\nu\beta\beta$ decay, the expression leads:

$$G^{0\nu}(0^+ \to 0^+) = \frac{2}{4g_A^4 R_A^2 \ln 2} \int_{m_e c^2}^{Q^{\beta\beta}+m_e c^2} f_{11}^0 w_{0\nu}\, d\epsilon_1 \tag{2.44}$$

where,

$$w_{0\nu} = \frac{g_A^4 (G\cos\theta_C)^4}{16\pi^5} (m_e c^2)^2 (\hbar c^2)(p_1 c)(p_2 c)\epsilon_1 \epsilon_2 \tag{2.45}$$

In the calculation, the Fermi constant $G = 1.16637 \times 10^{-5}$ GeV^{-2}, $\cos\theta_C = 0.9737$ and nuclear radius $R_A = 1.2A^{1/3}$ fm are used.

The electron phase factor f_{11}^0 is derived by solving Dirac equation in a central potential. In the recent calculation, influence of nuclear structure and electron screen effects are taken into account for a Coulomb potential:

$$V(Z, r) = \alpha\hbar c \int \frac{\rho_e(\vec{r'})}{|\vec{r} - \vec{r'}|} d\vec{r'} \tag{2.46}$$

which is derived by solving the Schrödinger equation for a Woods-Saxon potential. The charge density $\rho_e(\vec{r})$ in each single particle state is calculated from the proton (Woods-Saxon) wave function and occupation amplitude of the state. The screening effect is included by multiplying the $V(r)$ with a function $\phi(r)$, which is the solution of the Thomas Fermi equation. In case of $0\nu\beta^-\beta^-$ decay,

$$rV_{\beta\_\beta\_}(Z, r) = (rV(Z, r) + 2) \times \phi(r) - 2 \tag{2.47}$$

This PSF calculation with more exact Dirac equation caused significant difference compared to older calculations which assume point charge and constant charge density especially for heavier nuclei. In Ref. (Mirea, Pahomi, and Stoica, 2014 [27]), redefined PSF $G'^{0\nu}$ is introduced to separate the contribution of the axial vector coupling constant g_A, which satisfies $G^{0\nu} = G'^{0\nu} g_A^4 / m_e^2$. The computation results $G'^{2\nu}(^{136}\text{Xe}) = 1332 \times 10^{-21}$ yr^{-1} and $G'^{0\nu}(^{136}\text{Xe}) = 14.54 \times 10^{-15}$ yr^{-1}. Dominant uncertainty comes from the nuclear radius and there are small contribution from experimental error for Q-value measurement and the screening error. Total uncertainty is estimated to be ∼7 %.

2.3.4. Nuclear Matrix Element

If a single mechanism determined by lepton violating number η_κ involves it, half-life of $0\nu\beta\beta$ decay $T^{0\nu}_{1/2}$, having endpoint $Q_{\beta\beta}$ and the atomic number Z, is described as follows:

$$(T^{0\nu}_{1/2})^{-1} = G^{0\nu}(Q_{\beta\beta}, Z)|M'^{0\nu}_\kappa|^2|\eta_\kappa| \tag{2.48}$$

$|M'^{0\nu}_\kappa|$ and $G^{0\nu}$ are, respectively, nuclear matrix element and phase-space factor, which is numerically calculated assuming nuclear structure described later. The NME is defined as,

$$M'^{0\nu}_\kappa = \left(\frac{g_{A,\mathrm{eff}}}{g_A}\right)^2 M^{0\nu}_\kappa \tag{2.49}$$

which allows to separate uncertainty of "quenched axial-vector coupling constant" $g_{A,\mathrm{eff}}$.

Here we describe the most popular ν-to-$\bar{\nu}$ transition associated by exchange of light majorana-neutrino. In this case, η_ν is expressed with "effective neutrino mass" $\langle m_{\beta\beta}\rangle$ and electron mass m_e.

$$\eta_\nu = \left|\frac{\langle m_{\beta\beta}\rangle}{m_e}\right|^2 \tag{2.50}$$

NME is composed of Fermi (F), Gamow-Teller (GT) and tensor (T) part as

$$\begin{aligned} M^{0\nu}_\nu &= -\frac{M^{0\nu}_F}{(g_{A,\mathrm{eff}})^2} + M^{0\nu}_{GT} - M^{0\nu}_T \\ &= \langle 0^+_i|\sum_{kl}\tau^+_k\tau^+_l[-\frac{H_F(r_{kl})}{(g_{A,\mathrm{eff}})^2} + H_{GT}(r_{kl})\sigma_{kl} - H_T(r_{kl})S_{kl}]|0^+_f\rangle \end{aligned} \tag{2.51}$$

where,

$$S_{kl} = 3(\vec{\sigma}_k\cdot\hat{\mathbf{r}}_{kl})(\vec{\sigma}_l\cdot\hat{\mathbf{r}}_{kl}) - \sigma_k, \quad \sigma_{kl} = \vec{\sigma}_k\cdot\vec{\sigma}_l \tag{2.52}$$

The radial part of exchange potentials are

$$H_{F,GT,T}(r_{kl}) = \frac{2}{\pi}R\int_0^\infty \frac{j_{0,0,2}(qr_{kl})h_{F,GT,T}(q^2)q}{q+\overline{E}}dq. \tag{2.53}$$

R is the nuclear radius and $\overline{E}$ is the average energy of intermediate states used in closure approximation.

NME directly influences magnitude of $0\nu\beta\beta$ decay. The evaluation basically depends on theoretical calculation, which needs understanding of complicated nuclear structure. It starts from evaluation of two interacting particles with transition operator discussed in Sec. 2.3.2. Some information can be extracted from experiments. In the construction of the many body wave functions in the initial/final state, there are some features such as quenching effect on g_A and short range correlation. For the virtual intermediated states, closure approximation is adopted except for QRPA model. In this section, the main characteristics of construction and the uncertainties are described.

- Interacting shell model (ISM)
  Part of orbits in major shells around the Fermi level is considered, but all the possible correlations within the space are included. Proton-proton, neutron-neutron and proton-neutron pairing correlations are treated properly. Owing to significant progress in shell-model configuration mixing approaches, calculations are proceeded in several nuclei.

- Microscopic interacting boson model (IBM-2)
  The IBM is the boson model treating collective motion. All physical quantities are consists of d boson and s boson, having spin-parity 0^+ and 2^+, respectively, which reduces the number of parameters.

- Quasiparticle random phase approximation (QRPA)
  Random phase approximation is introduced to describe excitation of an even-even to an odd-odd nucleus. Quasi-particles of the pn mode is incorporated to treat the strong pairing force between two protons or two neutrons under the BCS approximation. Particle-particle strength of the nuclear Hamiltonian g_{pp} is fixed. Uncertainty of this variations in $0\nu\beta\beta$ decay can be significantly eliminated by adjusting it to $2\nu\beta\beta$ decay rate.

- Projected Hartree-Fock Bogoliubov method (PHFB)
  In the PHFB, wave functions of good particle number and angular momentum are obtained by projection on the axially symmetric intrinsic HFB states. The nuclear Hamiltonian is restricted only to quadrupole interaction.

- Energy Density Functional methods (EDF)
  It employs approach of the generating coordinate method, where initial/final many-body functions are found as linear combinations of particle number N, Z and angular momentum projection. The wave functions are solutions to the variation after particle number projection equations assuming axial quadrupole deformation. Rather constant NME values around the average 4.7, are derived for nuclei which does not have significant difference of deformation between initial and final states.

Uncertainty for calculated $0\nu\beta\beta$ decay NMEs is estimated up to factor of 2 or 3 depending on the target nucleus. It is mostly due to differences between the ISM and the other methods (QRPA, PHFB, EDF, IBM) and also due to unknown effective value of quenched axial-vector coupling constant g_A (discussed later). The various uncertainties in NME calculation are listed below.

- Closure approximation

- Two-nucleon short range correlations and finite nucleon size

- Effect of deformation

- Occupancies of individual orbits

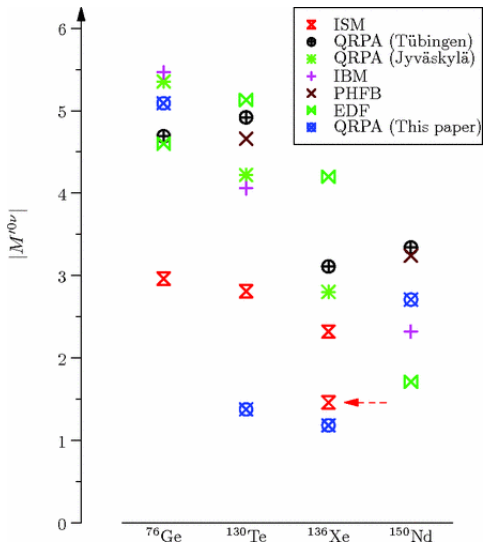

Figure 2.7.: The values of nuclear matrix elements for $g_A = 1.25$ in various models (Mustonen and Engel, 2013 [28]).

Quenching of Axial-Vector Coupling Constant

It is well known that calculated strength of Gamow-Teller β-decay transitions are significantly larger than experimental ones. The effect is known as quenching of the axial-vector current matrix elements. To make sense, quenched value $g_{A,\mathrm{eff}} = 1.0$ is introduced instead of true value $g_A = 1.269$ ($g_A = 1.254$ was considered previously), indicating up to 30 % of quenching effect. Currently, role of g_A become more important, since, as shown in Eqs. 2.48 and 2.49, $g_{A,\mathrm{eff}}$ appears to the fourth power in the decay rate, which significantly reduces half-life by as much as a factor 2-3.

The value of $g_{A,\mathrm{eff}}$ can be extracted from the knowledge of single-β and $2\nu\beta\beta$ decay. According to comparison of the calculated and experimental matrix elements of $2\nu\beta\beta$ decay, the quenched values are estimated to be $g_{A,\mathrm{eff}}^{\mathrm{IBM\text{-}2}} = 1.269A^{-0.18}$ and $g_{A,\mathrm{eff}}^{\mathrm{ISM}} = 1.269A^{-0.12}$ from its smooth dependence on the atomic number, A as shown in Fig. 2.8. In the extraction from single-β decay and electron capture, Fermi-surface quasiparticle model is used, where squared $g_{A,\mathrm{eff}}$ is expressed as the product of transition from even-even to odd-odd nuclei and the transition from odd-odd to even-even nuclei.

Thus, extraction of the quenched factor is highly dependent on model calculations and the assumption. The origin of the quenching is not understood completely, but thought as limitation of the model space in which calculations are done, and omission of non-nucleonic degrees of freedom. Further discussions and tests are proceeded for more accurate estimation.

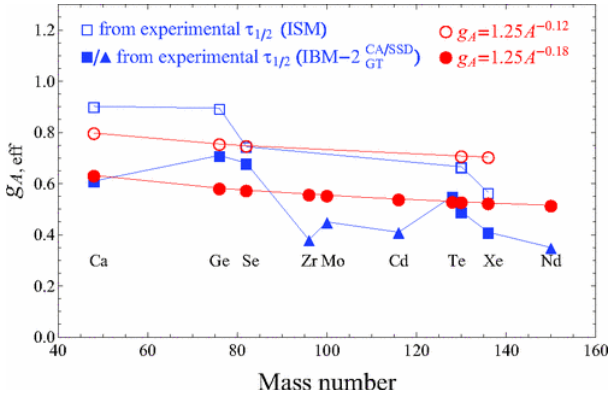

Figure 2.8.: The values of effective axial-vector coupling constant $g_{A,\mathrm{eff}}$ extracted from experiment and theoretical calculation assuming NME models of ISM and IBM-2 (Barea, Kotila, and Iachello, 2013 [29]).

2.4. Experimental Searches for Double-Beta Decay

Double-beta decay experiments are categorized into direct measurements and indirect measurements such as Geochemical measurements and Radiochemical measurements. In this section, experimental requirements and techniques of current mainstream i.e. direct measurement are described, with latest $0\nu\beta\beta$ results.

2.4.1. Choice of Isotopes

Selection of double-beta decay isotopes is the first issue to search $0\nu\beta\beta$ decay. The compatibility is taken account primary in terms of scalability and low background. Followings are fundamental points for the choice.

- high Q-value
  Q-values of double-beta decay isotopes directly influence have an affect on backgrounds in which one should pay attention to endpoint of natural γ radioactivity i.e. 2.615 MeV line of ^{208}Tl from thorium theries and ^{214}Bi (Q = 3.270 MeV) from uranium-series, especially. Fig. 2.9 shows Q-values of candidate isotopes, where are divided into three groups by above backgrounds. (^{48}Ca, ^{96}Zr, ^{150}Nd) are comparatively ideal due to Q-values high than ^{208}Tl and ^{214}Bi, though having difficulty in their enrichment. (^{76}Ge, ^{130}Te, ^{136}Xe) have to cope with buy they have another advantages i.e. a powerful detection technique for ^{76}Ge, high isotopic abundance for ^{130}Te and ease of enrichment for ^{136}Xe.

- high isotopic abundance
  To search neutrino mass region of interest, it requires large quantities of target isotopes. Natural abundances of candidate isotopes except for ^{130}Te (33.8 %) are below 10 % as shown in 2.3, which indicates necessity for enrichment. Especially, that of ^{48}Ca is extremely low (0.187 %).

Table 2.3.: Commonly used double-beta decay nuclei

	Q-value [MeV]	Isotopic abundance [%]	Enrichable by centrifugation
^{48}Ca	4.272	0.187	No
^{76}Ge	2.039	7.8	Yes
^{82}Se	2.995	9.2	Yes
^{96}Zr	3.350	2.8	No
^{100}Mo	3.034	9.6	Yes
^{116}Cd	2.814	7.5	Yes
^{130}Te	2.527	33.8	Yes
^{136}Xe	2.458	8.9	Yes
^{150}Nd	3.371	5.6	No

- ease of enrichment
  Enrichment of candidate isotopes is helpful for scalability and background reduction. The only technique extensively used so far for double-beta decay experiments is the gas-centrifuge one which is applicable only to gases. Not only ^{136}Xe gas, ^{76}Ge, ^{130}Te, ^{82}Se, ^{100}Mo and ^{116}Cd can be enriched since their gas compounds (normally fluorides) are stable. Compared to the enrichment cost of 50-100 \$/g for germanium, the approximate scaling factors are 1 for ^{82}Se and ^{100}Mo, 3 for ^{116}Cd, 0.2 for ^{130}Te, and 0.1 for ^{136}Xe.

Theoretically, large PSF and NME are favorable to get strict limits on $m_{\beta\beta}$ from Eq. 2.39, but their inverse correlation is reported in Ref. (ROBERTSON, 2013 [30]). It turns out that all isotopes have qualitatively the same decay rate per unit mass.

2.4.2. Fundamental Requirements

In order to search very rare $0\nu\beta\beta$ decay, followings are desirable features:

- Good energy resolution
  The requirement is important for not only distinction of sharp peak of $0\nu\beta\beta$ from flat backgrounds, but also protection from the intrinsic background $2\nu\beta\beta$. Contribution of $2\nu\beta\beta$ background in the $0\nu\beta\beta$ peak region is approximately expressed by their half-lives. Following $R_{0\nu/2\nu}$ is the ratio of approximate counts in the $0\nu\beta\beta$ peak,

$$R_{0\nu/2\nu} = \frac{m_e}{7Q_{\beta\beta}\delta^6} \cdot \frac{T^{2\nu}_{1/2}}{T^{0\nu}_{1/2}}, \tag{2.54}$$

  where $\delta = \Delta E_{\mathrm{FWHM}}/Q_{\beta\beta}$ is the fractional energy resolution at the Q-value. Slow $2\nu\beta\beta$ decay of ^{136}Xe ($T^{2\nu}_{1/2} = 2.165 \times 10^{21}$ yr) is more favorable than fast process, ^{110}Mo ($T^{2\nu}_{1/2} = 6.93 \times 10^{18}$ yr), as shown in Table. 2.2.

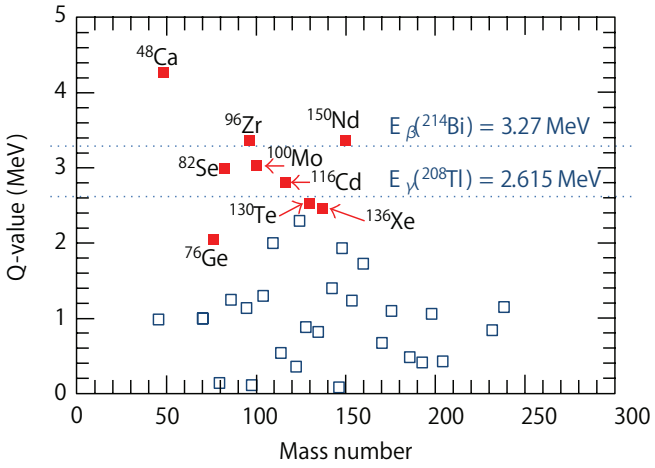

Figure 2.9.: Q-values of double-beta decay isotopes. Often-used ones are highlighted with primary natural radionuclides (Giuliani and Poves, 2012 [31]).

- Low background
  In order to detect very rare decay, extremely low impurity materials are desirable, which can compensated by various tracking and tagging methods. Well-designed passive or active shieldings are also needed.

- Large isotope mass
  To cover the inverted mass hierarchy, 100-1000 kg target mass is required compared to current status i.e. ∼10-100kg.

These cannot be met simultaneously in a single detector. Therefore, it is up to the experimentalists to choose which one to privilege in order to get the best sensitivity.

2.4.3. Current Status and Future Prospects

Time Projection Chambers

Particle tracking is a powerful technique to distinguish the $0\nu\beta\beta$ signal from a background events. The signal is characterized by a pair of very short tracks originated at the source position. It can distinguish with background signal with the same energy characterized by much longer tracks or by multi-site energy depositions (as in the case of γ or $\gamma + \beta$ emissions).

As to tracking detector using gas counters or Time Projection Chambers (TPC's), the $\beta\beta$ source is normally introduced separately from the detector. However, ^{136}Xe source enables the homogeneous detector owing to its emission of scintillation light. ^{136}Xe is filled as gas or liquid. Here, status of a running experiment EXO-200 (liquid-Xe case) and NEXT experiment under construction (gaseous-Xe) are described.

EXO-200 Enriched Xenon Observatory (EXO) is a experiment to search for ^{136}Xe $0\nu\beta\beta$ decay using a cylindrical TPC filled with liquid xenon (LXe). It is located at a depth of 1585 m.w.e in the WIPP. In the LXe enriched to (80.6 $\pm$ 0.1) % in the isotope ^{136}Xe, the ionization signal is read-out by crossing wires at the two end of the cylinder, which provides two-dimensional localization. The scintillation signal produced by particle interactions in LXe is also read-out. It provides complementary energy information used to improve energy resolution, to reject incomplete charge collection events or alpha particles, and to construct three-dimensional position (z-coordinate is obtained by using the difference in the arrival time between the ionization and scintillation signals). The spacial information enables to reject events from the chamber walls by setting a fiducial volume, and to classify signals in single-site (SS) and multi-site (MS), where $\sim$82.5 % of $\beta\beta$ signals belong to the SS (The residual is classified into MS because of bremsstrahlung). MS events are utilized for background estimation.

The first phase, EXO-200 started data taking in 2011 with 150 kg of enriched xenon (110 kg is inside the detector chamber due to continuous xenon circulation). At the latest report in 2014 (Albert, Auty, et al., 2014 [32]), the experiment achieved 4 % FWHM at $Q_{\beta\beta}$ FWHM and a background rate of 1.5×10^{-3} events/keV/kg/yr or 0.23 events/kg/yr in their ROI (2.250 - 2.600 MeV). The obtained limit on $0\nu\beta\beta$ half-life is

$$T^{0\nu}_{1/2}(^{136}\mathrm{Xe}) > 1.1 \times 10^{25}\ \mathrm{yr} \quad (90\%\mathrm{C.L.}).$$

A precise measurement of $2\nu\beta\beta$ decay half-life is also reported (Table. 2.2).

EXO-200 Phase-II began operation in Jan. 2016, where Rn level in air gap near the LXe vessel is reduced by a factor $\sim$10, and rejection efficiencies of primary backgrounds such as ^{232}Th and ^{137}Xe are improved. The sensitivity is expected to be $T^{0\nu}_{1/2} > 5.7\times10^{25}$ yr. As far future, nEXO experiment is proposed, treating 5 tonnes of enriched xenon. The goal sensitivity is $T^{0\nu}_{1/2} > 6.6 \times 10^{27}$ yr (90 % C.L.) after 5 yr of running. As the option, signal identification by tagging ^{136}Xe $\beta\beta$ decay daughter (^{136}Ba^{++}) is proposed.

NEXT More recently proposed experiment, Neutrino Experiment with a Xenon TPC (NEXT) uses enriched gaseous xenon in a high-pressure (1.5 MPa) TPC. The lower density of the gas enables longer tracks for electrons from $\beta\beta$ decay, providing a powerful tool to remove backgrounds from external γ-rays. Another advantage is very good ROI energy resolution of 0.5 - 0.7 % better than the other Xe approaches. The challenge is that, due to the low density detector, it requires low background vessel and shielding against external backgrounds.

Currently, NEXT uses depleted xenon for calibration, evaluation of energy resolution (0.58 % FWHM at $Q_{\beta\beta}$ is expected) and topological rejection. In $\sim$100 kg target mass phase, it intends to achieve background rate, $< 4 \times 10^{-4}$ events/keV/kg/yr in ROI, and $T_{1/2} = 6 \times 10^{25}$ yr (90 % C.L.) after 3 yr of running. Analogous experiment, PandaX-III is proceeded in China. It already purchased 150 kg of 90 % enriched xenon and the first module will be installed in 2017.

High Purity Germanium Detectors

Germanium is a semiconductor and can be converted into semiconducting radiation detectors that measure ionization charges directly. As with TPC, events are classified into multiple site events (MSE) and Single site events (SSE) by pulse shape, and the latter includes $\beta\beta$ events. Backgrounds in SSE originate from single Compton scattering, and from photoelectric or multi-site interactions very close to each other. High-Purity Germanium (HPGe) achieves contamination levels of less than one part in 10^{21} and have the best energy resolution of any $\beta\beta$ technology (0.15 % at $Q_{\beta\beta}$). The main drawbacks of germanium are the cost of detector fabrication and complexity associated with deploying many detectors. A slightly lower $Q_{\beta\beta}$ (2.039 MeV) requires consideration of more potential sources of background.

GERDA The GERmanium Detector Array (GERDA) uses coaxial arrays of ∼86 % enriched HPGe detectors which submerge directly in the cryogen, 64 m^3 of liquid argon (LAr). LAr also acts as active shield owing to its scintillation light. 590 m^3 of ultrapure water surround steel cryostat holding LAr. Main backgrounds are ^{208}Tl, ^{214}Bi (γ), cosmogenic ^{42}Ar (β), and ^{210}Po from electrode surface or ^{222}Rn in LAr (α).

GERDA started data taking of Phase I in 2011, collected 21.6 kg-yr exposure. By combining with previous experiments i.e. International GErmanium EXperiment (IGEX) and Heidelberg-Moscow (HDM) experiment, GERDA obtained a $0\nu\beta\beta$ decay limit (Agostini, Allardt, Andreotti, et al., 2013 [33]),

$$T^{0\nu}_{1/2}(^{76}\text{Ge}) > 3.0 \times 10^{25} \text{ yr} \quad (90\%\text{C.L.}).$$

GERDA started Phase-II from 2015, where target mass was doubled and background level reduced by factor ∼10. 30 new Broad Energy Germanium (BEGe) detectors for which, signal electrode is very small compared to standard HPGe, enhancing the differences between SSE and MSE pulses. The BEGe detector accomplished the lowest background in ROI, $7^{+11}_{-5} \times 10^{-4}$ events/keV/kg/yr. Preliminary result (Collaboration, 2016 [34]) combined with Phase I data, is reported as following,

$$T^{0\nu}_{1/2}(^{76}\text{Ge}) > 5.2 \times 10^{25} \text{ yr} \quad (90\%\text{C.L.}).$$

which corresponds to $\langle m_{\beta\beta} \rangle < 160 - 260$ meV (90 % C.L.).

MAJORANA The MAJORANA demonstrator also uses HPGe detectors, but does not have LAr like GERDA, which allows to search for low-energy rare events, such a light-WIMP dark matter and solar and cosmological axions. It intends to demonstrate backgrounds low enough to justify building a tonne scale experiment. The MAJORANA and GERDA intend to merge and pursue a joint tonne-scale $0\nu\beta\beta$ experiment that combines the best technology from both collaborations.

Loaded Organic Liquid Scintillators

The idea is to utilize huge liquid scintillator or water-Cherenkov detectors that were originally designed and employed for neutrino oscillation measurements, for $0\nu\beta\beta$ decay

searches, with minor modifications and limited expenses. These detectors already satisfy requirements for $0\nu\beta\beta$ measurements: low radioactivity, active shielding, underground location, huge detector size, and a high detector efficiency. It enables reaching higher sensitivity in a relatively short period, which is already demonstrated by KamLAND-Zen. The $\beta\beta$ source is dissolved in liquid scintillator, or placed an array of crystals inside its core. The disadvantage is the intrinsic poor energy resolution for liquid scintillator, which limits the choice of sources (one should select slow $2\nu\beta\beta$ decay isotopes), and does not have powerful background rejection techniques.

SNO+ The SNO experiment, located in the one of the deepest experimental sites (6010 m.w.e), was an imaging Cherenkov detector used for a successful campaign of solar neutrino measurements. The detector consists of a 12 m diameter transparent acrylic vessel, which contains 1 kton of ultra pure heavy water (D_2O). The vessel was submerged in normal water and observed by ∼9,500 phototubes. In SNO+, unenriched tellurium will be loaded to an organic liquid scintillator, Linear Alkyl Benzene (LAB) with a PPO fluor (2.5-diphenyloxazole), in place of heavy water medium. As the first stage, at least 0.3 % of natural tellurium (equivalent to 800 kg of ^{130}Te) will be loaded. The data taking will start in 2017, and the goal sensitivity is $T^{0\nu}_{1/2} > 9.4\times10^{25}$ yr. Upgrades of purification systems, PMTs, and data acquisition will be completed before the phase.

Bolometric Detectors

A thermal detector is a sensitive calorimeter which measures the energy deposited by a single interacting particle through the corresponding temperature rise. This is accomplished by running the detector at very low temperatures, since, according to the Debye law, the heat capacity of a single dielectric and diamagnetic crystal at low temperature is proportional to the ratio $(T/T_D)^3$ (T_D is the Debye temperature). The bolometer consists of following components:

- particle absorber (the sensitive mass of the device where the particles deposit their energy)
- temperature sensor
- thermal link to the heatsink

Requirements for the absorber is only a low heat capacity and the capability to stand the cooling in vacuum, which allows choosing the material quite freely. Therefore, it is compatible with rare event searches. The bolometer has also excellent energy resolution, since it is limited only by the thermodynamical fluctuations of thermal phonons through the thermal link.

On the other hand, there is a intrinsic noise coming from vibrations through the induced thermal dissipations (microphonic noise). And long thermal integration times tends to wash out any possible difference in the time development of the signals, which is crucial in the IH region. It requires hybrid techniques such as the simultaneous detection of scintillation.

CUORE The Cryogenic Underground Observatory for Rare Events (CUORE) is located at a depth of 3400 m.w.e in the LNGS. It uses cryogenic bolometers made from unenriched TeO_2. ^{130}Te $\beta\beta$ source has the highest isotopic abundance of any candidate isotopes (34.5 %) and has a good Q-value (2.527 MeV), though it is close to the sum energy (2.5057 MeV) of the gammas emitted in the decay of cosmogenic ^{60}Co from copper in the cryostat. In the predecessor of CUORE, CUORE-0 used 52 TeO_2 crystals (11 kg of ^{130}Te) with the size of $5\times5\times5$ cm^3, which are operated at 10 mK. The temperature sensor is a neutron-transmutation-doped Ge thermistor. Main drawbacks for background are contamination especially on or near crystal surfaces, complicated cryogenics, and signal readout. CUORE-0 achieved good energy resolution, 5.1 $\pm$ 0.3 keV at $Q_{\beta\beta}$. And it reported stringent limit on this half-life in 2015, with 9.8 kg-yr exposure and 5.8×10^{-2} events/keV/kg/yr, as follows (Alfonso et al., 2015 [35]),

$$T^{0\nu}_{1/2}(^{130}\text{Te}) > 4.0 \times 10^{24} \text{ yr} \quad (90\%\text{C.L., Bayesian}).$$

which includes the Cuoricino experiment result (19.75 kg-yr). In CUORE, 19 towers of 52 crystals (200 kg of ^{130}Te) will be arranged in a low-activity lead shield. It hopes to achieve a sensitivity of $T_{1/2} > 3.5 \times 10^{26}$ yr with 10 yr of measurement, and with background level of 10^{-3} events/kg/keV/yr. As a far future, CUORE Upgrade with Particle IDentification (CUPID) is proposed, where it explores entire of the IH, as hybrid bolometers using ^{130}Te, ^{82}Se, ^{100}Mo and ^{116}Cd.

Inhomogeneous Tracking Detectors

It separates the $\beta\beta$ sources from the detection device, so called "inhomogeneous" detector. The sources are inserted in the detector, which allows choosing any solid $\beta\beta$ sources. However, it has generally poorer energy resolution than homogeneous detectors such as HPGe and bolometers. This approach is established by NEMO-3 experiment, and its upgrade, SuperNEMO is under construction. Running experiment, DCBA/MTD (Drift Chamber Beta-ray Analyzer and Magnetic Tracking Detector) in Japan treats 30 g of natural ^{100}Mo.

SuperNEMO Predecessor of SuperNEMO, the Neutrino Ettore Majorana Observatory (NEMO-3) located at 4800 m.w.e at LSM, which ran from 2003 to 2011. The detector is combination of gas tracking counters and calorimeters. The tracker is associated with particle charge identification (owing to a presence of magnetic field), event characterization and timing. The full topological event reconstruction has ability to search for different mechanisms for $\beta\beta$ decay, e.g. neutrinoless quadruple beta ($0\nu4\beta$) decay as follows,

$$^{150}\text{Nd} \rightarrow {}^{150}\text{Gd} + 4e^- \quad (Q = 2.079\text{MeV})$$

Cylindrical detector is divided into 8 sectors, where specific study of each isotope (^{100}Mo, ^{82}Se, ^{116}Cd, ^{48}Ca, ^{150}Nd, ^{96}Zr, ^{130}Te) was operated. The backgrounds are originated from ^{214}Bi due to ^{222}Rn contamination in the gas counters, and from internal/external ^{208}Tl

(e.g. PMTs), which can mimic $\beta\beta$ events. Background rate 3×10^{-3} events/keV/kg/yr is achieved. Latest results about ^{100}Mo (7 kg) and ^{82}Se (1 kg) are as follows,

$$T^{0\nu}_{1/2}(^{100}\mathrm{Mo}) > 1.1 \times 10^{24}\ \mathrm{yr} \quad (90\%\mathrm{C.L.})$$
$$T^{0\nu}_{1/2}(^{82}\mathrm{Se}) > 3.6 \times 10^{23}\ \mathrm{yr} \quad (90\%\mathrm{C.L.})$$

SuperNEMO will have to reach a much better radio-purity in the $\beta\beta$ source foils as well as a stronger Rn suppression. It already succeeds following improvements compared to NEMO-3 performance: Rn level (5 mBq/m^3 $\rightarrow$ 0.15 mBq/m^3), energy resolution and (14 % $\rightarrow$ 8 % at 1 MeV). The remaining challenge is the reduction of internal contamination of ^{208}Tl and ^{214}Bi. The detector is composed of 20 modules, each containing 5-7 kg of $\beta\beta$ emitter. The tracking volume contains 2000 wire drift cells operated in Geiger mode in a magnetic field of 25 Gauss. ^{82}Se (or other, e.g. ^{150}Nd) will be selected as $\beta\beta$ source, not ^{100}Mo, since it requires much better improvement of energy resolution due to its fast $2\nu\beta\beta$ decay. The first module i.e. SuperNEMO demonstrator will complete by the end of 2016. The sensitivity will reach $T_{1/2} > 6.5 \times 10^{24}$ yr and exceed 10^{26} yr as for full SuperNEMO.

3. KamLAND Detector

KamLAND denotes **Kam**ioka **L**iquid scintillator **A**nti-**N**eutrino **D**etector. It detects scintillation light emitted by a neutrino interaction or a radioactive decay. KamLAND located approximately 1,000 m under the top of Ike Mountain (36.42°N, 137.31°E). Covering rocks corresponding to 2,700 meters water equivalent (mwe) reduce intensity of cosmic muons to 10^{-5}. Low radioactivity environment is achieved by purification systems: liquid-liquid extraction and distillation system.

The detector consists of an outer and an inner one. The outer detector (OD) is water Cherenkov detector to veto particles from outside, mainly cosmic muons. The inner detector (ID) for observing neutrino events has 1 kton liquid scintillator (LS) and approximately 2,000 photomultipliers (PMT) in a spherical tank.

In this section, detailed detector design and peripheral equipment that were constructed before the detector modification for the KamLAND-Zen (see Chap. 4), are described.

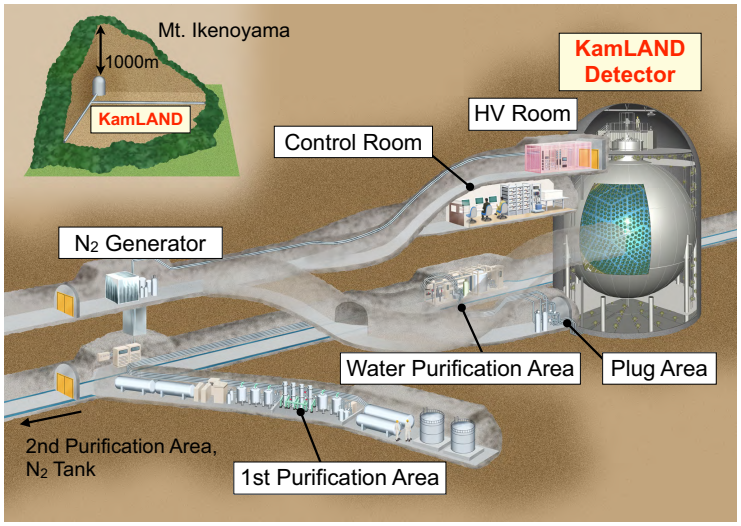

Figure 3.1.: KamLAND area in the Mt. Ikenoyama

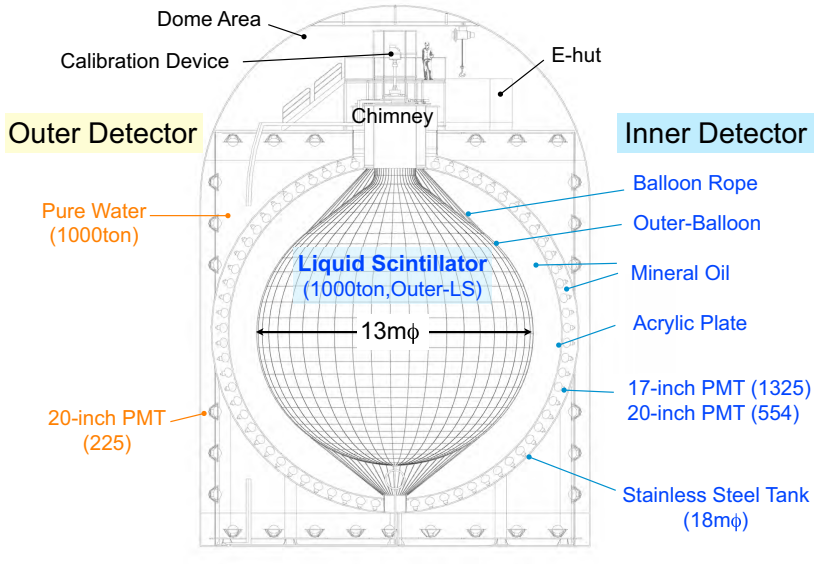

Figure 3.2.: KamLAND detector

3.1. Outer Detector

The OD is located between cylindrical tank (19 m in diameter, 20 m in height) and 18 m diameter stainless steel tank: the ID. It is filled with 3.2 kton pure water and flows upward. A water purification system always supplies pure water produced from RO sterilization of groundwater in the mine. The outer detector keeps temperature of the detector constant to avoid convection causing background instability. The water also has a role of shielding for external gamma rays and fast neutrons induced by surrounding rock and muon interaction. On the outer wall, 225 20-inch PMTs are mounted to detect chrenkov light.

In data analysis, it is important to reject muon events and muon induced events. The number of PMTs having detected a photoelectron are used for selecting muons or secondary particles (mainly electron, positron or gamma ray).

3.2. Inner Detector

We call a detector inside the stainless steel tank, the inner detector (ID). The detector has a layered structure so that the more inside, the less radioactivity becomes. There are 3 types of oils: the inner and outer LS and the buffer oil, and each one is separated by a balloon or acrylic boards. The outermost buffer oil plays not only as a buffer of balloon suspension but also as a passive shield against external gamma rays. The outer and inner LS are luminescent oils that is sensitive to low energy events. Scintillation or Chrenkov lights from various interactions are detected by 1879 photomultipliers secured

at the inner surface of the tank.

In this section, each component of the ID is described.

3.2.1. Liquid Scintillator

The liquid scintillator (LS) with the volume of 1,171 ± 25 m^3, is composed of followings:

- Normal paraffin (n-Dodecane, $C_{12}H_{26}$) : 82 % by volume
- Pseudocumene (1,2,4-Trimethylbenzene, C_9H_{12}) : 20% by volume
- PPO (2,5-Diphenyloxazole) : 1.36 ± 0.03 g/L

Paraffin oil has a long light transmittance to the scintillation light. It is extracted by fractional distillation, so ^{238}U and ^{232}Th concentration are originally low. And it also contains abundant protons as a anti-neutrino target and good chemical stability such as oxidation causing decrease of the light yield. For safety: high burning point and low pour point, n-Dodecan is selected. PPO is used as a luminescent agent, which is introduced in various large experiments. Pseudocumene (PC) is mixed for better discrimination of pulse shape. The LS light emission spectrum is shown in Fig. 3.4.

Current light yield is 200 p.e./MeV with 17-inch PMTs and 450 p.e./MeV with 17-inch and 20-inch PMTs. The attenuation length, 10 m at 400 nm wavelength is sufficiently longer than the radius of the LS. ^{238}U and ^{232}Th concentration are 2×10^{-19} g/g and 2×10^{-19} g/g respectively at the purest period. It was accomplished by 4855 m^3 volumes of LS purification by distillation and liquid-liquid extraction. The high purity enables to set 350 keV low energy threshold. And the LS has large quenching effect to alpha particles, which is important property for background rejection For example, 7.7 MeV alpha emitted by a ^{214}Po decay is quenched to ∼600 keV.

3.2.2. Buffer Oil

Buffer oil is mixture of paraffin oils, n-Dodecane and iso-Paraffin (n∼14). Loss of light yield is negligible owing to the long light transmittance of iso-Paraffin. Density is adjusted to be from 0.1 to 0.3% higher than that of the LS. The tank is separated by 3mm-thick acrylic boards to shield radioactive backgrounds from PMTs.

3.2.3. Outer Balloon

The outer balloon (OB) is a 13 m diameter holding 1 kton of the LS. The spherical shape is made by patching 44 boat-shaped films. Each film is welded with high frequency microwave not to use an adhesive. The balloon is subjected to a heavy load and stress. Based on the density difference between inside and outside the balloon, net weight is calculated 10 ton and tensile stress exceeds 2 kg/cm. Taking into account safety factor, it is hard to support massive LS only by the OB. That's why, most stress is given to braided Kevlar lopes. Withstand load is 4 ton per one lope, 10 times heavier than maximum load. 44 and 30 lopes are set toward the equator and the longitude respectively. Nevertheless

balloon also needs strength, so it's made of biaxially stretched Nylon (ON). Stretching can increase not only strength but also transparency and chemical resistance.

The OB also requires high gas barrier property. In outside of the balloon, ^{222}Rn from ^{238}U contained mainly in glass surface of PMT or stainless steel tank, dissolves. To protect LS purity, EVOH (polyvinyl alcohol, $-CH_2CH(OH)-$) is used, which is known as the lowest gas permeable film. It achieves no less strength than Nylon by biaxial stretching. Thus, the OB has 4 layers: XL/ON/ON/XL, total thickness is 135 um. This structure has sufficient strength and gas barrier properties. Transmittance was 96% at 400 nm.

3.3. Data Acquisition

KamLAND is operated 24 hours a day. Pulses of physical events are acquired by 2126 PMTs with self-developed electronics (KamFEE) and a trigger system. Digitized waveforms are read out at 11 flont-end computers through VME crates, then corrected to 4 back-end computers to record, analysis and to display. These system are processed by ∼10 MB/sec. Components for data acquisition are described below.

3.3.1. Photomultiplier Tube

The KamLAND uses Photomultiplier Tube (PMT) to detect scintillation light in the IB. It is also used as Cherenkov counter in the OD. An incident photon is multiplied by photo cathode and multi-stage dynodes. Photoelectrically produced electrons at photo cathode are amplified in each dynode by secondary electron emission phenomenon. Electrons finally gained $\sim 10^7$-fold, are observed as electrical pulse.

In the ID, two types of 20-inch PMTs, R3600 and R7250 are equipped. R7250 was developed on the basis of R3600 used for Super-Kamiokande. The dynode structure changed from Venetian blind to Box and line focus to maximize electron collection efficiency and timing response. Electron transit time has spread due to the track difference from the photo cathode to the first dynode. This change greatly improved the transit time spread (T.T.S) which is expressed as FWHM of asymmetric gaussian distribution, from 5.4ns to 3.1ns. However, photoelectron collection efficiency and timing response is not enough around photoelectric surface, so the effective photoelectric surface is limited to 17-inch for the R7250. That's why R7250 and R3600 are called 17-inch and 20-inch PMT respectively. Schematic view of each PMT is shown in Fig. 3.3. New dynode structure also significantly improved single photoelectron discrimination capability. It improved peak-to-valley from 1.7 to 5.7, which is the ratio of single p.e. peak and valley between noise and the peak.

The 17-inch PMT employs taper bleeder circuit to widen dynamic range, which is another modification from 20-inch PMT. In cosmic muons and showering events passing through the detector, normally ∼100p.e. and sometimes ∼5,000 p.e. level are observed per one PMT. The pulse linearity is kept up to ∼500 photoelectron (p.e.) level, and the output is not saturated even 10,000 p.e. level. It enables precise energy estimation. The gain is adjusted to be 10^7, and applied voltage is about 2,000V. As shown in Fig. 3.4,

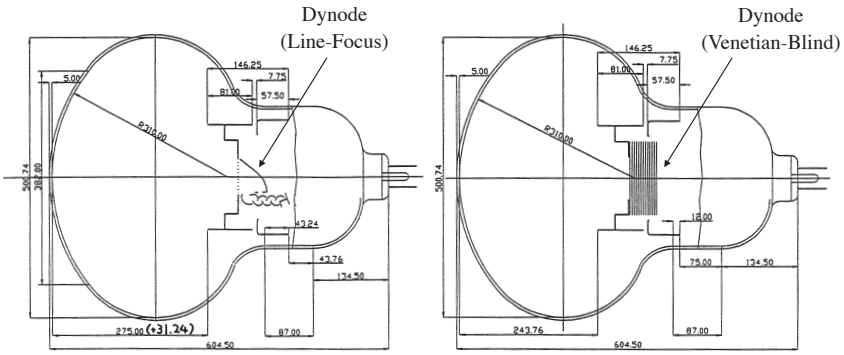

Figure 3.3.: Schematic view of 17" and 20-inch PMT

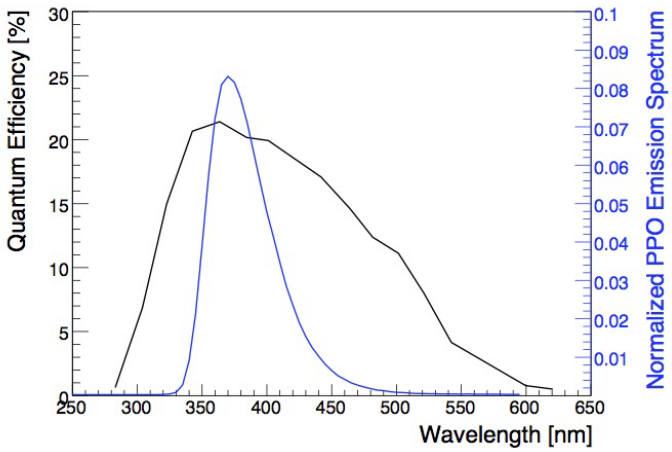

Figure 3.4.: Quantum efficiency of PMT with light emission spectrum

quantum efficiency (QE) representing photoelectron production rate, is ∼20 % around the PPO light emission peak.

3.3.2. Electronics : KamFEE

Flont-End Electronics developed at LBNL (KamFEE) is used to waveform capture and digitization (Fig. 3.5). In total, 200 boards are operating in connection with all PMTs of the ID and the OD (12 channels/board). The design requirements from the KamLAND experiment are listed below.

- timing better than that of PMT's
- minimal system and deadtime
- large dynamic range

- high single photoelectron detection efficiency

The schematic diagram of KamFEE is shown in Fig. 3.6. Input analog signal from PMT to FEE is branched in halves firstly. One is sent trigger system through FPGA (Field Programmable Gate Array), if it's greater than hit threshold of a primary discriminator. Meanwhile, another one is delayed to synchronize with signal capture command, and pre-amplified for digitization. After that, it is amplified in three gain, high (×20), medium (×4) and low (×0.5) gain. Only one waveform is recorded after the A/D conversion, e.g. if a small signal such as one photoelectron is detected in a PMT, high gain is applied. On the other hand, high charge cosmic muon events is sufficient with lower gain. ASIC called "ATWD" (Analog Transient Waveform Digitizer) has 128 capacitor arrays. The amplified signals are buffered in each array at intervals of 1.6ns. The sampling width is 10bit. If digitization commands are launched from FPGA, digitized waveform (approximately 256 bytes) are recorded to 32 MB memory on the board. If not, they are overwritten by the next signals.

Digitization and trigger command are controlled by FPGA. It collects 125 ns width hit pulses of 4 PMTs, then send summed hit information to the outer trigger system. If it implements trigger threshold, FPGA launches commands to hold signal concerned in capacitor arrays, and to convert to digital voltage. While this, ATWD cannot receive any signals, so 2 ATWDs (ATWD-A,-B) are equipped to minimize deadtime. High sampling rates of ∼0.63 GHz enables multiple samples and the timing accuracy of pulse arrival time achieves to sub-nanosecond. This is significantly better than ∼3 ns transit-time spread of 17 inch PMT's.

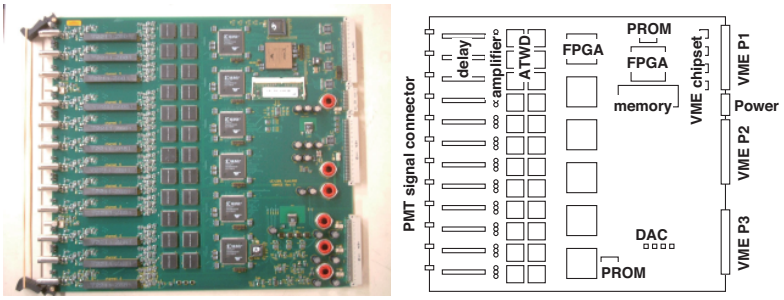

Figure 3.5.: KamLAND Front-End Electronics (KamFEE)

3.3.3. Trigger System

Trigger circuit is shown in Fig. 3.7. Trigger system treats mainly 3 types of triggers, "global", "forced" and "history". Global triggers normally based on nsum: the number of PMTs whose signal went above the discriminator level. If total nsum collected from all the FEEs meets a criteria, digitization is executed for hit channels. There are various kinds of triggers for each detector as follows.

- ID global triggers

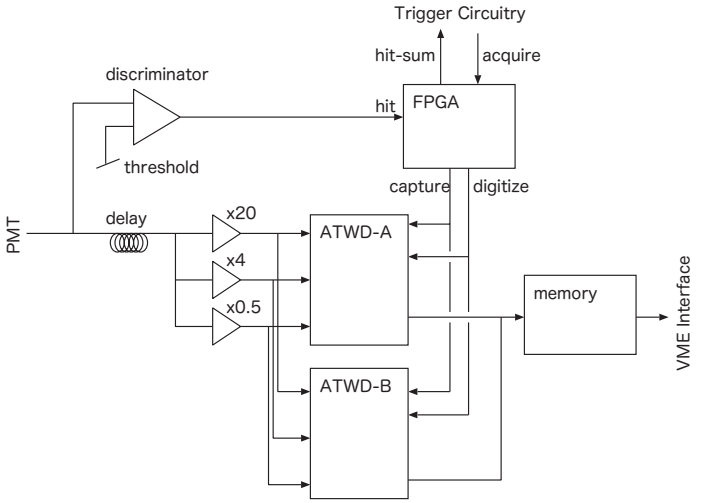

Figure 3.6.: Kam-FEE Diagram

  - single trigger : for single events
  - prompt/delayed trigger :
    for correlated events such as anti neutrino and Bi-Po radioactive decay events
  - prescale trigger : for low energy events
  - ID to OD trigger : issue OD global acquisition when ID trigger launches

- OD global triggers
  - top/upper/lower/bottom single trigger :
    single trigger in top, upper, lower and bottom side of OD.
  - OD to ID trigger : issue ID global acquisition when OD trigger launches

Forced triggers digitize all the ID or OD PMT's pulses with no reference to nsum, which is mainly used for some calibration. History trigger does not record waveforms. Only hit timing and the number of PMT hits are digitized by the trigger system, so the data size is very compact. It enables setting lower threshold.

Another important role of trigger system is the control of timing information. The system has 40MHz clock system and share with all FEEs. Clock counter value when trigger command reached FEE board is attached to digital waveform as Timestamp. All waveforms from the same event have the same timestamp. Channel-specific "launch offset": time difference between ATWD digitization and receiving trigger command (normally digitization precedes), is corrected for each waveform at offline analysis. Unixtime is also recorded by synchronization with GPS.

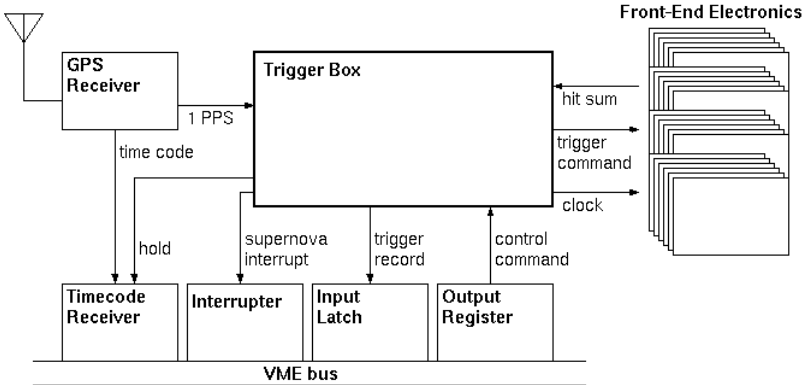

Figure 3.7.: Trigger circuit for Kam-FEE

3.4. Purification System

In the target energy region of the KamLAND, natural radioactive impurities are crucial backgrounds. To reduce them sufficiently, 1st (water extraction) and 2nd (distillation) purification systems are equipped in the mine.

3.4.1. Water Extraction System

The 1st purification system consists of filtering, water extraction and N_2 purge part. It is mainly reduces metal elements. Fig. 3.8 is a schematic view of the 1st purification system. The LS or buffer oil goes through water extraction tower after removing fine particles by pre-filter and input-filter (each pore size is 1 μm and 0.1 μm respectively). Water extraction is a chemical separation method using different partition coefficient liquids not dissolved each other. By flowing oil and pure water countercurrently in the tower, metal elements such as U, Th, and K are efficiently absorbed to water molecules having chemical polarity. And two liquids is separated at equilibrium by the difference of specific weight.

After that, purified oil is purged by nitrogen gas to remove Rn gas, remaining water and dissolved oxygen, which can be background sources or decrease light yield of the LS. Either method is simple and effective process operated under ordinary temperature and pressure.

3.4.2. LS Distillation System

The reduction efficiency by the water extraction was not maximized due to reusing of nitrogen gas, or forming of metallic oxide or metallic complex. For the further background reduction, 2nd purification system using fractional distillation method was constructed in the mine.

As shown in Fig. 3.9, the system is consisted of three distillation towers. PC, Decane and PPO with boiling points of 169°C, 174.2°C and 360°C respectively, are separated in the order of boiling point from lowest to highest. Material LS are sent from the 1st

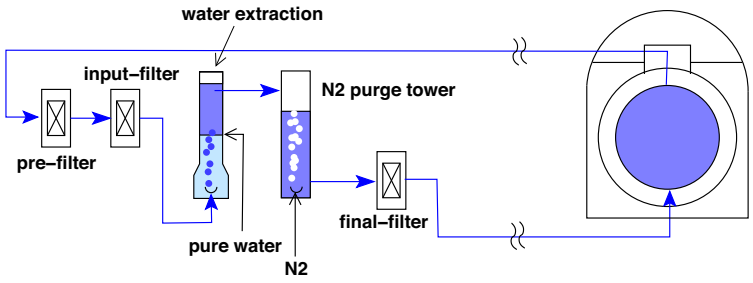

Figure 3.8.: 1st purification: water extraction system (Tajima, 2003 [36])

purification system to buffer tank. Each component is highly purified by reflux and sent to each adjustment tower. It was mixed in the mixing tank with the accuracy of 10^{-3}g/cm^3.

Mixed LS is filtered and purged by pure nitrogen gas vaporized at the liquid nitrogen tank. The flow rate is 20 times higher than that of LS. It can remove noble gas such as ^{222}Rn, ^{85}Kr, and ^{39}Ar. The nitrogen gas are also used for the sealing of distillation towers.

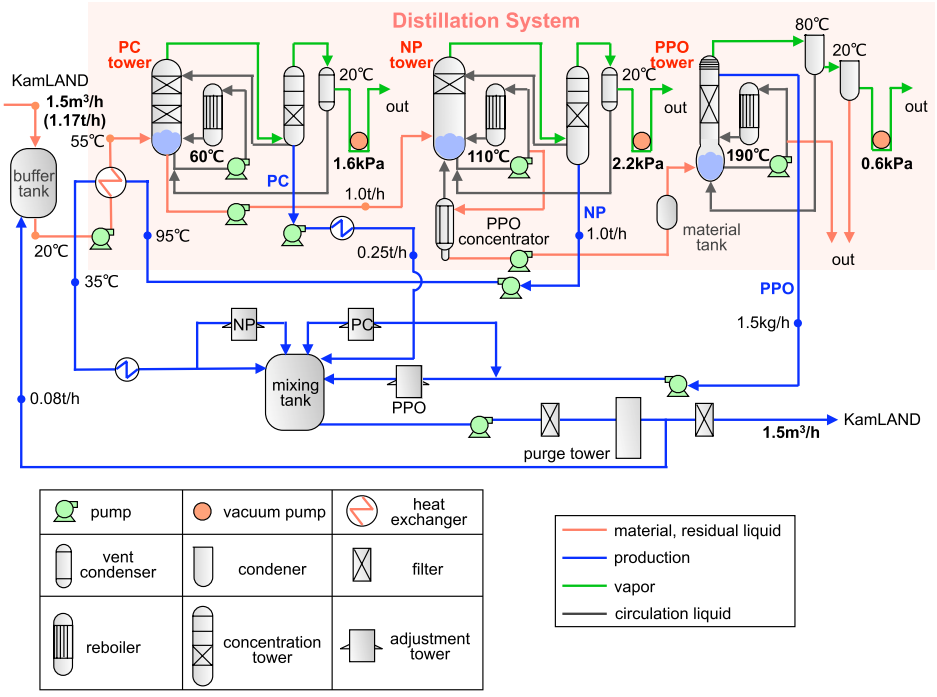

Figure 3.9.: 2nd purification: distillation system. (Nakajima, 2010 [37])

4. KamLAND-Zen Experiment

KamLAND-Zen (KamLAND Zero-neutrino) is the experiment to explore $0\nu\beta\beta$ decay in ^{136}Xe with the KamLAND detector. The KamLAND was originally designed to measure (reactor, geo, solar) neutrinos, which is, as already mentioned at Sec. 2.4.3, the need of a low background counting is common to the two research fields. KamLAND-Zen began by minimal detector modification in which only a smaller balloon containing Xe-loaded liquid scintillator (Xe-LS) was introduced into the center of the KamLAND, as shown in Fig. 4.1. Here, the details of added structures and these fabrication (Sec. 4.2), and installation into KamLAND (Sec. 4.5), is described. The reason that ^{136}Xe $\beta\beta$ source is selected is described in Sec. 4.2.1.

KamLAND-Zen successfully started at 2011, but some unexpected backgrounds were found, which prevented to achieve anticipated sensitivity. Therefore, we implemented intensive purification of the LS and Xenon gas (see Sec. 4.8). Here, following purification systems are used: water extraction system (Sec. 3.4.1), LS distillation system (Sec. 3.4.2) and Xe distillation system (Sec. 4.4). The motivation of this work is to estimate how the refining is effective. Let us define two data periods, KamLAND-Zen Phase-I and Phase-II. These interval corresponds to the purification phase.

- Phase-I
  - Oct. 12. 2011 - Jun. 14. 2012
  - (from the first run - before purification)
  - divided into sub-period, DS-1/DS-2 by filtration work
  - fiducial radius : 1.35 m
  - ^{136}Xe exposure : 89.5 kg-yr
- Phase-II (this work)
  - Dec. 11. 2013 - Oct. 27. 2015
  - (after purification - before source calibration)
  - fiducial radius : 2.0 m
  - ^{136}Xe exposure : 504 kg-yr ($R < 2$ m), 126 kg-yr ($R < 1$ m)

In this work, Phase-II data is analyzed to extract $0\nu\beta\beta$ result. It is combined with the Phase-I result previously reported (Sec. 4.7). Other updates from Phase-I are summarized in Sec. 4.9.

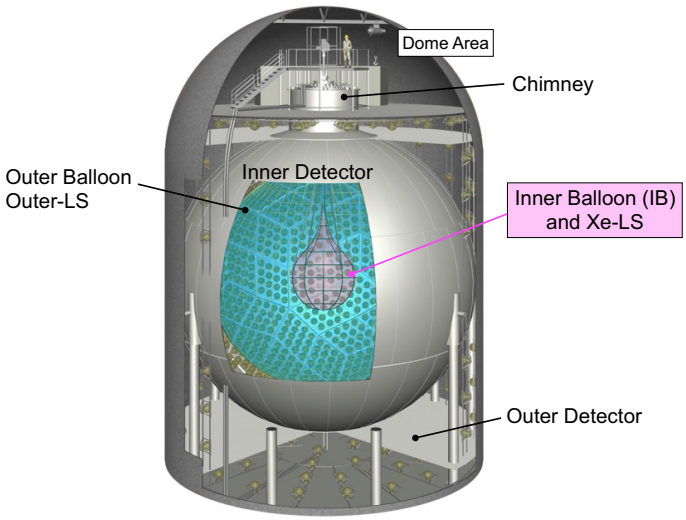

Figure 4.1.: KamLAND detector with components for KamLAND-Zen

4.1. Detection Method

As described in the previous chapter, double-beta decay accompanies emission of two electrons in each mode. As for $\beta\beta$ source ^{136}Xe ($Q_{\beta\beta}$ = 2.458 MeV), the decays are expressed as,

$$(2\nu \text{ mode}) \quad {}^{136}\text{Xe} \rightarrow {}^{136}\text{Ba} + 2e^- + 2\bar{\nu}_e$$
$$(0\nu \text{ mode}) \quad {}^{136}\text{Xe} \rightarrow {}^{136}\text{Ba} + 2e^-.$$

The KamLAND detector does not have techniques to distinguish two electrons, therefore their sum energy is recorded. Fig. 4.2 is the visible energy spectra of 2ν and 0ν decay mode expected in the KamLAND, for which the energy resolution is included. They are constructed based on the cross-sections calculated at (W.C. Haxton and G.J. Stephenson, 1984 [38]) and fermi function. Two decay modes are distinguishable by their spectra.

4.2. Detector Components for KamLAND-Zen

4.2.1. Xe-LS

Liquid Scintillator

The composition of liquid scintillator to dissolve Xe, is slightly different from original LS, called "outer-LS", as follows.

- Normal paraffin (n-Decane, $C_{10}H_{22}$) : 80.7 % by volume
- Pseudocumene (1,2,4-Trimethylbenzene, C_9H_{12}) : 19.3% by volume

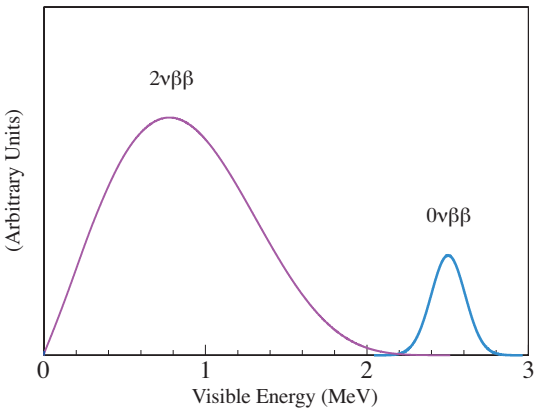

Figure 4.2.: Expected visible energy spectrum for ^{136}Xe double-β decay

- PPO (2,5-Diphenyloxazole) : 2.29 ± 0.03 g/L
- enriched Xenon : (2.91 ± 0.04) % by weight
- density : 0.78013 g/cm^3

As to the solvent, decane having less carbon number is used not dodecane ($C_{10}H_{22}$) used in outer-LS, in order to suppress the load weight on a thin balloon. It is also suitable in terms of the density, for which the density difference from outer-LS is adjusted within 0.1%. The reason that PPO concentration is almost doubled compared to outer-LS (1.36 ± 0.03 g/L), is to compensate enhancement of LS quenching effect by Xe. It is important to prevent vertex mis-reconstruction which is unignorable when the light yield difference between Xe-LS and outer-LS is larger than 15 %.

The light transmittance is measured to be approximately 10 m at 400 nm, where the requirement is not so strict since scintillation light can be detected as long as reaching outer-LS. The refractive index is 1.49 (at 380 nm, 15 °C), slightly lower than that of the outer-LS. The concentrations of natural radioisotopes in Phase-II are estimated to be $(1.7 \pm 0.1)\times10^{-16}$ g/g for ^{238}U and $(5.5 \pm 0.3)\times10^{-17}$ g/g for ^{232}Th from data analysis (discussed in Secs. 8.4.1, 8.4.2).

Enriched Xenon

^{136}Xe is one of the magnificent $\beta\beta$ sources adopted by various homogeneous detectors such as LXe or gaseous-Xe TPC. Followings are advantages to use it in the KamLAND.

- stable noble gas
  The chemical stability is very important for the KamLAND treating flammable liquid. And Xe does not influence the LS capability such as transparency.
- high enrichment enrichment factor
  Xenon gas is enriched by centrifugation with approximately ten part cost of ^{76}Ge.

Especially, ^{136}Xe is the heaviest of all natural xenon isotopes, therefore it is easily separated. ^{136}Xe with 8.9 % natural abundance, is enriched to ∼90%.

- slow $2\nu\beta\beta$ decay
  Liquid scintillator has intrinsically poor energy resolution, so unavoidable background $2\nu\beta\beta$ decay with long lifetime, is desirable to reduce overlap of these signals.

- ease of handling
  Xe is easily dissolved in the LS, and its extraction is the same.

- good solubility in LS
  Xenon has acceptable solubility in LS, which is helpful to suppress backgrounds increasing in proportion to volume, such as cosmogenic events.

Enriched Xe gas is dissolved in LS by pressurization (see Sec. 4.5.1). Followings are performance of enriched Xe gas and Xe-LS accomplished in Phase-II. The target mass used is the largest in current double-beta decay experiments, at this time. These systematic uncertainties are discussed at Sec. 9.2.

- Isotopic abundance :
  - ^{136}Xe : (90.77 ± 0.08) %
  - ^{134}Xe : (8.96 ± 0.02) %
  - Other isotopes are negligible.
- Xe mass dissolved in Xe-LS : (380.7 ± 3.2) kg
- Xe concentration : (2.91 ± 0.04) % by weight

4.2.2. Inner Balloon

Inner balloon (IB) is a holder of the Xe-LS (Larger balloon is called "outer balloon"). It is suspended by long corrugated pipe and strings, and located at the center of the ID. The major requirements for the IB are listed below.

- High strength
  Expected density difference between Xe-LS and outer-LS ($\Delta\rho$) is 0.1% at maximum. For rupture strength, 10 safety factor is desirable.
- Low radioactive impurities : ^{238}U, ^{232}Th $\sim 10^{-12}$ g/g, ^{40}K $< 10^{-11}$ g/g
- Xenon gas leak amount : $<$ 4 kg / 5 yr
- light transmittance $>$ ∼3 m IB diameter

Material and Structure

The material is biaxially stretched nylon 25 μm in thickness. The performance is balanced and the best of all candidates. The ^{238}U, ^{232}Th and ^{40}K concentration measured by ICP-MS are 9×10^{-12}, 11×10^{-12} g/g and 1.2×10^{-11} respectively after ultra pure water washing, which is the same level as the requirements. The cleanness is achieved by not using lubricant. Rupture strength is 4.9 kgf/cm that corresponds to $\Delta\rho = 6\%$. In addition, nylon can keep high strength and good gas barrier property after welding.

The thickness is optimized by taking account of strength and tagging efficiency of film background. ^{214}Bi-Po sequential decay in ^{238}U series can be normally rejected by delayed-coincidence tagging. However, α ray from ^{214}Po decay sometimes stops in the film due to large energy loss. In this case, residual ^{214}Bi event becomes serious background in the signal region. ^{214}Bi-Po tagging efficiency with 25 μm film is estimated to be 53%. The light transmittance is 99.4 $\pm$ 0.3 % at 400nm.

The diagram of the IB is shown in Fig. 4.3. The IB has tear-drop shape to avoid stress-focusing and to distance the balloon from supporting structures with much radioactive impurities. 1.5-m-length straight tube at the top of IB is also set for the purpose. 1.54-m-radius sphere and cone parts are made by welding 44 gores (boat-shaped) and 6 film pieces, respectively. Each welding line are reinforced by 2 nylon film bands.

Supporting Structures

The IB is suspended by belts like outer balloon, but the requirements for cleanliness is much more stringent. Thus sufficient strength have to be achieved using low radioactive material. Followings are supporting structures to meet the needs. These pictures are shown in Fig. 4.3.

(b) Corrugated tube
Approximately 7m-long corrugated pipe is connected to the chimney i.e. top end of the ID, and connection pipe at the lower end. The flexibility is helpful on the IB installation in a small clean room at the dome area.

(c) Strings
There is 12 belts suspending the IB, for which the upper part above $z \sim 3$ m is made of Vectran usually used as fishing line. The lower end starts from position of connection pipe described below, where contribution of its contamination to the IB region is negligible. But in order not to decrease light transmittance of outer-LS, the strings are washed by ultrasonic cleaning with PC/dodecane, ethanol and pure water. Contamination of Vectran after washing is 1.9×10^{-10} g/g, 4.4×10^{-10} g/g and 5.4×10^{-19} g/g, for ^{238}U, ^{232}Th and ^{40}K, respectively.

(d) Connection pipe
Connection pipe connects with film tube and corrugated tube without leak. The pipe is made of PEEK (PolyEther Ether Ketone) having sufficient LS-resistance

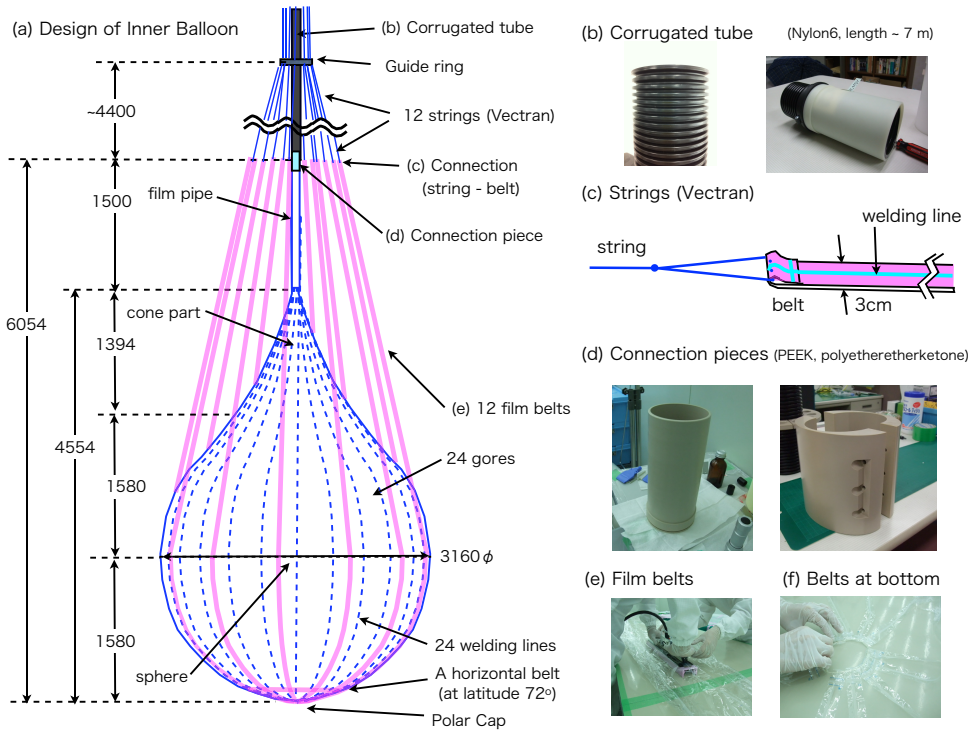

Figure 4.3.: The IB diagram and the supporting structures (Yoshida, 2014 [39]).

and strength against pressure from the LS. Abundant events from the pipe is used to estimate time dependence of event timing (Sec. 5.3.3).

(e) Film belts
The lower part of 12 supporting belts are made of films which is the same material as the IB, since they are close to the fiducial volume. In terms of radioactive impurities, the Nylon film is the best material. In order to increase the strength, one film belt is made using two films which are welded at their center lines. All belts are put on a Vectran loop at the IB bottom.

Fabrication of Inner Balloon

The IB was produced very carefully since the contamination cannot be refined after its installation, and Xe escaping into the outer-LS is hard to collect. Therefore we dedicated to cleanliness and finding scratches and pinholes for very thin film. The fabrication was implemented at the cleanest place so called super clean room classified as "class 1" cleanliness, which means the number of a dust in 1 feet^3 and the dust size is more than 0.5 μm. In our case, the particle size was monitored with 0.1 μm threshold. Following is fabrication process of the IB in the clean room. And the pictures are shown in Fig. 4.4.

1. Film cutting and washing
   The film cut into suitable size was washed by ultrasonic cleaning with pure water. It was dried with nitrogen and examined scratches and pinholes by eyes. If finding them, portion of or a whole of the film was discarded.

2. Film clipping and welding machine
   The films were clipped to parts such as 24 gores for a sphere part. Each part was unified by heat welding with 30-cm-long machine. This is one of the most difficult operations, since it is very sensitive to the conditions like heat temperature, welding time, cooling time, and force to push the heating machine. Especially, the load to the machine includes human error, which can cause inadequate welding or overheating, although other welding parameters are comparatively reliable owing to optimization on ahead. In order to minimize failure, the welding condition was frequently checked using test films.

3. Leak checking and patching the leak point
   Gas leakage is mainly caused along the welding lines. Leak from the IB inflated by helium gas is examined with its detector, and repaired by patching the film piece with glue. Finding all leak spots is also arduous task like welding, since the sensor is very small compared to balloon size. Obviously, the patching is difficult to undo, so it takes extreme care. Leak amount was checked after the patching again. If it exceeds acceptable level, additional repair was provided. Leak spots were concentrated around large curvature part i.e. the IB bottom, and cone part.

4. Assembling with supporting belts
   Belts supporting the IB were also made of Nylon films for cleanliness.

5. Transportation the box to the mine
   The IB with supporting structures was wrapped by the same Nylon film with the IB and packed in a clean box filled with nitrogen gas. The box was transported from Sendai, Japan (location of clean room) to the KamLAND area. It was unpacked in the clean room in the dome area;

These process took ∼3 months (May. - Aug. in 2011). The period corresponds to just after Fukushima-I nuclear reactor accident (11th Mar. 2011), by which fallout contamination was introduced to the IB. This detail is described in Sec. 8.5.1.

4.3. Xe Handling System

This system was newly built for the KamLAND-Zen experiment. It handles Xe gas dissolution(extraction), density adjustment of LS, filling to the detector, and so on. There are two tanks, main and subtank having 1 m^3 volume. One is used for filling, the other one is used for acceptor. It can operate with the both of continuous mode and batch mode.

LS Filling On LS filling, density is adjusted with PC or decane. They are sent to control tank from the 2nd purification system after distillation, then filled to main or sub tank while monitoring the density. On Xe dissolution, it is supplied from storage bottles and dissolved under increased pressure.

Xe Extraction On Xe extraction, LS and Xe evaporated by vacuum degassing are trapped to LS and Xe trap respectively using the difference of the boiling point. The Xe gas are once collected to reserver tank, then filled to Xe storage bottles by compressor. The bottles are placed on the weight scale, so it is easy to figure out total amount.

4.4. Xe Distillation System

Motivation of Xe gas purification is to remove ^{110m}Ag contamination found in Phase-I which suppresses sensitivity to $0\nu\beta\beta$ decay. We tried to refine Xe gas using a getter material which absorbs O_2, H_2O and metals, etc. In order to use getter, nitrogen concentration must be below 50 ppm. Therefore, Xe gas was purified with a distillation method as a preliminary step. It can remove not only nitrogen but also other known radio isotopes.

Xe distillation system was developed by XMASS collaboration in order to remove krypton in Xe gas (K. Abe et al., 2009 [41]). It separates gaseous krypton and liquid xenon in gas-liquid equilibrium. Boiling point of liquid krypton is 120 K at 1 atm, while that of xenon is 165 K. This method can also applied to xenon and nitrogen (77 K). Process speed is designed as 0.6 kg Xe/hour, and collection efficiency achieves 99 %.

Figure 4.4.: Pictures of the IB fabrication process. (1)-1 Washing a film by ultrasonic cleaning with pure water. (1)-2 Checking scratches and pin holes. (2)-1 Clipping films a gore. (2)-2 Welding films. (3)-1 Checking leakage from the IB with He detector. (3)-2 Patching in a leak spot. (4) Assembling the IB, connection pipe, supporting film belts and Vectran strings. (5) Wrapping the IB and packing into the plastic box. (A. Gando, 2012 [40]).

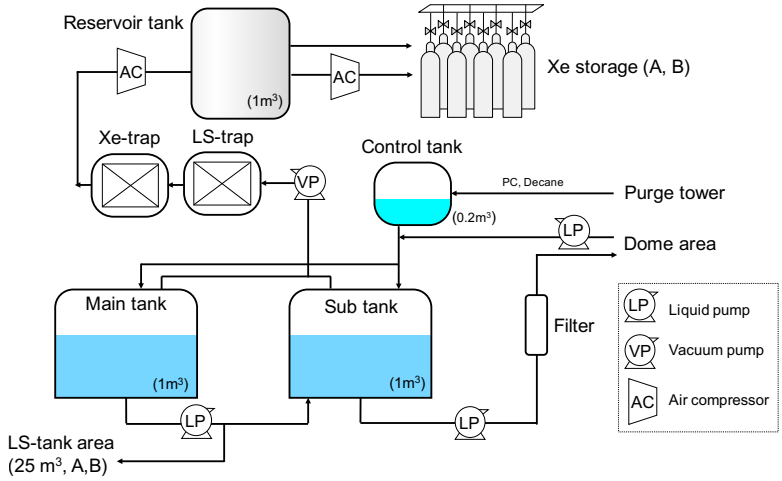

Diagram of the system is shown in Fig. 4.5. "Original-Xe" is separated into "Processed-Xe" with high purity and "Off-gas" with high nitrogen concentration. Each component is described below.

- Filters and getter
  Original-Xe flows through following filters and getter and pre-purified.
  1. Charcoal filter : remove vapor of LS (< 1 ppb), trap metal
  2. Sintered metal filter (SUS) : absorb particle (> 3 nm) with 99.9999 % efficiency
  3. Getter : remove (O_2, H_2O, N_2, CH_4, CO, CO_2) < 1 ppb, and metal.
  4. PTFE particle filter : pore size is 3 nm

- Heat exchanger (pre-cooling)
  It pre-cools xenon, where purified xenon gas extracted from the distillation apparatus is used as a cooling medium.

- Liquefier ($\sim$192 K)
  Pre-cooled xenon is further cooled down by a GM-type refrigerator. It has a cooling power of 100 W at around 180 K.

- Distillation tower ($\sim$178 K)
  Cooled xenon is fed into $\sim$3-m-length of distillation tower. There are 6 theoretical columns in the tower. Condenser is installed at the top of the tower in order to maintain a constant temperature profile in the tower. The temperature is kept at $\sim$178 K by an electrical heater. "reboiler" is a cylindrical copper vessel with a 200 mm diameter, placed at the bottom of the tower. A heater boiling liquid is attached to the reboiler. The reboiler has three liquid level sensors at 5 mm (LL level), 20 mm (L level) and 65 mm (H level), corresponding to 0.47 kg, 1.88 kg and 6.1 kg of xenon, respectively.

Xenon distillation was operated with following procedure.

1. Reduce N_2 concentration in original-Xe
   In order to let Original-Xe flow through the getter, nitrogen concentration is decreased to acceptable level.

2. Establish gas-liquid equilibrium
   First, xenon are liquefied until the liquid level in the reboiler reaches L level ($\sim$2 kg xenon). Then heater in the reboiler and condenser are switched on, and xenon liquid is circulated without collecting purified xenon and off-gas, to establish the initial gas-liquid equilibrium in the tower.

3. Extract processed-Xe and Off-gas
   Processed-Xe and Off-gas are extracted with flow rate 1.7 L/min and 0.17 L/min, respectively. Xenon feed is adjusted according to the liquid level: the flow rate is set to 2.3 L/min when the level reach L, and to 1.7 L/min until xenon in the reboiler retuned to L. Purified-Xe is sent to Xe storage in Xe handling system via the heat exchanger. Off-gas is exhausted to the atmosphere via Xe trap, or reserved to a tank in the Xe system.

In our test using unenriched xenon, we achieved 3.6 ppm of nitrogen concentration. 306 kg of xenon with $\sim$2 % N_2 (mainly extracted from Xe-LS in Phase-I) and 125 kg of new enriched xenon was purified, then 411.5 kg of xenon was collected.

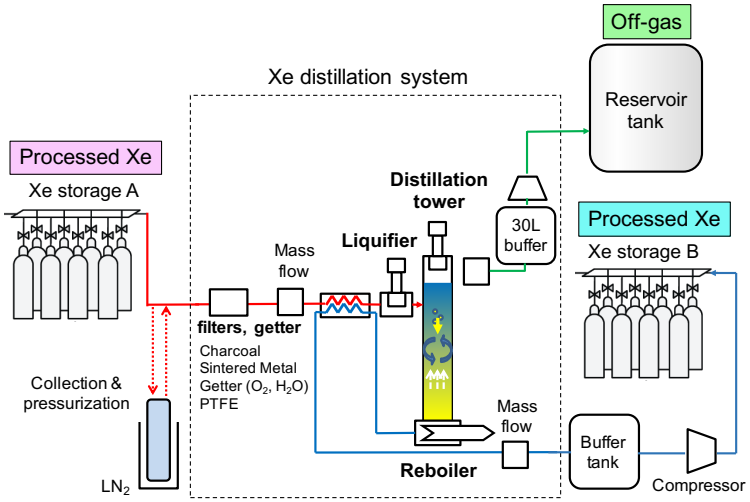

Figure 4.5.: Schematic diagram of Xe distillation system

4.5. Detector Modification

What we need to do is sink the IB and fill with Xe-LS, but there are some constraints and requirements. Size of ID opening located at chimney, is only 50-cm-diameter. We need to sink the IB passing it through the hole while keeping it clean and undamaged. Besides, one needs to take care in buoyancy given by air/nitrogen inside the IB.

The cleanliness in the dome area is much inferior to super clean room used for the IB fabrication. It is classified as "class 2000" which is unacceptable level. Hence we constructed a clean room in the area to cover the opening: the cleanliness is class 10 - 100. Rn level is measured to be 56 - 74 Bq/m^3. The installation was implemented in this room.

The procedure of the IB installation was determined as following, so that it meets above requirements.

1. Installation of folded IB with heavy-LS
2. Inflation of IB with heavy-LS
3. Replacement of heavy-LS with Xe-LS

Heavy-LS is 0.4 % heavier than outer-LS, and does not contain Xe. Preparation of heavy-LS and Xe-LS, and detail of the installation is described below.

4.5.1. Preparation of Xe-LS

Xe-LS components other than Xe are compounded at the 2nd purification system after purification i.e. water extraction (Sec. 3.4.1) and distillation (Sec. 3.4.2). Purified LS and PC for density adjustment is sent to the Xe handling system.

Following is the procedure of Xe-LS preparation. It is also shown in Fig. 4.6.

1. Send purified LS to the Xe system
2. Evacuate LS by a vacuum pump
3. Dissolve enriched Xe gas in LS
4. Adjust LS density using PC
5. Adjust temperature of Xe-LS

Density difference of heavy-LS and Xe-LS with outer-LS are +0.01 % and +0.035 % by weight, respectively. Preparation of heavy-LS is almost same as above one, except that pure nitrogen gas is filled in place of Xe. PPO concentration for heavy-LS is common with Xe-LS for the case of mixing with Xe-LS in the IB.

These operation method was implemented at detector modification in 2011. It was improved to make Xe concentration higher than this method. It is described in Sec. 4.8.5.

4.5.2. Installation of Inner Balloon

Followings are the procedure of the installation based on the requirements described above. Pictures of each operation is shown in Fig. 4.7.

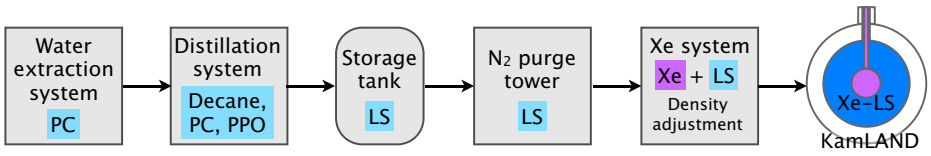

Figure 4.6.: Flow chart of Xe-LS preparation (A. Gando, 2012 [40]).

1. Installation of folded IB with heavy-LS
   The IB was folded up to pass through the narrow opening. Each welding line of the IB was folded upward. The film belts were sandwiched between adjoining welding lines so that they are arranged at equally spaces after the IB inflation. This folded IB was wrapped with protection films to avoid contamination during the installation. These wrapping was done before packing into the box in the super clean room.

   Protection films and mesh sheets tying the IB were untied and removed, when ropes connected to them were pulled from the clean room. It was done after the IB submerge in the LS wholly. The IB was slowly sunk in parallel with filling the heavy-LS.

2. Inflation of IB with heavy-LS
   The unfolded IB was inflated while filling heavy-LS. In order to reduce the load of the straight film tube, length of strings suspending the IB was adjusted. The strings are connected to load cells. Condition of the IB was monitored by cameras installed in the LS. After 17 m^3 of heavy-LS filling completed, data taking started. Using ^{222}Rn events introduced with filling, shape of the IB and absence of leakage from the IB were confirmed, as shown in Fig. 4.8.

3. Replacement of heavy-LS with Xe-LS
   Most important thing in this operation is to keep a layer of filled Xe-LS and drained heavy-LS. Because Xe drained with heavy-LS cannot be collect soon. In order to maximize Xe concentration, accurate control of Xe-LS density and filling temperature were required.

   Xe-LS with +0.025 % density difference of heavy-LS was filled from the bottom of the IB, and heavy-LS was drained from the top of the IB, with the same speed. The layer was checked with two ways: (i) measurement of Xe concentration in returned LS by gas-chromatography, (ii) vertex distribution of Rn events (event rate in Xe-LS is higher than heavy-LS due to its radioactive decay). At the end of the filling, Xe-LS was agitated by circulation to equalize the density. ∼60 kg Xe was contained in returned LS, in total. Xe concentration in returned LS increased in proportion to Xe-LS filling volume.

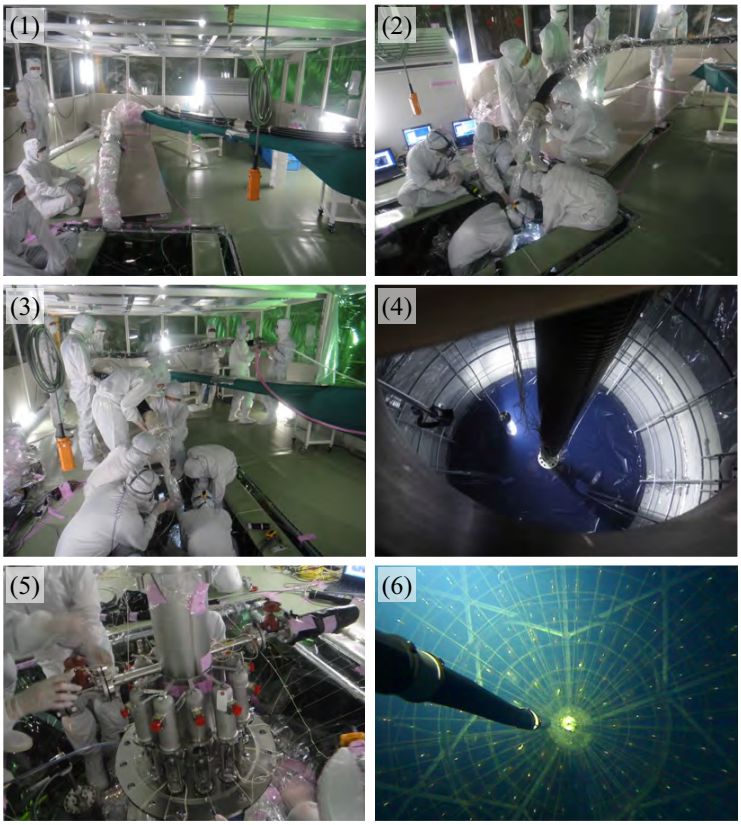

Figure 4.7.: Pictures of the IB installation. (1) Clean room above the chimney. (2), (3) Installation of the folded IB (4) Opening of the ID with the corrugated pipe (black line). The blue sheet is light shielding flapper covered with black sheets. (5) Flange connection with 12 load cells for Vectran. (6) Inside the ID after the detector modification. One can find the IB boundary (Acrylic frame is deformed by refraction of light), the black corrugated pipe and PMTs reflecting LED light . (A. Gando, 2012 [40]).

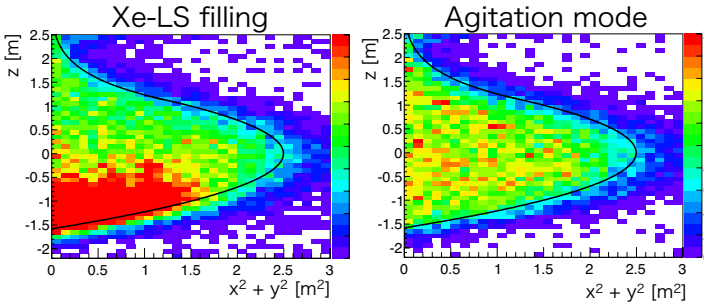

Figure 4.8.: Rn distribution during Xe-LS filling and agitation mode. Black line is the ideal IB shape. One can see a boundary between heavy-LS and Xe-LS.

4.6. MoGURA

In the KamLAND, high charge events exceeds 3,000 p.e. mainly muons are observed. It causes baseline fluctuation called overshoot with 470 μs time constant. while this, the signal depth continues to fall below the discriminator threshold. Such a long deadtime makes difficult tagging muons or muon induced events: neutron capture and spallation events. To improve this, new data acquisition system "MoGURA" was installed in 2009.

Analog waveforms from PMTs are split to Kam FEE and MoGURA. For MoGURA, it goes through BLR: an electronic circuit to stabilize a baseline with subtracting the overshot region. It significantly reduced deadtime after muon events to 1 μs, whereas the Kam FEE took 1 ms until the baseline goes back.

MoGURA board doesn't have an analog discriminator unlike Kam FEE. Despite that, It can digitize timing and charge information for all waveforms by using flash ADC. There are 4 gains P, H, M, and L gain, and each gain is 120, 24, 2.4 and 0.24. The sampling rate is 1 GHz by the P gain, 200 MHz by the H, M and L gain. Digitization depth is 8 bits.

Waveforms digitized by the P gain are used for hit discrimination. They are counted at system FPGA when they are greater than 0.3 photons. The number of hits is sent to MoGURA trigger board through VME.

MoGURA trigger system monitors Nhit that is the number of hits of all 17-inch PMTs within 120 ns. Mainly ID single or ID prescale is launched based on the hit information. The latter is set to observe lower energy events than the former: usual trigger. The trigger system sends a command system FPGA on the MoGURA board to acquire a digital waveform in a fixed time width or around a peek. After that, the waveform is recorded like Kam FEE.

Clock oscillator on the MoGURA board is synchronized with a timing that is generated based on not only GPS but also Rb atomic clock. Timestamp at the moment of trigger launch is recorded with a waveform. Launch offset - time difference from the trigger launches - is also recorded.

In this analysis, data taken with the new data acquisition system are used to tag muon induced spallation events. Triple tagging of muon and following neutrons and spallation event is very effective to reduce background events in the region of interest.

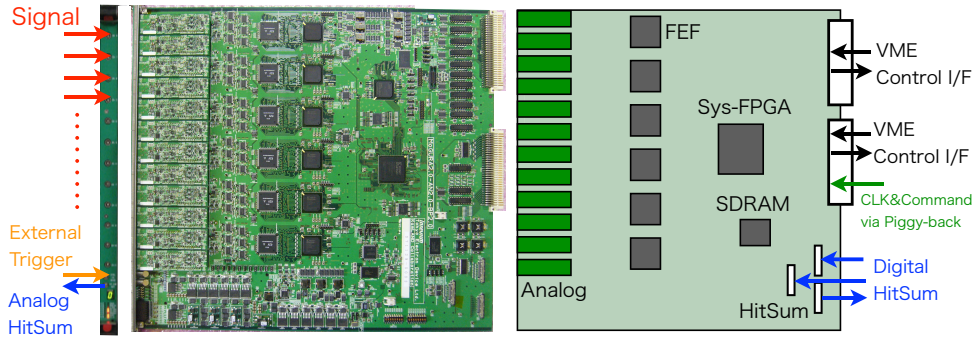

Figure 4.9.: MoGURA Electronics

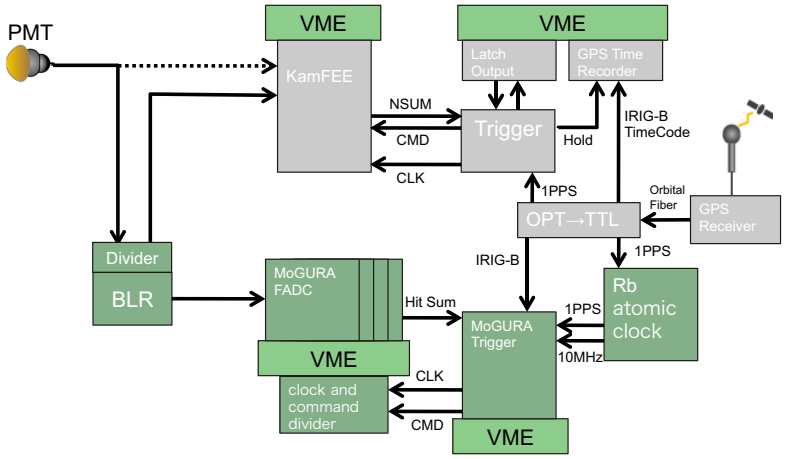

Figure 4.10.: KamLAND data acquisition system (KamFEE, MoGURA)

4.7. KamLAND-Zen Phase-I

4.7.1. Data Set

KamLAND-Zen Phase-I denotes a data period from the start of the experiment to just before the purification period described later. LS circulation by filtering was performed halfway, thereby two periods DS-1 and DS-2 are defined to facilitate analysis. In DS-2, fiducial volume is limited to avoid backgrounds from a pipe in the Xe-LS, and Xe concentration slightly changed as shown in Table. 4.1. Vertex and energy resolution was estimated to be 15.0 cm/$\sqrt{E}$ and 6.6 %/$\sqrt{E}$ with high statistic backgrounds and ThO_2W source calibration.

Table 4.1.: Data set in KamLAND-Zen Phase-I

	DS-1	DS-2	Total
date	Oct. 12 2011 - Feb. 9 2012	Mar. 1 2012 - June. 4 2012	-
livetime	112.3	101.1	213.4
fiducial mass (ton)	8.04	5.55	-
Xe concentration (wt%)	2.44	2.48	-
^{136}Xe exposure (kg-yr)	54.9	34.6	89.5

4.7.2. Background

Detector modification introduced some backgrounds not observed originally. ^{137}Cs and ^{134}Cs, fallout from a Fukushima dai-ichi nuclear power plant accident (FNPP1) are one of them, which contaminated the IB fabricated ∼90 km far from the plant. ^{134}Cs is still primary film background in $2\nu\beta\beta$ energy window in Phase-II.

It had a peak near the 2.458 MeV Q-value of ^{136}Xe $\beta\beta$ decay, and distributed in Xe-LS uniformly. By searching all possible decay, candidates were narrowed down to 4 nuclei: ^{110m}Ag, ^{208}Bi, ^{60}Co and ^{88}Y. And ^{110m}Ag was concluded as the dominant background of the 2.6 MeV peak. Sensitivity to $0\beta\beta$ decay was much suppressed by ^{110m}Ag. Therefore, we operated series of LS and Xe purification described in Sec. 4.8.

These detailed estimation are described later.

4.7.3. Search for Double-Beta Decay

$2\nu\beta\beta$

Event rate of ^{136}Xe $2\nu\beta\beta$ decay is measured to be $82.9 \pm 1.8(\text{stat}) \pm 3.4(\text{syst})$ (ton·day)$^{-1}$ in DS-1 and $80.2 \pm 1.8(\text{stat}) \pm 3.3(\text{syst})$ $(\text{ton} \cdot \text{day})^{-1}$ in DS-2, respectively. And the

half-life is obtained from DS-1 data as following (A. Gando et al., 2012 [42]);

$$T^{2\nu}_{1/2} = 2.30 \pm 0.02(\text{stat}) \pm 0.12(\text{syst}) \times 10^{21} \text{ yr}$$

$0\nu\beta\beta$

For ^{136}Xe $0\nu\beta\beta$ decay, 90% C.L. upper limits are obtained to be <16 events for DS-1, <8.7 events for DS-2, and <0.16 (kg·yr)$^{-1}$ in units of ^{136}Xe exposure, or $T^{0\nu}_{1/2} > 1.9 \times 10^{25}$ yr for combined result of DS-1 and DS-2. It is restricted by a presence of overriding ^{110m}Ag background as shown in Fig. 4.11.

Combination with a result reported by EXO-200 (Auger et al., 2012 [43]) gives a lower limit $T^{0\nu}_{1/2} > 3.4 \times 10^{25}$ yr. It corresponds to the following effective neutrino mass limit

$$\langle m_{\beta\beta} \rangle < (120 - 250) \text{ meV (90\% C.L.)}$$

According to its conversion to ^{76}Ge half-life using all NME, a positive claim of ^{76}Ge $0\nu\beta\beta$ decay (KLAPDOR-KLEINGROTHAUS and KRIVOSHEINA, 2006 [2]) is excluded above 97.5 % C.L. (Fig. 4.11).

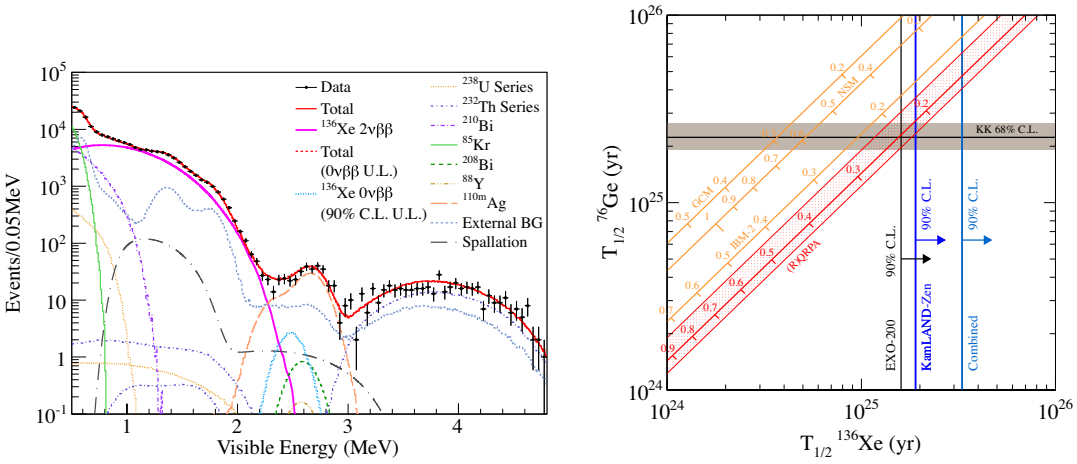

(a) (b)

Figure 4.11.: (a) Best-fit energy spectrum of Phase-I in R <1.35 m with $0\nu\beta\beta$ spectrum at upper limit. ^{110m}Ag overrides other backgrounds in the signal range. (b) ^{136}Xe and corresponding ^{76}Ge half-life limits obtained from KamLAND-Zen Phase-I (blue line) and from EXO-200 experiment (black line). Their combination result excludes a detection claim of ^{76}Ge $0\nu\beta\beta$ decay (gray band) at above 97.5 % C.L. including all NMEs. (A. Gando, Y. Gando, Hanakago, Ikeda, Inoue, Ishidoshiro, Kato, et al., 2013 [44])

Excited States

KamLAND-Zen can search exotic modes of double-beta decay such as transition into the excited states of the daughter nuclei, ^{136}Ba utilizing the difference of spectrum shape; summation of two electrons from double-beta decay and de-excitation γ. From Phase-I data, improved limits for $0^+ \to 2^+_1$ and first constraints for $0^+ \to 0^+_1$ and $0^+ \to 2^+_2$ are obtained (Asakura et al., 2016 [45]);

- $2\nu\beta\beta$ decay
  - $T_{1/2}(0^+ \to 0^+_1) < 8.3 \times 10^{23}$ yr
  - $T_{1/2}(0^+ \to 2^+_1) < 4.6 \times 10^{23}$ yr
  - $T_{1/2}(0^+ \to 2^+_2) < 9.0 \times 10^{23}$ yr
- $0\nu\beta\beta$ decay
  - $T_{1/2}(0^+ \to 0^+_1) < 2.4 \times 10^{25}$ yr
  - $T_{1/2}(0^+ \to 2^+_1) < 2.6 \times 10^{25}$ yr
  - $T_{1/2}(0^+ \to 2^+_2) < 2.6 \times 10^{25}$ yr

The limit of $0^+ \to 0^+_1$ for $2\nu\beta\beta$ constrains for a part of theoretical prediction $(1.3-8.9) \times 10^{23}$ yr.

Majoron Mode

Phase-I data also gives limits for ^{136}Xe $0\nu\beta\beta$ decay accompanying emission of one or two Majorons (A. Gando et al., 2012 [42]). In case of ordinary Majoron-emitting decay mode, the limit $T^{0\nu\chi^0}_{1/2} > 2.6 \times 10^{24}$ yr (90% C.L.) is obtained. It can be converted to the limits on the effective coupling constant of the Majoron to the neutrino $\langle g_{ee} \rangle < (0.8-1.6) \times 10^{-5}$ (90% C.L.) with the following relations;

$$T^{-1}_{1/2} = |\langle g_{ee} \rangle|^2 |M|^2 G \quad \text{for } 0\nu\beta\beta\chi^0 \tag{4.1}$$

$$T^{-1}_{1/2} = |\langle g_{ee} \rangle|^4 |M|^2 G \quad \text{for } 0\nu\beta\beta\chi^0\chi^0 \tag{4.2}$$

M and G represent the nuclear matrix elements and the phase space factors for the corresponding decay mode. It completely excludes a allowed region between a constraint by the observation of neutrinos from SN1987A and one from the supernova data; $2 \times 10^{-5} < \langle g_{ee} \rangle < 9 \times 10^{-5}$. It extended the excluded region by the SN1987A result down to $\langle g_{ee} \rangle < 4 \times 10^{-7}$, which indicates that ordinary Majoron-emitting decay modes does not have dominant contribution to light Majorana neutrino exchange for $\langle m_{\beta\beta} \rangle > 20$ meV.

4.8. LS and Xe Purification

LS and Xe purification are motivated by ^{110m}Ag backgrounds dominating $0\nu\beta\beta$ decay energy region. To reduce it, series of purification works were operated after Phase-I finished. Followings are the operations with each motivation and result.

- Filtration :
  This is the easiest purification method, but does not have reduction power. Purification of LS and Xe are needed.
- Xe extraction from Xe-LS :
  This revealed that 2.6 MeV events are background events, not $0\nu\beta\beta$ signal.
- Replacement by new purified LS : Reduction factor was 1/3 - 1/4. Further decrease was required.
- LS distillation in circulation mode :
  distilled LS without PPO was circulated.
- Xe-LS filling :
  After new LS with PPO was filled, Xe was dissolved to start Phase-II data taking.

Flow chart of these operations are shown in Fig. 4.12. During each operation, short period of data were taken to check effectiveness. The name of data periods are defined in Table. 4.2. In this section, outline of each operation is described with results.

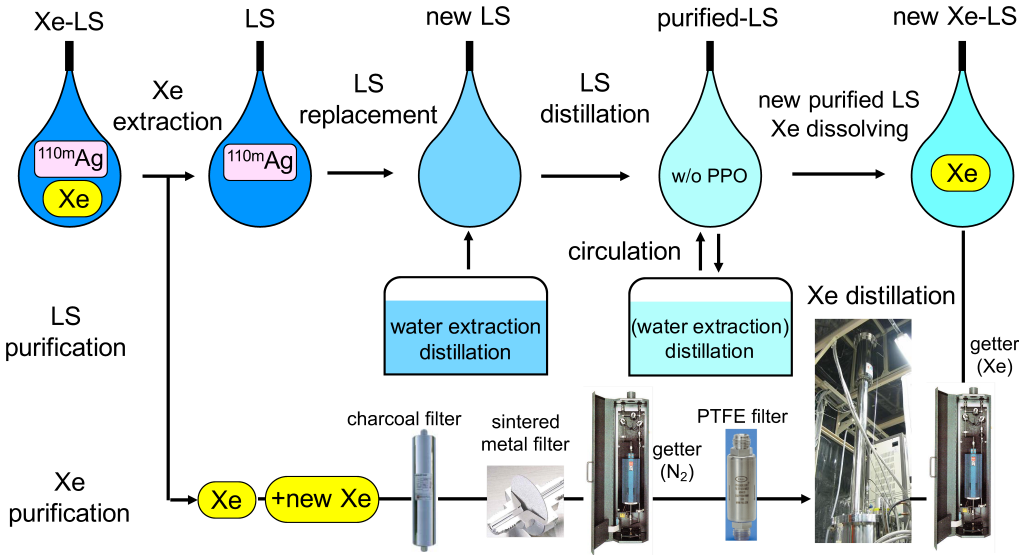

Figure 4.12.: Flow chart of LS and Xe purification

4.8.1. Filtration

We found 2.6 MeV peak background from DS-1 data in Phase-I. At that time, we do not know what kind of purification is effective. So we tried from the easiest purification method i.e. filtration. This operation was very simple. Xe-LS was circulated via 50 nm filter in Xe system while keeping boundary of filled/pre-filled Xe-LS by adjusting their temperature. 37,381 L of Xe-LS in total was filtered, which is equivalent to 2.3 times Xe-LS volume.

Table 4.2.: Summary of KamLAND-Zen operation

period	Data taking	Purification
Oct. 12, 2011 ∼ Feb. 9, 2012	Xe loaded LS (DS-1)	-
Feb. 9, 2012 ∼ Feb. 18, 2012	-	filtration
Mar. 1, 2012 ∼ Jun. 14, 2012	Xe loaded LS (DS-2)	-
Jun. 14, 2012 ∼ Jul. 7, 2012	-	Xe extraction
Jul. 7, 2012 ∼ Aug. 1, 2012	LS without Xe (DS-3)	-
Aug. 1, 2012 ∼ Aug. 29, 2012	-	fresh LS filling
Aug. 29, 2012 ∼ Nov. 9, 2012	new LS without Xe (DS-4)	-
Nov. 9, 2012 ∼ Nov. 20, 2013	-	distillation circulation
Dec. 11, 2013 ∼ Oct. 27, 2015	Xe loaded LS	-

After the operation, 101.1 days of data (DS-2) was taken, from which we concluded filtration does not have reduction power.

4.8.2. Xe Extraction

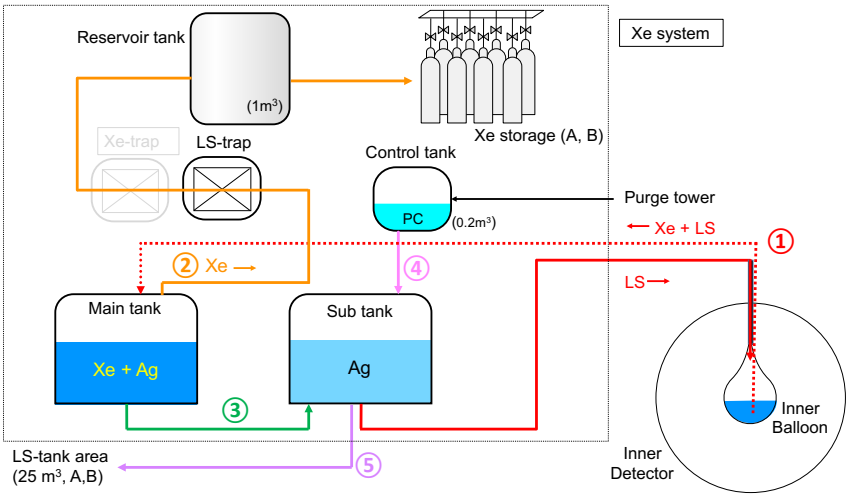

Figure 4.13.: Schematic diagram of procedure in Xe extraction. Following steps are repeated in batch mode: (1) Draining Xe-LS (from the bottom of the IB) and filling LS (from the top). (2) Collecting Xe by degassing Xe-LS and storing in a Xe storage. (3) Sending LS to the main tank. (4) Density adjustment using PC. (5) Discarding surplus LS to a storage tank.

As a next step, we collected Xe from the Xe-LS in the IB, in order to confirm that origin of the 2.6 MeV peak is not $0\nu\beta\beta$ decay signal but background events. In order to keep the original state, only purified pseudocumene (1.9 m^3 in total) was added to

supplement extracted Xe mass. This lighter LS was supplied from the top of the IB, and Xe-LS was extracted from a inlet located at z = -1.2 m. In order to maximize Xe collection efficiency, their LS boundary was kept by adjusting their densities and temperatures. Following is a procedure of the operation.

1. Draining Xe-LS and filling LS.
2. Collecting Xe by degassing Xe-LS and storing in a Xe storage.
3. Sending LS to the main tank.
4. Density adjustment by adding PC.
5. Discarding surplus LS to storage tank.

The schematic diagram is shown in Fig. 4.13. Approximately twice the amount of full volume in the IB was processed, though the operation stopped due to a pump trouble (see Sec. 4.8.6). 90 % of whole Xe in the IB was collected, which corresponds to 286.5 kg compared to ∼320 kg of total Xe. This residual was collected at the next operation namely LS replacement.

Fig. 4.14 shows 16.3 days of energy spectrum inside 1.2-m-radius after the Xe extraction (DS-3). There clearly exists a peak around 2.6 MeV, and consistency of its event rate between before/after the operation was confirmed. Thus, we concluded that events around the peak are background events.

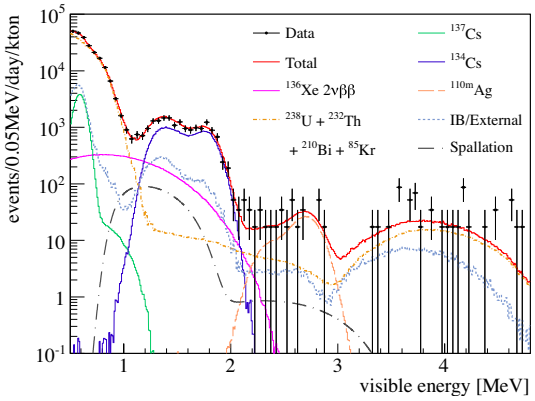

Figure 4.14.: Energy spectrum after the Xe extraction inside 1.2-m-radius with best-fit backgrounds which assumes dominance of ^{110m}Ag. Clear ^{110m}Ag peak is seen around 2.6 MeV. This event rate is consistent with that before the extraction. By the pump trouble during the operation, external backgrounds such as ^{137}Cs and ^{134}Cs were introduced (Yoshida, 2014 [39]).

4.8.3. LS Replacement

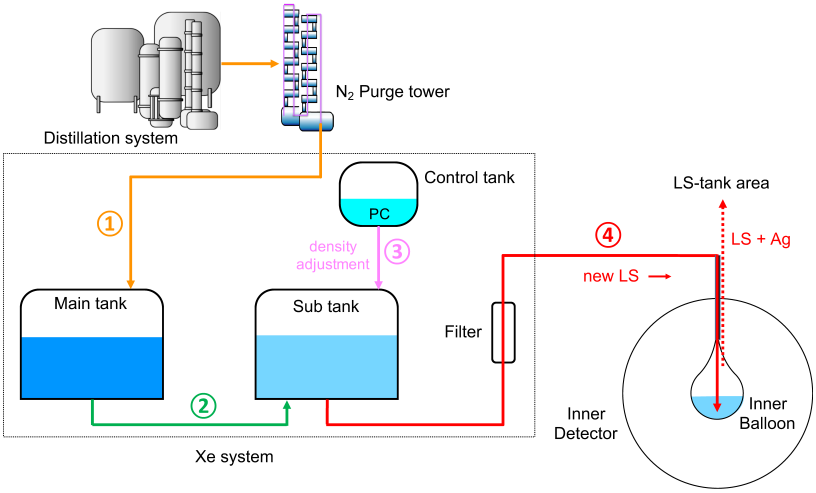

Figure 4.15.: Schematic diagram of procedure in LS replacement. Following is description of each step. (1) Delivering new purified LS from the purge tower. (2) Feeding the new LS to the sub tank. (3) Density adjustment by adding PC. (4) Filling the new LS (purified) and draining LS containing ^{110m}Ag abundantly

By the data after Xe extraction, presence of dominant ^{110m}Ag background was confirmed. In this operation, to reduce it, LS in the IB was replaced to new LS which was purified by water extraction and distillation method. Following is a procedure of the operation.

1. Delivering new purified LS from the purge tower in the 2nd purification area.
2. Feeding the new LS to the sub tank.
3. Density adjustment by adding PC.
4. Filling the new LS and discarding LS containing abundant ^{110m}Ag

The schematic diagram is shown in Fig. 4.15. As same as the previous operation, control of LS boundary is very important to maximize background reduction efficiency. Heavier LS (new LS) was filled from the bottom of the IB, and filling speed was kept to 170 L/hour.

Reduction factor of ^{110m}Ag is estimated from its time variation, shown in Fig. 4.16. Other known backgrounds such as ^{214}Bi in Xe-LS is already subtracted, where the contributions are evaluated by spectral-fit. Event rates before/after the LS replacement is obtained by fitting the data with the exponential decay curve of ^{110m}Ag. Thus, the reduction factor is estimated to be $\sim$1/3 - 1/4. Including reduction by radioactive decay, it becomes $\sim$1/9 - 1/12. Though the LS boundary was well maintained, the factor is less

than expectation from Xe recovery (∼3/4). There is potential that ^{110m}Ag distributing around the IB moved to the Xe-LS.

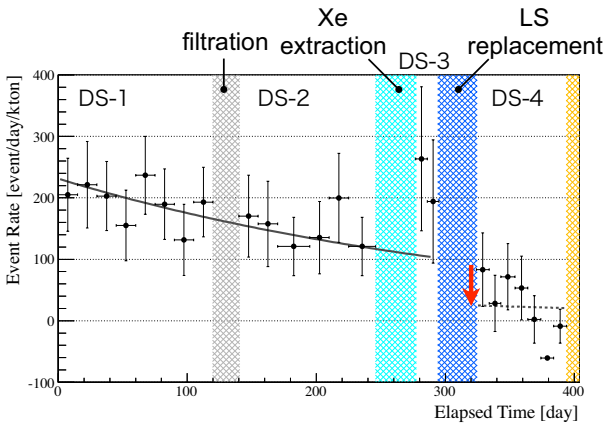

Figure 4.16.: Time variation of ^{110m}Ag background events inside 1.2m-radius. Background components such as ^{214}Bi is already subtracted, where the contributions are evaluated by spectral-fit. Reduction factor is obtained by fitting with the exponential decay curve of ^{110m}Ag ($\tau = 360$ day), for the data before the LS replacement (DS-1, 2, 3) and for the data after that (DS-4). It is estimated to be 1/3 - 1/4 without including reduction by radioactive decay.

4.8.4. LS Distillation in Circulation Mode

^{110m}Ag reduction factor by LS replacement is estimated to be ∼1/3. In order to achieve reduction by more than 2 orders of magnitude compared to the initial rate in DS-1, we performed LS distillation in circulation mode. The circulation was processed 3 cycles which corresponds to triple amount of LS in the IB. In the last cycle, new purified LS with PPO was fed in place of distilled LS. Thus, reduction factor is expected to be $1/3^4 \sim 1/100$, including the first LS replacement described above.

In this operation, drained LS from the IB is distilled then fed to the IB again, without replacing with new LS. PPO distillation was omitted as time-consuming, so the distilled LS does not contain it. Following is a procedure of the operation.

1. Filling purified LS and draining LS from the IB.
2. Xe collection by N_2 purge.
3. LS distillation.
4. Delivering LS without PPO to the sub-tank via the purge tower.
5. Degassing and adjusting LS density by adding PC.

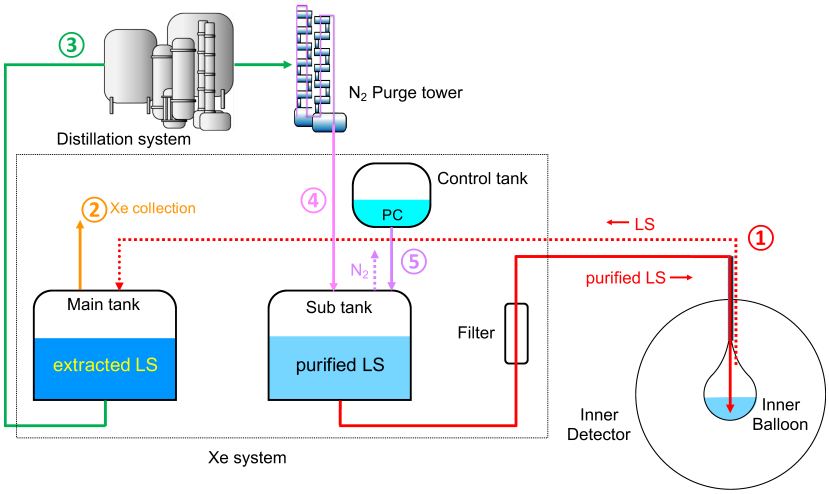

Figure 4.17.: Schematic diagram of procedure in LS distillation in circulation mode. (1) Filling purified LS and draining LS. (2) Xe collection by N_2 purge. (3) LS distillation. (4) Delivering LS without PPO to the sub-tank via the purge tower. (5) Degassing and adjusting LS density using PC.

Xe remaining in the IB was collected. The steps was also processed while keeping the LS boundary.

4.8.5. Xe-LS Filling

After filling the new LS with PPO, we started Xe-LS filling: the final operation in the series of purification. As to enriched Xe, collected Xe from the initial Xe-LS and new Xe was used, rectified by Xe distillation system. Following is a basic procedure of the operation, though it was irregular due to a failure of liquid pump used to send LS from the main tank to the sub tank.

1. Filling Xe-LS while feeding a pressure with Xe, and draining new LS from the IB.
2. Density adjustment by adding Decane.
3. Sending LS to the sub tank.
4. Dissolving Xe in LS
5. Density adjustment by adding Decane.
6. Xe collection by degassing
7. Discarding surplus LS without Xe in the main tank to the LS storage tank.

Xe gas passed through the getter and filters before dissolving it in LS. A crucial difference with Xe-LS filling in Phase-I is that Xe contained in drained LS is collected to the reservoir

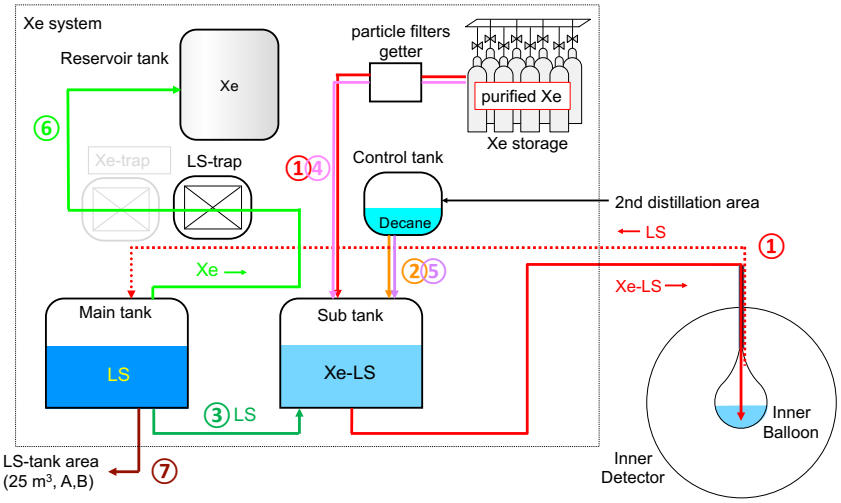

Figure 4.18.: Schematic diagram of procedure in Xe-LS filling. (1) Filling Xe-LS while feeding a pressure with Xe, and draining new LS from the IB. (2) Density adjustment by adding Decane. (3) Sending LS to the sub tank. (4) Dissolving Xe in LS (5) Density adjustment by adding Decane. (6) Xe collection by degassing (7) Discarding surplus LS without Xe in the main tank to the LS storage tank.

tank, then dissolved in LS again. In the Phase-I, drained LS was sent to LS storage tank without collecting Xe. Besides, Xe gas is continued to supply during Xe-LS filling to the IB (step 1.) while keeping inside-tank pressure to approximately 100 kPa, in order to dissolve Xe more efficiently. Finally, ∼380 kg of enriched Xe dissolved in LS (∼340 kg in Phase-I).

After the filling, Xe-LS was agitated via Xe system to uniform the Xe concentration. And two teflon tubes used to feed and drain LS was removed.

4.8.6. Contamination during Purification

Unfortunately, some troubles introducing contamination inside the IB happened during purification period. The most serious contamination was caused by the breakdown of a diaphragm pump placed at the Dome area. It was used to pump up Xe-LS from the IB during Xe extraction. Dumper of the pump to stabilize flow broke due to the aging degradation and bad operation, then radioactive impurities contained in compressed air (used for the pump and the dumper), from a leak point, was introduced into the LS pipe line.

Fig. 4.19 shows measured Rn concentration of LS in the IB from the start of Phase-I to the start of LS distillation period. LS filling normally accompanies Rn contamination, but the quantity at this trouble was overwhelming. It caused serious background contamination. Impurities distributing in LS was removed by the series of LS circulation, however a part of that sank into the bottom of the IB. Much increases of ^{214}Bi in

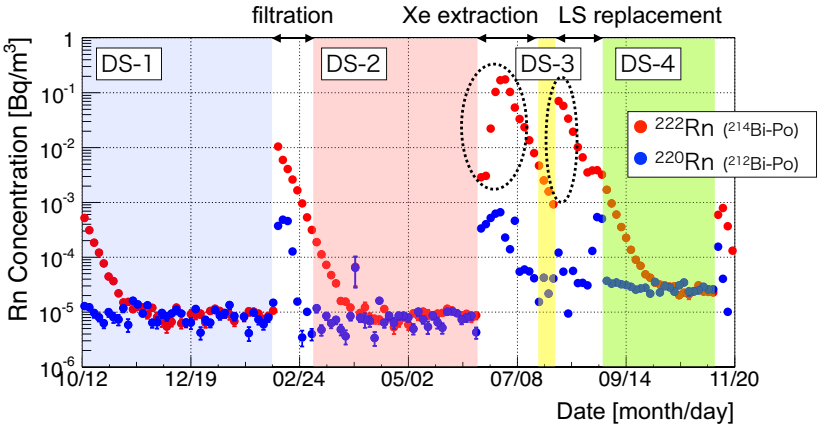

Figure 4.19.: Rn concentration during Phase-I and purification period. Increases inside dotted circles were caused by the break of diaphragm pump and exchange of the filter. The quantity is overwhelms other concentrations.

^{238}U-series, ^{208}Tl in ^{232}Th-series, , ^{134}Cs and ^{137}Cs were found after the trouble. The origin of ^{134}Cs and ^{137}Cs are considered as FNPP1. Because the pump was made and assembled in the north of Kanto area. Evaluation for each contamination are described in the chapter of "background estimation".

Another much increasing of Rn concentration is seen at the beginning of the first LS replacement, which was caused at the exchange of a particle filter placed in a LS supply line. This trouble also introduced massive Rn, but most of impurities was removed by the later LS circulation.

4.9. KamLAND-Zen Phase-II

After the LS and Xe purification, Phase-II started in Dec. 2013. In this section, difference from Phase-I and updates of analysis procedure are summarized.

Exposure Xe mass dissolved in LS increased ∼40 kg from Phase-I, owing to improvement of Xe dissolving procedure. Livetime also increased from 213.4 days (Phase-I) to 534.5 days (Phase-II).

Background Reduction As shown in Fig. 4.20, Background events in internal region reduced, owing to Xe-LS purification and radioactive decay. However, backgrounds around the IB increased in whole energy region, because of the troubles during purification. These estimation are described in the Chap. 8.

^{10}C Rejection ^{10}C spallation product is one of primary backgrounds in $0\nu\beta\beta$ energy region. In Phase-II, muon-neutron-^{10}C triple coincidence rejection is applied for the first time, owing to deadtime-free electronics i.e. MoGURA. Though this rejection was not

used due to large deadtime after muons in Phase-I, thereafter, new trigger to solve it was developed for Phase-II (Oki, 2013 [46]). The rejection procedure and efficiency are described in Secs. 7.3.4 and 8.6.1, respectively.

Fiducial Volume Optimization All volume analysis is applied for the first time. Though fiducial volume was limited to $R < 1.35$ m by ^{214}Bi on the IB ($R = 1.54$ m), multi-volume selection enabled to use whole volume inside 2-m-radius.

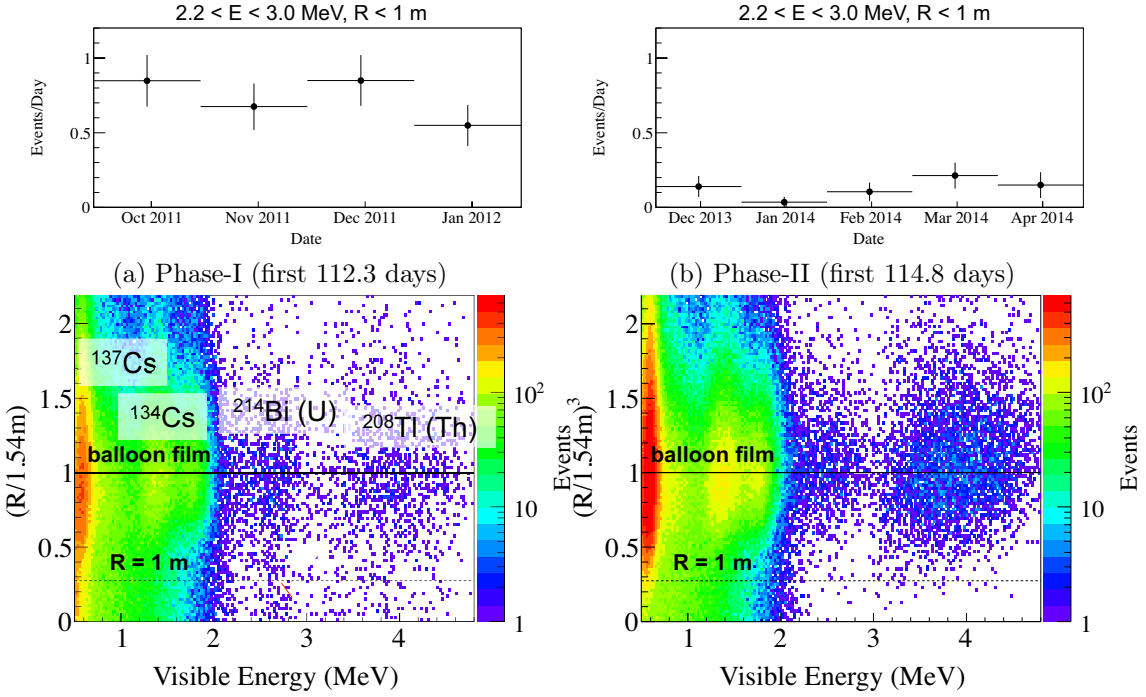

(a) Phase-I (first 112.3 days)

(b) Phase-II (first 114.8 days)

(c) Phase-I (first 112.3 days)

(d) Phase-II (first 114.8 days)

Figure 4.20.: Background reduction in Phase-I and Phase-II. Only the first ∼110 days were used to show their differences. Each energy region of 2ν and 0ν mode are defined as 1.2 - 2.0 MeV and 2.2 - 3.0 MeV here. (a), (b) Time variation of 0ν region events inside 1-m-radius. In Phase-II, there are evident reduction compared to Phase-I. (c), (d) Correlation of vertex and energy. In 0ν region, events in internal region decrease, as also seen in (a) and (b). Though ^{214}Bi dominates events around the IB ($R = 1.54$ m), ^{110m}Ag is also contributor in the Phase-I. In phase-II, events around the IB increase in all energy region, because contamination was introduced into the IB bottom by troubles during purification.

5. Event Reconstruction

In KamLAND detector, vertex and energy are reconstructed using charge and hit timing information extracted from acquired waveforms with 1879 PMTs. They have offsets and biases caused by change of detector status, so various corrections and calibrations are applied before event reconstruction.

The brief procedure of reconstruction is as follows:

1. Waveform analysis (charge and hit timing extraction)
2. Bad channel rejection
3. 1 p.e. gain calibration, timing correction
4. Muon track reconstruction
5. Vertex reconstruction
6. Energy reconstruction

In this chapter, estimation method and time dependence of each correction or calibration, and event reconstruction method are described.

5.1. 1 p.e. Gain Correction

Area of charge distribution is used for energy estimation, which needs standardization of 1 p.e. amplitude. 1 p.e. gain is defined as ratio of 1 p.e. charge peak in between a run being analyzed and a run in Jan. 2004. In this section, procedure of gain correction is described.

5.1.1. 17 inch PMT

1 p.e. peak in a 17 inch PMT is evaluated by a mean value assuming gauss distribution. Event selection of 1 p.e. events and fitting procedure is listed below.

- run selection
  - run time $\geq$ 10 hours
- event selection
  - 1 p.e. selection : $120 < N_{\mathrm{ID}} < 230$ hits
  - muon event cut

  - 2 msec veto after muon
  - 100 μsec veto after all events
- pulse selection
  - 1 peak in waveform
  - distance from PMT location > 5.6m
- gain estimation
  1. determine fit range
     - define the highest bin between 0.1 and 4.0 p.e as the center of fit range.
     - select narrowest fit range. the lower edge is selected from the maximum among 0.1 p.e., RMS and HWHM of the histogram. The upper edge is the minimum of RMS and HWHM.
  2. reject bad 1 p.e. distribution having poor RMS, unclear peak or low statistics
  3. fit by gauss distribution

Cut for N_{ID} (number of ID hits) is determined to select 1 p.e. events assuming poisson statistics. Peak is estimated run by run and channel by channel. Fig. 5.1(a) shows typical 1 p.e. charge distribution with fitting result. For the most of PMTs, gain is estimated to be $\sim$1 and is stable through this data set. But some peaks fall down along with temporal fall of resistance, and they do not recover as shown in Fig. 5.2. The cause is suspected to be short of bleeder circuit. Though the number of low charge PMTs continues to increase, peak estimation can deal with the variation by changing fit range.

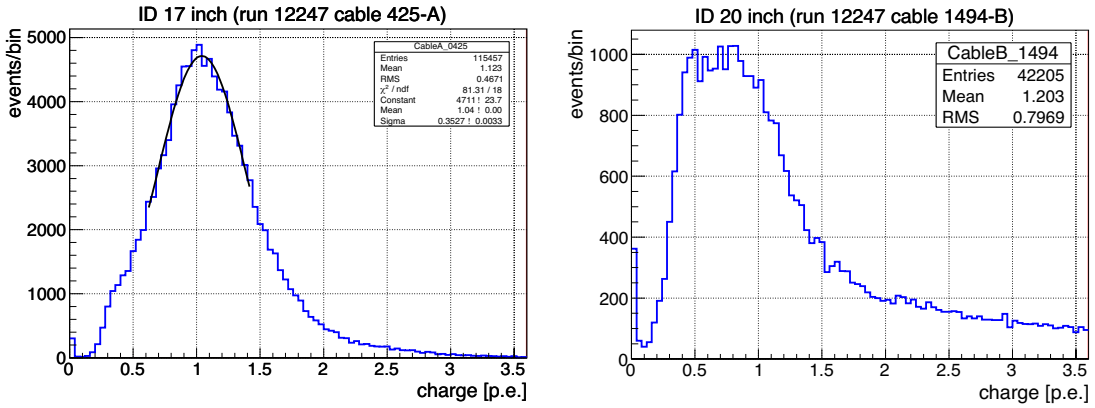

(a) 17 inch (b) 20 inch

Figure 5.1.: 1 p.e. charge distribution for 17"/20" PMTs. 17" gain is evaluated from its gaussian fit (black line). 20" distribution has worse resolution, so charge ratio of 17" and 20" with muon events is used instead.

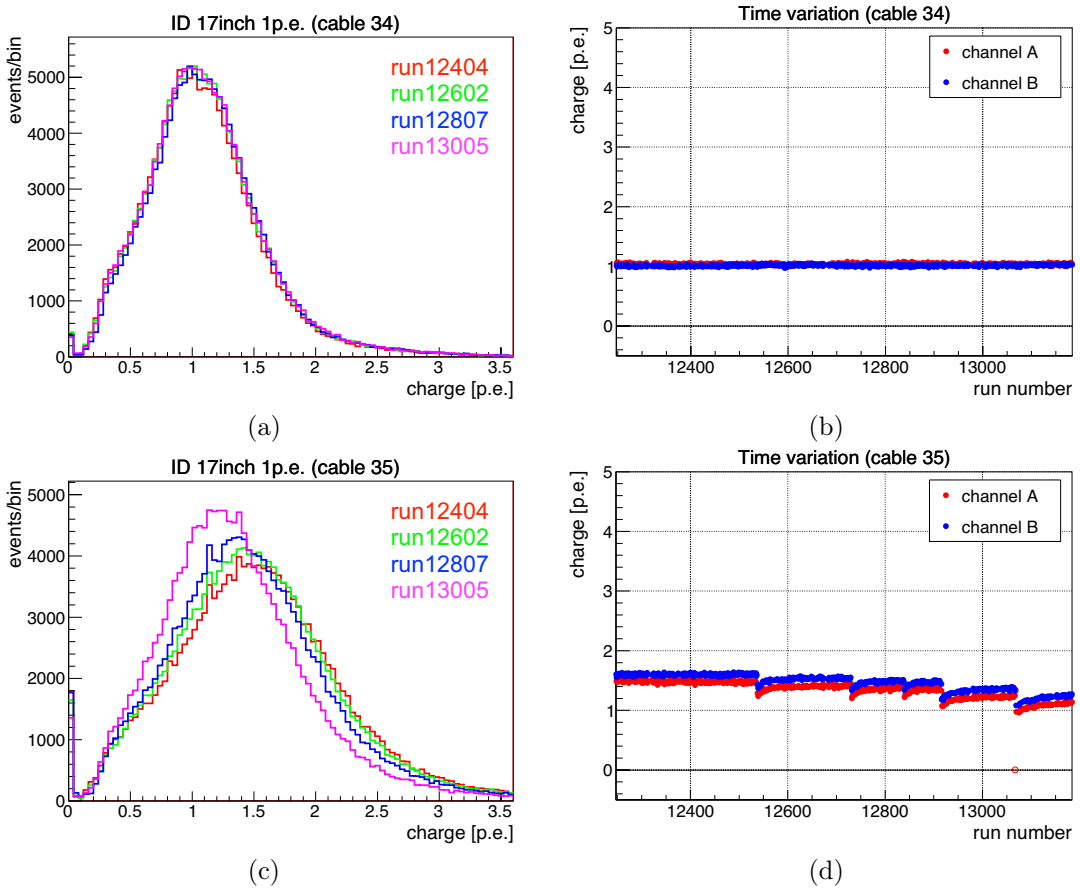

Figure 5.2.: Time variation of 1 p.e. charge distribution for (a)(b) normal and (c)(d) charge-decreasing 17" PMTs. Most of PMTs maintain stable values, but discontinuous drop is seen for some PMTs. It incurs increase of bad channels.

5.1.2. 20 inch PMT

20 inch PMTs have worse timing resolution as shown in Fig. 5.1(b), which makes it difficult to determine 1 p.e. peak. As an alternative way, charge ratio of 17 and 20 inch PMTs of muon events (Q_{ratio}) is used for 20 inch gain estimation, defined as follows.

$$Q_{\mathrm{ratio}} = \frac{Q_{\mathrm{20inch\text{-}target}}}{Q_{\mathrm{17inch\text{-}average}}} \times \left(\frac{17}{20}\right)^2 \tag{5.1}$$

where,

$$Q_{\mathrm{17inch\text{-}average}} = \frac{1}{N_{\mathrm{ref}}} \sum_{i=1}^{N_{\mathrm{ref}}} (Q_{\mathrm{corrected}})_i \tag{5.2}$$

$Q_{\mathrm{17inch\text{-}average}}$ is average of corrected charge ($Q_{\mathrm{corrected}}$) in 17 inch PMT, which is located close to a target 20 inch PMT. For $Q_{\mathrm{corrected}}$, 1 p.e. gain correction described in Sec. 5.1.1 is applied. To prevent misestimation by 20 inch PMT specific bad linearity in high energy, neighbor 17 inch PMTs are referred. The number of reference PMTs (N_{ref}) takes primary 5-8 PMTs, where low gain PMTs are eliminated.

- event selection
  - veto noise events
  - veto not muon events
  - NsumMax $\geq$ 1000
  - $Q_{\mathrm{ID}} \geq 10,000$ p.e.
- reference 17 inch PMT selection
  - veto low statistics in 1 p.e. distribution
  - 0.45 $<$ 1p.e. gain $<$ 4.0
  - $1.0 \leq Q_{\mathrm{corrected}} \leq 10,000$ p.e.
  - $300 < Q_{\mathrm{17inch\text{-}average}} < 5000$ p.e.

Fig. 5.3 is normal charge ratio distribution of one 20 inch PMT with gaussian fit, where linearity between 17" and 20" PMT is also checked.

Trend of 1 p.e. gain is presumable from average of all PMTs shown in Fig. 5.4. It indicates low gain PMTs increase, resulting increase of bad channels discussed in the next section.

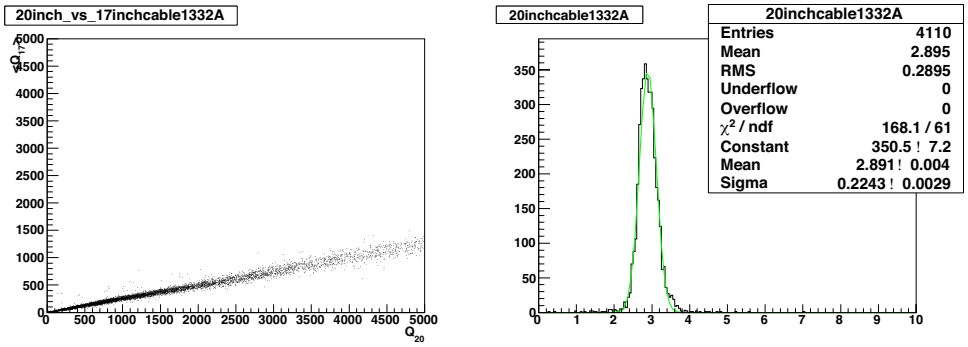

Figure 5.3.: Charge ratio distribution defined at Eq. 5.2, with its linearity between 17" and 20" PMTs. Fitted peak (green line) is used for 20" gain.

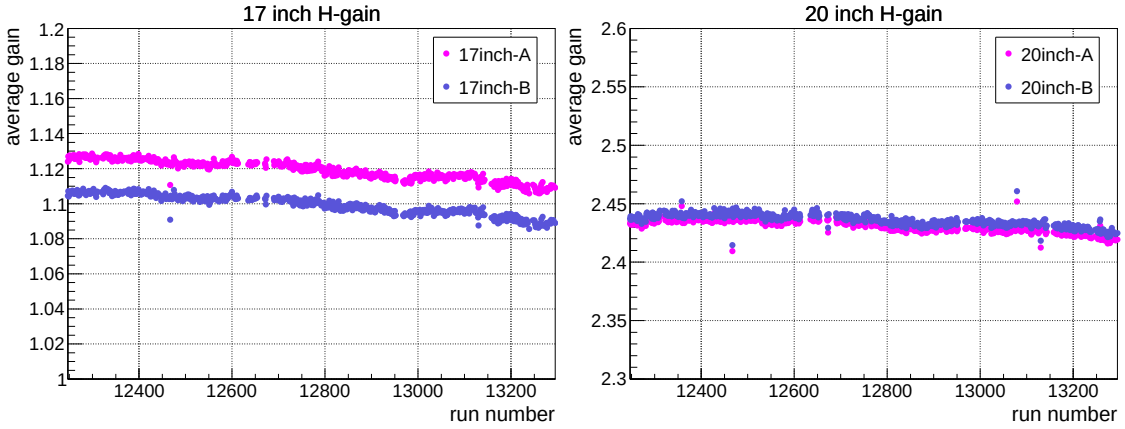

Figure 5.4.: Time variation of 17"/20" PMT average gain. Both slightly decreases due to increase of low gain PMTs.

5.2. Bad Channel

Channel behavior sometimes become bad by accidental electronics failure or trip of high-voltage by overcurrent and PMT degradation. These channels needs to be removed from vertex and energy estimation for the better resolution.

Bad channel criteria based on the number of hits are applied to each sub-run period divided by constant number of events so that a channel becoming temporarily unstable can be detected. When there is a period satisfying any of following criteria in a daily run, corresponding channel is regarded as bad. The criteria are set for the ID and OD PMTs, respectively. For the ID PMTs, there are restriction for charge and 1 p.e. gain other than following criteria. Fig. 5.5 shows time variation of run-specific bad channel. Increase of 17" PMT bad channel is mainly caused by increasing low gain PMTs, relative to stability of 20" PMT.

ID criteria

1. Small number of hits ($N < 600$) within 10,000 events
2. Small number of hits ($N < 80$) within 100 high energy muon events (charge sum $Q_{\mathrm{ID}} > 316,000$ p.e.)
3. Small number of hits ($N < 480$) within 10,000 events except muon events
4. Large number of missing waveforms whose ADC sum equals zero ($N > 1,000$) within 10,000 events
5. Large difference between the number of hits of ATWD A (N_{A}) and B channel (N_{B}) within 10,000 events.

   $$\frac{|N_{\mathrm{A}} - N_{\mathrm{B}}|}{N_{\mathrm{A}} + N_{\mathrm{B}}} > 0.18$$

6. large difference in expected charge from neighbor PMTs

   $$\frac{1}{N_{\mathrm{period}}} \sum_{i=1}^{N_{\mathrm{period}}} \left(\frac{1}{N_{\mathrm{event}}} \sum_{j=1}^{N_{\mathrm{event}}} \frac{(\bar{Q_j} - Q_j)^2}{\bar{Q_j}} \right) > 1,000 \text{ p.e.}$$

   $\bar{Q_j}$: average charge of neighbor 17 inch PMTs
   N_{event} : the number of events in one period ($= 100$)
   N_{period} : the number of period in one run

7. abnormal 1 p.e. gain

   17inch PMT : $(\text{gain} \leq 0.4) \cup (\text{gain} \geq 4.0)$
   20inch PMT : $(\text{gain} \leq 0.4) \cup (\text{gain} \geq 6.0)$

OD criteria

1. Small number of hits ($N < 5$) within 10,000 events

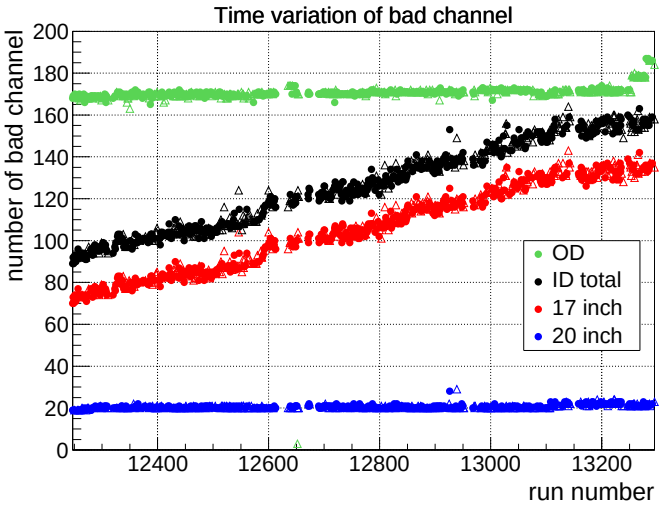

Figure 5.5.: Time variation for the number of bad channels for 17"(red)/20"(blue) PMTs and its total(black); point = good run, triangle = half-bad run.

5.3. Timing Correction

Hit timing information being essential for vertex reconstruction has delay caused by various factors listed below. To get better vertex resolution, timing calibration is applied for each cable and each ATWD channel.

- Photon flight time from a photon emission point to a PMT position
- Multiplying time in a PMT
  Multiplying speed varies by high voltage and incident angle to a photoelectric surface. And the box-and-line focus structure in a 17-inch PMT has better timing response than the venetian-blind structure in a 20-inch PMT.
- Transmission time in signal cable
  Cable length from a PMT to the electronics circuit differs in each cable. One meter of a cable causes ∼5 ns delay.
- Processing time in the electronics system
  Time difference derived from the electronics system are trigger launch offset, time scale digitization and cable extension by BLR installation. Time scale is calibrated by clock pulse test every day. Launch offset is recorded with the data.
- Leading edge delay of waveform depending on the number of emitted photons

5.3.1. Charge Dependence

To correct these timing delay difference, laser calibration was operated in 2004. Dye-laser connected to optical fiber was installed at the center of the detector. ∼500 nm wavelength light was transferred to isotropic scintillation light. Light intensities varying from single photo-electron to 5,000 photo-electron level, provides information to estimate charge dependence of transit time.

Correction by this calibration T_{laser} is defined as Eq. 5.3. The function depends on ADC sum, corresponds to collected photons in a PMT. Constant factors T_0, T_1, and T_2 were determined by this calibration. First term means constant offset derived from signal cable length and multiplier structure of PMT. Second and third terms represent correlation between charge and timing.

$$T_{\text{laser}} = T_0 + T_1 \cdot \log_{10}(\text{ADC sum}) + T_2 \cdot \log_{10}(\text{ADC sum})^2 \tag{5.3}$$

Fig. 5.6 shows calibrated correction functions called "TQ map". That of 20" PMT has generally stronger dependence about emitted photons.

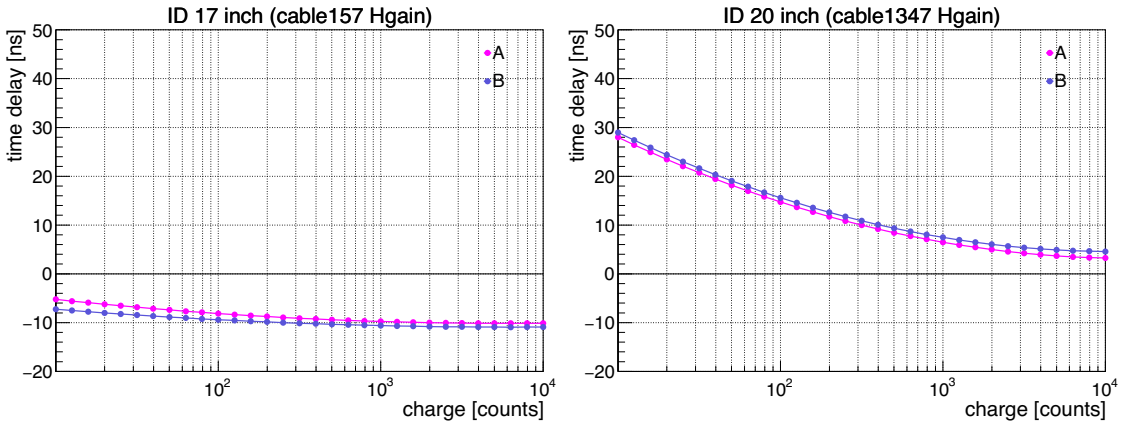

(a) ID 17 inch PMT

(b) ID 20 inch PMT

Figure 5.6.: Charge dependence of time delay for (a) 17" and (b) 20" PMTs (TQ map) determined by laser-calibration. X-axis indicates ADC sum. Correction function is estimated in each cable and ATWD channel.

5.3.2. Cable Extension

BLR was installed between PMTs and ATWDs. At that time, signal cables were extended. It caused additional timing delay shown in Table 5.1. The delay time is divided into 4 values by PMT type and VME crate physical location. It was measured by oscilloscope as the installation. There is no cable extension for OD 20 inch PMTs.

Table 5.1.: Cable extension and the delay by BLR installation

channel	cable length[m]	delay[nsec]
ID 17inch in the upper VME crates	1.92	8.4
ID 17inch in the lower VME crates	4.43	23.4
ID 20inch in the upper VME crates	0.44	2.4
ID 20inch in the lower VME crates	1.50	9.9

5.3.3. Time Dependence

Regular ^{60}Co source calibration before KamLAND-Zen enabled to monitor time variation of transit time. However in KamLAND-Zen, there is one-time-only calibration at the end of the data period to avoid contamination inside the inner-balloon.

As an alternative of ^{60}Co source, a PEEK (Poly Ether Ether Ketone) pipe was used, which connects corrugated pipe and top edge of inner-balloon. A lot of ^{40}K events was observed around the PEEK, which is enough for day by day correction. The connection pipe is located at Z $\sim$4.3 m, hit timing varies by the distance between the pipe and a PMT. so only relative variation of hit timing is applied as correction.

Construction of Base Function

Fitting function of hit timing distribution was originally gaussian, and its time variation introduced $\sim$3 ns uncertainty. For the better determination and stability, base function for the fitting was constructed, based on PEEK events itself selected by the procedure as shown below.

1. Event selection
   These are selections for PEEK events. Data at the beginning of the KamLAND-Zen experiment is used, in which time jitter of hit timing is negligible.
   - veto muon events and 2ms after muon events
   - $4.2 < Z < 4.8$ m
   - $\rho < 0.8$ m
   - NsumMax > 210
2. PMT classification
   Common function is constructed from neighbor PMTs whose shapes are expected the same. All PMTs are classified into 16 groups for 17" and 20" PMTs respectively, according to PMT Z position. The definition is shown in Table. 5.2.
3. Integration of hit timing spectra
   To remove timing offset of each channels, half maximum bin is defined as the origin.

After the alignment and rejection of bad shape spectra, they are merged in each group.

Fig. 5.7 is the normalized base function in each PMT type and each group. As PMT Z position become high, time shape become sharper due to the PEEK location. Difference in PMT type results from its structure.

Table 5.2.: Classification of PMT. All 17" and 20" PMTs are classified by 1 m Z width. The bottom PMTs have low statistics due to long distance from the PEEK, so the width is extended to 2 m. Each group has comparable number of entries although PMT entries are different.

Z range	PMT entries		hit entries	
	17"	20"	17"	20"
-8.5 ∼ -6.5 m	140	59	1.3×10^7	5.9×10^6
-6.5 ∼ -5.5 m	80	44	7.6×10^6	5.0×10^6
-5.5 ∼ -4.5 m	80	35	8.2×10^6	4.5×10^6
-4.5 ∼ -3.5 m	80	30	9.0×10^6	3.8×10^6
-3.5 ∼ -2.5 m	85	35	1.0×10^7	4.6×10^6
-2.5 ∼ -1.5 m	75	30	9.4×10^6	3.8×10^6
-1.5 ∼ -0.5 m	85	35	1.1×10^7	5.4×10^6
-0.5 ∼ 0.5 m	90	30	1.3×10^7	4.5×10^6
0.5 ∼ 1.5 m	85	34	1.3×10^7	5.8×10^6
1.5 ∼ 2.5 m	70	35	1.1×10^7	6.5×10^6
2.5 ∼ 3.5 m	90	30	1.7×10^7	6.1×10^6
3.5 ∼ 4.5 m	75	35	1.6×10^7	7.7×10^6
4.5 ∼ 5.5 m	80	35	1.9×10^7	8.6×10^6
5.5 ∼ 6.5 m	85	39	2.5×10^7	1.2×10^7
6.5 ∼ 7.5 m	75	34	2.8×10^7	1.4×10^7
7.5 ∼ 8.5 m	50	14	2.1×10^7	6.5×10^6

Fitting

PEEK event selection is the same as in base function construction. After normalizing base function to fit data, relative timing based on base function (ΔT) is determined to minimize χ^2 from -50 to 130 ns, as shown in Fig. 5.8. Fitting error is normally 0.1 ∼ 0.3 ns. Deviation of ΔT from the beginning of KamLAND-Zen is applied for correction as T_{run}. Though hit timing is stable for most of channels, replacement of dead electronics

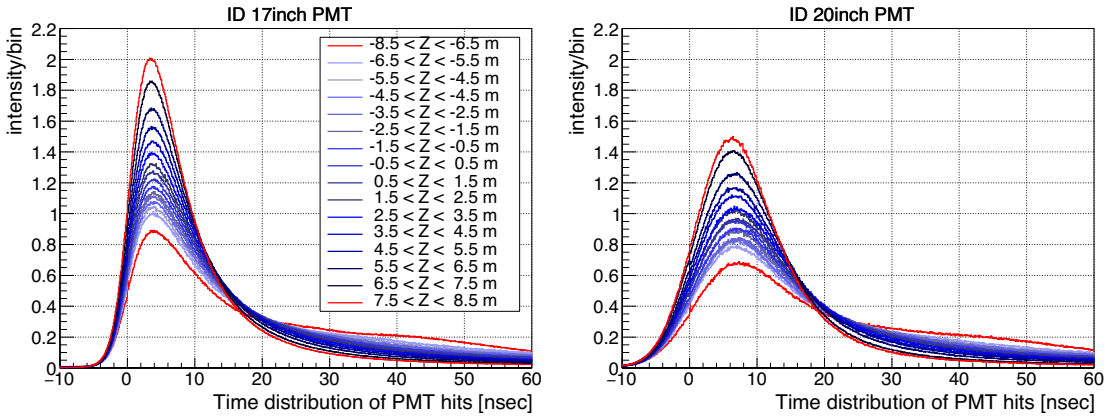

(a) ID 17 inch PMT (b) ID 20 inch PMT

Figure 5.7.: Hit timing base function constructed by PEEK events. As PMT Z position become high, time shape become sharper due to the PEEK location. Difference in PMT type results from its structure.

board cause approximately 1 - 5 ns shift. This method enabled its accurate estimation, which leads to improvement of vertex stability, as described in Sec. 6.2.2.

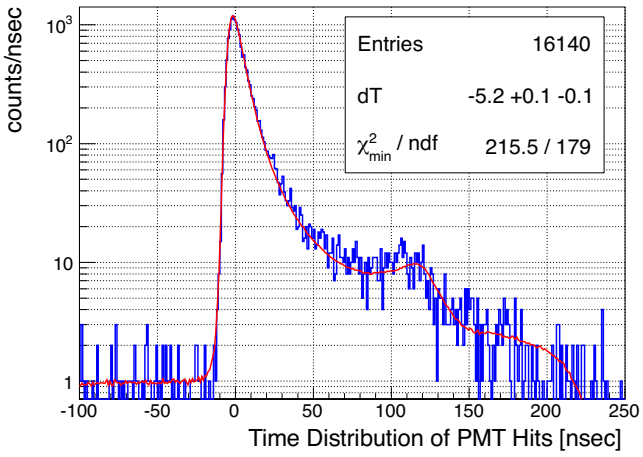

Figure 5.8.: Hit timing distribution with the best-fit base function. Estimated relative time is used for correction.

Final timing correction is defined as follows. It is applied each channel and each ATWD of each run.

$$\begin{aligned} T_{\text{correction}} &= T_{\text{raw}} - T_{\text{offset}} \\ &= T_{\text{raw}} - (T_{\text{trigger}} + T_{\text{laser}} + T_{\text{cable}} + T_{\text{run}}) \end{aligned} \tag{5.4}$$

where,

T_{trigger} : trigger launch offset

T_{laser} : correction from laser calibration (Eqn. 5.3)

T_{cable} : cable extension correction

T_{run} : time dependence correction

5.4. Dark Energy

Dark energy is accidental noise pulse arising from thermal electrons emitted from photoelectric and dynode surface or light emitting by dropped out electrons. It strongly depends on detector status: temperature and operation mode such as LS filling. The contribution is determined in each run, then subtracted on energy estimation.

For vertex reconstruction, "dark charge" like average of all hit PMTs are used. On the other hand, energy reconstruction needs cable-specific information for which position dependent temperature varying ∼1.7 ∘C between top and bottom of the detector is reflected. Thus cable by cable dark charge called "dark ring" is also estimated.

5.4.1. Dark Charge

The procedure of "dark charge" estimation is as follows:

1. event selection
   - veto muon events and 2ms after muon events
   - reject events outside 2 m radius to reduce TOF dispersion
2. off-time window search
   In hit timing distribution of all 17" PMTs, 50 ns hit-time window is determined that the number of hits within the window takes maximum. 50 ns off-time window is set 50 ns before the start of the hit-time window as shown in Fig. 5.9(a).
3. dark charge calculation
   get average in the off-time window after vetoing charge below 0.3 p.e. threshold. Dark charge is calculated as follows:

$$(\text{dark charge}) = \frac{\text{charge sum of hit PMTs in off-time window}}{\text{number of hit PMTs in off-time window}} \tag{5.5}$$

Dark charge is affected by detector condition such as the temperature and LS convection. Fig. 5.9(b) shows time variation of dark charge in this data set, which indicates critical change did not occurred.

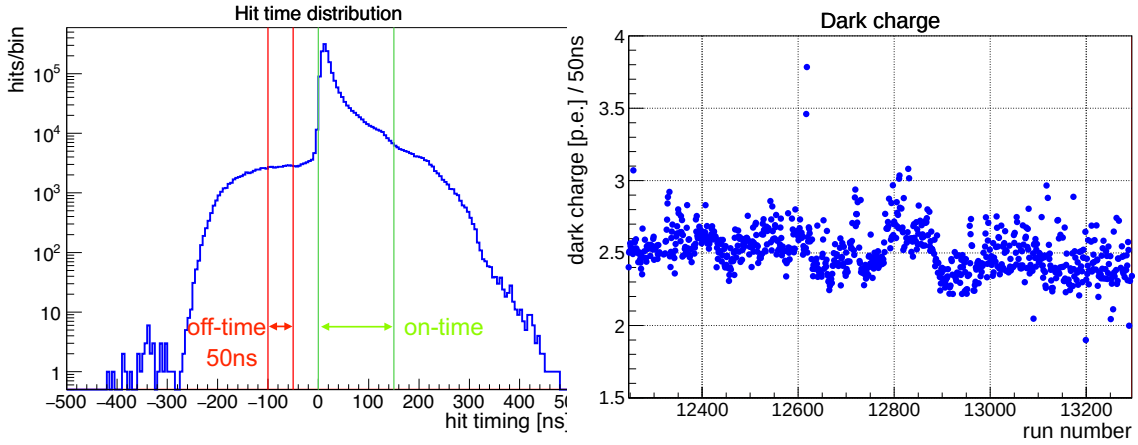

(a) Hit time distribution

(b) Time variation of dark charge

Figure 5.9.: (a) Hit timing distribution of 17" PMTs in one run. Noise events within off-time window are counted to dark charge. (b) Time variation of dark charge.

5.4.2. Dark Ring

Estimation of dark ring i.e. cable-specific noise charge basically follows that of dark charge. The difference is listed in below.

1. event selection
   In addition to the selection in "dark charge" flasher events are rejected, because it makes "dark ring" more than 10 times higher than typical value. They are caused by light emission from a PMT, and most of charge concentrates around one PMT. They are selected as the ratio of maximum charge to total charge is higher than 0.6.

2. off-time window search in the same method as in "dark charge".

3. dark ring calculation
   get average charge in each channel. To reduce statistical uncertainty, all channels are classified to 111 groups by PMT Z location (one group is called "ring"), then the average in each ring is used as "dark ring". In this calculation, bad channels are rejected. Fig. 5.10 shows row dark ring and the average.

5.5. Muon Reconstruction

KamLAND is located under the ∼1000 m overburden, corresponding to 2,700 m.w.e. It reduces cosmic-ray muon rate going through the KamLAND detector to ∼ 0.34 Hz. Muon events can be easily identified by their large energy deposit. Their tracks are

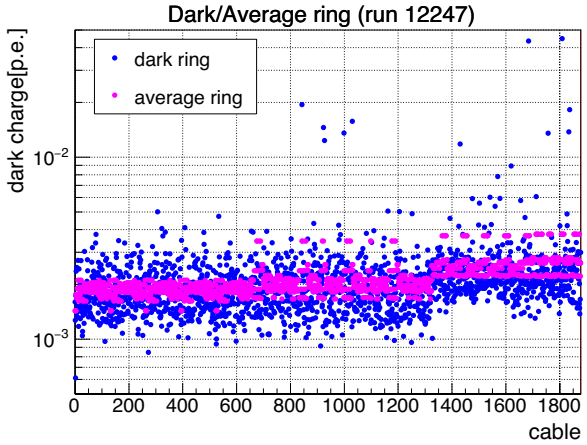

Figure 5.10.: Dark ring and average ring

reconstructed by the established method, which are used for background estimation of spallation products induced by muon events. In this section, muon event selection, tracking algorithm and the performance are described.

5.5.1. Selection Criteria

Muon events observed in the KamLAND detector are divided into "showering muon" ($\Delta Q > 10^6$ p.e.) and "non-showering muon" ($\Delta Q < 10^6$ p.e.) by residual charge ΔQ described in Sec. 5.5.3. Non-showering muon dominating ∼90 % of all muons is further categorized into "through going muons" go through inside the liquid scintillator (LS), and "clipping muons" crossing buffer-oil(BO). These are distinguishable with light intensity caused by light yield difference between LS and BO, as shown in Fig. 5.11(b). The selection criteria is as follows.

- $Q_{17} \geq 10,000$ p.e. (∼30MeV) : for "through going muons"
- $(Q_{17} \geq 500$ p.e.$) \cap (N_{200\mathrm{OD}} \geq 5$ hits) : for "clipping muons"

Q_{17} is the total charge sum of the 17 inch PMTs. And $N_{200\mathrm{OD}}$ is the number of hits in the outer-detector (OD), which is used to avoid high charge noise events as shown in Fig. 5.11(a). Their event rates are measured to be 0.32 Hz for "through going muons" and 0.036 Hz for "clipping muons", 0.36 Hz in total. Instability of clipping muon rate at the end of period is probably caused by increase of dead OD PMTs seen in Fig. 5.5.

5.5.2. Algorithm for Muon Track Reconstruction

Track of "through going muons" can be reconstructed via arrival times of the first-arriving Cherenkov or scintillation photons at the PMTs, because earliest scintillation light proceeds at the Cherenkov angle for relativistic muons, and it has enough light yield to generate an photoelectron in each PMT. Fig. 5.13 shows track of the earliest photons

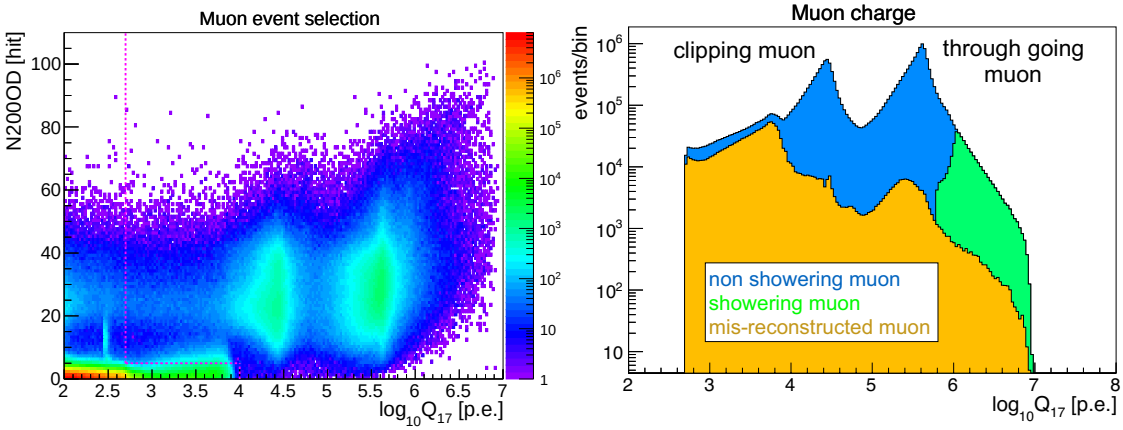

(a) OD hit v.s. total charge (17" PMT)

(b) Total charge (17" PMT)

Figure 5.11.: Muon charge distribution and correlation with OD hit. Muon events are selected by their total charge for 17" PMT and number of OD hits. The thresholds are drawn in (a) with magenta dotted lines.

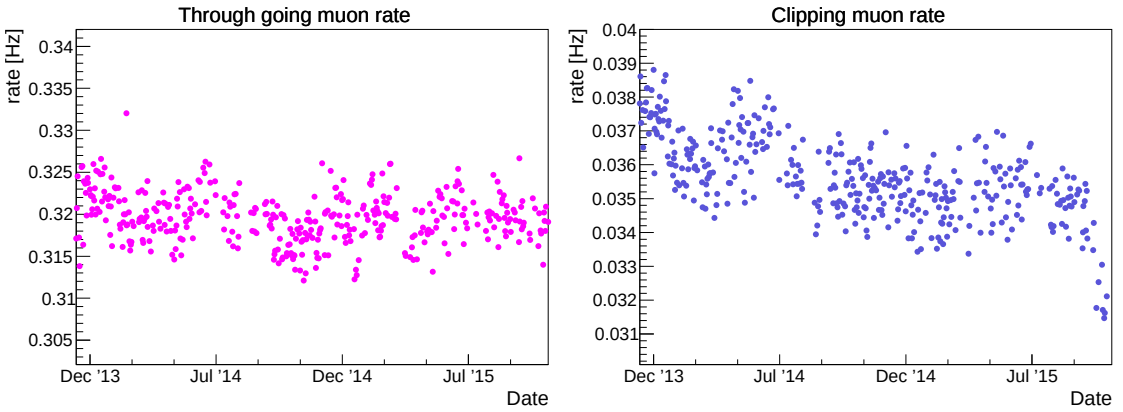

(a) Through going muon

(b) Clipping muon

Figure 5.12.: Event rate stability for (a) "through going muons" and (b) "clipping muons". Their average rates are measured to be 0.32 Hz and 0.036 Hz, respectively.

from a muon track. Difference between time entering to LS and photon arrival time of the earliest photon at a PMT (ΔT) is represented as the summation of the duration the relativistic muon runs until the light emission, and the duration the photon runs to a PMT.

$$\begin{aligned}\Delta T &= \frac{l}{c} + \frac{(z-l)/\cos\theta}{c/n} \\ &= \frac{z-\rho/\tan\theta}{c} + \frac{\rho/\sin\theta}{c/n}\end{aligned} \tag{5.6}$$

ΔT is also represented as a function of θ (the angle from a track). which satisfies $\cos\theta = 1/n = \cos\theta_c$ at $\Delta T/d\theta = 0$. From this equation, muon entrance position and track direction can be derived. Refractive index n is calculated by taking into account the difference between LS and BO. For "through going muons", n takes from 1.5 to 1.65, and for "clipping muons" it takes from 1.4 to 1.5.

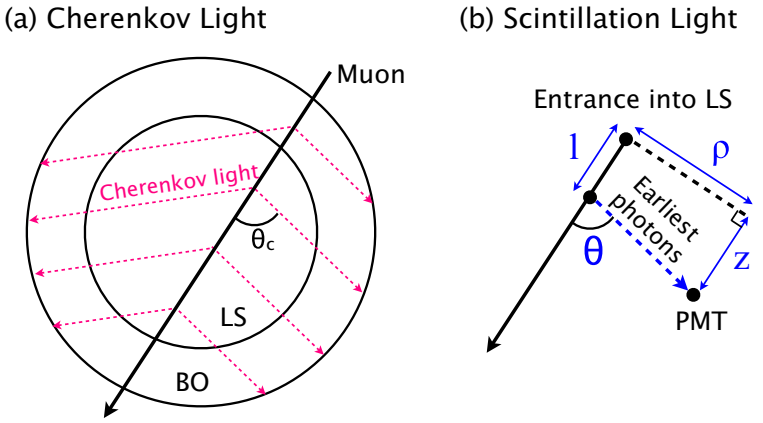

Figure 5.13.: Schematic view of muon track with (a) Cherenkov light and (b) scintillation light emission (A. Gando, 2012 [40]).

5.5.3. Tracking Performance

Track reconstruction converges for 97 % of "through going muons". Track model of single-muon cannot be applied to multiple-muons and electromagnetic or hadronic showers ("showering muons"), so they are badly reconstructed, dominating 7.8 % of all muons. It is described by "residual charge" (ΔQ), for which track light yield in LS and BO is subtracted from total charge sum. L_{BO} and L_{LS} are track length in LS and BO, respectively. And $\left(\frac{dQ}{dX}\right)^{\mathrm{ideal}}$ represents light yield of Cherenkov and Scintillation light per unit track length. They are evaluated using muons at the earlier KamLAND runs.

Fig. 5.14 shows the shortest distance between reconstructed muon track and the center of the detector, called "impact parameter". There is clear boundary between LS and BO

region at 6.5 m. It well reproduces correlation between muon charge and track position.

$$\Delta Q = Q_{17} - L_{\mathrm{BO}} \left(\frac{dQ}{dX}\right)^{\mathrm{ideal}}_{\mathrm{Cherenkov}} - L_{\mathrm{LS}} \left(\frac{dQ}{dX}\right)^{\mathrm{ideal}}_{\mathrm{Scintillation}} \tag{5.7}$$

$$\left(\frac{dQ}{dX}\right)^{\mathrm{ideal}}_{\mathrm{Cherenkov}} = \frac{Q_{17}}{L_{\mathrm{BO}}} = 31.45 \text{ p.e. / cm} \tag{5.8}$$

$$\left(\frac{dQ}{dX}\right)^{\mathrm{ideal}}_{\mathrm{Scintillation}} = \frac{Q_{17} - L_{\mathrm{BO}} \left(\frac{dQ}{dX}\right)^{\mathrm{ideal}}_{\mathrm{Cherenkov}}}{L_{\mathrm{LS}}} = 629.4 \text{ p.e. / cm} \tag{5.9}$$

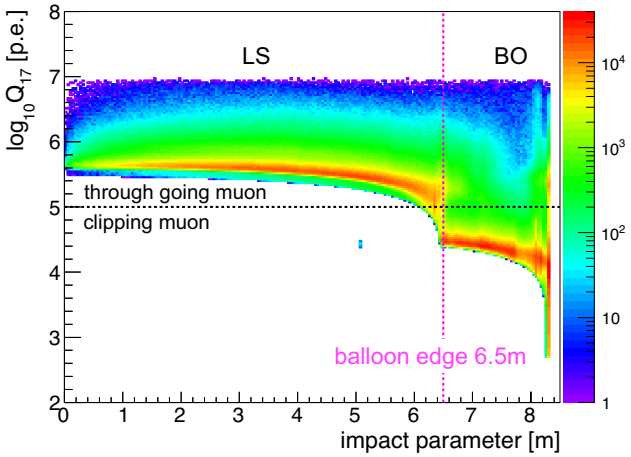

Figure 5.14.: Correlation of total charge and impact parameter defined as shortest distance between muon track and detector center. Reconstructed muon track well reproduces track position of "through going muons" and "clipping muons".

5.5.4. Muon Gain Correction

Total charge sum of muon events fluctuates by increase of bad channels and variation of LS/BO light property. Fig. 5.16 shows time variation of muon charge peak. In KamLAND-Zen 2nd phase, Cherenkov light yield decreases approximately 2%. To keep muon selection efficiency constant, charge correction factor called muon gain is estimated run by run using "clipping muons". The event selection is shown below:

- muon event selection
  - after pulse veto
  - OD flasher veto
  - OD noise veto

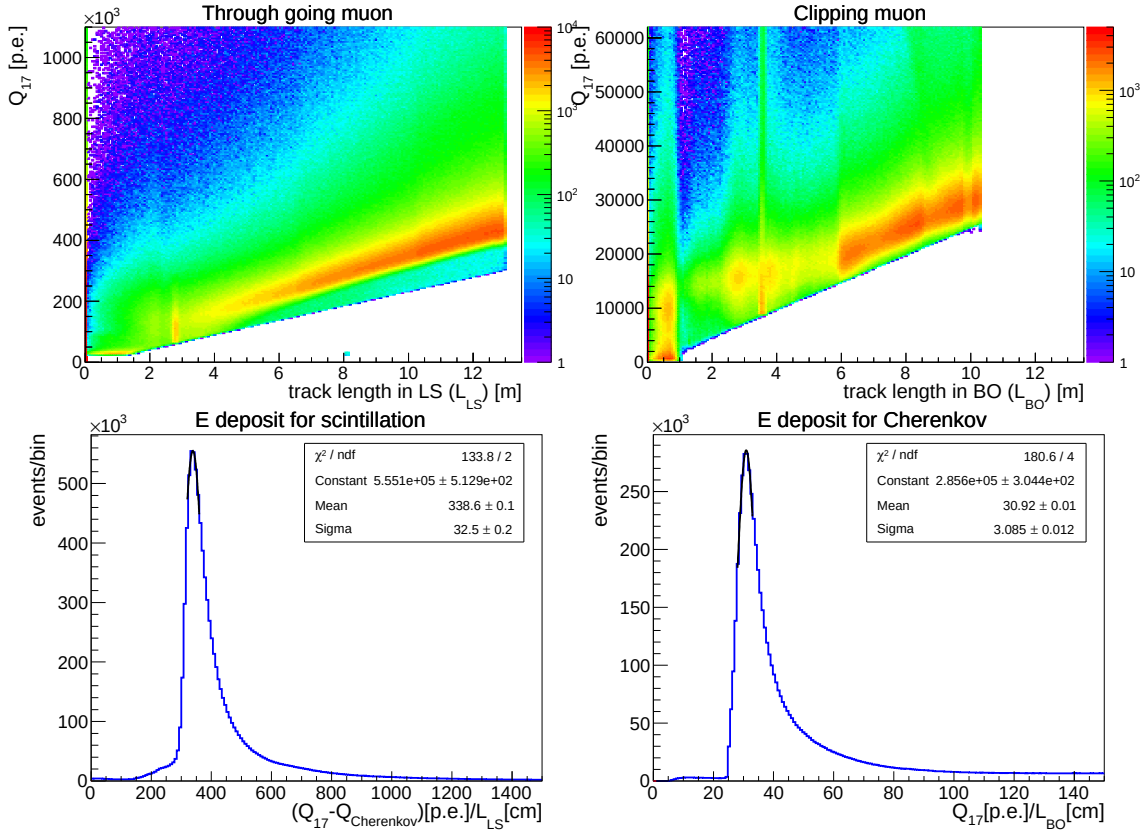

Figure 5.15.: Reconstructed muon track length and its energy deposit for scintillation light and Cherenkov light calculated from Eqs. 5.8 and 5.9.

- run selection
  - run time $\geq$ 5 hours
  - reject runs including long deadtime.

Charge peak is determined by gaussian fitting. And the charge ratio between a target run and a base run is applied to Q_{17} as correction factor.

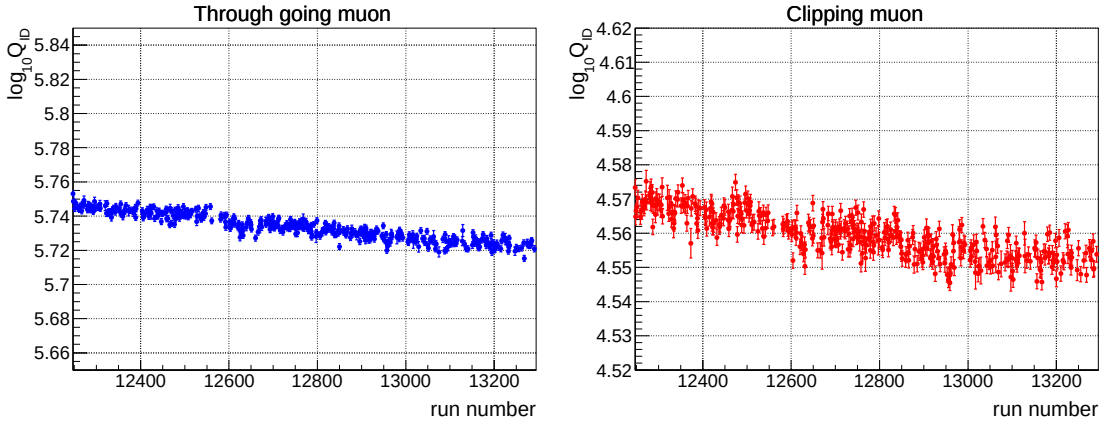

Figure 5.16.: Time variation for charge peak of (a) "through going muons" and (b) "clipping muon". It decreases along with increase of dead PMTs. Charge ratio between a target run and a base run is used as muon gain correction.

5.6. Vertex Reconstruction

Event vertex is reconstructed from hit timing spectra of all enabled PMTs, using two fitters, "LT Vertex" and "V2 fitter". The former behaves as rough estimator, and the latter does fine tuning. In this section, reconstruction algorithm of two fitters are described.

LT Vertex

Given a vertex position (x, y, z), photon emission time t_i can be calculated in relation to the i-th PMT.

$$t_i(x, y, z) = T_{detected,i} - TOF_i(x, y, z) \tag{5.10}$$

$T_{\text{detected},i}$ is the photon arrival time and $TOF_i(x, y, z)$ is TOF (Time Of Flight) subtracted time, defined as follows,

$$TOF_i(x, y, z) = \frac{\sqrt{(x - x_i)^2 + (y - y_i)^2 + (z - z_i)^2}}{c/n_{\text{eff}}} \tag{5.11}$$

It denotes photon traveling time from vertex (x, y, z) to i-th PMT location (x_i, y_i, z_i). c/n_{eff} is the effective light speed in the LS, which inclusively represents all processes related to average photon propagation speed. It is determined 16.95 cm/ns from source

calibration tuning. $T_{\mathrm{detected},i}$ is also affected from the detected number of photons. This multi-photon effect is corrected according to charge in each PMT.

(x, y, z) is adjusted to minimize deviation of the set t_i. However it does not converged well due to the time spread of photon emission time and absorption/re-emission processes. So independence of t_i and space-time correlation dt_i/dx ; derivatives of t_i are assumed. In ideal vertex point, there is no correlation in the two variables. Therefore the covariance $\sigma_{t_i,dt_i/dx}$ should be zero.

$$\frac{dt_i}{dx} = \frac{n_{\mathrm{eff}}(x_i - x)}{c\sqrt{(x - x_i)^2 + (y - y_i)^2 + (z - z_i)^2}} \tag{5.12}$$

$$\sigma_{t_i,dt_i/dx} = \frac{1}{\sum_i w_i} \sum_i w_i (t_i - \langle t_i \rangle) \left(\frac{dt_i}{dx} - \left\langle \frac{dt_i}{dx} \right\rangle \right) \tag{5.13}$$

$\langle t_i \rangle$ and $\langle dt_i/dx \rangle$ denotes mean value of t_i and dt_i/dx. And w_i is the weighting factor depending on $TOF_i(x, y, z)$ and t_i. PMT nearer from (x, y, z) and $\langle t_i \rangle$ is more weighted. The fitter iterates calculation of the distance from the previous vertex in order that the covariance for x, y, z, t converges on zero.

V2 Fitter

In the more accurate vertex estimator "V2 fitter", using LT Vertex result as initial vertex, position is found by likelihood maximization of probability density function (PDF) constructed with experimental data.

PDF Calculation Observable PDF $\phi(t)$ can be calculated from pulse shape of photoelectron arrival time $\psi(t)$. The integral of $\psi(t)$ represents total occupancy (λ) denoting the fraction of hit PMTs of all PMTs.

$$\phi(t) = e^{-\int_{-\infty}^{t} \psi(\tau) d\tau} \psi(t) \tag{5.14}$$

$$\int_{-\infty}^{+\infty} \psi(\tau) d\tau = \lambda \tag{5.15}$$

The difference between $\psi(t)$ and measured $\phi(t)$ are comfortably small when the total occupancy is small ($\lambda < 1$). For ^{68}Ge calibration, average hit PMTs are 400-500 hits. Therefore $\psi(t)$ can be calculated from $\phi(t)$ based on observed pulse shape. Ultimate $\psi(t)$ is obtained by iterating numerical calculation of the following until $\psi_{i+1}(t)$ is indistinguishable from $\psi_i(t)$.

$$\psi_{i+1}(t) = \phi(t) e^{-\int_{-\infty}^{t} \psi_i(\tau) d\tau} \tag{5.16}$$

The initial $\psi(t)$ is measured ^{68}Ge calibration itself; $\psi_0(t) = \phi(t)$.

PDF Normalization In applicative format, $\psi(t)$ is written as $\psi(t) = \lambda\tilde{\psi}(t)$ so that $\tilde{\psi}(t)$ is normalized to unity. Integrating Eq. 5.14 of right side,

$$\int_{-\infty}^{+\infty} \lambda\tilde{\psi}(t)e^{-\lambda\tilde{\Psi}(t)}dt = \lambda\int_{0}^{1} e^{-\lambda u}du = 1 - e^{-\lambda} \tag{5.17}$$

$\tilde{\Psi}(t)$ is cumulative distribution function of $\tilde{\psi}(t)$ Therefore $\phi(t)$ is written as,

$$\phi(t) = \frac{1}{1-e^{-\lambda}}\psi(t)e^{-\int_{-\infty}^{t}\psi(\tau)d\tau} \tag{5.18}$$

$$= \frac{\lambda}{1-e^{-\lambda}}\tilde{\psi}(t)e^{-\lambda\tilde{\Psi}(t)} \tag{5.19}$$

Incorporating the Dark Rate Eq. 5.19 has to be used to incorporate the dark rate δ of the hit PMT by taking:

$$\tilde{\psi}(t) \quad \rightarrow \quad \tilde{\psi}_d(t) = \frac{\lambda\tilde{\psi}(t) + \delta}{\lambda + D} \tag{5.20}$$

$$\tilde{\Psi}(t) \quad \rightarrow \quad \tilde{\Psi}_d(t) = \int_{-\infty}^{t}\tilde{\psi}_d(\tau)d\tau \tag{5.21}$$

$$\lambda \quad \rightarrow \quad \lambda_d = \lambda + D \tag{5.22}$$

D is the average number of dark hit in a event. Finally, the observable PDF is given as

$$\phi(t) = \frac{\lambda\tilde{\psi}(t) + \delta}{1-e^{-\lambda+D}}e^{-\lambda\tilde{\Psi}(t)+D} \tag{5.23}$$

Likelihood Maximization The likelihood function is represented with the space of vector $\mathbf{s} = (t, \mathbf{r})$ (t and $\mathbf{r}$ are time and vertex position to be fit) for N hit PMTs in a event.

$$L(\mathbf{s}) = \prod_{i}^{N}\phi(\tau_i(\mathbf{s})) \tag{5.24}$$

where,

$\tau_i = t_i - t - \Delta t(\mathbf{r}, \mathbf{r_i})$	:	emitted time of detected photon at i-th PMT
t_i	:	detected time of photon at i-th PMT
$\Delta t(\mathbf{r}, \mathbf{r_i})$	:	time of flight from vertex $\mathbf{r}$ to i-th PMT position $\mathbf{r_i}$

For t_i timing correction described in Sec. 5.3 is applied for each PMT. Vertex $\mathbf{r}$ and time t are obtained to maximize logarithm of the likelihood by searching for a zero of its gradient.

$$\frac{\partial}{\partial s_k}\ln L = \sum_{i}^{N}\frac{1}{\phi(\tau_i)}\frac{d\phi(\tau_i)}{d\tau_i}\frac{\partial\tau_i}{\partial s_k} \tag{5.25}$$

5.7. Energy Reconstruction

5.7.1. Charge to Energy Conversion

Mean number of photons hitting i-th PMT μ_i assuming visible energy E MeV is expressed as the summation of photons generated from signal and PMT dark noise:

$$\mu_i = b_i(\mathbf{r})E + d_i \tag{5.26}$$

where,

$$\begin{aligned} b_i &: \text{expected charge without any loss [p.e./MeV]} \\ d_i &: \text{dark charge in analysis time window, 367 ns [p.e.]} \end{aligned} \tag{5.27}$$

The transform coefficient b_i is calibrated with neutron capture events by protons before the KamLAND-Zen experiment. It is common for 17" PMT or for 20" PMT. For 20" PMT, difference of surface area is additionally taken account. Charge losses caused by following factors are corrected.

- Attenuation length
- Shadow effect correction
- Charge discrimination effect

Position dependent effect is calculated from reconstructed vertex $\mathbf{r}$ and PMT position. Dark charge d_i is just the scale of average dark-ring described in Sec. 5.4.2.

5.7.2. PDF

Energy estimation also employs maximum likelihood approach like the vertex reconstruction. Likelihood function for energy depends on hit, charge and hit timing information. They are described using basic probability distribution functions.

$$\begin{aligned} \kappa_{i,j} &: \text{PDF to be hit by } j \text{ photons for } i\text{-th PMT} \\ f_{i,j} &: \text{PDF of charge for } i\text{-th PMT} \\ \psi_i &: \text{PDF of hit time for } i\text{-th PMT} \end{aligned}$$

Hit

Probability that μ_i photons hits to i-th PMT is generally expressed by Poisson distribution:

$$\kappa_{i,j} = \frac{(\mu_i)^j}{j!} e^{-\mu_i} \tag{5.28}$$

Due to 0.3 p.e. charge threshold set to reduce PMT dark noise, 1 p.e. detection efficiency of the threshold ϵ is estimated to be 0.964. In case of no-hitting, there is contribution of

subthreshold effect. Therefore, no-hit and hit probabilities are expressed as follows,

No-hit probability ($j = 0$) :

$$\begin{aligned} P_{\text{no-hit},i} &= \kappa_{i,0} + (1-\epsilon)\kappa_{i,1} \\ &= e^{-\mu_i} + (1-\epsilon)\mu_i e^{-\mu_i} \\ &\equiv \nu_i e^{-\mu_i} \end{aligned} \tag{5.29}$$

Hit probability ($j > 0$) :

$$\begin{aligned} P_{\text{hit},i} &= 1 - P_{\text{no-hit},i} \\ &= 1 - \nu_i e^{-\mu_i} \end{aligned} \tag{5.30}$$

From this equation, $\kappa_{i,j}$ is written down as,

$$\kappa_{i,j} = P_{\text{hit},i} \cdot \left(\frac{1}{P_{\text{hit},i}} \frac{(\mu_i)^j}{j!} e^{-\mu_i} \right) \tag{5.31}$$

for later use.

Charge

Charge information is important to reduce the difference between hit and charge distribution. However, we cannot know charge distribution above 1 p.e. strictly. So Gaussian distribution is supposed as an alternative.

$$\begin{aligned} f_{i,j} &= f_{i,j}(q_i) \\ &= \frac{1}{\sqrt{2\pi j\sigma^2}}\, \mathrm{e}^{-\frac{(q_i-j)^2}{2j\sigma^2}} \end{aligned} \tag{5.32}$$

where,

$$\begin{aligned} q_i &: \text{ observed number of p.e. at } i\text{-th PMT} \\ \sigma &: \text{ charge resolution of 1 p.e. distribution } (= 0.39) \end{aligned}$$

Resolution diminishes in proportion to square root of observed photons. The validity of the model is checked with source calibration. Charge PDF is represented as product of conditional probability to be hit by j photons and the hit probability.

$$\begin{aligned} \sum_{j=1}^{\infty} \kappa_{i,j} f_{i,j} &= P_{\text{hit},i} \cdot \sum_{j=1}^{\infty} \left(\frac{1}{P_{\text{hit},i}} \frac{(\mu_i)^j}{j!} \mathrm{e}^{-\mu_i} \frac{1}{\sqrt{2\pi j\sigma^2}}\, \mathrm{e}^{-\frac{(q_i-j)^2}{2j\sigma^2}} \right) \\ &\equiv P_{\text{hit},i} \cdot \sum_{j=1}^{\infty} P_{\text{charge},ij} \end{aligned} \tag{5.33}$$

It is calculated up to $j = 100$.

Hit Time

Hit timing is powerful information to distinguish signal from noise. The probability distribution ψ_i is pulse shape itself, and it only depends on TOF-subtracted time t_i in each PMT. Charge detected near the event timing is the most weighted, and dark hit like constant contribution is neglected by contrast. Probability to observe μ_i is expressed as a fraction of time-weighted charge and normal one (Eq. 5.26)

$$P_{\text{time},i} = \frac{\psi_i(t_i) b_i E + d_i}{\mu_i} \equiv \frac{s_i}{\mu_i} \tag{5.34}$$

5.7.3. Likelihood Maximization

Likelihood function L as variable of visible energy E is configured from Eq. 5.29, 5.30, 5.33 and 5.34.

$$L(E) = \prod_{i \in no-hit} P_{\text{no-hit},i} \prod_{i \in hit} \left[P_{\text{hit},i} \left(\sum_{j=1}^{\infty} P_{\text{charge},ij} \right) P_{\text{time},i} \right] \tag{5.35}$$

And logarithm of L is expressed as,

$$\begin{aligned} \log(L) = & \sum_{i \in no-hit} \log P_{\text{no-hit},i} + \sum_{i \in hit} \log P_{\text{hit},i} \\ & + \sum_{i \in hit} \log \left(\sum_{j=1}^{\infty} P_{\text{charge},ij} \right) + \sum_{i \in hit} \log P_{\text{time},i} \end{aligned} \tag{5.36}$$

Energy maximizing $\log L$ is found by solving Likelihood equation $\frac{d \log L}{dE} = 0$, The root is found using the Newton-Raphson method (Press et al., 2007 [47]) in which the declination ε_n between true value and tentative root E_n can be described with function and its derivative:

$$\begin{gathered} \varepsilon_{n+1} = \varepsilon_n - \frac{(\log L(E_n))'}{(\log L(E_n))''} \\ (n \ : \ 0, 1, ..., N = 4) \end{gathered} \tag{5.37}$$

The first term is given from the number of hits of 17inch PMTs.

$$E_0 = \log \left(\frac{N_{\text{all}}}{N_{\text{all}} - N_{\text{hit,17inch}}} \right) \tag{5.38}$$

N_{all} is the number of all 17 inch PMTs. It stops by five iteration as reaching enough accuracy. Therefore, the reconstructed energy is written as following,

$$E_N = E_{N-1} + \varepsilon_{N-1} \tag{5.39}$$

It is found independently for 17 inch and 20 inch PMT ($\equiv E_{N,17}$, $E_{N,20}$).

The series of steps can be calculated just from input of vertex, charge and time $(\mathbf{r}, q_i, t_i)$.

5.7.4. Energy Combination of 17 inch and 20 inch PMTs

Energy reconstructed from 20 inch PMT is calculated using PDF of 17 inch PMT, it causes larger energy bias. To reform it, correction function is calibrated by 17 inch energy.

$$\tilde{E}_{N,20} = \frac{E_{N,20}}{p_0 + p_1 E_{N,20} + p_2 (E_{N,20})^2 + p_3 (E_{N,20})^3} \tag{5.40}$$
$$(p_0 = 1.01,\ p_1 = -1.50 \times 10^{-3},\ p_2 = 8.33 \times 10^{-4},\ p_3 = -3.32 \times 10^{-5})$$

These constant values are determined based on calibration before KamLAND-Zen. The energy of all PMTs are gotten from the combination of two types of PMTs energy (Eq. 5.39, 5.40).

$$E_{\mathrm{vis}} = (1 - \omega) E_{N,17} + \omega \tilde{E}_{N,20} \tag{5.41}$$

The weighting factor $\omega = 0.3$ is optimized to minimize energy resolution.

6. Detector Calibration

Procedure of vertex and energy reconstruction are described in the previous chapter. Here additional corrections and reconstruction performance are discussed. The qualities estimated using calibration sources are summarized in Table. 6.1.

Table 6.1.: Summary of event reconstruction qualities

Energy resolution	(7.3 ± 0.4) % / $\sqrt{E}$
Energy bias	< 1 % inside the IB
Energy stability	< 1 %
Relative light yield (Xe-LS / outer-LS)	1.07
Center of inner-balloon	$(x, y, z) = (3.7, 1.5, -6.38)$ cm
Vertex bias	< 2.0 cm inside the IB < 1.0 cm for $\lvert z \rvert < 1$ m

6.1. Calibration Sources

In KamLAND-Zen, calibration runs using γ-ray sources were taken only once at the end of the Phase-II. To make up for it, easily tagged backgrounds are used, such as ^{214}Bi ($\beta + \gamma$), ^{214}Po (α) and spallation neutron (γ).

6.1.1. ^{214}Bi-Po in Xe-LS

LS filling supplies ^{222}Rn in ^{238}U-series into LS. It decays with 3.824 day half-life, so remains a while even after Xe-LS filling (high Rn period). This progeny, ^{214}Bi and ^{214}Po are tagged by delayed coincidence method (Sec. 7.3.2).

^{214}Bi, $\beta + \gamma$ source is mainly used to estimate energy nonlinear effect. This abundant events distributing uniformly in Xe-LS, are also useful to evaluate fiducial volume uncertainty (Sec. 9.1.2). The uniformity is confirmed in Fig. 7.9(a). Diffusion of ^{214}Po α-ray is much lower than β and γ particles, due to larger energy loss, hence it is appropriate to estimate position dependence of energy.

6.1.2. Spallation Neutron

Highly energetic cosmic muons generate neutrons in the detector, which are mainly captured by hydrogen and emit 2.225 MeV γ-rays. These events are observed uniformly

with constant rate, thus they are used to check position dependence and time variation of energy.

6.1.3. Radiation Source

A composite source produced for KamLAND-Zen calibration was deployed into the ID using a calibration device, at the end of Phase-II. It was the first-time calibration that the source was deployed inside the IB.

Calibration Device

"MiniCAL" is a ultra-clean calibration system deploying radiation sources along the vertical axis of the KamLAND, developed before KamLAND-Zen (Banks et al., 2015 [48]). It was installed on the top of the chimney in the clean room, after some modification for KamLAND-Zen calibration.

The new MiniCAL deploys sources by paying out and reeling Vectran cable (same material with supporting belts of the IB), relying on cable marks with precise interval. Accuracy of source position is ∼1 mm, depending on precision of the marks. This cable is shorter than length to the IB bottom for safety. Source capsule is coated with PTFE in order to protect the IB, and a weight is attached approximately 10 cm above the source. These apparatus are enclosed in a hermetically sealed housing, "MiniCAL box" inside a glove box, in order to prevent Rn penetration (Fig. 6.1). Nitrogen gas is supplied continuously during calibration. Source position was monitored using a infrared camera (Fig. 6.1), and also checked by on-line analysis.

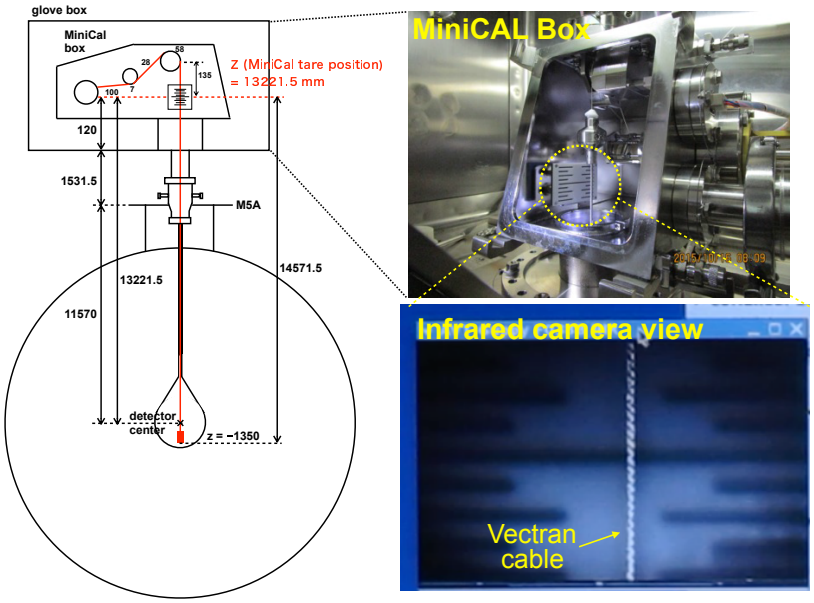

Figure 6.1.: calibration device : MiniCAL (modified for KamLAND-Zen)

Composite Source

Composite source including ^{137}Cs, ^{68}Ge and ^{60}Co was produced at university of Alabama (Tsang, Piepke, and Busenitz, 2015 [49]). Solution of each source was injected into to the Delrin bottle using a syringe. The activity was adjusted by counting it with Ge detector. Leakage of solution was checked before/after capsuling sources into stainless-steel containers by electron-beam welding, and zero consistent intensities were measured. Activity of each button source were measured by Ge detector. Consistent results are obtained in MC simulation (Table. 6.2).

The composite source was deployed to the KamLAND in Oct. 2016. Data was taken from z = -135 cm to +200cm at intervals of 5 or 10 cm as shown in Fig. 6.2(a). Fig. 6.2(b) shows energy spectrum of the source at the detector center, where clear peaks of ^{137}Cs, ^{68}Ge and ^{60}Co are seen.

Just after the calibration, the IB was uninstalled from KamLAND.

Table 6.2.: Activities of composite source for KamLAND-Zen. Initial and estimated intensities indicates measurements by Ge detector and MC simulation, respectively.

Isotope	Visible Particle	$T_{1/2}$	Real Energy [keV]	Initial intensity [Bq]	Estimated intensity [Bq]
^{137}Cs	1 γ	30.07 y	661.7	181	180
^{68}Ge	2 γ	270.8 d	511.0 + 511.0	419	356
^{60}Co	2 γ	5.271 y	1173.2 + 1332.5	322	315

6.2. Vertex Reconstruction Quality

6.2.1. Vertex Correction

Reconstructed detector center is matched with the center of the IB, in order to make spherical volume cut easy. Vertical correction is determined by ^{134}Cs film backgrounds at the IB bottom, where radius distribution is fitted by simulation spectra of ^{134}Cs in the IB and $2\nu\beta\beta$ in XeLS. Left of Fig. 6.6 is a sample of the fit. Adding to their event rates, vertical offset are optimized as free parameters, then z position of the IB center was estimated to be -6.38 cm.

Coordinate of KamLAND-Zen is defined as Fig. 6.3(a). Horizontal offset generates a oscillation in azimuth angle (ϕ) distribution. Using parameters defined in Fig. 6.3(b), deviation of horizontal radius between the IB center (ρ_0) and origin without vertex

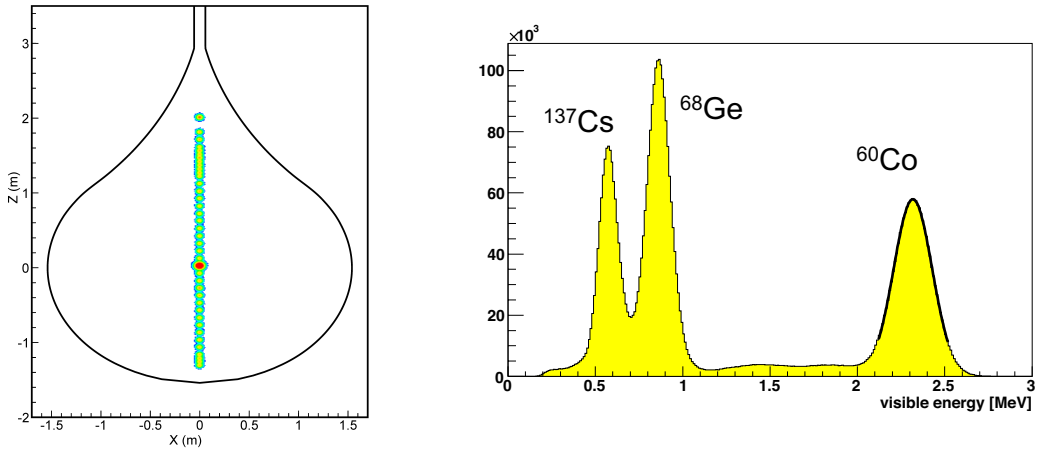

(a) Source positions reconstructed from the data (b) Energy spectrum at the detector center

Figure 6.2.: Composite source positions and energy spectrum. In (a), resolution is exaggerated and each color corresponds to the intensity of detected activity.

correction (ρ), is expressed with periodic functions:

$$\rho - \rho_0 = \rho_0 \left(1 - \left(\frac{\rho'}{\rho_0} \sin(\phi - \phi') \right)^2 - 1 \right) - \rho' \cos(\phi - \phi') \tag{6.1}$$

As with vertical offset, horizontal position biases are estimated using radius distribution fit, in 19 zenith angle (θ) regions, then they are determined to be $\Delta x = 6.5$ cm and $\Delta y = 3.0$ cm. Fig. 6.4(b) shows ϕ distribution of balloon radius around the equator before/after the vertex correction (the radius is estimated by gaussian fitting, so it is different from actual radius). It indicates the biases are well corrected.

6.2.2. Time Stability

Quality of vertex reconstruction depends on accuracy of PMT hit time information. In Phase-II analysis, evaluation method of timing correction is optimized, which uses the connecting pipe located at $z \sim 4.3$ m as calibration source (Sec. 5.3.3). The new timing correction improved vertex stability. Fig. 6.5 shows time variation of z position for the connection pipe. This period corresponds to ∼3 years, from the start of Phase-I to middle of the Phase-II. The position stability decreases from ∼0.1 cm to ∼0.03 cm. As to the outer-balloon, it decreases from ∼10 cm to ∼2 cm in the same period. This effect is seen around the IB. Fig. 6.6 is the R^3 distributions reconstructed using original/new timing correction. In case of new correction, it is evidently sharper than the old one. It contributes to suppress the film background tail in internal region.

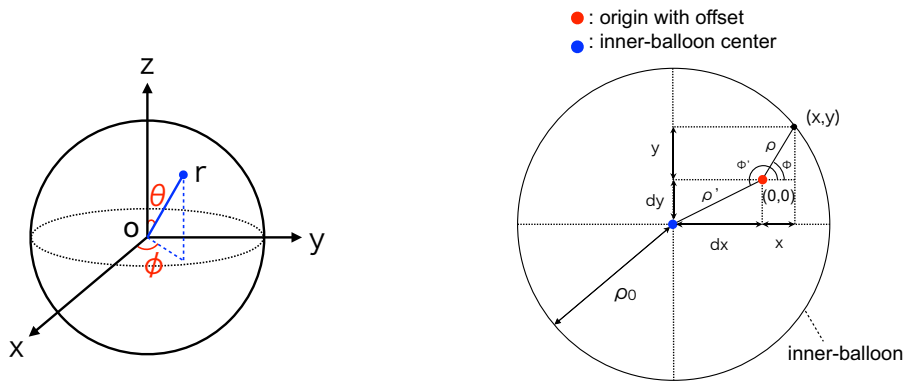

(a) Coordinate of KamLAND-Zen (b) Horizontal offset of the IB

Figure 6.3.: Coordinate system of KamLAND-Zen

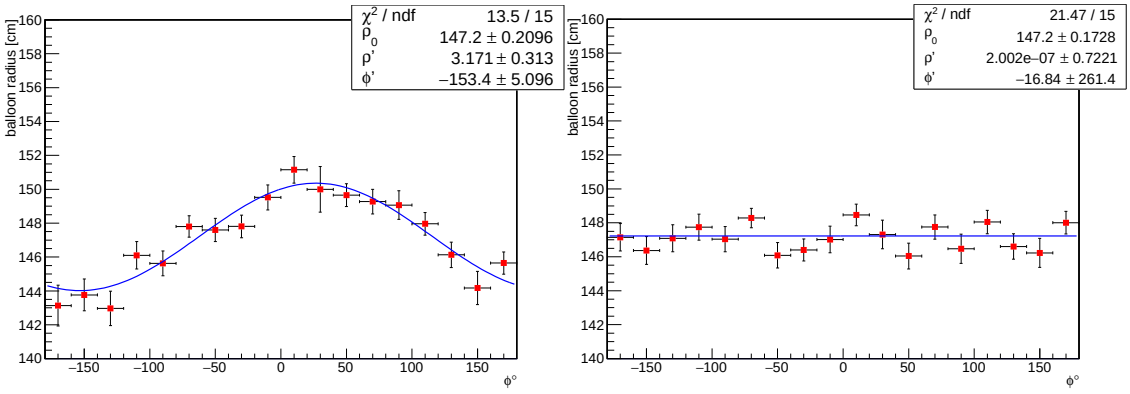

(a) Before vertex correction (b) After vertex correction

Figure 6.4.: Azimuth angle (ϕ) dependence of the IB radius in (a) before and (b) after the vertex correction around the equator. Blue lines are fit result with Eq. 6.1.

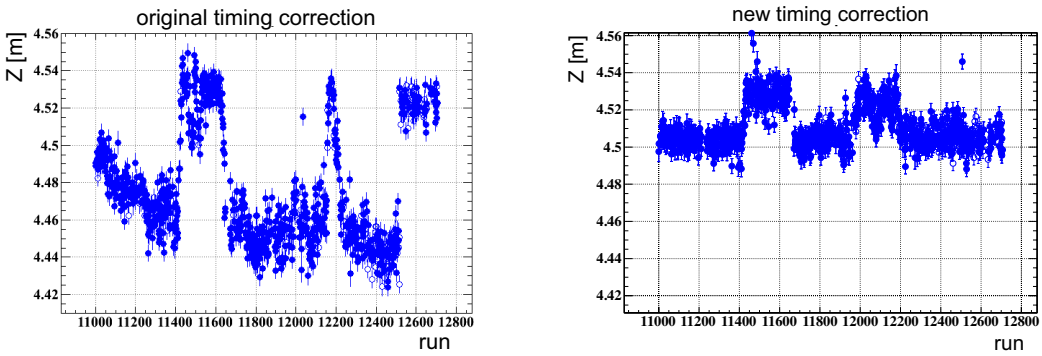

(a) Original timing correction (b) New timing correction

Figure 6.5.: Time variation of z position for the connecting pipe using (a) original correction and (b) new correction. Some jumps may occur by outer-LS convection because it coincides with LS purification period.

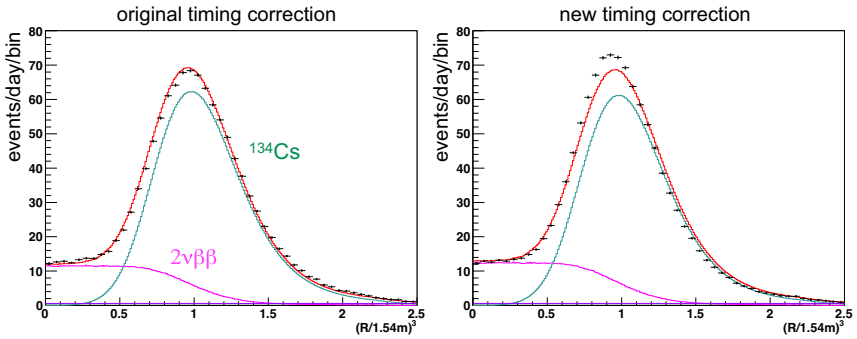

Figure 6.6.: R^3 distribution with best-fit backgrounds. Each vertex is reconstructed using original/new timing correction, and the same expected distribution are used for the fitting. Right figure, in case of new correction, the distribution is evidently sharper than the old one.

6.2.3. Vertex Bias

Position dependence of vertex bias is estimated with the composite source. Deviation of reconstructed vertex from real source position is estimated by gaussian fit to vertex distribution. It results the bias is less than 2.0 cm inside the inner-balloon, and 1.0 cm for $|z| < 1$ m, as shown in Fig. 6.7.

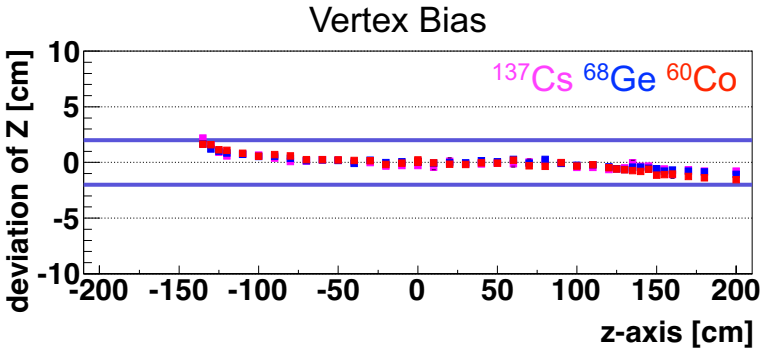

Figure 6.7.: z deviation of reconstructed vertex and ^{137}Cs-^{68}Ge-^{60}Co composite source position. Each vertex is determined by gaussian fit of vertex distribution. Though it makes balloon size smaller than real, the bias is allowable influence (less than 2.0 cm inside the IB, and 1.0 cm for $|z| < 1$ m).

6.3. Energy Reconstruction Quality

Performance of energy reconstruction is evaluated with the composite source and spallation neutron events. Energy resolution is estimated to be (7.3 ± 0.4) % from correlation of ^{137}Cs, ^{68}Ge and ^{60}Co energy resolution (Fig. 6.8(a)). Each mean resolution is evaluated with gaussian fitting. Energy bias is less than 1 % for all source positions (Fig. 6.8(b)).

The light yield of Xe-LS is lower than that of outer-LS, due to quenching effect by Xe. Increase of Xe mass from Phase-I enhanced this effect, hence the light intensity decreased $\sim$2 %. Fig. 6.9 is energy deviation of spallation neutrons. Relative light yield of outer-LS to Xe-LS is estimated to be 1.07. This value is used to calculate energy deposit in MC simulation.

6.3.1. Energy Correction

Visible Energy

Reconstructed energy is scaled to reproduce 2.225 MeV capture γ energy of spallation neutron events. The scaling factor in Phase-II is 1.30, which is 2 % higher than that of Phase-I due to larger Xe mass. Fig. 6.10 shows energy spectrum of spallation neutron events after scaling. The mean energy is estimated to be 2.224 ± 0.003 MeV.

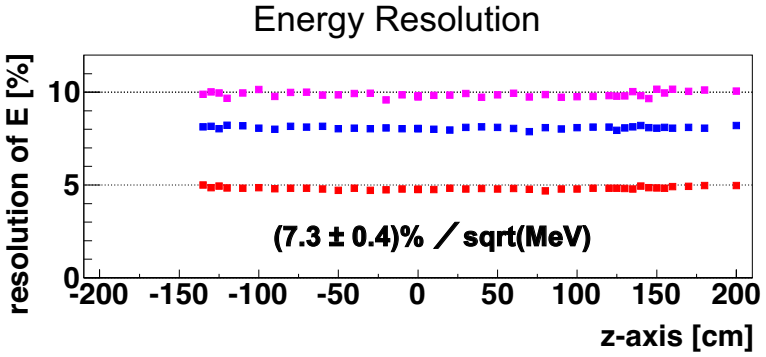

(a) Energy resolution of the composite source

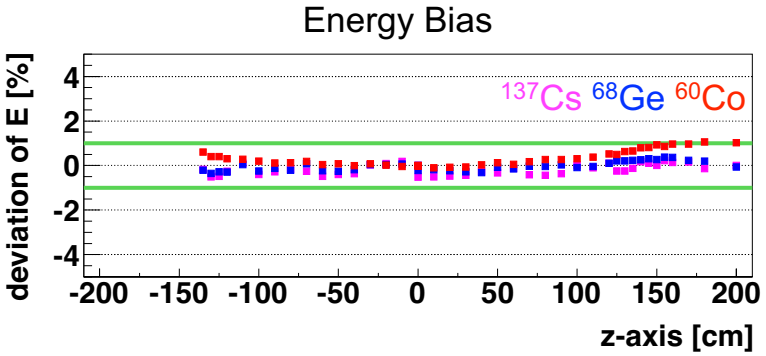

(b) Energy deviation of the composite source

Figure 6.8.: Energy resolution and position dependent bias estimated with ^{137}Cs-^{68}Ge-^{60}Co composite source calibration data. The resolution is estimated to be (7.3 ± 0.4) % and energy bias is less than 1 % for all source positions.

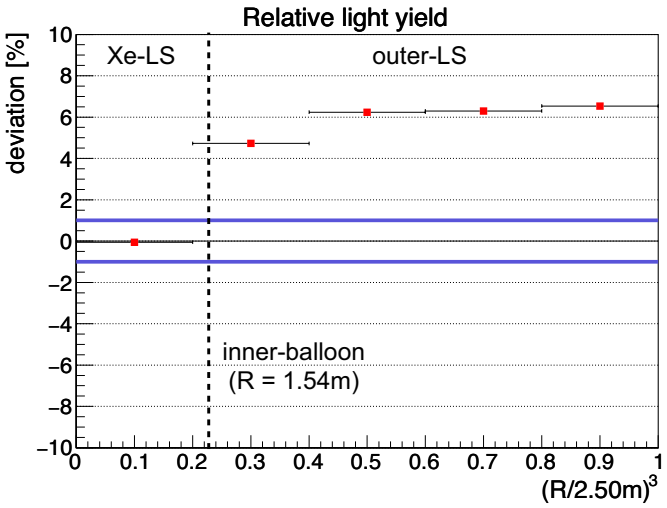

Figure 6.9.: Energy deviation of neutron capture γ in Xe-LS and outer-LS. Relative light yield of outer-LS to Xe-LS is estimated to be 1.07.

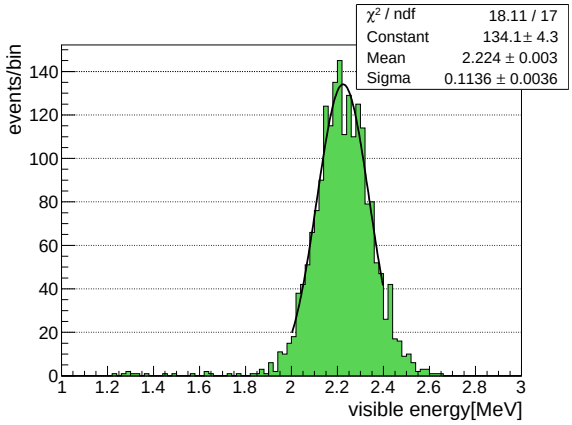

Figure 6.10.: Energy spectrum of spallation neutron events inside 1.2m-radius.

Position Dependence

Position dependence of energy is estimated using α-ray from ^{214}Po decay. Total charge in each shell volume is estimated by gaussian fitting. Fig. 6.11(a) is ^{214}Po decay charge deviation relative to innermost region. Energy around the IB is 2 % lower than that around the center. Correction function is constructed by adding vertex resolution at Q-value of ^{136}Xe $\beta\beta$ decay. Fig. 6.11(b) is visible energy deviation in which constructed correction is applied. The dependence is within 1 %.

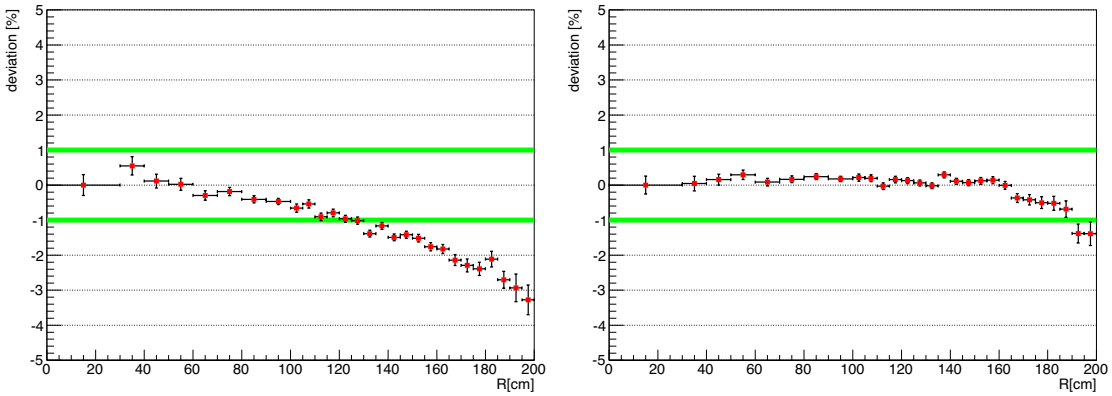

(a) Before correction (b) After correction

Figure 6.11.: Energy deviation of ^{214}Po α decay. (a) Total charge deviation relative to innermost region. (b) Visible energy deviation in which constructed correction is applied.

6.3.2. Energy Scale Uncertainties

Energy scale uncertainties are summarized as follows.

- Time variation
  Time stability of energy is checked with spallation neutrons. Fig. 6.12(a) is the time variation of energy deviation from mean capture-γ energy inside 1.2m-radius, during Phase-II. It is stable within 1 %.

- Position dependence
  Uncertainty of position dependence is also estimated using spallation neutron events. As shown in Fig. 6.12(b), the uncertainty is within 1 % inside 1.4m-radius. The higher energy around the IB is due to outer-LS contribution, having larger light yield.

- Contribution of Cherenkov light
  Cherenkov photons are emitted from charged particles. Though their direct photons are hard to detect, since their dominant wavelength is below absorption length of the scintillator. However, they are detected via light reemission, and contributes

to energy distortion. This effect is parameterized as the ratio of Cherenkov light to scintillation light, denoted as R. The energy nonlinearity effect is expressed with R and k_B described below.

- Quenching effect
  Emitted light intensity per unit path length (dL/dx) is ideally proportional to the specific energy loss of particles (dE/dx): $dL/dx = L_0(dE/dx)$. L_0 is the scintillation efficiency. Actually, quenching is assumed to occur, in proportion to ionization density along particle track, then causes decrease of scintillation efficiency. The light intensity including this effect is expressed as,

$$\frac{dL}{dx} = \frac{L_0 \cdot dE/dx}{1 + k_B(E/dx)} \tag{6.2}$$

  k_B is a proportional constant for quenching probability, called "Birks constant". This Birk's law is the most practical relation, first proposed by Birks. In experiments, k_B is treated as parameters.

  Thus, energy nonlinearity effect is optimized by the combining of this k_B and R. Various sources are used for this calibration, since the quenching effect depends on kind of particles and energy. In Phase-II, above parameters are constrained by γ-calibration data (^{137}Cs, ^{68}Ge, ^{60}Co, n^1H, n^{12}C) and ^{214}Bi ($\beta + \gamma$), using visible and real energy conversion table for e^- and γ and ^{214}Bi energy spectrum, as shown in Fig. 6.13. ^{214}Bi in Xe-LS includes only statistical error, and γ-sources have time dependent and position dependent errors.

  Individual calibrations indicated that there is $\sim 2\sigma$ tension between γ-sources and ^{214}Bi: the best-fit values are (k_B, R) = (0.24, 0.04) for γ-sources and (0.29, 0.00) for only ^{214}Bi, respectively. This discrepancy implies that energy nonlinearity effect changes during Phase-II (^{214}Bi is originated from Rn just after Xe-LS filling and calibration data was taken at the end of Phase-II). The most possible explanation is variation of detector status. Energy fitter depends on charge hit probability, in which 1 p.e. threshold efficiency ϵ is included. Though ϵ is determined from the 1 p.e. distribution as 0.964 previously, it may change to 1.00. Best-fit values from ^{214}Bi, where correction for the two 1 p.e. threshold effects is applied, become (0.35, 0.00), which is consistent with the result of γ-sources.

  Consequently, combined result of γ-calibrations and ^{214}Bi are used as best-fit values, that is (k_B, R) = (0.34, 0.00). In Fig. 6.14, anticorrelation of these parameters are seen. These nonlinearity parameters, k_B and R are introduced in spectral fit for $\beta\beta$ analysis, in which the best-fit values and uncertainties are used for constraint.

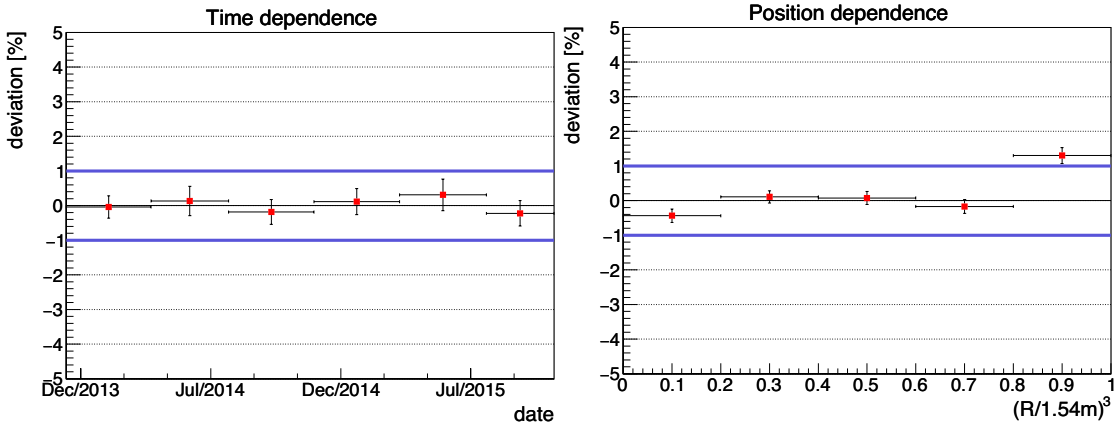

(a) (b)

Figure 6.12.: Stability of energy scale. (a) Time dependence of neutron capture energy in $R < 1.2$ m. Deviation from mean energy 2.224 MeV is within 1 % through this data set. (b) Position dependence of neutron capture energy inside the inner-balloon. Though energy outside-1.4m-radius slightly deviates due to contribution of the outer-LS taking light yield 7 % higher than the inner-LS, it is stable in the inner region with small contribution from the outer-LS.

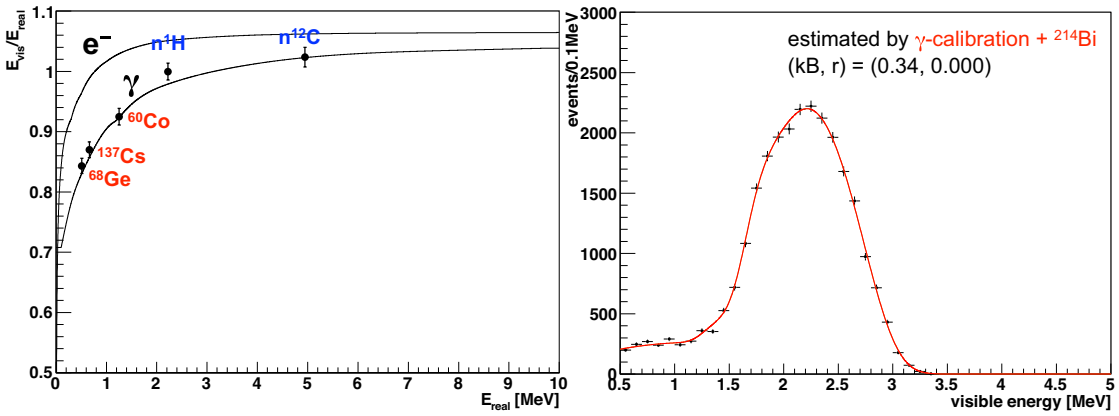

(a) Conversion from visible energy to real energy (b) Optimized ^{214}Bi energy spectrum

Figure 6.13.: Observed quenching effect and spectral distortion with expectation from best-fit energy nonlinearity parameters.

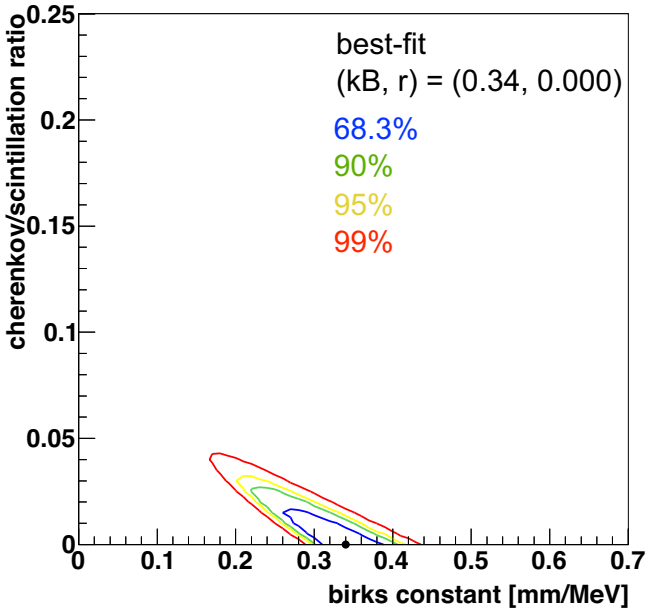

Figure 6.14.: Correlation of energy-nonlinear parameters, k_B and R.

6.4. Event Badness

Quality of vertex and energy reconstruction can be verified with *"VertexBadness"* based on 9 parameters including hit, time and charge information. Each definition is described as follows.

- Characteristics around the peak
  - R_{N45} : sharpness of time spectrum
    It is represented as hit count ratio between 45 ns window around a peak and whole event time window (150 ns) for all good PMTs. The peak of time spectrum is found to maximize the number of hits within 45 ns. The term time spectrum here is a time of flight (TOF) subtracted timing deviation from event time.

  - H_T : peak height of time spectrum [hit/ns]
    The parameter utilizes energy dependence of sharpness of time spectrum, focusing on the peak more than R_{N45}. The peak is searched with 4 ns time window, thus H_T is given as (the peak height within 4 ns) / 4 ns / (the number of live PMTs having hit in 45 ns around the peak).

- Deviation of distribution
  - σ_Q : Standard deviation of charge ratio Q_{obs} / Q_{exp}

It is defined as total deviation of 17 inch $\sigma_{Q,17}$ and 20 inch PMT $\sigma_{Q,20}$:

$$\sigma_Q = \sqrt{\frac{N_{17}(\sigma_{Q,17})^2 + N_{20}c(\sigma_{Q,20})^2}{N_{17} + N_{20}}} \tag{6.3}$$

N_{17} and N_{20} are the number of live PMTs for 17 inch and 20 inch, and c is correction factor denoted as ratio of typical $\sigma_{Q,17}$ and $\sigma_{Q,20}$. Deviation for ratio of observed charge $Q_{i,\mathrm{obs}}$ to expected charge $Q_{i,\mathrm{exp}}$ is calculated for hit channels within 150 ns $N_{\mathrm{hit},17}$, $N_{\mathrm{hit},20}$:

$$(\sigma_{Q,17})^2 = \frac{1}{N_{\mathrm{hit},17}} \sum_{i=1}^{N_{\mathrm{hit},17}} \left(\frac{Q_{i,\mathrm{obs}}}{Q_{i,\mathrm{exp}}}\right)^2 - \left(\overline{\frac{Q_{i,\mathrm{obs}}}{Q_{i,\mathrm{exp}}}}\right)^2 \tag{6.4}$$

$\sigma_{Q,20}$ is also expressed with the same format.

- σ_T : Standard deviation for time distribution
  The definition basically follows σ_Q though no distinction between 17 inch and 20 inch PMT. It treats time spectrum t_i described in R_{N45}, for all hit PMTs ($N_{\mathrm{hit}} = N_{\mathrm{hit},17} + N_{\mathrm{hit},20}$) :

$$\sigma_T = \sqrt{\frac{1}{N_{\mathrm{hit}}} \sum_{i=1}^{N_{\mathrm{hit}}} (t_i)^2 - \bar{t}_i^2} \tag{6.5}$$

- Hit information
  - R_{hit} : detected N_{hit} within 150 ns / expected N_{hit}
  - R_{N150} : detected $N_{\mathrm{hit},17}$ within 150 ns / NsumMax
- Correlation with distance to the PMT
  - χ^2_Q : Chi-square for charge
    Position dependence of charge is dominated by r^{-2} effect, besides transparency and shadow effect depending on zenith angle θ and azimuth angle φ. The correlation is verified with 32 (17 inch) or 22 (20 inch) θ-φ specific bins, resulting $\mathrm{ndf}_{17,20}$,

$$\chi^2_Q = (\chi^2_{Q,17} + \chi^2_{Q,20}) \ / \ \mathrm{ndf}_{17,20} \tag{6.6}$$

    where, χ^2_Q in each PMT type are expressed with Q_{obs}, Q_{exp} and total error

related to expected charge ($a_{\theta,\varphi}$) :

$$\chi^2_{Q,17} = \sum_{\theta,\varphi}\left(\frac{Q^2_{\rm obs}}{a}\right)_{\theta,\varphi} - \left\{\sum_{\theta,\varphi}\left(\frac{Q_{\rm obs}Q_{\rm exp}}{a}\right)_{\theta,\varphi}\right\}^2 \Big/ \sum_{\theta,\varphi}\left(\frac{Q^2_{\rm exp}}{a}\right)_{\theta,\varphi} \tag{6.7}$$

$\chi^2_{Q,20}$ is also given with the same format.

– χ^2_T : Chi-square for time
Timing information also depends on the distance to the PMT. It treats t_i sorted by charge exploiting the position dependence of charge discussed above. The chi-square is given as summation of $\chi^2_{T,17}$ and $\chi^2_{T,20}$ with $\mathrm{ndf}_{17,20}$

$$\chi^2_T = \left(\chi^2_{T,17} + \chi^2_{T,20}\right)/\mathrm{ndf}_{17,20} \tag{6.8}$$

– χ^2_{hit} : Chi-square for hit count
Parameter of χ^2_{hit} is difference between total $N_{\rm hit}$ and expected $N_{\rm hit}$ for each PMT, which is also sorted by its charge like χ^2_T.

Thus *VertexBadness* is derived with total chi-square $\chi^2_{\rm tot}$ as summation of above parameters. Mean values and error values such as $\langle\sigma_T\rangle$ and $\Delta\sigma_T$ are calculated from functions of reconstructed energy, obtained by the past source calibration.

$$\begin{aligned}
\chi^2_{\rm tot} &= 12\cdot(\chi^2_T + \chi^2_Q + \chi^2_{\rm hit}) \\
&\quad + \left(\frac{\sigma_T - \langle\sigma_T\rangle}{\Delta\sigma_T}\right)^2 + \left(\frac{\sigma_Q - \langle\sigma_Q\rangle}{\Delta\sigma_Q}\right)^2 \\
&\quad + \left(\frac{H_T - \langle H_T\rangle}{\Delta H_T}\right)^2 + \left(\frac{R_{N45} - \langle R_{N45}\rangle}{\Delta R_{N45}}\right)^2 \\
&\quad + \left(\frac{R_{\rm hit} - \langle R_{\rm hit}\rangle}{\Delta R_{\rm hit}}\right)^2 + \left(\frac{R_{N150} - \langle R_{N150}\rangle}{\Delta R_{N150}}\right)^2 \\
\tilde{\chi}^2_{\rm tot} &= \frac{\chi^2_{\rm tot}}{ndf} \\
\mathit{VertexBadness} &= c\,\ln\left(1 + \frac{\tilde{\chi}^2_{\rm tot}}{c}\right),\ c = \frac{20}{\ln 10}
\end{aligned} \tag{6.9}$$

It demonstrates powerful discrimination capability between noise events and physical events, discussed in Sec. 7.2.6.

7. Event Selection and Systematic Uncertainties

Detected events are categorized into unphysical noise events and background events. They can be rejected using hit, time, charge, and energy information. The most important selections are "Bi-Po sequential cut" and "spallation products", which aim to reject Bi-Po and ^{10}C backgrounds, contributing to $0\nu\beta\beta$ energy region.

In this chapter, rejection efficiencies and systematic uncertainties listed in Table. 7.1 are discussed with description of each selection criteria.

Table 7.1.: Summary of detector related uncertainty

Source	Uncertainty
Flasher event cut	2.3×10^{-5} %
Badly reconstructed event cut	3.2×10^{-2} %
Clipping muon event	6.6×10^{-3} %
Anti-neutrino event cut	0.86 %
^{214}Bi-Po event cut	0.046 %
^{212}Bi-Po event cut	5.1 %
Livetime calculation	1×10^{-2} %
Xe mass	0.8 %
Abundance of ^{136}Xe	0.04 %

7.1. Data Set

Analysis period of this work is called "KamLAND-Zen Phase-II", 685 days elapsed time between just after the purification period and just before the extraction of inner-balloon for the detector refurbishment, as listed in Table. 7.2. Data acquired with MoGURA electronics is only used to search spallation neutron events induced by muon, since KamFEE data have large inefficiency caused by the dead time.

7.2. Bad Event Rejection

Following bad condition events itself or subsequent one are eliminated as unphysical events utilizing their characteristics.

Table 7.2.: Data set of KamLAND-Zen Phase-II

	date	run (KamFEE)	run (MoGURA)
start	Dec. 11 2013 8:30	12247	3301
end	Oct. 27 2015 5:44	13295	4386

- Flasher event
- Post 1pps trigger event
- Post muon event
- Post missing waveform event
- Post deadtime event
- Badly reconstructed event

7.2.1. Flasher Event

Flash light from a PMT is occasionally detected, caused by discharge of its dynode as shown in Fig. 7.1. Named flasher event can be identified using a feature that comparatively high charge is distributed locally. The event selection is as follows:

1. Not muon event
2. Not noise event
3. (Total charge in ID) $>$ 2500.0 p.e.
4. (Max charge in ID) / (Total charge in ID) $\geq$ 0.6
5. (Neighbor charge) $\geq$ 20 p.e.

"Max charge" is the highest charge among all hit cables. And "Neighbor charge" is average of adjacent cables for a target one. Neighbor cables are selected from 17 inch cables other than bad channels, taking 4 - 7 typically.

Fig. 7.2 demonstrates the availability of the selection. 6 events are tagged with above 1. - 4. selection inside 2-m-radius, one of which is rejected due to 72 p.e. neighbor charge, satisfying selection 5. The residual and most of events with slightly high maximum charge ratio are also rejected due to its bad reconstruction status, described later. Flasher event ratio compared to the good candidate events is 2.3×10^{-5} %, so the selection inefficiency is estimated to be less than 2.3×10^{-5} %.

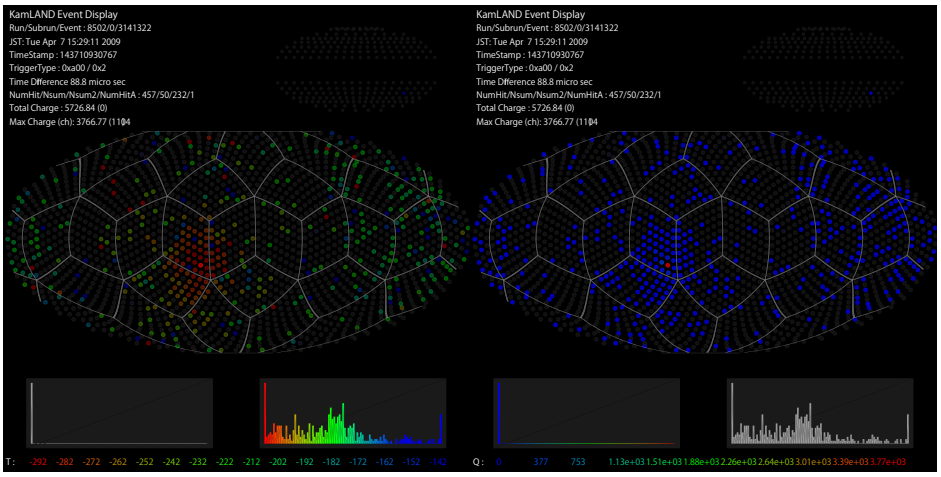

Figure 7.1.: Event display of a typical flasher event. Each point indicates hit time (left) and charge (right) in each PMT.

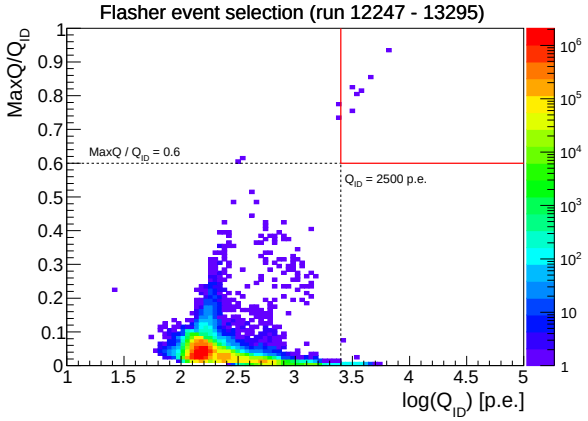

Figure 7.2.: Charge and timing distribution of flasher events. Correlation of total charge in the ID (Q_{ID}) and max charge ratio (Max Q/Q_{ID}) in $R < 2$ m after rejecting muon and noise events. 1 event within 6 events enclosed with red line satisfies all items of flasher event selection including neighbor charge, taken out from candidate events.

7.2.2. Post 1PPS Trigger Event

1 pps trigger is a forced acquisition trigger issued once per second for all PMTs, based on input signal from a GPS module. The accompanying noises are frequently found in 32 - 36 μs after the issues (Fig. 7.3). The cause is presumed to be trigger overlap during approximately 25.6 μs digitization of waveforms. They are rejected by time interval:

- Time interval from the preceding 1 pps trigger < 100 μs

As displayed in Fig. 7.3, most of events distributes below 2 MeV, only 1 event with 2.85 MeV energy is rejected at $R = 1.36$ m vertex. The inefficiency is discussed in the livetime section.

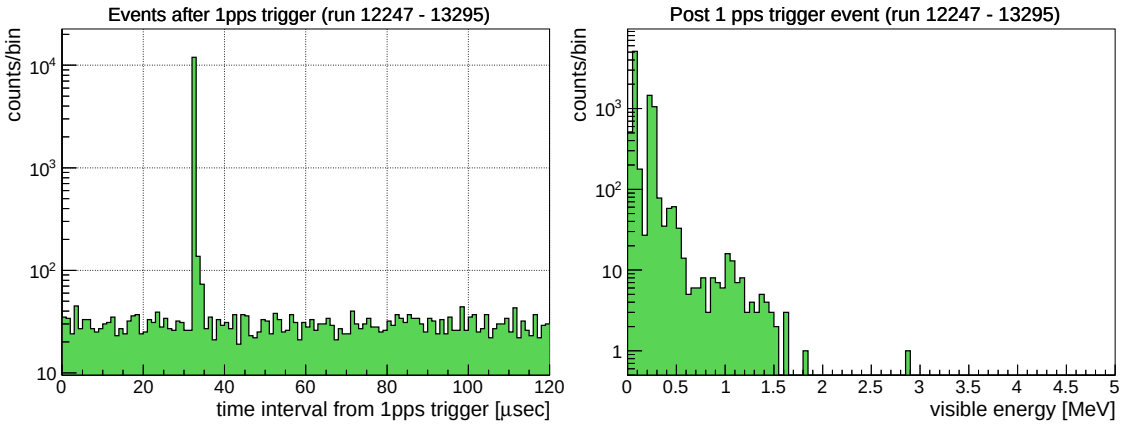

(a) Time distribution

(b) Energy spectrum

Figure 7.3.: Time and energy distribution of post 1 pps events. (a) time interval from the preceding 1 pps trigger. (b) energy spectrum of selected post 1 pps events (time interval < 100 μs, $R < 2$ m, other rejections are applied.)

7.2.3. Post Muon Event

High charge events like muons make it difficult to take data of proceeding events due to overshoot of waveform baseline and PMT afterpulses. Therefore, events within 2 ms from the muon are vetoed. Event satisfying either of following criteria is regarded as muon event:

- through going muon: $Q_{17} \geq 10,000$ p.e. ($\sim$30MeV)
- clipping muons : $(Q_{17} \geq 500 \text{ p.e.}) \cap (N_{200\text{OD}} \geq 5 \text{ hits})$

For about muon itself cut, only the clipping muons are cut with their OD hit information (Sec. 7.3.1).

7.2.4. Post Missing Waveform Event

High event rate such as muon sometimes exceeds processing speed in a ATWD, causing loss of waveform information. It becomes noise events called "missing waveform event". They are discriminated with the number of acquired waveforms, $Nhit_{17}$ is less than that of hits recorded in the trigger, NsumMax. Furthermore, subsequent events are also vetoed as noisy period:

- selection of missing waveform event
  - time from muon event $<$ 2 msec
  - $Nhit_{17} <$ NsumMax
  - 200 $\leq$ NsumMax
- veto time after the missing waveform event
  - 2 ms (200 $\leq$ NsumMax $<$ 1200)
  - 2 s (1200 $\leq$ NsumMax)

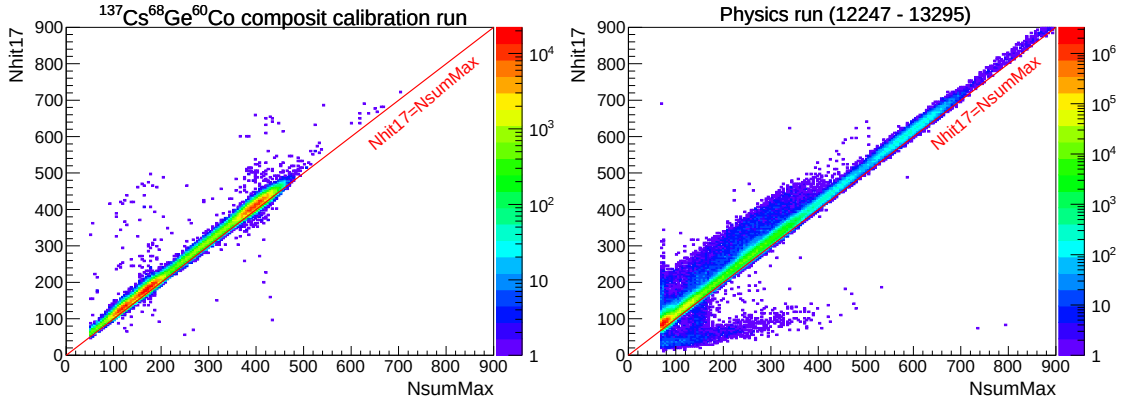

(a) Composit source events (b) Single events

Figure 7.4.: Correlation of $Nhit_{17}$ and NsumMax for (a) composit source and (b) single events ($R <$ 2 m). Above and below regions of red line indicates normal events and missing waveform events, respectively. Position of the composite source including ^{137}Cs, ^{68}Ge and ^{60}Co varies -1.35 $\leq z <$ 2 m along the central axis.

7.2.5. Post Deadtime Event

For ^{10}C Decay Event One of spallation nuclei, ^{10}C decay is a serious background for $0\nu\beta\beta$ analysis. It is rejected by triple coincidence tagging method with preceding muon and neutron, described in Sec. 7.3.4. However it cannot be applied when muon is detected during deadtime. To reduce ^{10}C rejection inefficiency, events after a deadtime period are rejected. Vetotime is determined to cover decay lifetime of ^{10}C (τ = 27.8 sec).

- veto 3 min since the first event of a run for KamFEE and MoGURA
- veto 3 min since the end of a deadtime period for KamFEE and MoGURA

Data taken with MoGURA electronics are used for spallation tagging, so its deadtime becomes a target of the veto.

For Missing Muon Event Muon event is normally rejected by criteria in Sec. 7.2.3 but recording muon information sometimes fails, then 2 msec veto for subsequent events is not applied. To eliminate left noise events called "missing muon", it is selected as follows:

- $N_{\mathrm{ID}} > 100$
- $N_{100} < N_{\mathrm{ID}}/2$ - 10

N_{ID} is total number of ID hit and N_{100} is maximum number of ID hit in 100 ns, respectively. Missing muon events within 1 ms are bounded up, then time interval between the first missing muon event and the last one is determined as deadtime ("missing muon period").

7.2.6. Badly Reconstructed Event

The difference of behavior between physical and unphysical events can be distinguished by a parameter "*VertexBadness*" defined at Eq. 6.9. Its selection criterion depending on visible energy E MeV are determined to eliminate clusters in low energy:

$$\mathit{VertexBadness} < 41.1 \times \mathrm{e}^{-9.7\times10^{-3}\times E[\mathrm{MeV}]} + 2.31 \tag{7.1}$$

Events exceeding the criterion are regarded as bad events. Fig. 7.5 shows correlation between "*VertexBadness*" and energy for composite source events and single events. It demonstrates discrimination capability of the parameter as almost source events are categorized to good events. Selection inefficiency given from ratio of rejected events to total events using calibration data is calculated to be 3.2×10^{-2} %.

However, part of physical events called "pileup" events are rejected, that is two correlated/uncorrelated events having different energies are detected in one event time window as shown in Fig. 7.10(b). Typical pileup event in the double-beta decay analysis is Bi-Po sequential decay originated from U, Th-series, mainly distributing along the IB. "*VertexBadness*" of the pileup events tends to be high because double pulses are not distinguished. Thus the part events untagged by a delayed-coincidence method described in Sec. 7.3.2 makes bad event fraction higher than calibration events (Fig. 7.6). Since in the inner volume contribution from IB-derived pileup events is negligible, the bad event ratio is below 1 %. The inefficiency is consistent with that of calibration events.

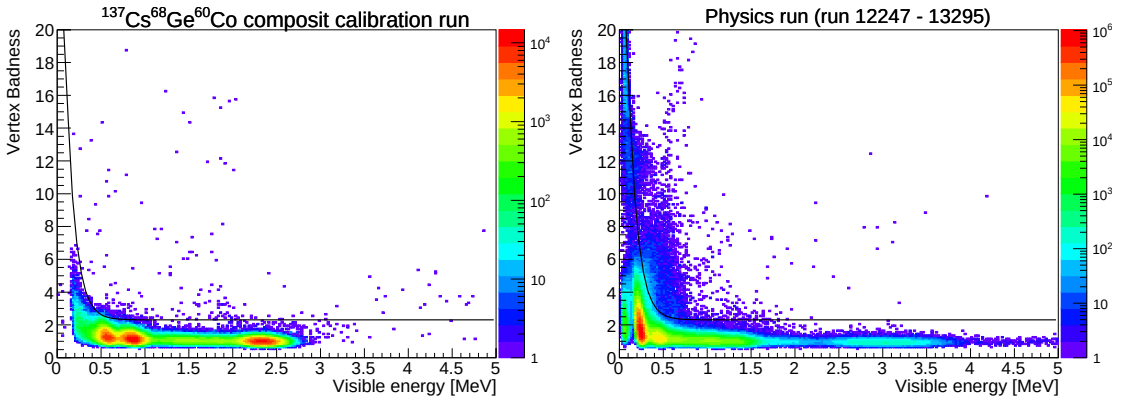

(a) Composite source events (b) Single events

Figure 7.5.: Correlation between *VertexBadness* and energy within 2-m-radius for (a) composite source events and (b) single events. The black line is bad event criterion shown in Eq. 7.1, higher badness events are regarded as bad events. Bi-Po decay including pileup events are already rejected to emphasize difference between physical and unphysical events.

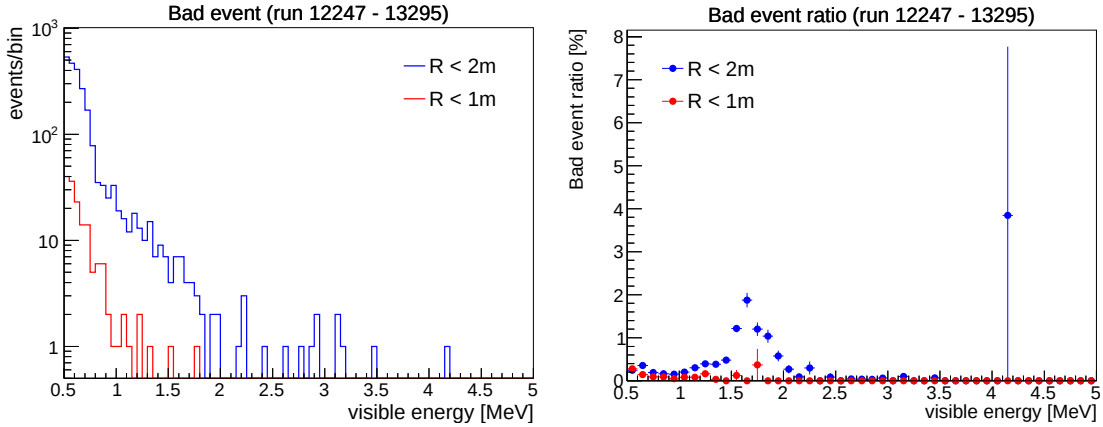

(a) Bad single events (b) Bad event ratio

Figure 7.6.: (a) Energy spectrum of bad single events for $R < 2$ m, $R < 1$ m, respectively. (b) Ratio of bad events to good events. Untagged Bi-Po pileup events makes it high in the external region. The ratio in $R < 1$ m falls below 1 % in whole energy window.

7.3. Background Event Rejection

Some background events can be tagged using characteristics of the event. In this section, rejection method and efficiency of background events listed below are described.

- Clipping muon event
- Bi-Po sequential decay event
- Anti-neutrino event
- Spallation products

7.3.1. Clipping Muon Event

High energy events such as muon events have little effects on the signal energy window, thus relatively low energy events, namely clipping muons going through only buffer-oil are targets of rejection. To minimize selection inefficiency, only hit information is included without charge information used in usual KamLAND analysis as following:

- $N_{200OD} \geq 5$ hits

"N_{200OD}" is the number of hits in the outer-detector within 200 nsec window. For $0.5 <$ E < 5 MeV and $R < 2$ m, 38 events are selected, mostly distributing below 2 MeV. The selection inefficiency is estimated to be less than 6.6×10^{-3} % from source calibration data.

7.3.2. Bi-Po Sequential Decay Event

Sequential decays from bismuth to polonium in downstream of the uranium series or thorium series shown in Eq. 7.2 can be identified using its appropriate correlation. They are tagged in the two ways: "delayed coincidence" and "pileup detection" methods. Most of ^{214}Bi-Po decays are tagged by the former, and the latter is effective for ^{212}Bi-Po having much shorter lifetime.

$$\begin{aligned} {}^{214}\mathrm{Bi} &\xrightarrow[Q_\beta = 3.272\,\mathrm{MeV},\, 99.979\,\%]{T_{1/2} = 19.9\,\mathrm{min}} {}^{214}\mathrm{Po} \xrightarrow[Q_\alpha = 7.833\,\mathrm{MeV}]{T_{1/2} = 164.3\,\mu\mathrm{sec}} {}^{210}\mathrm{Pb} \\ {}^{212}\mathrm{Bi} &\xrightarrow[Q_\beta = 2.254\mathrm{MeV},\, 99.989\,\%]{T_{1/2} = 60.55\,\mathrm{min}} {}^{212}\mathrm{Po} \xrightarrow[Q_\alpha = 8.954\,\mathrm{MeV}]{T_{1/2} = 0.299\,\mu\mathrm{sec}} {}^{208}\mathrm{Pb} \end{aligned} \tag{7.2}$$

Delayed Coincidence Tagging

This method utilizes delayed energy (E_d) and space (ΔR) or time correlation (ΔT) regarding β-decay of Bi as prompt signal and α-decay of Po as delayed signal. Cut for the prompt energy (E_d) is not included to suppress the inefficiency. All possible pairs are checked if the following criteria is satisfied:

- $0.2 \leq E_\mathrm{d} \leq 1.3$ MeV

- $\Delta R < 170$ cm
- $\Delta T < 1.9$ ms

Fig. 7.7 shows events applied above criteria except for cut to own parameter. To emphasize ^{214}Bi-Po decays, ^{212}Bi-Po contribution is rejected with additional cuts. Clear energy peak of Bi and Po decays and clear correlation are confirmed. Fitted decay half-life is estimated to be 168.4 μs, almost consistent with that of ^{214}Po. Parent nuclides, radon is supplied from LS pipe line during LS circulation, so much Bi-Po events are observed in Xe-LS just after the circulation (Fig. 7.9). This data set includes a part of the high Rn period as shown in Fig. 7.8. After the decay, tagged event are primary originated from the IB.

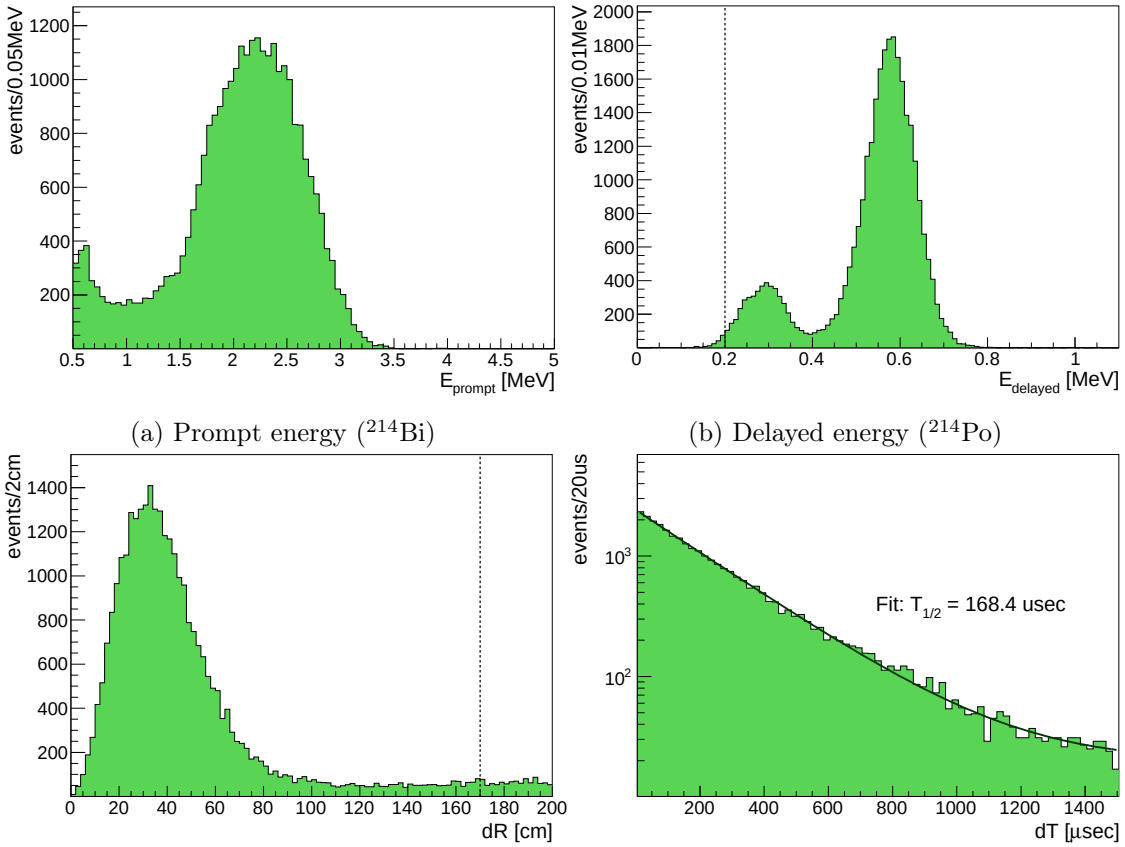

(a) Prompt energy (^{214}Bi)

(b) Delayed energy (^{214}Po)

(c) Space correlation

(d) Time correlation

Figure 7.7.: ^{214}Bi-Po decay events tagged by delayed coincidence method within 2-m-radius. Dotted lines indicates selection criteria for each parameter. Additional cut of $E_{\mathrm{p}} > 0.5$ MeV and $\Delta T > 5$ μs are applied to avoid ^{212}Bi-Po events. Small peak in (b) is also ^{214}Po absorbed after passing through the IB. Fitted decay curve with $T_{1/2} = 168.4$ μs in (d) is almost consistent with that of ^{214}Po.

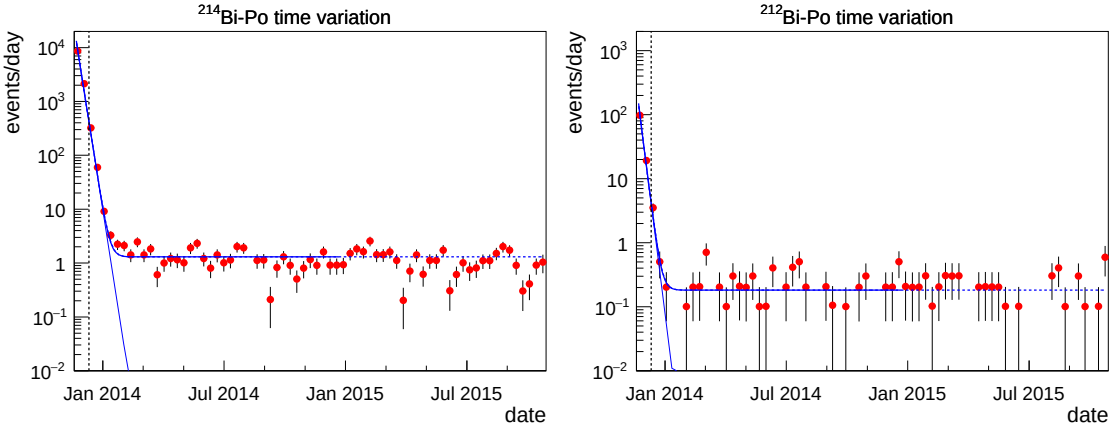

(a) ^{214}Bi-Po events (b) ^{212}Bi-Po events

Figure 7.8.: Time variation of tagged ^{214}Bi-Po and ^{212}Bi-Po events within 1.2-m-radius. Blue lines show fitted decay curves of ^{222}Rn ($T_{1/2} = 3.824$ days) and ^{224}Ra ($T_{1/2} = 3.66$ days) assuming no constant contribution other than ^{222}Rn and ^{224}Ra. Black dotted line is the start of Phase-II, so it includes a part of high Rn period.

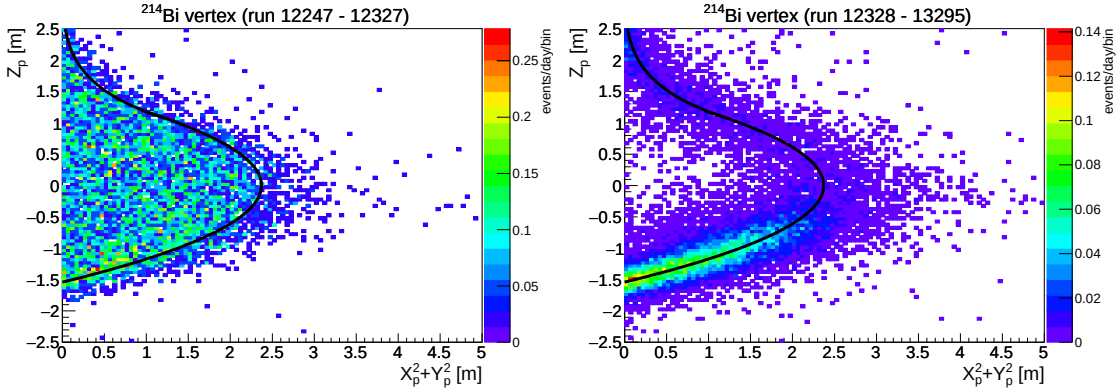

(a) High Rn period (40 days) (b) Low Rn period (495 days)

Figure 7.9.: Vertex distribution of ^{214}Bi tagged by delayed coincidence method for (a) high Rn period and (b) low Rn period. The former is dominated by initial Rn contamination at LS circulation, the latter is primary originated from the inner-balloon.

PileUp Tagging

Pileup is a event, where two pulses are detected in one event time window of ∼200 ns. It is reconstructed as a single event, generating background with total energy of two events, though some events are rejected by the "*VertexBadness*" cut. Approximately 40 % of ^{212}Bi-Po decay is detected as pileup event due to the short life of ^{212}Po. Their total energy overlaps with $0\nu\beta\beta$ energy, thus they should be rejected. In this section, detection method and selection of pileup event is described.

Hit Time Pulse This method detects double pulses from a hit time distribution of all hit PMTs. Hit time for i-th hit PMT, t_i is defined as deviation of TOF subtracted time $(t_{\mathrm{obs},i} - TOF_i)$ from event time T_0.

$$t_i = t_{\mathrm{obs},i} - TOF_i - T_0 \tag{7.3}$$

Though the pulse shape essentially depends energy and vertex for a event, it is stable around 2 MeV and in $R < 2$ m within 2 %.

Base Function Fitting function of hit time pulse is constructed from $2\nu\beta\beta$ events in $1.6 < E < 2.2$ MeV to reduce misidentification of $0\nu\beta\beta$ signal. The hit time distribution of Eq. 7.3 is normalized with the average energy and the total hit counts. This single pulse is denoted as $H(t_j)$ for j-th time bin. Double pulse function, f_j is expressed as summation of prompt and delayed single pulses weighted by the energy as follows.

$$f_j = E_{\mathrm{p}} \cdot H(t_j - T_{\mathrm{p}}) + E_{\mathrm{d}} \cdot H(t_j - T_{\mathrm{p}} - \Delta T) + D \tag{7.4}$$

Where,

- E_{p} : prompt energy
- E_{d} : delayed energy
- T_{p} : prompt hit time
- ΔT : time difference of prompt and delayed signal
- D : dark rate

Minimization The best values of above 5 parameters for the number of detected hits for j-th time bin, h_j are searched to minimize chi-square below:

$$\chi^2 = \begin{cases} 2\sum_{t_j} \left[f_j - h_j + h_j \log(h_j/f_j) \right] & (h_j \neq 0) \\ 2\sum_{t_j} f_j & (h_j = 0) \end{cases} \tag{7.5}$$

The detail of the fitter development is described in (Hachiya, 2016 [50]). Fig. 7.10 shows typical single/double pulse events with the base function optimized by the double pulse fitter.

Pileup Event Selection Furthermore, prompt/delayed energies are re-defined to compare $E_{\rm vis}$: visible energy reconstructed by the energy fitter as a single pulse.

$$E'_{\rm p} = \frac{E_{\rm p}}{E_{\rm p}+E_{\rm d}} \cdot E_{\rm vis} \tag{7.6}$$

$$E'_{\rm d} = \frac{E_{\rm d}}{E_{\rm p}+E_{\rm d}} \cdot E_{\rm vis} \tag{7.7}$$

Selection criteria for pileup events are listed using optimized energies and their time difference:

- $E'_{\rm p} > 0.1$ MeV
- $E'_{\rm d} > 0.5\ \exp\left(-\frac{\Delta T-13.5}{5.5}\right) + \exp\left(-\frac{\Delta T-13.5}{50}\right) + 0.15$ MeV
- $E'_{\rm d} < 1.2$ MeV

Time dependent lower bound for $E'_{\rm d}$ is optimized to select both short-lived and long-lived factors effectively. The quality of the fitter can be estimated from correlation of $E'_{\rm d}$ and ΔT shown in Fig. 7.11. Other event rejection and above prompt energy cut are applied to plotted data on ahead. In $3.0 < E_{\rm vis} < 5.0$ MeV, single pulse event of ^{208}Tl dominates, so the most of events are out of double pulse region surrounded by two black lines. On the other hand, in ^{212}Bi and ^{214}Bi energy region ($1.0 < E_{\rm vis} < 3.0$ MeV), two clusters exists in double pulse region. A cluster around $E'_{\rm d} \sim 0.7$ MeV and $50 < \Delta T < 100$ ns, indicates ^{212}Po events. The estimated energy and time difference are consistent with events tagged by the delayed coincidence method. The other cluster in $130 < \Delta T < 200$ ns includes both ^{212}Po losing the energy at the IB and also ^{214}Po. The time dependent slope is considered that uncounted hit signal out of event time window increases with ΔT. Misidentification probability is estimated to be less than 1 % in $1.0 < E_{\rm vis} < 5.0$ MeV from single pulse events such as ^{60}Co calibration data, $2\nu\beta\beta$ events.

Tagging Inefficiency

Total tagging efficiency for Bi-Po events is estimated using number of events tagged by the delayed coincidence method ($N_{\rm dc}$) and by the double pulse fitter ($N_{\rm pileup}$). Expected events is evaluated by fitting ΔT distribution with decay curve of polonium as shown in Fig. 7.12. ΔT is divided into 5 or 6 bins and the efficiency is calculated in each i-th bin. For delayed coincidence criteria, additional cut is applied to reduce accidental events.

$$\begin{aligned}
(\text{Bi-Po tagging efficiency}) &= \sum_i (\text{event ratio})_i \cdot (\text{tagging efficiency})_i \\
(\text{event ratio})_i &= \int_{t_i}^{t_{i+1}} \left(\frac{p_0}{\tau}\cdot \mathrm{e}^{-t/\tau}\right) dt \Big/ \int_0^{1.9\ \text{ms}} \left(\frac{p_0}{\tau}\cdot \mathrm{e}^{-t/\tau}\right) dt \\
(\text{tagging efficiency})_i &= \frac{N_{\rm dc}+N_{\rm pileup}}{\text{number of expected Bi-Po events}}
\end{aligned} \tag{7.8}$$

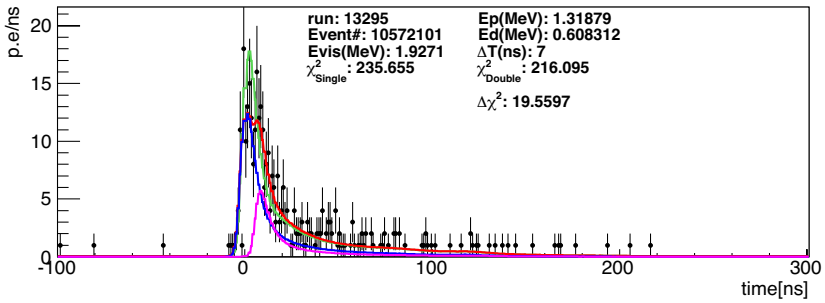

(a) Single pulse event

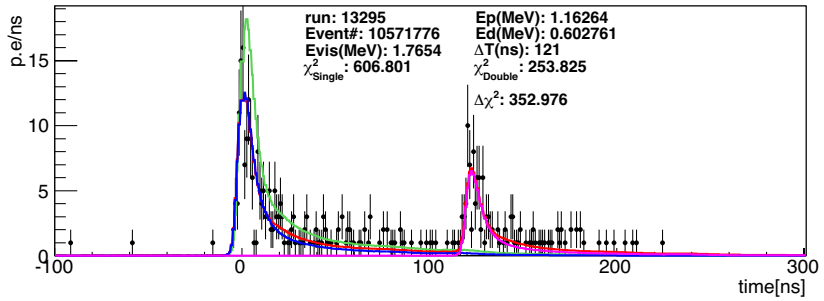

(b) Double pulse event

Figure 7.10.: Hit time distribution for typical single/double pulse events. The fitted base function is composed of prompt signal with blue line and delayed signal with magenta line. It reproduces the data histogram well as a double pulse event. In this case, energy and time difference is estimated to be $E_{\rm p} = 1.16$ MeV, $E_{\rm d} = 0.60$ MeV, $\Delta T = 121$ ns. Green line is the fit result assuming single pulse.

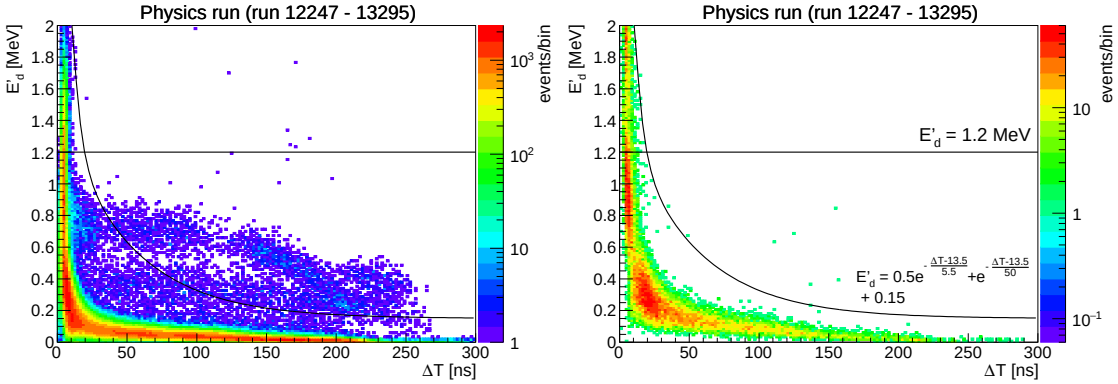

(a) $1.0 < E_{\mathrm{vis}} < 3.0$ MeV (b) $3.0 < E_{\mathrm{vis}} < 5.0$ MeV

Figure 7.11.: Correlation of prompt energy (E'_{d}) and time difference (ΔT) about double-pulse fit. (a) ^{212}Bi an ^{214}Bi energy region. Clusters of ^{212}Po an ^{214}Po events can be seen in double pulse region surrounded by two black lines. (b) ^{208}Tl energy region. Most of events are regarded as single pulse events. The misidentification probability is estimated to be less than 1 % though it increases along with the energy.

τ is lifetime of ^{212}Po or ^{214}Po. $p_0 = 3.189 \times 10^3$ is a variable optimized by decay curve fit including constant component. Calculated values are listed in Tables 7.3 and 7.4. From the total tagging efficiencies, the rejection inefficiencies is calculated to be (100 - 94.9) = (5.1 $\pm$ 2.7)% for ^{212}Bi-Po events and (100 - 99.954) = (0.046 $\pm$ 17)% for ^{214}Bi-Po events.

Table 7.3.: Tagging efficiency of ^{212}Bi-^{212}Po decay events

ΔT window (ns)	Event ratio (%)	Tagging efficiency (%)	Tagged event ratio (%)
0 - 13.5	3.08	0	0
13.5 - 70.5	12.00	87.46	10.50
70.5 - 162.5	16.32	100	16.32
162.5 - 287.5	17.27	97 $\pm$ 16	16.75 $\pm$ 2.68
287.5 - 1.9$\times 10^6$	51.32	100	51.32
Total	100	-	94.89 $\pm$ 2.7

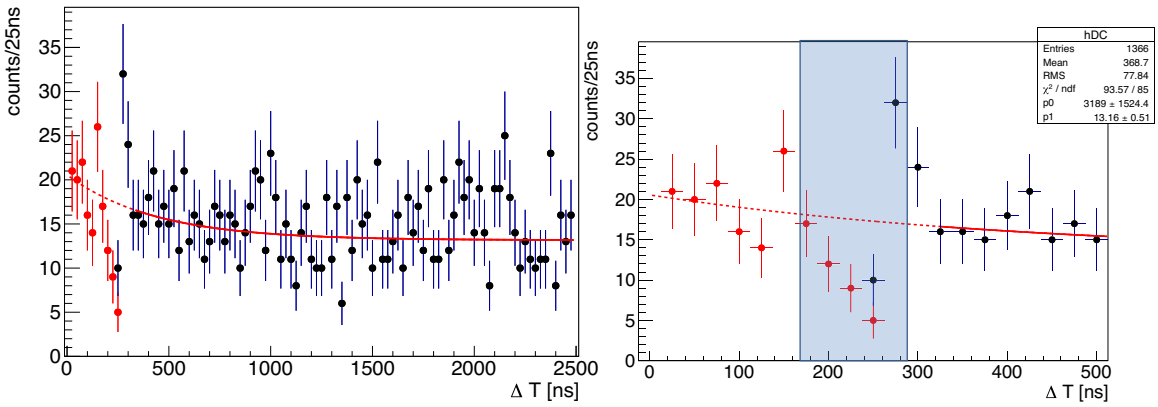

(a) ΔT distribution (b) Closeup of (a)

Figure 7.12.: ΔT distribution for tagged Bi-Po events. Red points indicates events tagged by the double pulse fitter, and blue points are events tagged by the delayed coincidence method. The red line shows fitted ^{212}Po decay curve. Expected number of events is calculated from the exponential function. For $162.5 < \Delta T < 287.5$ ns (shaded blue region in (b)), total tagged events is $N_{\mathrm{dc}} + N_{\mathrm{pileup}} = 43 + 42 = 84$ events relative to 87.8 expected events, thus the tagging efficiency in this time region is calculated to be 97 %.

Table 7.4.: Tagging efficiency of ^{214}Bi-^{214}Po decay events

ΔT window (ns)	Event ratio (%)	Tagging efficiency (%)	Tagged event ratio (%)
0 - 13.5	5.7×10^{-3}	0	0
13.5 - 70.5	2.404×10^{-2}	74.32	1.787×10^{-2}
70.5 - 162.5	3.879×10^{-2}	100	3.879×10^{-2}
162.5 - 287.5	5.268×10^{-2}	97 ± 16	$(5.110 \pm 0.8177)\times10^{-2}$
287.5 - 1.9×10^{6}	99.846	100	99.846
1.9×10^{6} - inf.	3.30×10^{-2}	0	0
Total	100	-	99.954 ± 0.008

7.3.3. Anti-Neutrino Event

Anti-neutrino produces a positron and a neutron by interaction with a proton namely inverse β decay (Eq. 7.9), which also can be identified with delayed-coincidence tagging method like Bi-Po decay.

$$\bar{\nu}_e + p \rightarrow e^+ + n \tag{7.9}$$

As shown in Fig. 7.13, two 511 keV γ produced by annihilation of positron and electron are tagged as prompt signal. And neutron is captured by hydrogen nucleus after thermalization then emits 2.2 MeV deexcitation γ, tagged as delayed signal.

Anti-neutrino selection is set up to reject dominator "reactor neutrino", however almost all nuclear plants are under suspension since the Fukushima Dai-ichi Nuclear Power Plant (FNPP1) accident occurred in 2011, so the contribution is substantially small. Selection criteria and inefficiencies are summarized in Table. 7.5. The calculation method is as follows:

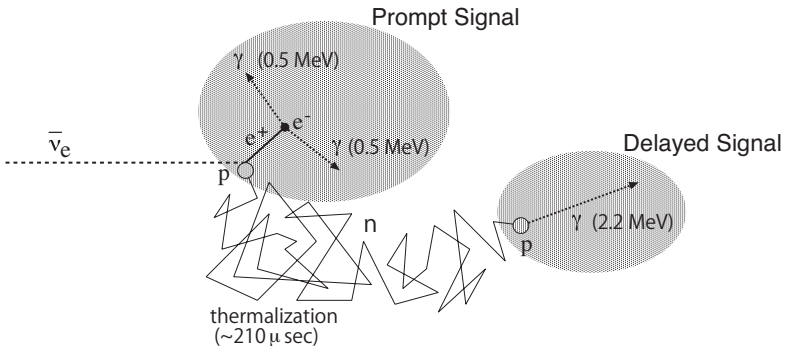

Figure 7.13.: Delayed coincidence events of inverse β decay of $\bar{\nu}_e$ (Enomoto, 2005 [51])

- Delayed energy (E_d)
  Inefficiency for the delayed energy is calculated assuming gauss distribution. The mean energy and energy resolution are estimated to be 2.225 MeV and $\sigma/\sqrt{E[\mathrm{MeV}]} \sim 7.3\%/\sqrt{E}$.

$$\begin{aligned}(\text{Inefficiency of } E_d \text{ cut}) &= 1 - \frac{1}{\sqrt{2\pi\sigma^2}} \int_{1.5\,\mathrm{MeV}}^{\infty} \exp\left(-\frac{(E-2.225)^2}{2\sigma^2}\right) dE \\ &< 1.0 \times 10^{-8}\ \%\end{aligned} \tag{7.10}$$

- Space correlation (ΔR)
  Distance from the prompt signal to the delayed signal is evaluated with AmBe composite source calibration data regarding 4.4 MeV γ-rays as prompt and 2.2 MeV neutron capture γ-rays as delayed signal. The inefficiency of $\Delta R < 2$ m is estimated to be 0.16 %. Though current vertex resolution degenerated by 0.3 % compared to calibration data, it has little influence.

- Time correlation (ΔT)
  Selection inefficiency of ΔT is calculated using mean capture time of neutron; $\tau = 209.5 \pm 3.9$ μs from the past neutron events (Watanabe, 2015 [52]).

$$\begin{aligned}(\text{inefficiency of } \Delta T \text{ cut}) &= 1 - \frac{1}{\tau}\int_0^{1\,\text{ms}} \exp\left(-\frac{t}{\tau}\right) dt \\ &= 0.85 \pm 0.08\%\end{aligned} \tag{7.11}$$

Table 7.5.: Anti-neutrino event selection criteria and inefficiency

parameters	criteria	inefficiency [%]
Delayed energy	$E_{\text{d}} \geq 1.5$ MeV	$< 1.4 \times 10^{-8}$ %
Space correlation	$\Delta R < 200$ cm	0.16 %
Time correlation	$\Delta T < 1$ ms	0.85 %
Total	-	0.86 %

7.3.4. Spallation products

Spallation nucleus is induced by highly energetic cosmic muon. Unstable isotopes are produced, originated from major composition of Xe-LS (^{12}C, ^{136}Xe). ^{10}C spallation shown in Fig. 7.14 is one of primary backgrounds for $0\nu\beta\beta$ decay, the lifetime τ = 27.8 s is too long to apply time veto. It is estimated to accompany neutrons with ~90 % probability, so tagging by triple coincidence of muon-neutron-^{10}C is effective. Identification of muon and ^{10}C decay is better to use KamFEE data for the performance of muon tracking and vertex reconstruction. However KamFEE data have large neutron detection inefficiency due to overload to the electronics and to dead time arising from the high event multiplicity following the muon. To overcome the problem, MoGURA was developed as dead time free electronics, but part of data was still lost due to saturation of the digital data buffer. The problem was solved by developing a new trigger optimized for detecting neutron peak from high-frequency component (Oki, 2013 [46]). Thus neutron detection efficiency improved 20 %, which enabled triple coincidence with high efficiency for the first time.

In this paragraph, procedure of triple tagging is described. Neutron peak is detected by searching maximum value of subtracted hit count denoted as N_{s}. It is calculated from hit time distribution by setting following time windows:

- event time window (200 ns)
- hit time window (30 ns) : T_0(event time) ±15 ns
- off-time window (170 ns) : (event time window) - (hit time window)

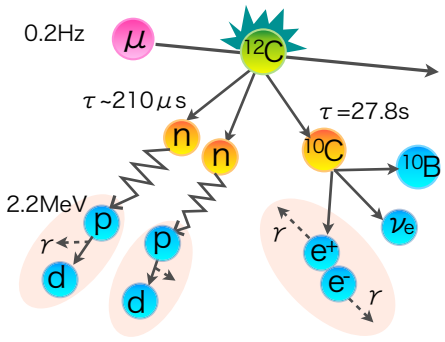

Figure 7.14.: Schematic view of ^{10}C spallation induced by muon

Start time of the event time window fluctuates ∼300 ns or ∼500 ns to cover hit time with 1 ns interval. $N_{\rm s}$ defined at Eq. 7.12 is calculated in each event time window as follows:

1. Set a event time window
2. Determine event time "T_0" by vertex reconstruction using hit PMTs within event time window
3. Calculate $N_{\rm s}$ for the TOF and T_0 subtracted hit time distribution

$$\begin{aligned} N_{\rm s} &= N_{\rm in} - N_{\rm out} \cdot \frac{30 \text{ ns}}{(200-30) \text{ ns}} \\ N_{\rm in} &: \text{the number of hits in hit time window} \\ N_{\rm out} &: \text{the number of hits in off-time window} \end{aligned} \tag{7.12}$$

In order to maximize N_s, the procedure above is repeated by changing time window. Fig. 7.15(a) is an example of hit time distribution at the maximum N_s. Threshold of N_s to detect neutron peak is determined to be 50, however exceptional criteria is needed for the busiest period shortly after the a muon. Fig. 7.15(b) shows correlation between N_s and time difference between muon and neutron (ΔT). A cluster around $N_s \sim 230$ indicates neutron events. Time dependence in short ΔT period is caused by massive after-pulse, which makes N_s relatively low. So N_s threshold is set to 80 for $10 < \Delta T < 30$ us. In further short time region below $\Delta T = 10$ us, N_s cannot be calculated correctly any more, thus it is rejected from neutron candidate. Neutron event tagged in MoGURA is identified in FBE data using unixtime of the event, preceding muon is searched for $\Delta T < 1200$ us. Furthermore, spallation products are searched using time correlation with muon and space correlation with neutron. Thus selection criteria of triple coincidence is listed as follows:

- Muon selection
  - KamFEE data
  - Through going muon: $Q_{17} \geq 10,000$ p.e.

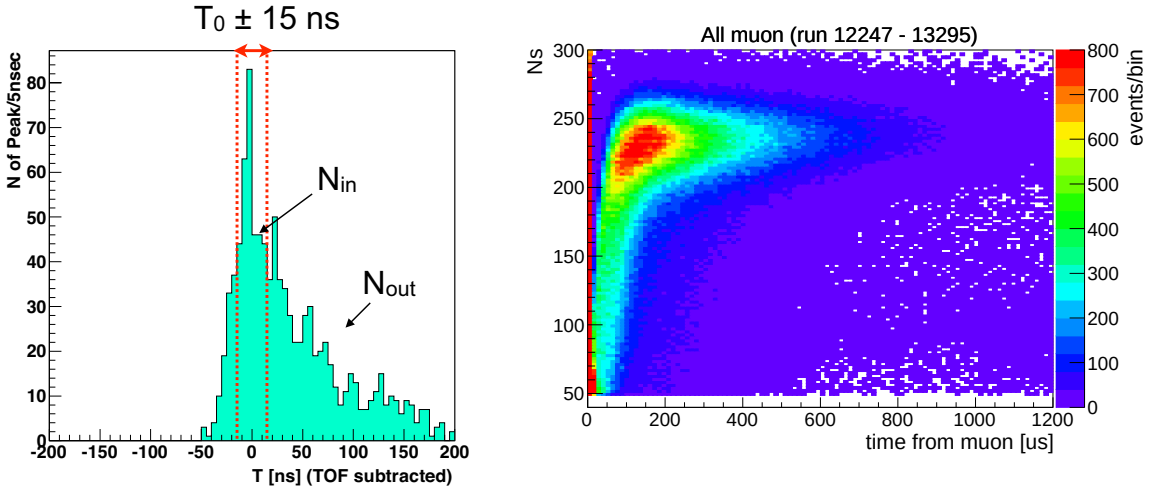

(a) Hit time distribution

(b) Correlation between N_{s} and ΔT

Figure 7.15.: N_{s} of neutron peak and correlation with ΔT. (a) TOF subtracted hit time deviation from event time for a event. (b) Correlation between N_{s} and ΔT. A cluster around $N_s \sim 230$ indicates neutron events. Time dependence in short ΔT period is caused by massive after-pulse, which makes N_s relatively low. In further short time region below $\Delta T = 10$ us, N_s cannot be calculated correctly.

  - Clipping muons : $(Q_{17} \geq 500$ p.e.$) \cap (N_{200\mathrm{OD}} \geq 5$ hits$)$

- Neutron selection
  - MoGURA data
  - Total hit : $N_{\mathrm{in}} + N_{\mathrm{out}} \geq 150$
  - Subtracted hit :
    - $10 \leq \Delta T < 30$ μs : $N_{\mathrm{s}} > 80$
    - $\Delta T \geq 30$ μs : $N_{\mathrm{s}} \geq 50$
  - Time from the preceding muon: $10 \leq \Delta T < 1200$ μs

- Spallation products
  - KamFEE data
  - Time from muon : $0 < \Delta T < 180$ s
  - Distance from the nearest neutron : $\Delta R < 160$ cm

Fig. 7.16 shows characteristics of tagged neutron events. For the captured energy spectrum, clear peak of n^1H can be seen, though it is relatively lower than real energy. Fig. 7.16(b) shows neutron capture time. The mean lifetime $\tau = 215.9 \pm 0.8$ μs estimated from fitting with a function $f(t) = N/\tau \cdot \mathrm{e}^{-t/\tau} + \mathrm{const.}$, is consistent with another

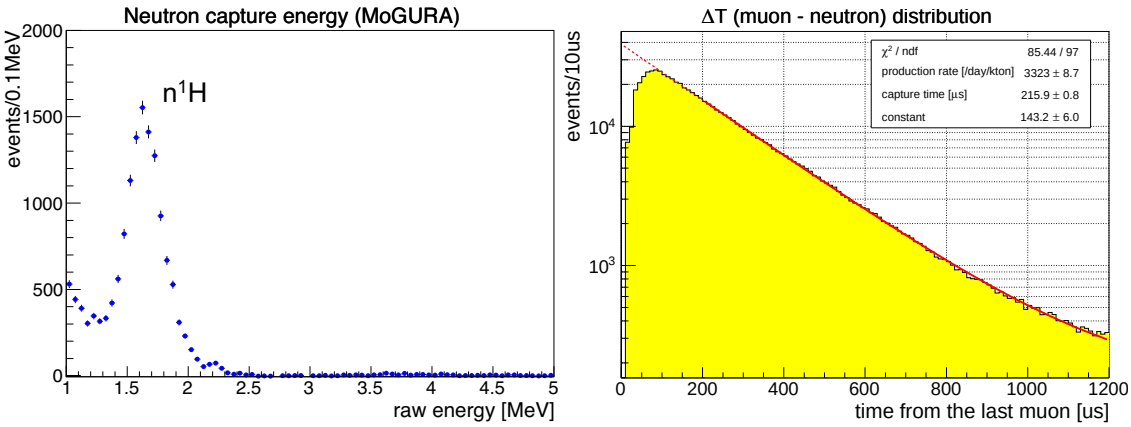

(a) Energy spectrum

(b) Time difference from muon

Figure 7.16.: Neutron capture time and captured energy for all muon inside 5.5m-radius. Xe-LS region is rejected.

estimation. Fitted production rate 3323 ± 9 /day/kton is also consistent with previous measurement 3575 ± 462 /day/kton (S. Abe, Enomoto, et al., 2010 [53]). Neutron tagging inefficiency assuming estimated capture time is calculated to be (25.7 ± 0.1) %. It will be improved by selection criteria for short ΔT period.

7.3.5. Summary of Background Event Rejection

All background rejection described in this section are applied to data in addition to bad event rejection. Fig. 7.17 demonstrates the effectiveness of the selection. Final single events are used to double-beta decay analysis.

7.4. Livetime

Livetime is time of well-operated data period to be analyzed. It is estimated from three types of period defined as follows:

- RunTime : time of data taking period.
- DeadTime: time of no data period or known abnormal data period.
- VetoTime: time of rejection period for background or noise events.

7.4.1. Runtime

Runtime of a run is defined to be duration between a first event time and a last event time. The uncertainty of runtime is evaluated to be ∼9 ms given from ∼110 Hz of history trigger rate. It corresponds to 1.0×10^{-5} % for typical 24 hours run.

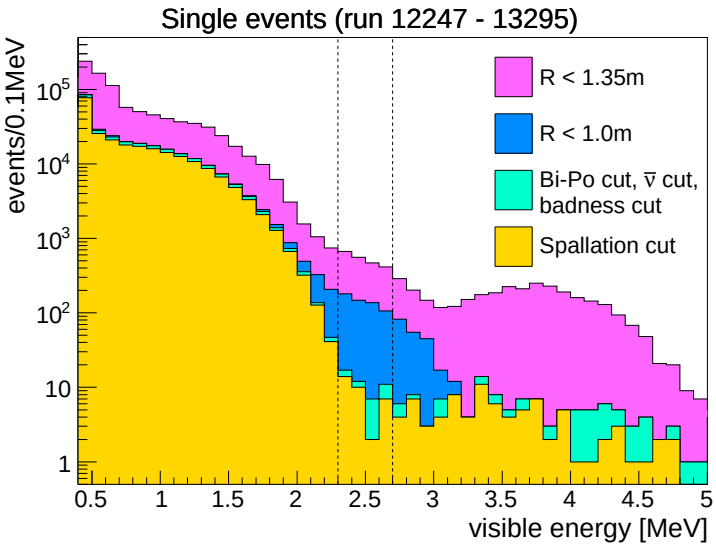

Figure 7.17.: Energy spectrum each event cut is applied. An item in the legend indicates added selection to previous cuts. Radius cut is the most effective to reject backgrounds from the IB. Bi-Po cut substantially reduces ^{214}Bi contribution in $0\nu\beta\beta$ energy region surrounded with dotted lines ($2.3 < E < 2.7$ MeV). The number of events of each spectrum in this region is counted to be 2106, 571, 47 and 33 events, respectively.

7.4.2. Deadtime

Deadtime is categorized into three kinds of time period below.

- Run base deadtime period
  KamFEE run is divided into 3 main run types.
  - Bad run :
    By reason of too short runtime, too long dead period, or badness of data taking quality, whole runtime is vetoed.
  - Half-bad run :
    Part of run is regarded as deadtime. Suspension of PMT HV caused by its overcurrent, failure of a KamFEE board, or drastic change of trigger rate are the case of deadtime period. Not rejected time is used for analysis.
  - Good run :
    Run does not include primary deadtime period unlike bad run and half-bad run, though secondary deadtime described in the next item exists.
- Secondary short deadtime period
  - Trigger dead period :
    When buffer of KamFEE trigger board is almost full, disable trigger suspending data taking for ∼0.4 ms is launched automatically.

  - Missing muon period :
    Time period detecting cluster of "missing muon" events defined in 7.2.5. Interval from the first noise event to the last one of a cluster is vetoed.

- MoGURA deadtime period :
  Data acquired with MoGURA is used for spallation neutron search, so its deadtime is also vetoed. Primary factor is time interval for run change. The system switches a run along with daily run change in KamFEE. Besides, it changes sub-run automatically according to quality of data taking. Thus, duration from the last event to the first events in the next run becomes deadtime.

7.4.3. Vetotime

Vetotime composed of 6 items below is estimated in each run. The details are described at Secs. 7.2.2, 7.2.3, 7.2.4 and 7.2.5.

- Post 1pps : 100 μs veto since 1pps trigger
- Post muon : 2 ms veto since a muon event
- Post missing waveform : 2 ms or 2 s veto since a missing waveform event
- Post deadtime :
  - 3 min veto since the first event or the end of a deadtime
  - 2 ms veto since missing muon period and trigger disable period

7.4.4. Livetime Calculation

Livetime in each run cannot be expressed subtraction of deadtime and vetotime from runtime, because it needs to take into account overlap of each deadtime and vetotime. The livetime is defined as follows using fraction R_{alive}:

$$\begin{aligned} \text{Livetime(run)} &\equiv \text{Runtime} \times R_{\text{alive}}\text{(run)} \\ R_{\text{alive}}\text{(run)} &= \frac{\text{number of alive events after applying all cuts in } R < 1\text{m}}{\text{number of generated events in } R < 1\text{m}} \end{aligned} \tag{7.13}$$

Generated events herein indicates temporally random events distributing uniformly in LS, approximately 10^4 events in typical 24-hours run within 1-m-radius. All event cuts and time veto except for periodical 1pps events are applied to the MC events, thus R_{alive} are given as combined vetotime ratio. Total livetime is calculated to be 534.5 days relative to 609.2 days of runtime, so practical vetotime is estimated to be (runtime) - (livetime) = 74.7 days.

Uncertainty of the livetime calculation is dominated by the statistics of generated events. Approximately 10 % of 6×10^6 total generated events are vetoed for good runs, so the ratio of vetoed events to the total generate events become 1×10^{-4}. Thus the

uncertainty is calculated to be 1×10^{-2} %.

Total systematic error for livetime is derived from a quadratic sum uncertainty for runtime (1.0×10^{-5} %), combined vetotime (2.0×10^{-3} %) and livetime calculation (1×10^{-2} %), that is $\sqrt{(1.0 \times 10^{-5})^2 + (2.0 \times 10^{-3})^2 + (1 \times 10^{-2})^2} = 1 \times 10^{-2})^2$ %.

7.4.5. Summary of Livetime

Livetime information is summarized in Table. 7.6.

Table 7.6.: Summary of livetime

runtime	609.2 days
livetime	534.5 days
vetotime	74.2 days
uncertainty of runtime	1.0×10^{-5} %
uncertainty of vetotime	2.0×10^{-3} %
uncertainty of livetime	1.0×10^{-2} %

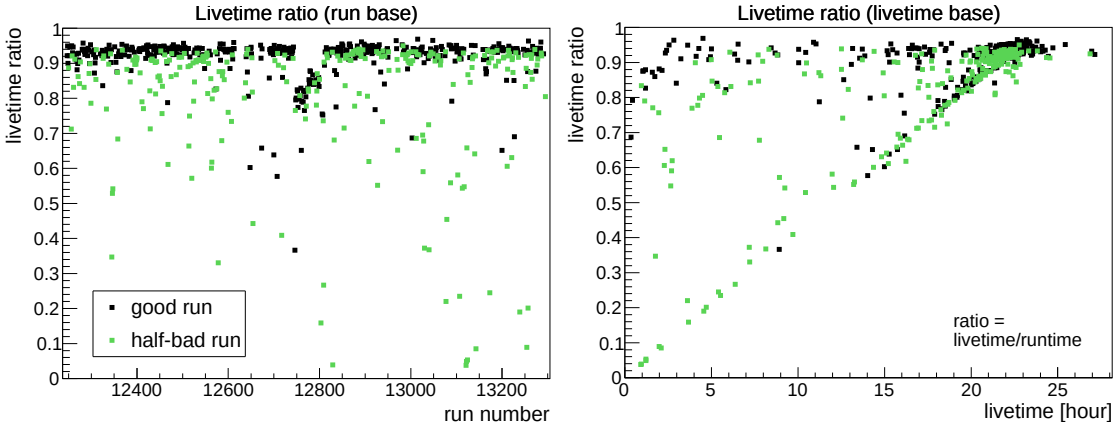

(a) (b)

Figure 7.18.: Ratio of livetime to runtime for each (a) run number, and (b) livetime. For half-bad run, the ratio tends to be low because of its dead period. Abnormal values around run12800 was resulted by trigger test with MoGURA electronics.

8. Background Estimation

8.1. Overview of Backgrounds

In this section, characteristics and quantities of following backgrounds are discussed using single events to which selections in Chap. 7 are applied.

- Natural radionuclides
  - ^{238}U series : ^{214}Pb, ^{214}Bi, ^{210}Bi, ^{85}Kr
  - ^{232}Th series : ^{212}Bi, ^{208}Tl
  - ^{40}K
- Radioactive fallout : ^{134}Cs, ^{137}Cs
- Spallation products induced by muon
  - light isotope: ^{11}C, ^{10}C, ^{6}He, ^{12}B
  - heavy isotope: ^{137}Xe
- Potential backgrounds : ^{110m}Ag, ^{208}Bi, ^{88}Y, ^{60}Co

Their characteristics are summarized in Table. 8.1. Potential backgrounds are candidates of ∼2.6 MeV peak observed in Phase-I, which are narrowed down from all nuclei by the lifetime and spectrum shape. Reduction of dominator ^{110m}Ag is the motivation of serial LS purification, and is the greatest concern for $0\nu\beta\beta$ analysis.

Other primary backgrounds in $0\nu\beta\beta$ energy region above 2 MeV are ^{214}Bi, ^{212}Bi, ^{10}C and ^{137}Xe. As to ^{214}Bi originated from the IB, accuracy of vertex distribution is improved, in order to ensure its contribution at the innermost region. Improvement of event rejection is seen in ^{212}Bi and ^{10}C. ^{212}Bi rejection efficiency is enhanced thanks to redeveloped double-pulse fitter. For ^{10}C, spallation cut using MoGURA electronics is applied for the first time. ^{137}Xe is added to $0\nu\beta\beta$ analysis for the first time, because it became unignorable due to background reduction by LS purification. Production rate of ^{137}Xe is estimated from its capture cross section, for which consistency with MC simulation is confirmed.

In $2\nu\beta\beta$ analysis, ^{134}Cs, ^{137}Cs, ^{210}Bi, ^{85}Kr and ^{40}K cause uncertainty for the rate estimation and fiducial volume is confined. Nuclei in $E < 1$ MeV such as ^{210}Bi, ^{85}Kr and ^{40}K are difficult to measure the quantities independently due to whelming $2\nu\beta\beta$ events but included empirically. ^{134}Cs, ^{137}Cs observed around the IB are unexpected backgrounds identified by their spectrum shapes.

Background spacial distribution are determined by the following material source. It is basically uniform or radiated, which is important information for background discrimination.

- Internal backgrounds (Xe-LS)
- External backgrounds :
  - Inner balloon (IB)
  - Outer-LS
  - (Connection tube at Z∼3.3 m)
- Spallation products

8.2. MC Simulation

MC simulation is necessary for background estimation such as contamination amount, spacial distribution. In this analysis, simulation toolkit GEANT4 is used, which manages from particle generation to hit and digitization including every interaction and optical processes (Agostinelli et al., 2003 [54]), (Allison et al., 2006 [55]). The event reconstruction is processed as follows.

1. Event generation
   Based on actual detector geometry, primary positions are generated as uniform random numbers in Xe-LS or in the IB film. Some backgrounds non-uniformly distributes along vertical direction of the IB, for which a model estimated from data is introduced as described in Sec. 8.3.1. Momentum direction is isotropic as expressed with uniform random numbers r [0, 1] as $(\sqrt{4r(1-r)}\cos(2\pi r), \sqrt{4r(1-r)}\sin(2\pi r), 1-2r)$. Initial energy is determined by taking account of all radioactive decay modes of each nucleus.

2. Particle Tracking
   The simulation tracks all propagated particles including secondary particle until their decay, attenuation, absorption or detection. Optical photon is propagated according to configured photon emission spectrum, and go though scintillation and Cherenkov processes. Reflection and refraction at medium boundaries are also included. Material properties and optical parameters are tuned on a basis of source calibration data.

3. Event reconstruction
   - Energy
     In the simulation, particle track is divided into short steps. Total energy deposit is simply defined as sum of quenched energy deposit in each step without using optical information. It is calculated from i-th quenched energy

Table 8.1.: Background summary

Nuclide	Decay	Q-value [MeV]	Lifetime	Material
Natural radionuclides				
Th-series (^{212}Bi,^{208}Tl)	-	-	-	Xe-LS, Film
U-series (^{214}Pb,^{214}Bi)	-	-	-	Xe-LS, Film
^{210}Bi	β^-	1.16	7.23 d	Xe-LS, Film, Outer-LS
^{40}K	$\beta^-\gamma$	(β^-:1.31, EC:1.50)	1.84×10^9 yr	Xe-LS, Film, Outer-LS
^{85}Kr	β^-	0.687	15.5 yr	Xe-LS
Radioactive fallout				
^{134}Cs	$\beta^-\gamma$	(β^-:2.06, EC:1.23)	2.97 yr	Film
^{137}Cs	$\beta^-\gamma$	0.662	43.4 yr	Film
Spallation products				
^{137}Xe	$\beta^-\gamma$	4.17	5.5 min	uniform
^{11}C	β^+	1.98	29.4 min	uniform
^{10}C	$\beta^+\gamma$	3.65	27.8 s	uniform
^{6}He	β^-	3.51	1.16 s	uniform
^{12}B	β^-	13.4	29.1 ms	uniform
^{8}Li	$\beta^-\alpha$	16.0	1.21 s	uniform
Potential backgrounds				
^{110m}Ag	$\beta^-\gamma$	3.01	360 day	Xe-LS, Film
^{88}Y	ECγ	3.62	154 day	Xe-LS
^{60}Co	$\beta^-\gamma$	2.82	7.61 yr	Xe-LS
^{208}Bi	ECγ	2.88	5.31×10^5 yr	Xe-LS

deposit in the inner-LS (Xe-LS) namely $E_{\mathrm{in},i}$ and j-th quenched energy deposit in the outer-LS, $E_{\mathrm{out},j}$:

$$E_{\mathrm{tot}} = \sum_i E_{\mathrm{in},i} + \alpha \sum_j E_{\mathrm{out},j} \tag{8.1}$$

α indicates light yield ratio of outer-LS to inner-LS, estimated to be 1.07. In addition, resolution effect is imported using normal random number x and energy resolution $R = 7.3\%/\sqrt{E_{\mathrm{tot}}[\mathrm{MeV}]}$.

$$E = E_{\mathrm{tot}} + xR\sqrt{\alpha E_{\mathrm{tot}}} \tag{8.2}$$

Quenching effect is derived from the conversion table of real/visible energy shown in Fig. 6.14(a), which is estimated from source calibration data and initial ^{214}Bi events.

- Vertex
  After the simulation, following effects during data processing are applied into hit photons.
  - PMT activation : mask part of PMTs based on actual bad channel list in a specific run.
  - PMT timing resolution :
    add a asymmetric Gaussian random number.
  - Photoelectron resolution :
    add a random number from empirical 1 p.e. distribution in each cable.
  - Late pulse :
    It is caused by elastic or inelastic back scattered electron inside a PMT. The spectrum is deconvoluted from real data.
  - Trigger threshold

  Then vertex is reconstructed by V2 fitter, which is the same way as for real data.

Quality of MC simulation can be confirmed by composite source calibration data. Fig. 8.1 shows vertex and energy distributions for simulated and observed events of ^{137}Cs, ^{68}Ge and ^{60}Co located at the center of the detector. The statics of simulation is approximately 2 % of observation. To ensure the background estimation in sensitive region for $0\nu\beta\beta$ decay search, spatial distribution tail of ^{214}Bi background from the IB should be reproduced with great accuracy. If it is assumed that 8 % tail discrepancy observed in ^{60}Co can be substituted for that of ^{214}Bi, expected ^{214}Bi events inside 1-m-radius is only 0.016 % of total events, which corresponds to $\sim$0.2 events in analysis data set as discussed later. Thus the quality of simulated vertex distribution is within tolerance level. For energy spectrum, simulation data is slightly higher than observation, but the scale factor is re-tuned in final spectral fit. Discrepancy seen in ^{68}Ge is considered to be originated from source position in the capsule.

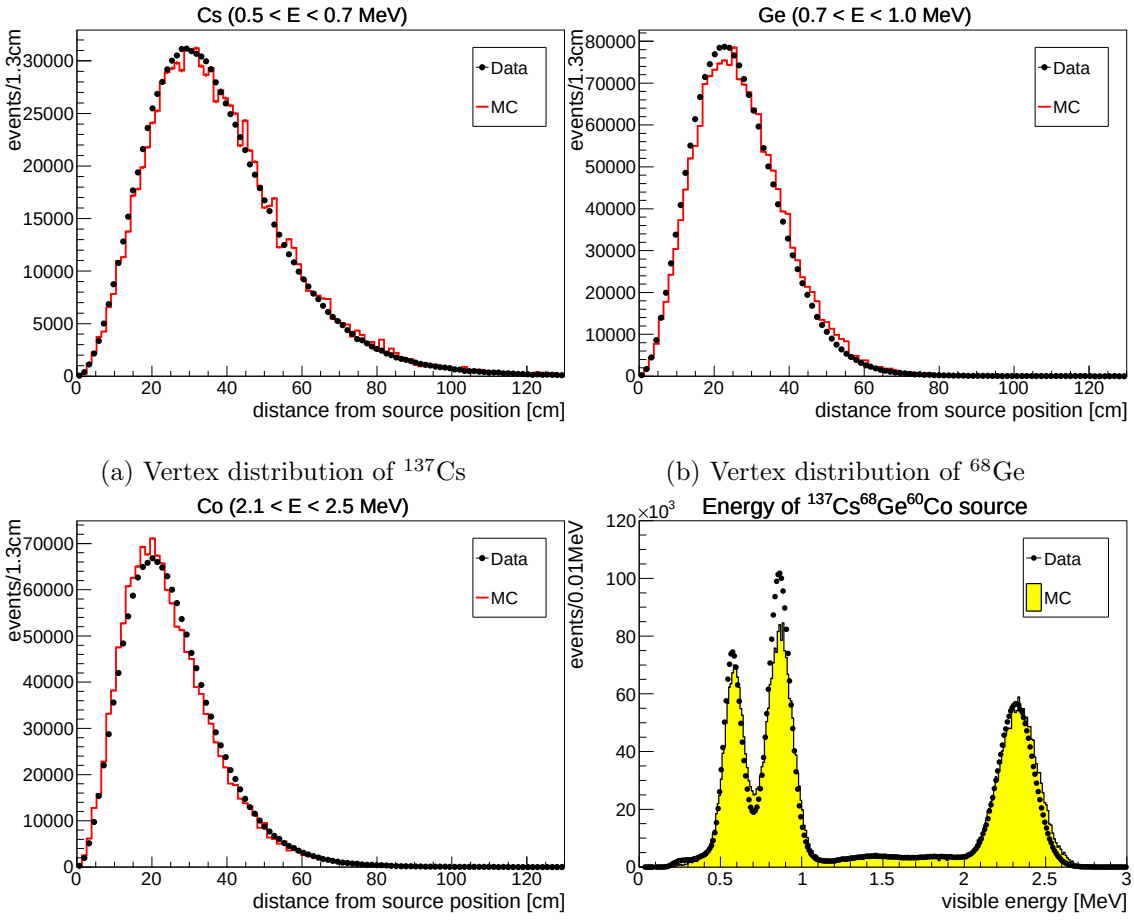

(a) Vertex distribution of ^{137}Cs

(b) Vertex distribution of ^{68}Ge

(c) Vertex distribution of ^{60}Co

(d) Energy spectrum of composite source

Figure 8.1.: Comparison of vertex and energy distribution of composite source calibration between real data and MC simulated data. The source position is the center of the detector. Discrepancy seen in ^{68}Ge is considered to be originated from source position in the capsule.

8.3. IB Film Background Model

8.3.1. Non-uniform Vertical Distribution

Film background distribution has z-dependence, as shown in Fig. 8.2. It causes non-negligible discrepancy of vertex distribution for internal region against uniform background. For more accurate estimation, the non-uniformity was evaluated for dominant backgrounds, ^{134}Cs, ^{214}Bi and ^{208}Tl.

Z-dependent background intensity is extracted by reproducing R^3 distribution of event rate, in small zenith angle (θ) division. Energy windows are selected where backgrounds in Xe-LS and IB as listed in Table. 8.2. Cosθ volume division is determined according to their statistics. Xe-LS contribution is subtracted by the difference of vertex distribution. Fig. 8.3 is the fit result with ^{214}Bi and ^{110m}Ag, for which estimated rate in each cosθ region is summarized into Fig. 8.4. Quality of constructed model based on the fit is confirmed by fitting R^3 for either of north or south hemisphere. distribution again (Fig. 8.5). Though local discrepancies are seen around film peak and the tail in ^{134}Cs and ^{208}Tl, which is not critical for $0\nu\beta\beta$ analysis due to difference of energy region. expected distribution of the most important background ^{214}Bi is well consistent with observation in both of hemispheres.

Table 8.2.: Event selection to estimate vertical non-uniformity of the IB

Energy window [MeV]	Xe-LS	IB	Number of cosθ region
$1.7 \leq E < 2.2$	^{136}Xe $2\nu\beta\beta$	^{134}Cs	28
$2.2 \leq E < 3.0$	^{110m}Ag	^{214}Bi	23
$3.0 \leq E < 5.0$	^{208}Tl	^{208}Tl	25

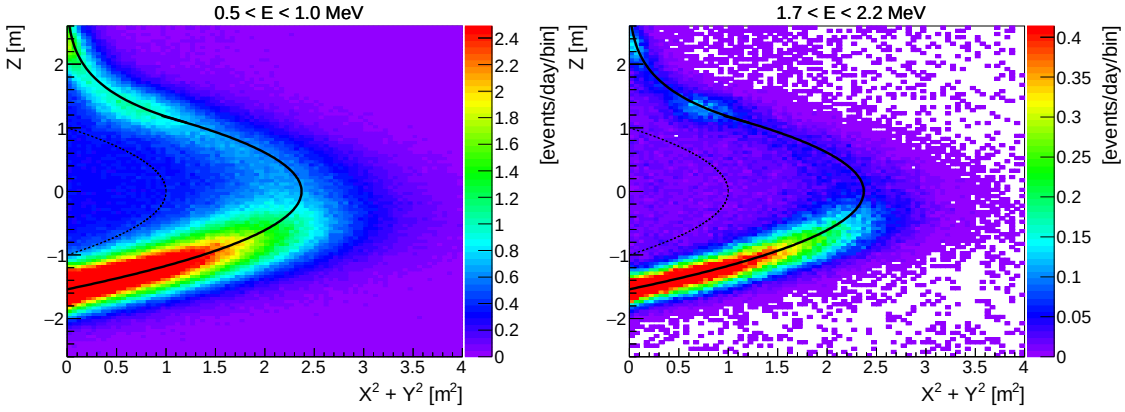

(a) $0.5 < E < 1.0$MeV (^{137}Cs)

(b) $1.7 < E < 2.2$MeV (^{134}Cs)

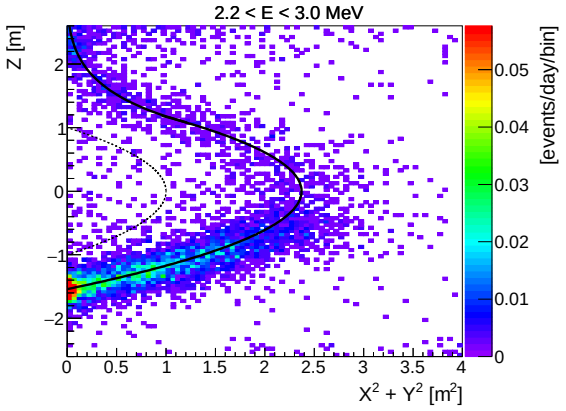

(c) $2.2 < E < 3.0$MeV (^{214}Bi)

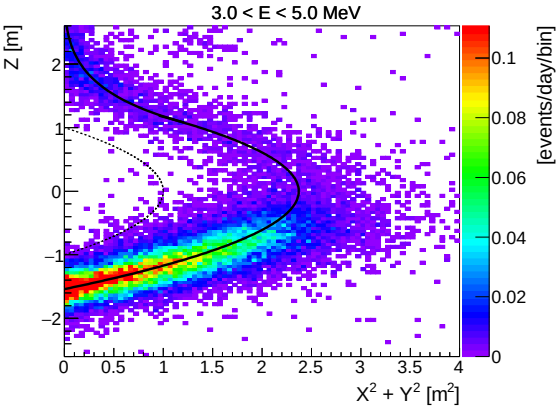

(d) $3.0 < E < 5.0$MeV (^{208}Tl)

Figure 8.2.: Vertex distribution of single events for each energy window. Solid line and dotted line indicate expected IB position and 1-m-radius, respectively. Non-uniform distribution concentrated in IB bottom is common among dominant film backgrounds ^{137}Cs, ^{134}Cs, ^{214}Bi, ^{208}Tl.

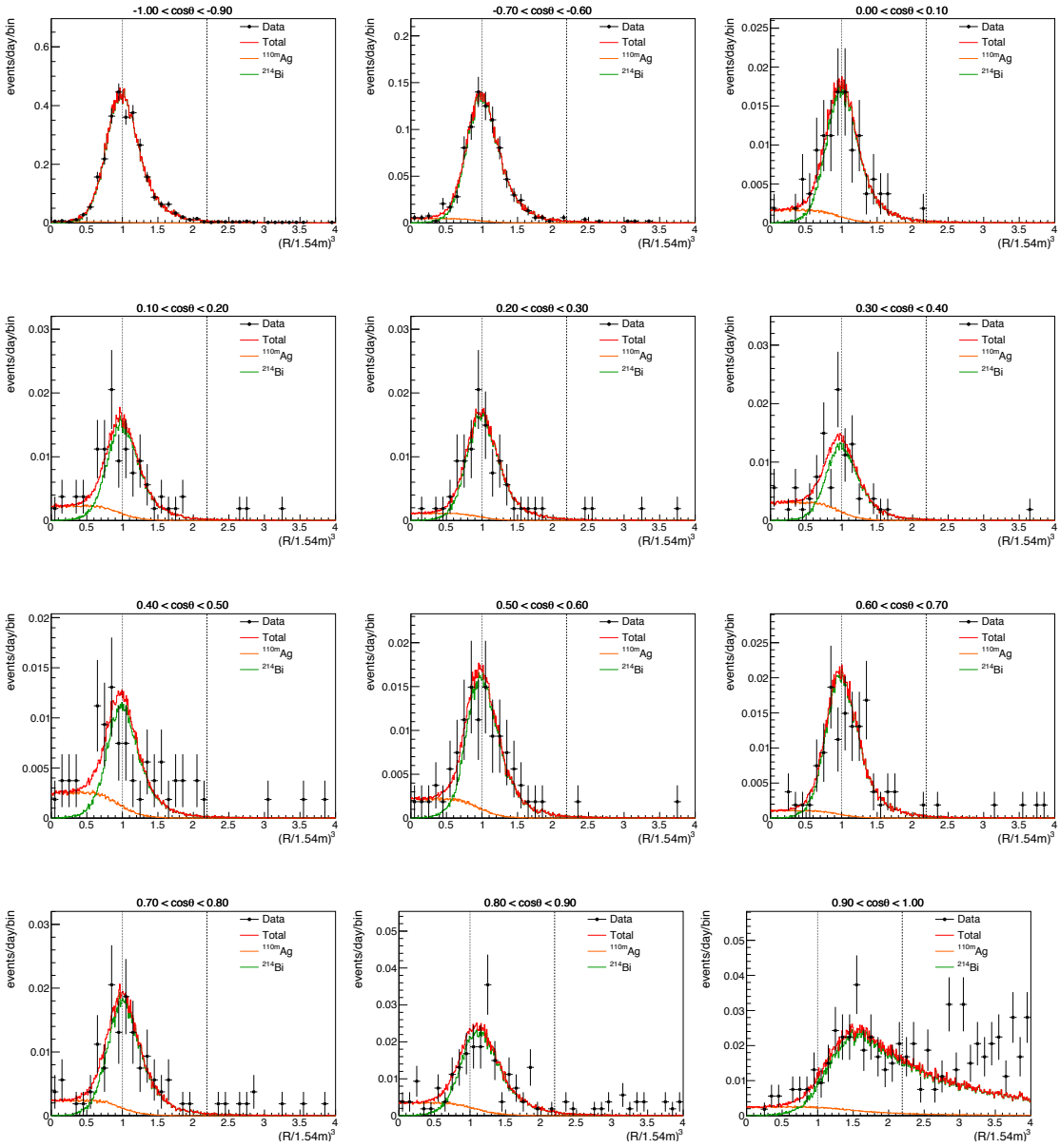

Figure 8.3.: R^3 distribution in $2.2 < E < 3.0$ MeV with best-fit backgrounds in each cosθ region. Single events is fitted with IB and XeLS components; ^{214}Bi (green) and ^{110m}Ag(orange). Dotted line and dashed line indicates IB radius in spherical part and 2-m-radius boundary of fiducial volume. For north hemisphere, only two regions are shown.

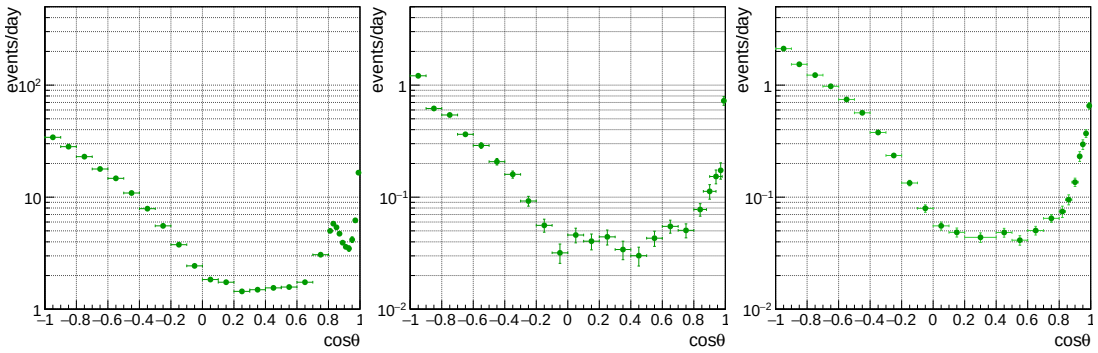

(a) ^{134}Cs (b) ^{214}Bi (c) ^{208}Tl

Figure 8.4.: cosθ distribution of film backgrounds ^{134}Cs, ^{214}Bi and ^{208}Tl given from R^3 distribution fitting. high rate points around cosθ $\sim$0.8 comes from hot spot.

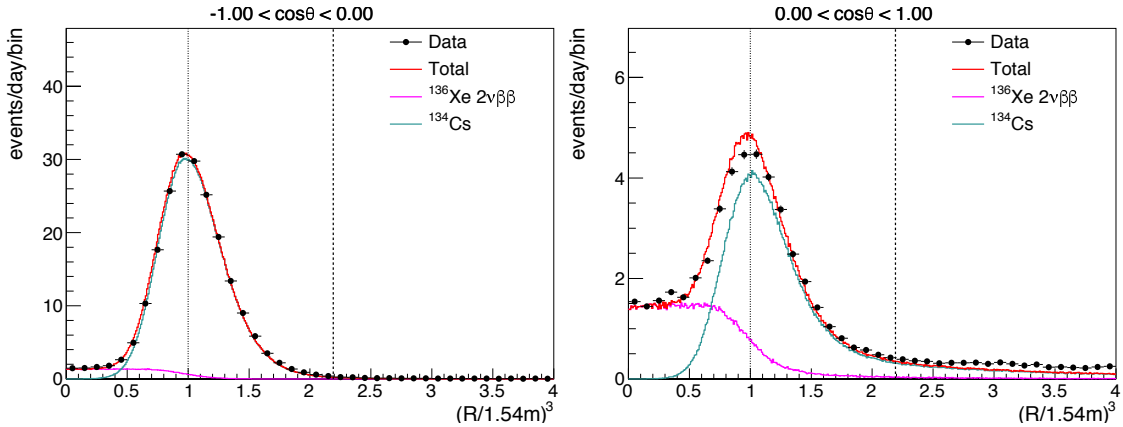

(a) $1.7 < E < 2.2$ MeV ($Z < 0$)

(b) $1.7 < E < 2.2$ MeV ($Z > 0$)

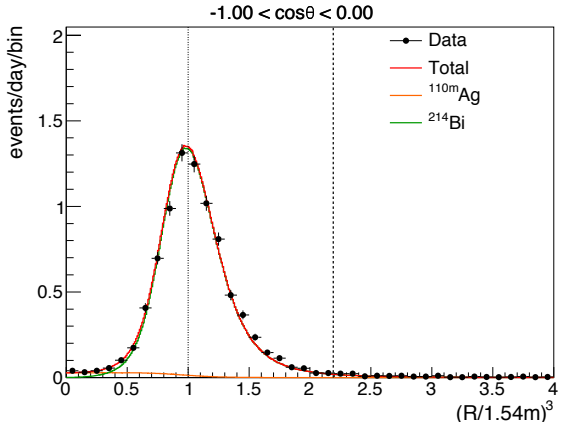

(c) $2.2 < E < 3.0$ MeV ($Z < 0$)

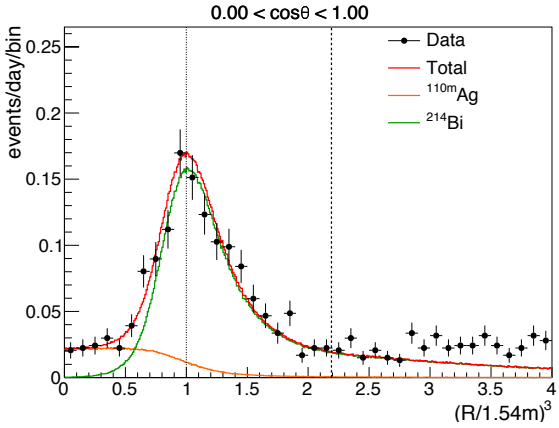

(d) $2.2 < E < 3.0$ MeV ($Z > 0$)

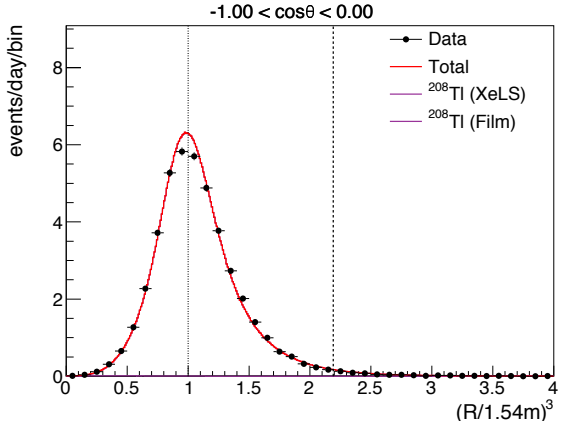

(e) $3.0 < E < 5.0$ MeV ($Z < 0$)

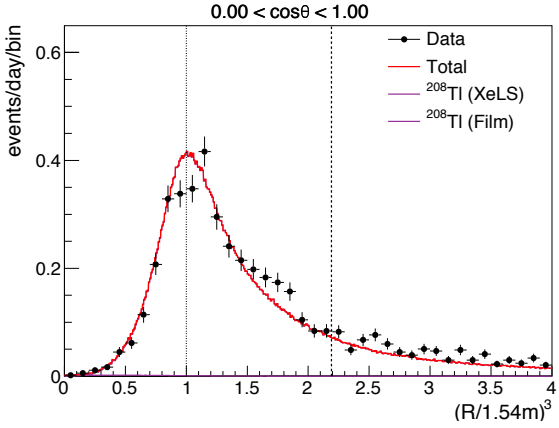

(f) $3.0 < E < 5.0$ MeV ($Z > 0$)

Figure 8.5.: R^3 distribution with tuned background model in each energy window.

8.3.2. Non-uniform Horizontal Distribution

This long-run data set revealed more detailed structure of horizontal distribution on the film, which makes possible consideration about source of contamination. Figs. 8.7, 8.8, 8.9, 8.10 and 8.11 indicate development view and x-section of the IB in this data set. For the former plot, events around the IB are selected as much as possible by radial or horizontal cut from the bottom to top of the IB cone part. To show original distribution hidden by the dust contamination after the Phase-I described above, the same plot as Fig. 8.7 is drawn for Phase-I (Fig. 8.6). X-sectional Xe-LS and IB distributions are divided into four Z regions. It makes sure each hot spot is on the IB, though uniform $2\nu\beta\beta$ events dominates in $1.2 < E < 2.0$ MeV. In the bottom part (Fig. 8.8(a)), there are central spot which fits with diameter of polygonal cap connecting with all gores by welding, and go-around string bundling film straps for suspension of the IB. In terms of quantity of matter, string may overwhelming. There is also a pattern circling around the central spot with ∼80 cm in diameter, corresponding to location at $-0.5 < Z < 0.0$ m in Fig. 8.6(b). In whence, relatively many patching places for leak distributes because of strain between film gores. Multi-spots at close Z may indicate adhesive for repair is the second factor of contamination. Next, it should be picked up that hot spot places are not the same between cesium and ^{214}Bi/^{208}Tl namely ^{238}U/^{232}Th natural radionuclides. It can be confirmed by comparing spots at Figs. 8.7, 8.8, 8.10 and 8.11. It reveals existence of minor contribution other than repair or welding, which may be associated with more accidental factor coming from instruments or worker. ^{214}Bi on the IB become main background of $0\nu\beta\beta$ events and cannot be reduced by purification, thus thoroughness of cleanness will become more important in the next phase. There is no clear distinction between ^{214}Bi and ^{208}Tl distribution, so source of U/Th impurities may be similar in each hot spots.

In conclusion, existence of accidental impurity was confirmed, the reduction of which improves sensitivity for double-beta decay search. The nonuniformity is not modeled because ϕ information is not used in double-beta analysis. The intensity is projected into vertical direction.

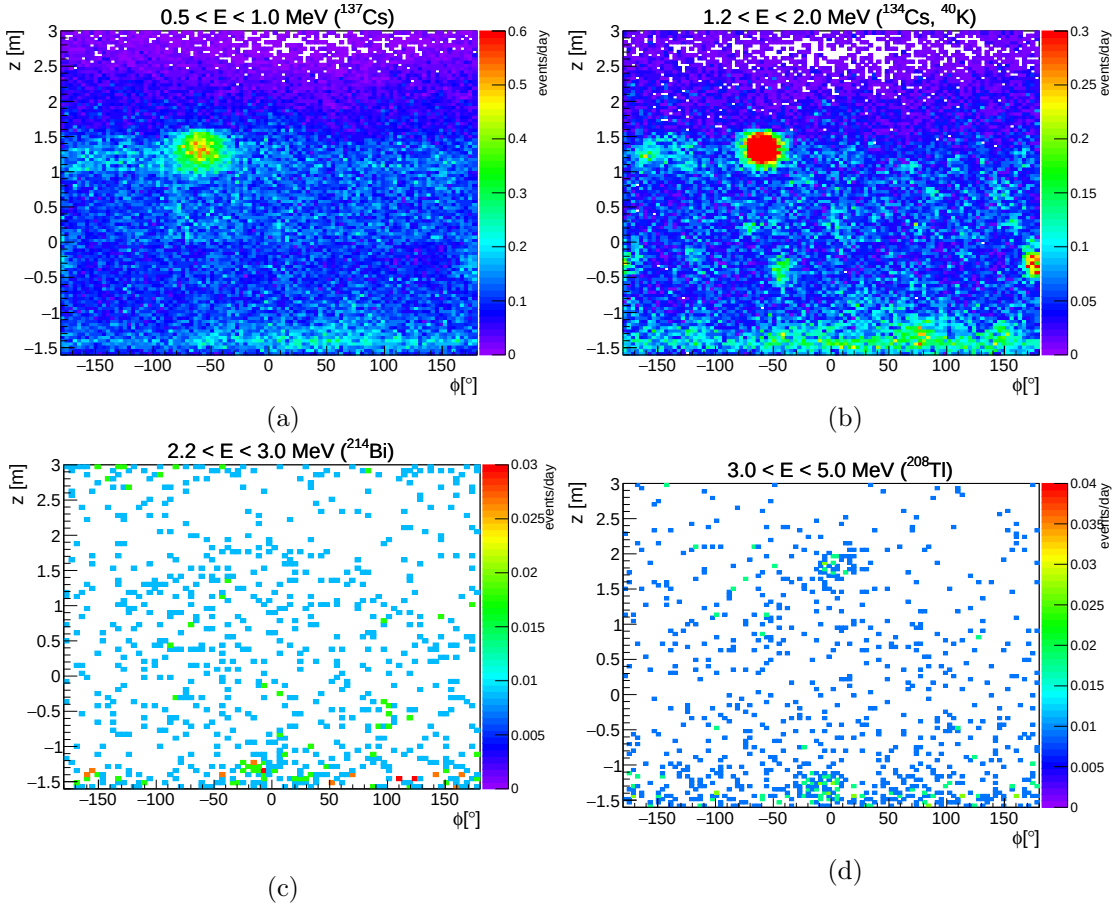

Figure 8.6.: Development view of the IB in Phase-I. Volume within approximately ±10 cm from the IB position is selected by radial or horizontal cut.

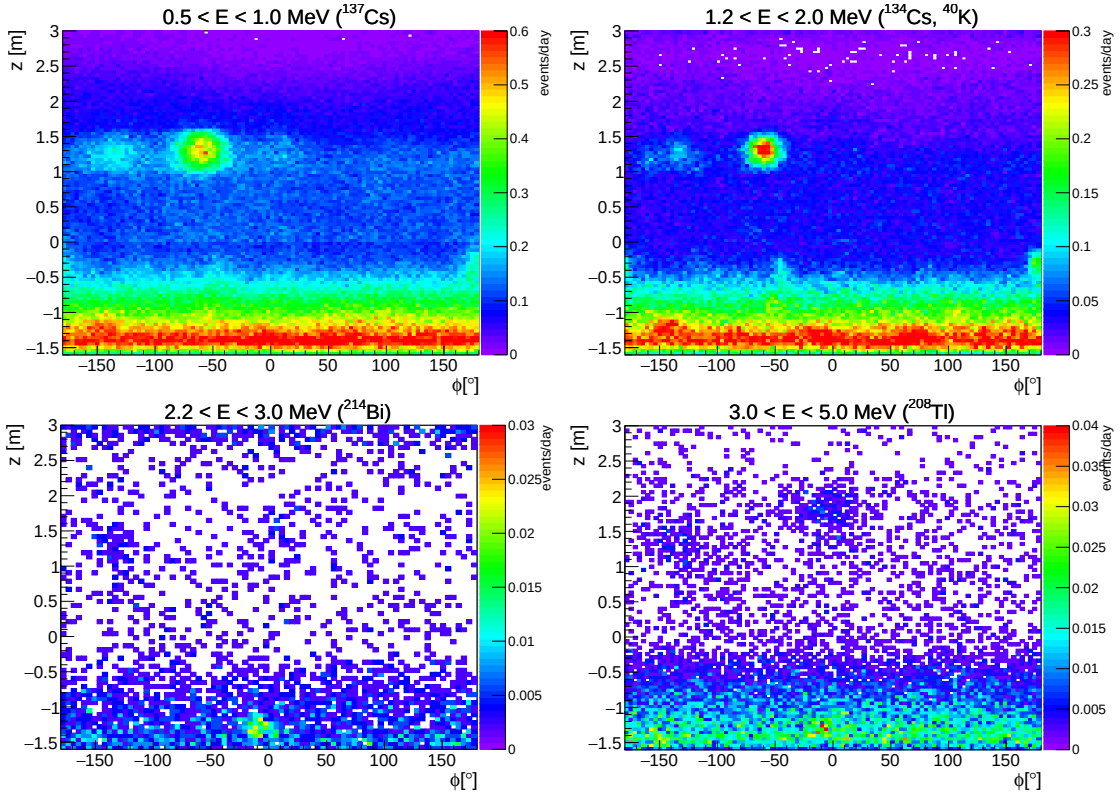

Figure 8.7.: Development view of the IB in Phase-II. Volume within approximately ±10 cm from the IB position is selected by radial or horizontal cut.

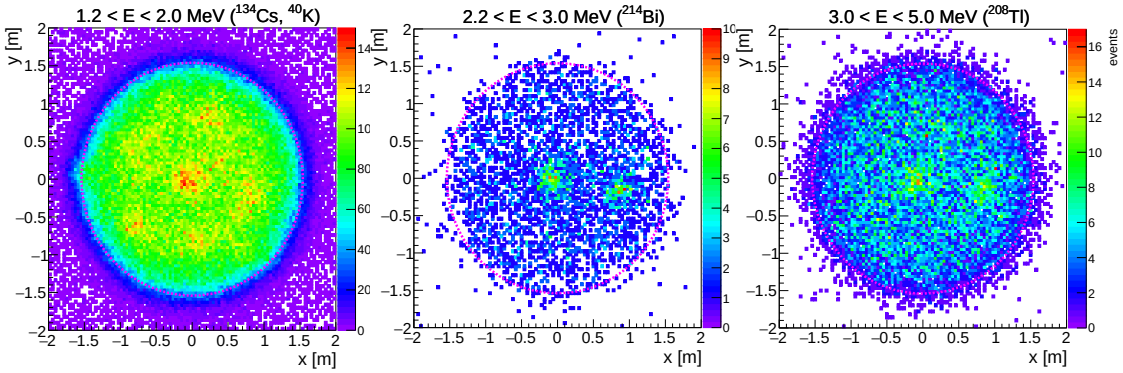

(a) (b) (c)

Figure 8.8.: X-section of the IB in -1.6 $< Z <$ 0.0 m. Magenta dotted line indicates radius of the IB.

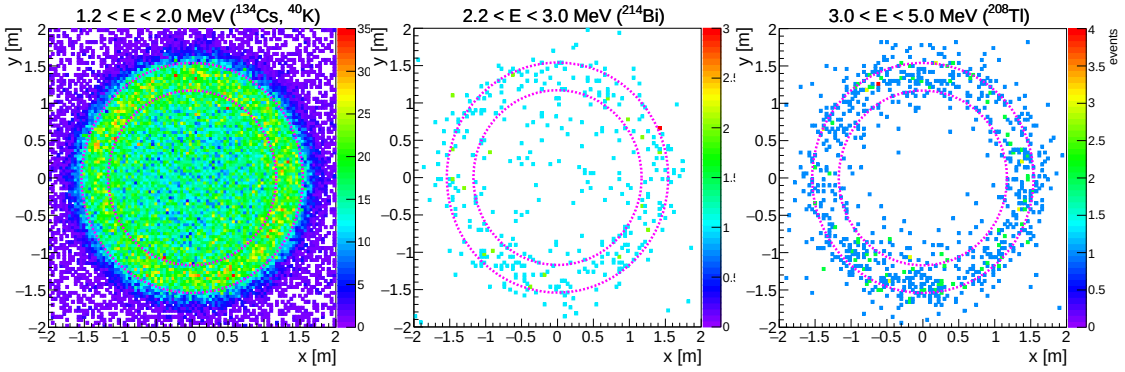

(a) (b) (c)

Figure 8.9.: X-section of the IB in $0.0 < Z < 1.0$ m. Magenta concentric circles indicate ideal IB position at the low end and the top.

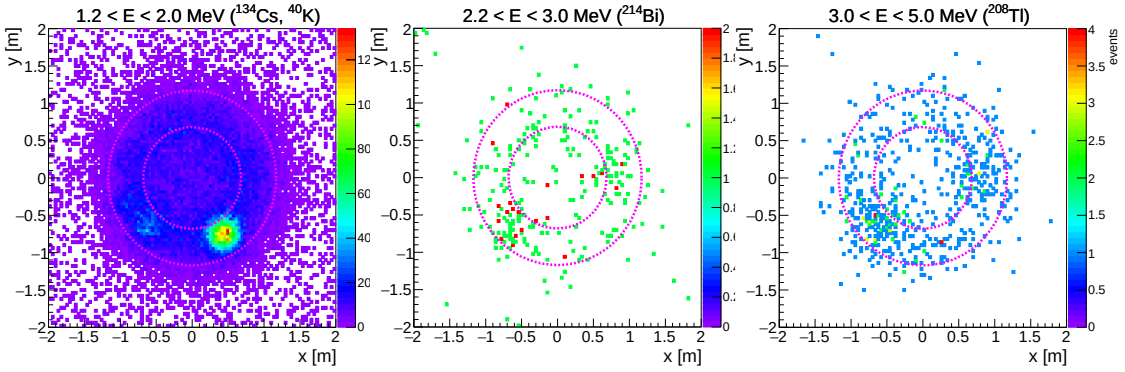

(a) (b) (c)

Figure 8.10.: X-section of the IB for $1.0 < Z < 1.6$ m

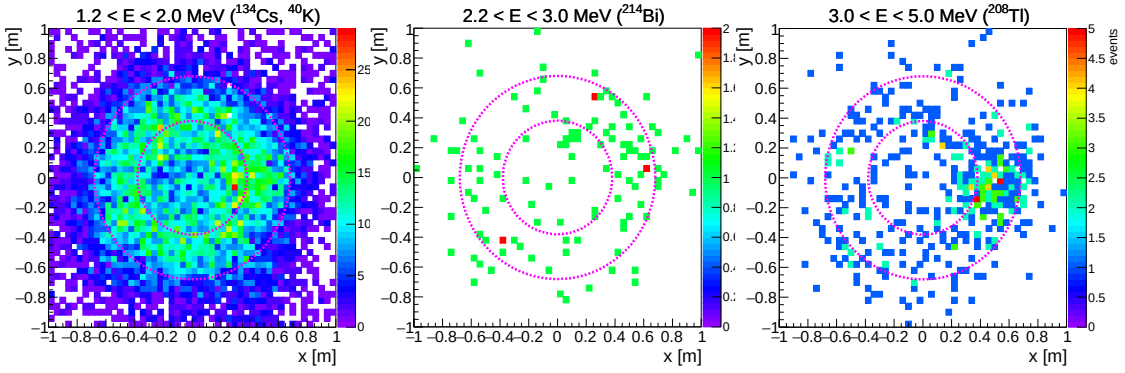

(a) (b) (c)

Figure 8.11.: X-section of the IB for $1.6 < Z < 2.0$ m

8.4. Natural Radionuclides

8.4.1. ^{238}U Series

^{238}U is one of the natural radionuclide with $T_{1/2} = 4.468\times10^{9}$ yr, having decay process down to the stable nucleus ^{206}Pb. In this analysis, nuclides contributing above 0.5 MeV are counted, namely ^{214}Pb, ^{214}Bi and ^{210}Bi. Their expected energy spectra are shown in Figs. 8.12(a) and 8.15. Event ratio of ^{214}Pb and ^{214}Bi are fixed by assuming radiative equilibrium, in contrast to ^{210}Bi being supplied from both of the parents ^{210}Pb and ^{238}U.

^{214}Bi

^{214}Bi is the most important background for $0\nu\beta\beta$ analysis. It continuously supplied from ^{238}U included in the Xe-LS and the IB, so it should be taken out thoroughly. Especially impurity around the IB film cannot be removed after the installation. On the other hand, another supply source ^{222}Rn generated by emanation from stainless-steel pipes for LS transportation decays with only $T_{1/2} = 3.824$ days, which provides massive ^{214}Bi events utilized for check of Xe-LS uniformity, detector calibration and estimation of fiducial volume error. ^{214}Bi can be tagged as sequential decays of its β-decay and α-decay of the daughter ^{214}Po by delayed-coincidence method (Sec. 7.3.2). ^{214}Bi events in Xe-LS can be tagged with high efficiency, though there is small contribution from ^{222}Rn at the beginning of the data set. In contrast, the tagging efficiency of ^{214}Bi events from the IB is much lower, because ^{214}Po α-ray frequently loses the energy in the non-luminescent IB film. Untagged ^{214}Bi is observed as a single event, thus it has impact on $0\nu\beta\beta$ decay search even in the innermost region far from the IB. It is required to accurately evaluate its spatial distribution tail, discussed later (Sec. 9.3.3). The energy spectrum is reproduced using events from initial Rn as described in Sec. 6.3.2.

Impact of LS purification and contamination during the work can be tested by comparing ^{238}U concentration which is estimated from ^{214}Bi events by assuming radiative equilibrium:

$$^{238}\text{U concentration [g/g]} = \frac{X_{\text{Bi}}\ [\text{Bq}]\ /\ 0.9998}{B_{\text{U}}\ [\text{Bq/g}] \cdot M\ [\text{g}]} \tag{8.3}$$

X_{Bi} is total ^{214}Bi event rate in a target material, B_{U} is specific activity of ^{238}U, 1.24×10^{4} [Bq/g], and M is total mass of the material, Xe-LS or the IB film. Each mass is calculated that $M_{\text{Xe-LS}} = 13.01$ ton and $M_{\text{IB}} = 1137$ g. The factor $1/0.9998$ indicates the branching ratio into ^{214}Bi-Po decays. ^{214}Bi in Xe-LS is simply derived from tagged events by delayed coincidence assuming 100 % tagging efficiency, given as (2.4 ± 0.1) events/day or $(1.7 \pm 0.1)\times10^{-16}$ [g/g]. It indicates little reduction effect compared to $(1.3 \pm 0.2)\times10^{-16}$ [g/g] in Phase-I estimated with the same way. Rn rich period is rejected from the estimation. For the IB events, ^{214}Bi events can be regarded as summation of tagged and single events in $2.4 < E < 3.0$ MeV, because events in this region are dominated by untagged ^{214}Bi. Hence total ^{214}Bi rate is that (tagged) + (untagged) = $(34.7 \pm 0.3) + (21.4 \pm 0.4) = (56.1 \pm 0.5)$ events/day, corresponding to $(4.61 \pm 0.04)\times10^{-11}$ [g/g]. It results tagging efficiency of ^{214}Bi from IB as (61.9 ± 0.7) %. ^{110m}Ag contribution is unignorable

in Phase-I, so the concentration is calculated from only tagged events by applying the same tagging efficiency with that of Phase-II. It gives $(1.4 \pm 0.1)\times10^{-11}$ [g/g], which indicates troubles during purification work contaminated the IB threefold. It is possible to overwhelm reduction effect in Xe-LS. These results are summarized in Table. 8.3.

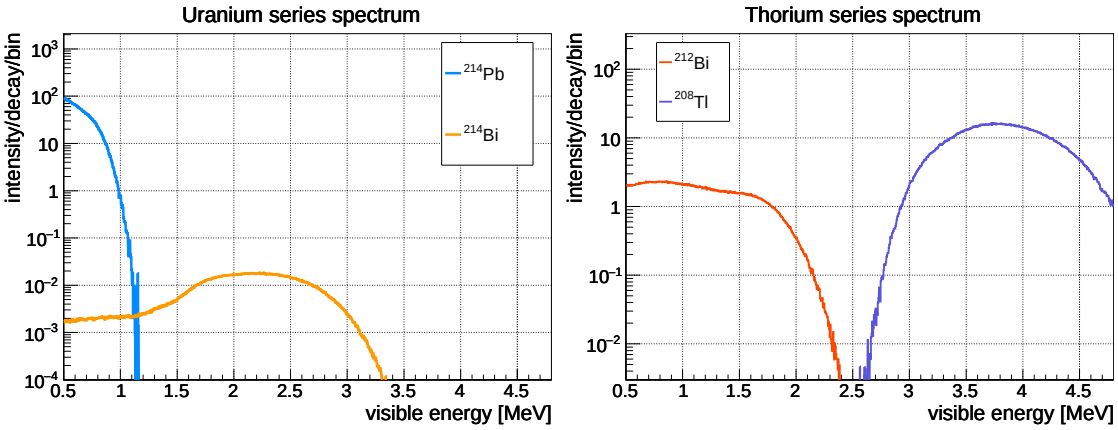

(a) (b)

Figure 8.12.: Expected visible energy spectrum for (a) U-series and (b) Th-series.

Table 8.3.: ^{238}U concentration in Xe-LS and the inner-ballon in each phase. For ^{214}Bi rate in unit of (events/day), correction for coincidence tagging or energy selection are already applied.

		Phase-I	Phase-II
Run period		11082 - 11212	12350 - 13295
^{214}Bi rate	(in Xe-LS)	1.8 ± 0.3	2.4 ± 0.1
	(in IB)	17.1 ± 1.0	56.1 ± 0.5
^{238}U concentration [g/g]	(in Xe-LS)	$(1.3 \pm 0.2)\times10^{-16}$	$(1.7 \pm 0.1)\times10^{-16}$
	(in IB)	$(1.4 \pm 0.1)\times10^{-11}$	$(4.61 \pm 0.04)\times10^{-11}$

^{210}Bi

^{210}Bi is radionuclide in uranium series, decaying to ^{210}Po with 5.01 day half-life. It is supplied from ^{210}Pb with 22.3 yr half-life, a daughter nucleus of ^{222}Rn introduced during LS circulation. It is one of the primary backgrounds of $2\nu\beta\beta$ events with 1.162 MeV Q-value (Fig. 8.15). In this analysis, parameters distributing in Xe-LS, Outer-LS and IB film are included.

In outer-LS, ^{210}Bi is supplied from the outer-balloon contaminated by ^{210}Pb, which enters inside region by LS convection or the past circulation. It causes spatially non-

uniform distribution, varying ^{210}Bi activity between 35.7 and 681.1 μBq/m^3 (A. Gando, Y. Gando, Hanakago, Ikeda, Inoue, Ishidoshiro, Ishikawa, et al., 2015 [56]), corresponding to 3.95×10^3 and 7.545×10^4 (kton·day)$^{-1}$. Therefore, ^{210}Bi contribution in outer-LS is broken into upper and lower hemisphere, where fivefold activity is measured in upper one (Fig. 8.14). The time variation is stable within ±25 % and ±5 % in lower/upper region respectively, though large uncertainty in lower one due to massive film backgrounds.

The spatial non-uniformity seen in outer-LS is not observed in Xe-LS, which is checked with ^{214}Bi-Po events from initial Rn. ^{210}Bi rate in Xe-LS is strongly correlated with ^{40}K in Xe-LS, which causes uncertainty for $2nu\beta\beta$ estimation.

8.4.2. ^{232}Th Series

Natural radionuclides ^{232}Th also has decay process as ^{238}U series, in which ^{212}Bi and ^{208}Tl shown in Fig. 8.12(b) are treated.

^{212}Bi

^{212}Bi with 2.254 MeV endpoint is also tagged by the delayed coincidence, but the efficiency 94.9 % is slightly lower than ^{214}Bi because of its shorter half-life (0.299 us). Part of untagged events are observed as pileup with ^{212}Po, for which their summed energy (approximately 2.95 MeV at maximum) can contribute to $0\nu\beta\beta$ region of $2.3 < E < 2.7$ MeV. Though rejection efficiency increased approximately 30 % than the past owing to improvement of the double-pulse fitter, events decaying within 20 ns time difference cannot be identified by the current fitter, which dominates ∼4.5 % of total ^{212}Bi-Po events. This impact can be calculated roughly. Expected number of ^{212}Bi events with 534.5 livetime is estimated to be 1 events in R < 1m and in $2.3 < E < 2.7$ MeV, assuming 1 % of energy cut efficiency (0.1 % without pileup events). Furthermore, reduction factor by pileup tagging is estimated to be ∼1/10 in the energy region from MC simulation, thus 0.1 untagged events is expected in this data set. It goes below 0.16 events contribution from the lowest background i.e. spallation product of ^{6}He. For this reason, pileup contribution is neglected in this analysis. ^{212}Bi rate is determined from ^{208}Tl events with assuming radiative equilibrium in the final spectral fit.

^{208}Tl

^{208}Tl decay dominates above 3 MeV far from $0\nu\beta\beta$ region. Low energetic γ cascades can be observed in the KamLAND in addition to 2.6 MeV deexcitation γ-ray, thus successive energy spectrum are observed above 2.6 MeV as shown in Fig. 8.12(b). From ^{208}Tl single events, ^{232}Th concentration is derived by assuming radiative equilibrium. By using B_{Th} =4.10×10^3 [Bq/g] and branching ratio 35.94 %, the concentration is calculated as listed in Table. 8.4. Quadruple increase for the IB concentration is almost consistent with that of ^{238}U contamination. Reduction factor for Xe-LS, ∼0.04 conflicts with that of ^{238}U concentration. Obvious reduction is confirmed for ^{208}Tl events, so floating of uranium rich impurity during data taking is likely. The hypothesis is supported by that

there is unsteady rate period of the delayed-coincidence events and single events only in the early part of data set.

Table 8.4.: ^{232}Th concentration in Xe-LS and the inner-ballon in each phase estimated from ^{208}Tl rate (events/day).

		Phase-I	Phase-II
Run period		11036 - 11212	12350 - 13295
^{208}Tl rate	(in Xe-LS)	2.5 ± 0.3	0.09 ± 0.05
	(in IB)	11.4 ± 0.4	48.6 ± 0.3
^{232}Th concentration [g/g]	(in Xe-LS)	$(1.5 \pm 0.2)\times10^{-15}$	$(5.5 \pm 0.3)\times10^{-17}$
	(in IB)	$(7.9 \pm 0.3)\times10^{-11}$	$(3.36 \pm 0.02)\times10^{-10}$

8.4.3. ^{40}K

^{40}K is natural radioactive metal element with 0.012 % natural abundance, presenting in a lock in plenty. It decays by emitting β ray or capturing orbital electron with long half-life 1.28 $\times10^9$ yr (Figs. 8.13(a)(b), 8.15). It is found in the LS and external components such as balloon film, surfaces of the PMTs and suspension kevlar ropes. Contaminant in LS can be refined by water extraction.

In this analysis, ^{40}K distributing in Xe-LS, Outer-LS and IB are taken into account. Xe-LS contribution is 0 consistent with upper limit < 0.9 (ton·day)$^{-1}$ (90% C.L.). Total rate in the IB is ∼1.5 times higher than measurement before the purification (Yoshida, 2014 [39]), which indicates dust contamination during purification introduced ^{40}K to the IB bottom as seen in ^{238}U and ^{232}Th. Though it is difficult to estimate its vertical non-uniformity in detail due to massive ^{134}Cs events, ratio with dual partitioning can be evaluated. From the spectrum fit using free parameters broken into upper and lower hemisphere, approximately (60 ± 12) % is concentrated on the lower region. ^{40}K in outer-LS is estimated to be 4.2×10^3 events/day/kton on average (Fig. 8.14), which is much higher than previous measurement 184.5 events/day/kton (A. Gando, Y. Gando, Hanakago, Ikeda, Inoue, Ishidoshiro, Ishikawa, et al., 2015 [56]). It might be supplied from external by LS convection.

8.4.4. ^{85}Kr

^{85}Kr is anthropogenic radioisotope, discharged to atmosphere by reprocessing spent nuclear fuel. It disintegrates with 10.76 yr half-life, but the concentration in the atmosphere continues to increase, exceeding 1 Bq/m^3 (Nitta et al., 2014 [57]).

This noble gas is purged by nitrogen, the residue is included to LS, so distribution in LS are considered. ^{85}Kr on the IB can be neglected compared to dominant background ^{137}Cs. ^{85}Kr contained in Xe-LS is difficult to estimate because of $2\nu\beta\beta$ events, therefore the uniformly distributed model is included. The event rate is measured to be on the

order of 100μBq/m^3 by the spectrum fit. Concentration in the outer-LS varies from 4.9 to 19.2 μBq/m^3 due to spatial non-uniformity caused by the past LS purification (A. Gando, Y. Gando, Hanakago, Ikeda, Inoue, Ishidoshiro, Ishikawa, et al., 2015 [56]). If the condition is kept afterward, ^{85}Kr rate is expected $\sim$1 % of $2\nu\beta\beta$ events in $R < 2$ m, thus it is negligible in spectrum fit.

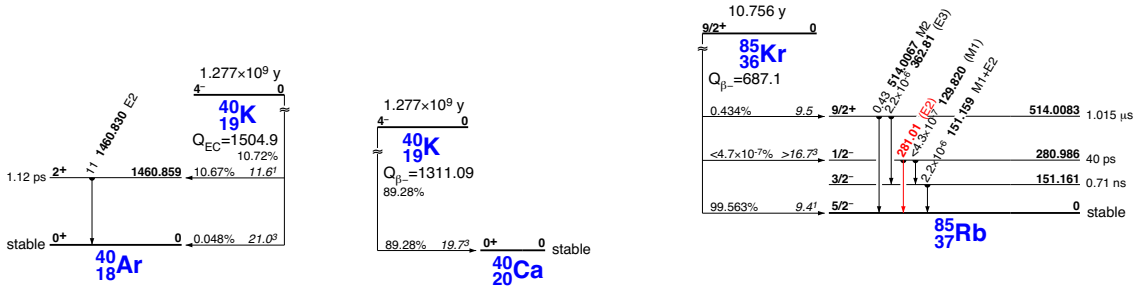

(a) ^{40}K (EC) (b) ^{40}K (β^-) (c) ^{85}Kr

Figure 8.13.: Level diagram for ^{40}K and ^{85}Kr

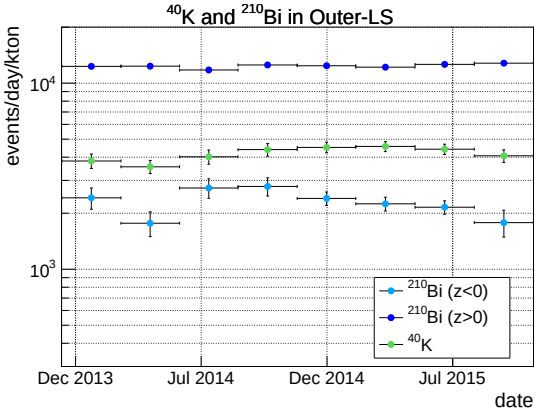

Figure 8.14.: Time variation of ^{40}K and ^{210}Bi event rate in outer-LS. It is derived from spectrum fit in $R < 2$ m. Each average rate is 4.2×10^3 events/day/kton (^{40}K), 2.3×10^3 events/day/kton (^{210}Bi in lower) and 1.2×10^4 events/day/kton (^{210}Bi in upper).

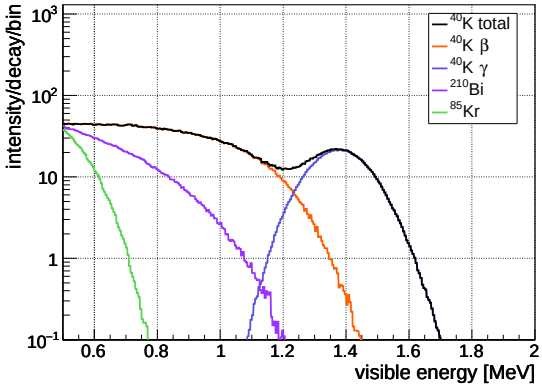

Figure 8.15.: Expected visible energy spectrum for ^{40}K, ^{210}Bi and ^{85}Kr in Xe-LS

8.5. Radioactive Fallout

8.5.1. ^{134}Cs, ^{137}Cs

Existence of artificial radioisotope ^{137}Cs and ^{134}Cs are confirmed around the IB (Fig. 8.2(a)(b)), which are not observed before KamLAND-Zen They are introduced by the fallout from Fukushima Dai-ichi Nuclear Power Plant(FNPP1) accident occurred in 2011. ^{134}Cs/^{137}Cs activity ratio reflecting operational status of nuclear power plant was consistent between KamLAND-Zen Phase-I data and measurement of soil samples or seawater around the accident site (WATANABE et al., 2012 [58]); (Aoyama et al., 2016 [59]). Cs attached to the IB on its fabrication at Sendai (∼90 km north of the power plant), which started 3 months after the accident. Level diagrams and expected visible energy spectra of ^{137}Cs and ^{134}Cs decays are shown in Figs. 8.16 and 8.17.

Fig. 8.18 is time variation of ^{134}Cs and $2\nu\beta\beta$ decays from the start of Phase-I (October 12, 2011) to the end of Phase-II (October 27, 2015). Each event rate in the whole Xe-LS volume or the hemispherical IB is extracted from simultaneous fit to the energy spectra for some equal-volume bins with other backgrounds. Clear radioactive decay curve are found with half-life 2.16 ± 0.13 yr (blue dashed line) and 2.38 ± 0.11 yr (red dashed line) fitted using Phase-II data, which are consistent with ^{134}Cs decay ($T_{1/2}$ = 2.06 yr).

However, rate in lower hemisphere conflicts with that of Phase-I unlike upper one. The contamination was caused by dust contamination during the LS circulation after Phase-I. We suspect that Cs from fallout of FNPP1 accident attached during the pump fabrication and air leakage trouble at the pump lead contamination to the LS. Fig. 8.2(b) is vertex distribution of Phase-II in ^{134}Cs energy window, in which bottom events obviously increased compared to Phase-I (Fig. 8.19). ^{134}Cs activity in the lower hemisphere increased 4.4 ± 0.9 times more than Phase-I, 6.3 ± 1.3 times as to ^{137}Cs.

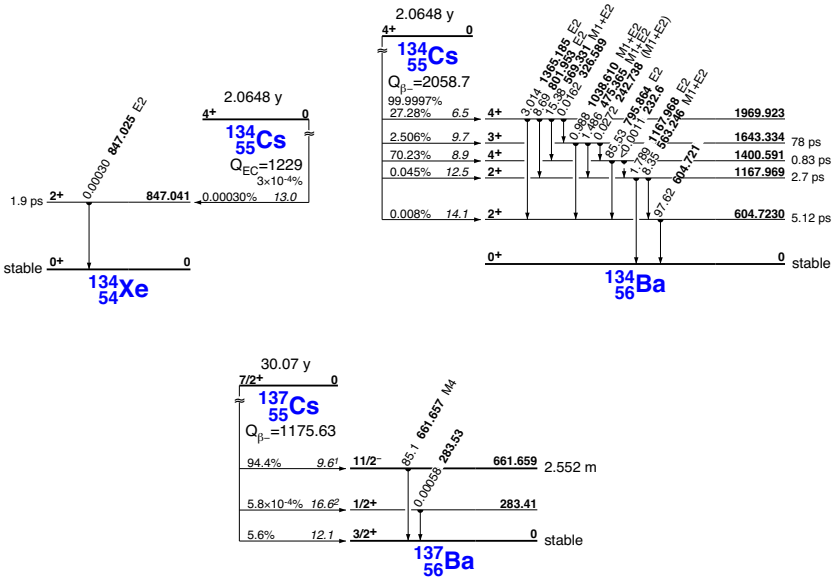

Figure 8.16.: Level diagram for ^{134}Cs and ^{137}Cs

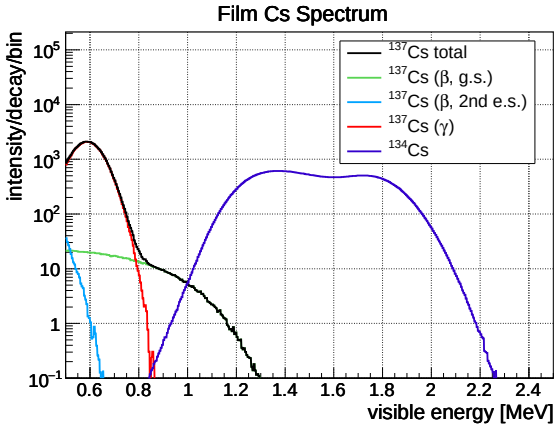

Figure 8.17.: Expected visible energy spectrum for ^{134}Cs and ^{137}Cs with 0.5 MeV analysis energy threshold.

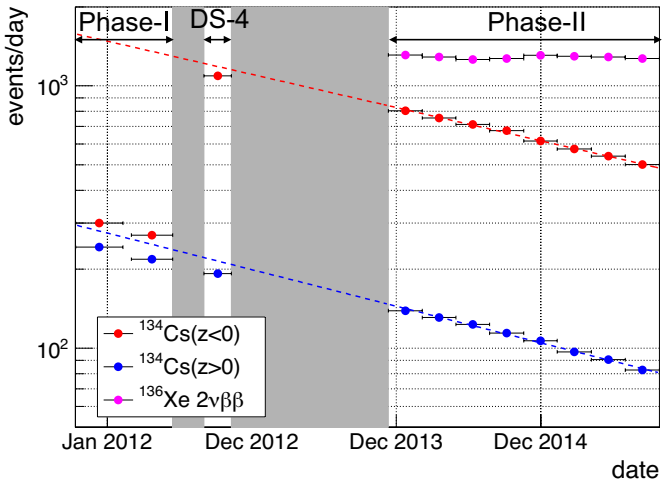

Figure 8.18.: Event rate trend of film ^{134}Cs and $2\nu\beta\beta$ in all volume for 3 period: Phase-I, Phase-II and Xe-depleted phase (DS-4). Each rate is extracted from simultaneous fit to the energy spectra. Shaded region indicates under LS circulation. Dashed lines are decay curve expected from the trend of Phase-II. The best-fit 2.16 ± 0.10 yr (blue) and 2.38 ± 0.11 yr (red) are consistent with ^{134}Cs half-life (2.06 yr). Rate of Phase-I refers (Yoshida, 2014 [39]). ^{134}Cs activity in the lower IB increased approximately fourfold by the contamination during LS purification,

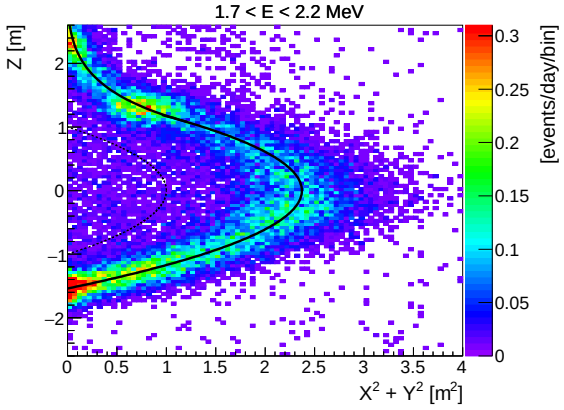

Figure 8.19.: Vertex distribution of single events in phase-I ($1.7 < E < 2.2$ MeV).

8.6. Spallation Products Induced by Muon

Muon-initiated nuclides are categorized into light isotopes produced by spallation of ^{12}C which is the most abundant nucleus heavier than ^{1}H in the LS, and heavy isotopes produced by spallation of ^{136}Xe which is the target of double-beta decay. Production rate of the former can be measured using powerful statistics, but the latter is mainly inferred by MC simulation because of no previous measurement including other experiments. Estimation method of production rate for each nucleus is described.

8.6.1. Light Isotopes

Production rate for light isotopes are estimated separately for ^{11}C and for short-lived isotopes, ^{10}C, ^{6}He, ^{12}B and ^{8}Li.

^{11}C

^{11}C is produced by eight kinds of reactions of ^{12}C with muon and secondary particles such as $e^{\pm}$, γ, n, p and $\pi^{\pm}$ (Galbiati et al., 2005 [60]). γ rays and electrons are prominent secondaries for negatively charged muon at 260 GeV (the average energy at Kamioka), besides ^{12}C cross section for γ rays has giant dipole resonance around 25 MeV. Exchange reaction $^{12}\mathrm{C}(\gamma, n)^{11}\mathrm{C}$ dominates above 60 % of total production rate. Reaction with electrons is not so important, because direct interaction with electrons or positrons through a virtual photon namely $^{12}\mathrm{C}(e, e + n)^{11}\mathrm{C}$ is suppressed. In the previous KamLAND measurement (S. Abe, Enomoto, et al., 2010 [53]), (96.3 ± 2.0)% of produced ^{11}C accompanies a free neutron in the final state, and the residual is processed by $^{12}\mathrm{C}(p, d)^{11}\mathrm{C}$ and $^{12}\mathrm{C}(\pi^{+}, \pi + N)^{11}\mathrm{C}$.

Using the highly visible fraction, triple tagging of muon-neutron-^{11}C can be applied for estimation to constrain the production rate in the final spectral fit, though the events cannot be rejected due to long life of ^{11}C decay (τ = 29.4 min). Following selection criteria is applied into data before the KamLAND-Zen to avoid $2\nu\beta\beta$ events covering whole of the ^{11}C decay ($^{11}\mathrm{C} \rightarrow {}^{11}\mathrm{B} + e^{+} + \nu_e$) and subsequent positron annihilation as shown in Fig. 8.20.

- muon :
  normal muon identification (Sec. 7.3.4)
- neutron :
  at least one neutron identified with 2.225 MeV γ of capture energy for $10 \leq \Delta T <$ 2500 μs window.
- ^{11}C :
  - $R < 3.5$ m
  - $1.4 \leq E < 2.0$ MeV
  - reject the first 5 h of the typical 24-hours run to avoid inefficiencies.

ΔT indicates time difference from muon. The number of ^{11}C is extracted from the likelihood fit to the ΔT distribution for events satisfying above criteria. Fig. 8.21 shows background-subtracted energy spectrum and ΔT distribution of ^{11}C decay. Thus, production rate is estimated to be (1106 ± 178) (kton·day)$^{-1}$ after corrections of energy cut and neutron detection efficiency. Taking account of 22 % uncertainty of spallation neutron yield caused by existence of xenon target, the error results $\sqrt{(16\%)^2 + (22\%)^2} = 27\%$, corresponding to 299 (kton·day)$^{-1}$. These values are used in the spectral fit.

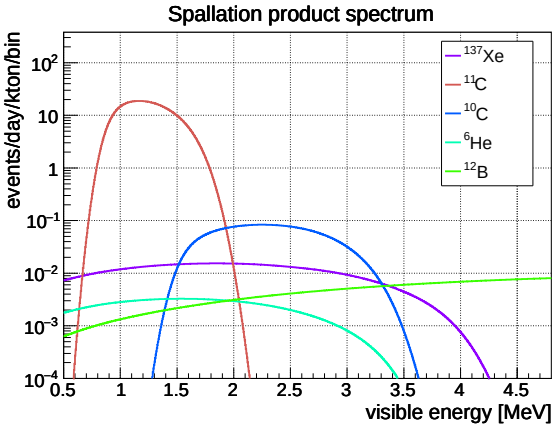

Figure 8.20.: Expected visible energy spectrum for spallation products scaled by the evaluated rates.

^{10}C, ^{6}He, ^{12}B, ^{8}Li

For short-lived products relative to ^{11}C, ^{10}C is the main background of $0\nu\beta\beta$ region with small contribution from ^{6}He, ^{12}B and ^{8}Li, which are produced by secondary particles such as neutron and pion when passing through a ^{12}C target. Expected energy spectra of these nuclides are shown in Fig. 8.20. They are partly rejected by triple coincidence method described in Sec. 7.3.4. Their tagging efficiencies are estimated all together by fitting summation of their exponential decay curves like follows:

$$\frac{dN}{dt} = \sum_i N_i e^{-t/\tau_i} + c \tag{8.4}$$

It is converted by defining $x = \log_{10} t$ like following:

$$\frac{dN}{dx} = \sum_i N_i \cdot \ln(10) \cdot 10^x \mathrm{e}^{-10^x/\tau_i} + c \cdot \ln(10) \tag{8.5}$$

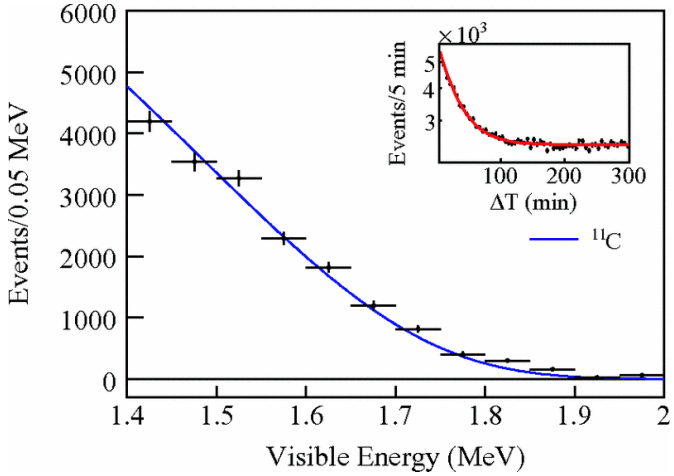

Figure 8.21.: Background-subtracted energy spectrum and ΔT distribution of ^{11}C decay. For energy spectrum, on-time and off-time events are selected from $5 \leq \Delta T < 90$ min and $185 \leq \Delta T < 270$ min, respectively. Binned maximum likelihood fit results χ^2d.o.f = 76/57 (S. Abe, Enomoto, et al., 2010 [53]).

where,

$$\begin{aligned} t &: \text{time difference from the last muon [s]} \\ N_i &: \text{production rate of } i\text{-th spallation isotope} \\ \tau_i &: \text{mean lifetime of } i\text{-th spallation isotope} \\ c &: \text{accidental background rate} \end{aligned} \tag{8.6}$$

Optimal rates are given by likelihood fit to time distribution from muon with Eq. 8.5, floating focused N_i with fixed lifetime τ_i listed in Table. 8.5. For 26 energy bins in 2.2 $< E <$ 15.2 MeV, fit with time window (-2.5 $< x <$ 2.5) is implemented simultaneously. Accidental rate floats in each energy bin. Event selection of spallation event is as follows.

1. muon :
   - normal muon identification (Sec. 7.3.4)
   - LS muon : $Q_{17} >$ 40,000 p.e.
     - showering muon : $\Delta Q > 10^6$ p.e.
     - non-showering muon : $\Delta Q < 10^6$ p.e., $\Delta L <$ 1 m
2. neutron : $\Delta R <$ 1.6 m (defined in Sec. 7.3.4)
3. spallation isotopes : $2 < R <$ 3.5 m (out of Xe-LS)

ΔQ is the residual charge defined at Eq. 5.7. ΔL indicates distance of spallation event from muon track, used to reduce accidental events. Common ΔL cut efficiency is assumed for all nuclei, which is estimated to be (68.2 $\pm$ 3.6) % from ^{12}B events.

Table 8.5.: Short-lived spallation products induced by muons with their fit condition. Fixed rate is expressed for (showering muon, non-showering muon), respectively.

	Lifetime	Energy (MeV)		Condition	Fixed rate (events/day/kton)
^{10}C	27.8 s	3.65	$(\beta^+\gamma)$	floated	-
^{11}Be	19.9 s	11.5	(β^-)	fixed	1.0, 0.4
^{8}Li	1.21 s	16.0	$(\beta^-\alpha)$	floated	-
^{6}He	1.16 s	3.51	(β^-)	floated	-
^{8}B	1.11 s	18.0	$(\beta^+\alpha)$	fixed	2.9, 0.8
^{9}Li	257.2 ms	13.6	$(\beta^-\gamma n)$	fixed	2.4, 0.9
^{9}C	182.5 ms	16.5	(β^+)	fixed	3.6, 0.6
^{12}N	15.9 ms	17.3	(β^+)	fixed	1.7, 0.6
^{12}B	29.1 ms	13.4	(β^-)	floated	-

Fig. 8.22 shows the time distribution with fitted decay curve in one energy bin dominated by ^{10}C, ^{8}He and ^{12}B events. Estimated energy spectrum in each nuclei is also drawn with observed data, which demonstrates energy information is indispensable. Production rates induced by showering and non-showering muon are summarized in Table. 8.6, where more than 70 % of spallation events are induced by highly energetic muons. The reason why total rates for all muon falls below previous estimation (S. Abe, Enomoto, et al., 2010 [53]) in all nuclei, is unsolved. The rates are presumed to fall in xenon loaded LS moreover in the simulation against increase of spallation neutron. Although ^{10}C tagging efficiency is estimated to exceed 90 % in the MC simulation, it achieves only 64 % as shown in Table. 8.7. The most critical factor is suspected to be loss of spallation neutron getting buried in massive after pulses just after muon, which probably hinds the primary process, $^{12}\mathrm{C}(\pi^+, np)^{10}\mathrm{C}$. It will be improved by setting dedicated selection criteria or using correlation with muon track. Other inefficiencies are sufficiently low: ΔT cut inefficiency is calculated to be 0.2 % from ^{10}C decay curve, and energy cut inefficiency is estimated to be lower than 4 %. Untagged rates are conclusively given as shown in Table. 8.7, which remain as background. The error includes 22 % uncertainty for production rate of spallation neutron in Xe-LS. For ^{10}C, combining 14 % of fitting error, it is calculated to be $\sqrt{(14\%)^2 + (22\%)^2} = 26$ % of the untagged rate. These mean value and errors are used as constraints in the final fit.

Purity of ^{10}C products in events tagged by triple coincidence (Sec. 7.3.4) is confirmed in Outer-LS region with larger statistics. Fig. 8.24(a) shows background subtracted energy distribution with expected visible energy spectrum of ^{10}C in $2.0 < R < 3.5$ m (Outer-LS region). They are consistent within ^{10}C energy region ($2.2 < E < 3.5$ MeV). Fig. 8.24(b) is background subtracted space correlation between spallation isotope and the nearest

Table 8.6.: Production rate of short-lived light isotopes for showering muons ($dQ > 10^6$ p.e.) and non-showering muons ($dQ < 10^6$ p.e.). It is separated by the presence or absence of requirement of space correlation between free neutron and spallation nuclei. Each units is [events/day/kton]. For non-showering muon, Correction for ΔL cut efficiency estimated from ^{12}B events (68.2 ± 3.6 %) is applied.

	Showering muon		Non-showering muon	
	(w/ n)	(w/o n)	(w/ n)	(w/o n)
^{10}C	14.8 ± 0.8	20.6 ± 0.7	3.6 ± 0.4	8.0 ± 0.8
^{8}Li	14.3 ± 0.7	16.5 ± 0.3	3.0 ± 0.4	3.3 ± 0.3
^{6}He	7.8 ± 1.3	9.3 ± 0.6	3.6 ± 1.0	2.8 ± 0.5
^{12}B	33.2 ± 0.9	38.6 ± 0.4	9.5 ± 0.7	11.3 ± 0.7

Table 8.7.: Production rate of short-lived light isotopes for all muons including showering and non-showering muons. Tagging efficiency of the isotopes by triple tagging method is defined as the ratio of "production rate for all muons w/ neutron requirement" to "production rate for all muons w/o neutron requirement". Untagged events remains as candidate events for double-beta decay analysis.

	All muon(w/ n) (kton·day)$^{-1}$	All muon(w/o n) (kton·day)$^{-1}$	Tagging efficiency (%)	Untagged rate (kton·day)$^{-1}$
^{10}C	18.4 ± 0.9	28.6 ± 1.1	64 ± 4	10.1 ± 2.6
^{8}Li	17.3 ± 0.8	19.8 ± 0.4	87 ± 4	2.5 ± 1.1
^{6}He	11.4 ± 1.6	12.1 ± 0.8	94 ± 15	0.7 ± 1.8
^{12}B	42.7 ± 1.1	49.9 ± 0.8	86 ± 3	7.2 ± 2.1

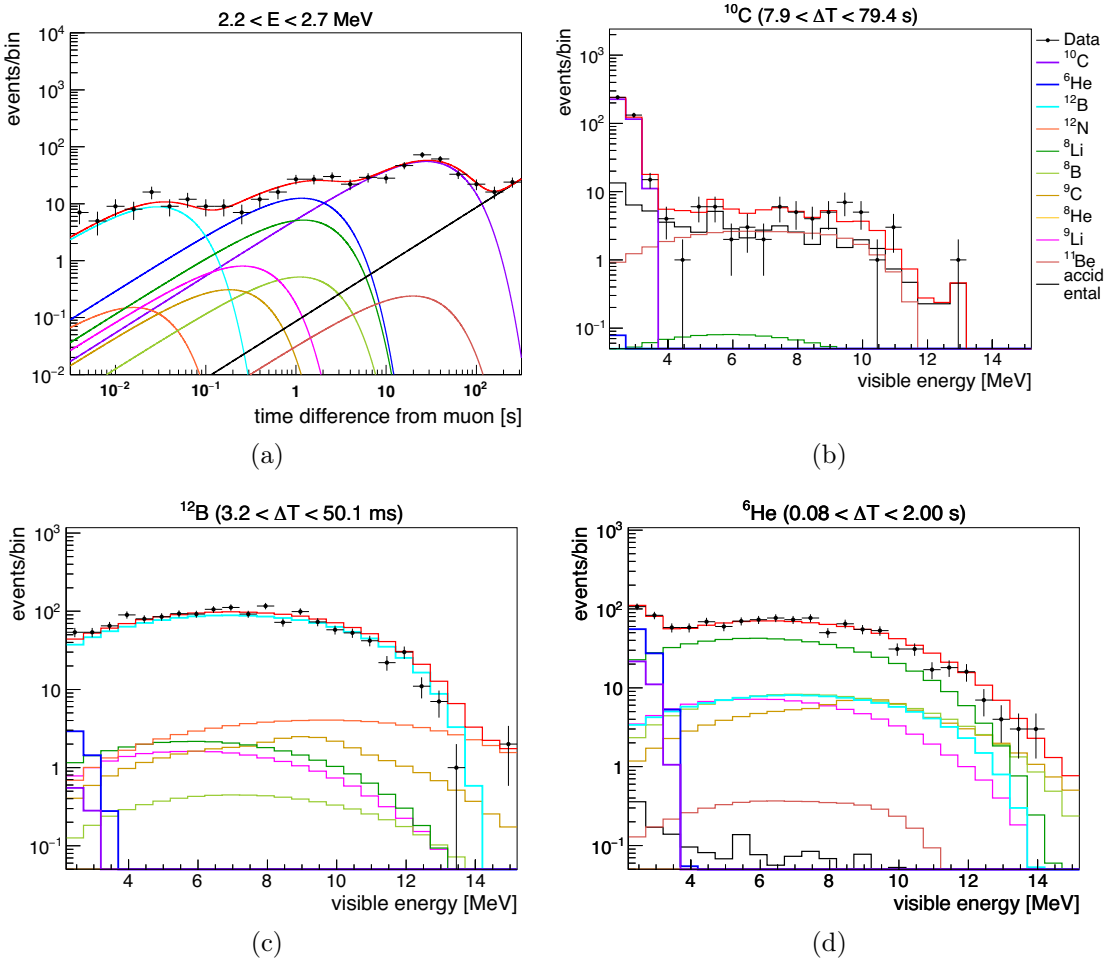

Figure 8.22.: Fit to the time distribution for light spallation products. Red line in each figure is the total expected distribution to be compared with the data. (a) Time distribution for showering muons in one energy bin ($2.2 < E < 2.7$ MeV) dominated by ^{10}C, ^{6}He and ^{12}B. (b) energy spectrum in $7.9 < \Delta T < 79.4$ s dominated by ^{10}C and ^{11}Be. (c) energy spectrum in $3.2 < \Delta T < 50.1$ ms dominated by ^{12}B. (d) energy spectrum in $3.2 < \Delta T < 50.1$ ms dominated by ^{6}He and ^{8}Li.

neutron in ^{10}C energy region. Approximately 98 % of tagged events are observed within $\Delta R < 160$ cm, relative to events in $\Delta R < 250$ cm. Comparing with total events, the inefficiency is below 4 % at 1σ. Fig. 8.24(c) shows time difference of tagged events from muon in ^{10}C energy region. Events at the first bin are dominated by short-lived nuclei. ^{10}C production rate, (21.8 ± 1.1) events/day/kton given by fitting with ^{10}C decay curve (red line) is almost consistent with the result (18.4 ± 0.9) events/day/kton introduced by simultaneous fitting of ΔT and energy (Table. 8.7), and with previous measurement in KamLAND: 21.1 ± 1.8 events/day/kton (S. Abe, Enomoto, et al., 2010 [53]). In Xe-LS region within 1-m-radius, 30 events are rejected as shown in Fig. 8.23).

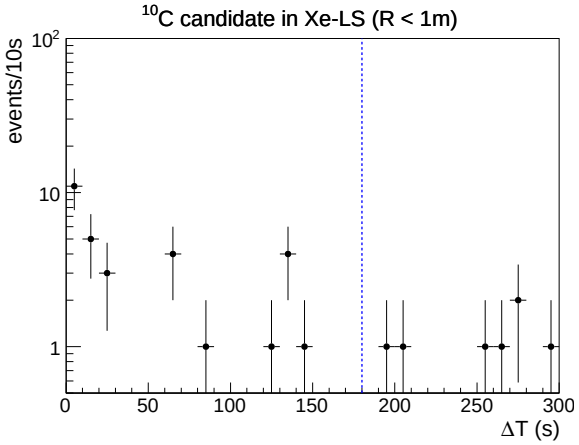

Figure 8.23.: ΔT distribution of ^{10}C candidate events in Xe-LS within 1-m-radius, with cut for ^{10}C energy region ($2.2 < E < 3.5$ MeV). 30 events are rejected by ΔT threshold (dotted blue line).

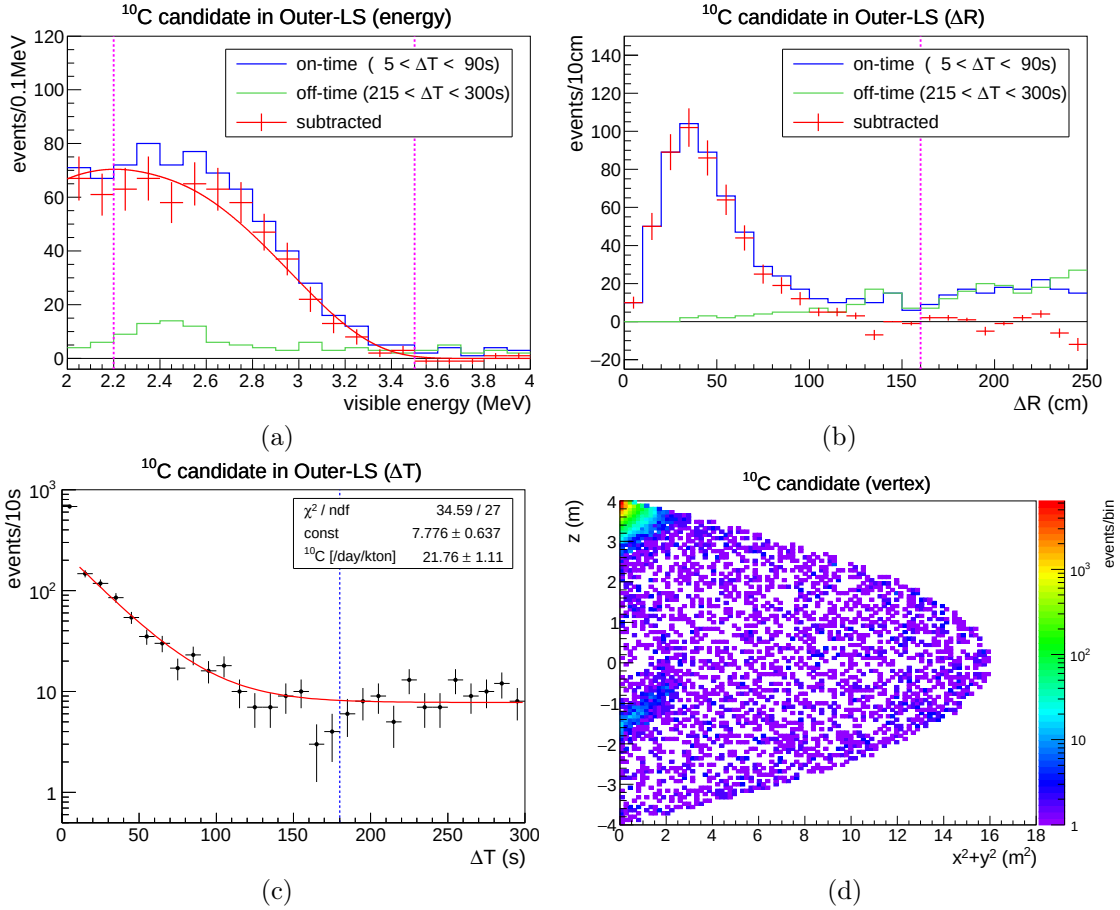

Figure 8.24.: ^{10}C candidate events tagged by the triple coincidence method. (a) Background subtracted energy distribution with expected visible energy spectrum of ^{10}C (red line) in $2.0 < R < 3.5$ m. They are consistent within ^{10}C region surrounded by dotted magenta lines ($2.2 < E < 3.5$ MeV). (b) Background subtracted space correlation between spallation isotope and the nearest neutron in ^{10}C energy region. Approximately 98 % of tagged events are observed within the cut threshold written with dotted magenta line ($\Delta R < 160$ cm), relative to events in $\Delta R < 250$ cm. (c) Time difference of tagged events from muon in ^{10}C energy region and in Outer-LS region. Dotted blue line indicates ΔT cut threshold. ^{10}C production rate, (21.8 ± 1.1) events/day/kton given by fitting with ^{10}C decay curve (red line) is almost consistent with the result (18.4 ± 0.9) events/day/kton introduced by simultaneous fitting of ΔT and energy. (d) Vertex distribution of tagged events in ^{10}C energy region within 4-m-radius.

8.6.2. Heavy Isotopes

Massive Xe atoms in LS become spallation target, which produces various kinds of heavy isotopes. There exists potential backgrounds involved in $0\nu\beta\beta$ energy region. From previous simulation, contributive background is narrowed down to ^{137}Xe. In order to estimate other contributions, MC simulation with abundant events is implemented.

^{137}Xe

^{137}Xe is primarily produced by thermal neutron capture on ^{136}Xe. This production rate is calculated from spallation neutron flux and capture cross section, since we have no significant observation of ^{137}Xe in KamLAND. The neutron flux in Xe-LS is estimated to increase (20 ± 2) % more than that of outer-LS, due to existence of xenon target. And capture rate is calculated by taking other components listed in Table. 8.9 into consideration, that is $R_i = N_i\sigma_i / \sum_i N_i\sigma_i$ (i : ^{1}H, ^{12}C, ^{136}Xe, ^{134}Xe). N_i is the number of target per unit of Xe-LS mass, and σ_i is capture cross section for $i-$th nucleus. Capture ratio of ^{137}Xe relative to neutron yield is obtained as $R_i(^{136}\mathrm{Xe}) = 0.011$ %. Consequently, ^{137}Xe production rate is estimated to be $(3.9 \pm 2.0)\times10^{-3}$ (ton·day)$^{-1}$, which includes 22 % error from neutron flux and capture cross section detailed in (Albert, Daugherty, et al., 2016 [61]). This value is used as its constraint in the spectral fit for $0\nu\beta\beta$ search. This production rate is consistent with expectation from FLUKA simulation, described below.

FLUKA Simulation

In order to confirm ^{137}Xe production rate and to estimate smaller contribution, FLUKA simulation is implemented. It models nuclear and particle physics from thermal neutrons to heavy-ion collisions (Battistoni et al., 2007 [62]); (Ferrari et al., 2005 [63]). In the simulation, simplified detector geometry is installed, where only cubic Xe-LS with 40-m-thickness is placed. It is composed of CH_2 0.768 g/cm^3 (97.04 %) and ^{136}Xe (2.96 %), neglecting ^{134}Xe atoms. Energy of injected muons is calculated by MUSIC simulation code (Antonioli et al., 1997 [64]), which evaluates muon energy spectrum at the KamLAND site by considering the slant depth, rock type, and density. 10^7 muons are injected to one direction. Production rate is calculated by counting survived products and hydrogen capture γ.

Fig. 8.25 shows simulated production rates of all generated isotopes (including elastic scattering). There are two clusters around main Xe-LS components, ^{136}Xe and ^{12}C. Adding to ^{137}Xe and ^{10}C, ^{110m}Ag, ^{88}Y and ^{60}Co are greatly concerned isotopes, since they have decay energies very close to 0ν region. As shown in Table. 8.8, all of them indicate finite production yields, although it cannot distinguish ^{110}Ag meta stable from other states. ^{110}Ag and ^{60}Co are directly produced and ^{88}Y is generated by radioactive decay of parents, ^{88}Zr and ^{88}Nb. Further upstream parents, ^{88}Mo and ^{88}Tc are not produced. The production yield of ^{110m}Ag, ^{88}Y and ^{60}Co are significantly low, which is $\sim$1/300 of ^{137}Xe at most.

	$(N-Z, Z)$	production rate $[\times 10^{-7}\mu^{-1}\mathrm{g}^{-1}\mathrm{cm}^2]$	primary process
^{137}Xe	(29,54)	3.070 ± 0.044	$^{136}\mathrm{Xe}(n,\gamma)$
^{110}Ag	(16,47)	$(6.43 \pm 2.03)\times 10^{-3}$	directly produced
^{88}Y	(10,39)	$(9.7 \pm 2.5)\times 10^{-3}$	^{88}Zr, ^{88}Nb
^{88}Zr	(8,40)	$(3.99 \pm 0.5)\times 10^{-2}$	-
^{88}Nb	(6,41)	$(9.0 \pm 2.4)\times 10^{-3}$	-
^{88}Mo	(4,42)	0	-
^{88}Tc	(2,43)	0	-
^{60}Co	(6,27)	$(6.4 \pm 6.4)\times 10^{-4}$	directly produced
^{60}Fe	(8,26)	0	-
^{60}Mn	(10,25)	0	-
^{60}Cr	(12,24)	0	-
^{10}C	(-2,6)	10.96 ± 0.08	$^{12}\mathrm{C}(\pi^+, np)$

Table 8.8.: Simulated production yield for heavy isotopes and ^{10}C. It counts products without distinction of energy state. Using FLUKA simulation, 10^7 muons are injected to cubic Xe-LS. ^{137}Xe production yield is consistent with estimation from thermal neutron capture cross section. As to greatly concerned isotopes i.e. ^{110m}Ag, ^{88}Y and ^{60}Co, at least one is produced, although the production of ^{110m}Ag is unknown. ^{110}Ag and ^{60}Co are directly produced and ^{88}Y is generated by radioactive decay of parents, ^{88}Zr and ^{88}Nb.

In conclusion, contribution of these three nuclei are negligible. ^{88}Y will become a future background after substantial ^{10}C rejection. And ^{137}Xe production yield is consistent with estimation from thermal neutron capture cross section. In the simulation, 260.65 mbarn is adopted (Mughabghab, 2006 [65]).

8.7. Potential Backgrounds

In Phase-I data, unexpected background was found having 2.6 MeV peak near the 2.458 MeV Q-value of ^{136}Xe $\beta\beta$ decay, and distributed in Xe-LS uniformly. By searching all possible decay, candidates were narrowed down to 4 nuclei: ^{110m}Ag, ^{208}Bi, ^{60}Co and ^{88}Y shown in Fig. 8.27. In this section, following topics are described: search for candidate source of the peak in Phase-I, their reduction by purification and treatment in double-beta analysis.

Table 8.9.: Capture ratio of thermal neutron in Xe-LS calculated from each number of target and cross section (Shibata et al., 2011 [66]); (Albert, Daugherty, et al., 2016 [61]).

	E_γ [MeV]	σ [mb]	Number/g	Capture ratio in Xe-LS	
^{1}H	2.225	332.0	8.31051×10^{22}	99.32	%
^{12}C	4.946	3.86	4.16849×10^{22}	0.57	%
^{136}Xe	4.026	238	1.17212×10^{20}	0.10	%
^{134}Xe	6.364	265.1	1.15686×10^{19}	0.011	%
total	-	-	-	100.0	%

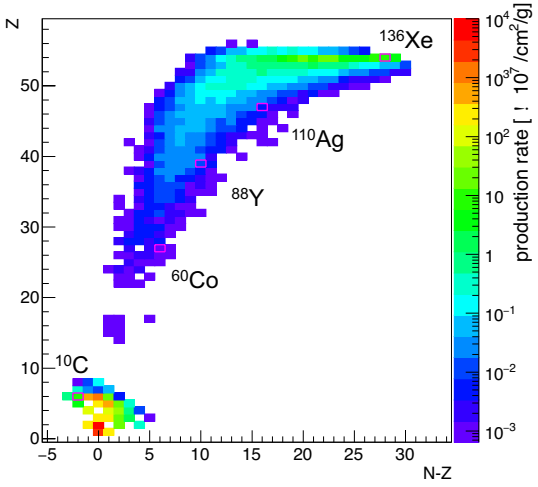

Figure 8.25.: Simulated production yield of all products. The horizontal axis is difference of neutron number and atomic number and the vertical axis is atomic number. Bins enclosed in magenta lines indicate important or potential backgrounds for $0\nu\beta\beta$ analysis, i.e. ^{137}Xe and ^{10}C, ^{110m}Ag, ^{88}Y and ^{60}Co.

8.7.1. Search for Candidate Source

In $0\nu\beta\beta$ decay (Q-value = 2.458MeV) region, ∼2.6 MeV peak distributed in Xe-LS uniformly was found. There was possibility that it is introduced on the detector modification or induced by muon spallation, contribution except for the signal was confirmed more than 5σ C.L.. Background was searched from all nuclei listed in ENSDF database ([67]) including all secondaries. From the condition that it has $2.4 - 2.8$ MeV peak for visible energy spectra applied detector nonlinear energy response, and has more than 30 days ancestor lifetime, the candidate was narrowed down to 4 nuclei;

- ^{110m}Ag (β^- decay, τ =360 day, Q = 3.01 MeV)
- ^{208}Bi (EC decay, τ =5.31×10^5 yr, Q = 2.88 MeV)
- ^{88}Y (EC decay, τ =154 day, Q = 3.62 MeV)
- ^{60}Co (β^- decay, τ =7.61 yr, Q = 2.82 MeV)

^{60}Co is excluded for the reason that $0\nu\beta\beta$ decay is more favored in a χ^2 test of energy spectrum. ^{208}Bi can be produced environmentally or artificially. In the former case, it is supplied from a natural isotope ^{209}Bi, however its contamination in Xe-LS is beyond detection sensitivity limit of ICP-MS measurement. In the latter case, ^{208}Bi should accompany ^{207}Bi contamination originated in the past nuclear tests, but only upper limit is obtained. Hence ^{208}Bi is excluded as a dominant contributor. ^{88}Y is also strongly suppressed by its shorter lifetime, though it can be produced as a cosmogenic nuclide by Xe spallation.

The most probable nuclei is ^{110m}Ag favored at χ^2 tests in both energy and time spectrum (Fig. 8.26), and hypothesis of no contribution from ^{110m}Ag is excluded above 3σ C.L. (A. Gando et al., 2012 [42]). ^{110m}Ag is thought to be produced in Xe bottles during its aerial transportation then supplied into Xe-LS on Xe dissolving, the validness is supported by a simulating of 1 GeV cosmic-ray proton and ^{136}Xe interaction. ∼2.6 MeV peak is also found along the IB, ^{110m}Ag contamination originated from the Fukushima dai-ichi nuclear power plant accident cannot be excluded since ^{110m}Ag is detected from soil samples around the IB fabrication area.

8.7.2. ^{110m}Ag

^{110m}Ag was the most favored as the dominant background in comparison of time and energy spectra. As the origin of its contamination, following two ways are suspected; one is production from Xenon spallation by cosmic-ray under airfreight of its gas bottles, and the other is fallout from FNPP1 accident like cesium. ^{110m}Ag rate including ^{208}Bi, ^{60}Co and ^{88}Y was evaluated to be 0.20 ± 0.03 (ton·day)$^{-1}$ with DS-1 (A. Gando, 2012 [40]). To reduce these backgrounds, LS and Xe purification was carried out as described in Sec. 4.8.

How ^{110m}Ag decreased holds the key to the $0\nu\beta\beta$ decay search sensitivity. It is estimated from Fig. 8.28. Fig. 8.28(a) plots energy spectra before purification (DS-1) and

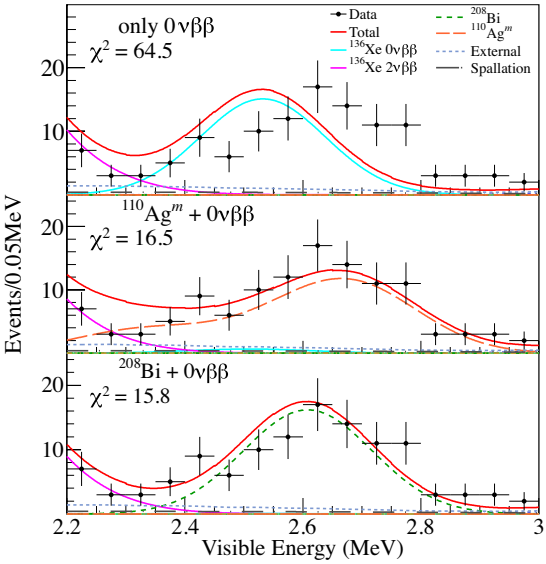

(a) Energy spectrum (A. Gando et al., 2012 [68])

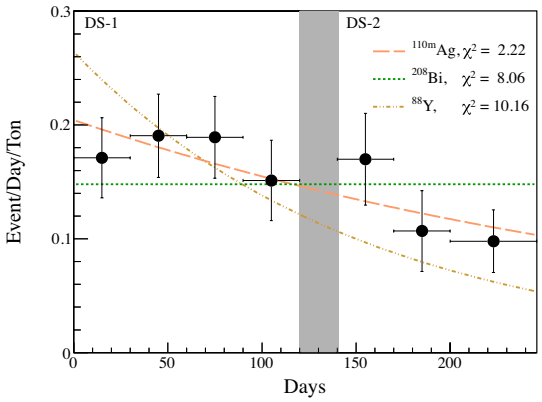

(b) Time spectrum (A. Gando, Y. Gando, Hanakago, Ikeda, Inoue, Ishidoshiro, Kato, et al., 2013 [44])

Figure 8.26.: Energy and time spectra of $0\nu\beta\beta$ energy region in Phase-I. (a) Energy spectra assuming only $0\nu\beta\beta$ (top), $0\nu\beta\beta$+^{110m}Ag (middle), and $0\nu\beta\beta$+^{208}Bi (bottom) with χ^2 in $2.2 < E < 3.0$ MeV using part of DS-1 data. No background hypothesis is excluded more than 5σ C.L.. (b) Time spectrum in $2.2 < E < 3.0$ MeV after known background subtraction, with fit results by ^{110m}Ag, ^{208}Bi and ^{88}Y decay curves assuming no background reduction by filtration work (shaded region).

after purification (Phase-II) in R <1 m, which shows considerable decrease of ^{110m}Ag, including radioactive decay with $T_{1/2}$ = 250 days. Reduction by purification can be expected from Fig. 8.28(b). Time variation in ^{110m}Ag energy region is drawn from the beginning of Phase-I to the end of Phase-II. For reference, ^{110m}Ag decay curve is drawn assuming initial value as primary observed rate 0.55 events/day and constant term by other backgrounds 1.8×10^{-2} events/day estimated with Phase-II. It seems to support no reduction effect by purification.

However, inactivity in the latter half of Phase-II indicates effects of purification. The disagreement is likely to be due to convection: Fine particles including ^{110m}Ag sank to the IB bottom over the long term. In likelihood ratio test to verify ^{110m}Ag variable model, standard ^{110m}Ag decay model is rejected by 95 % C.L. . Spectrum fit using whole volume (R < 2 m) also supports the hypothesis. According to the estimation with two periods in Phase-II: Period-1 and Period-2 (divided by dashed line), Best-fit ^{110m}Ag is 15 ± 5 (kton·day)$^{-1}$ in Period-1, and 0 (kton·day)$^{-1}$ with upper limit < 3.1 (90% C.L.) in Period-2 even though standard decay expects ∼6 events/day. As a result, reduction factor of ^{110m}Ag is considered less than tenth part of original contamination including decay, which can expects improvement of $0\nu\beta\beta$ search sensitivity.

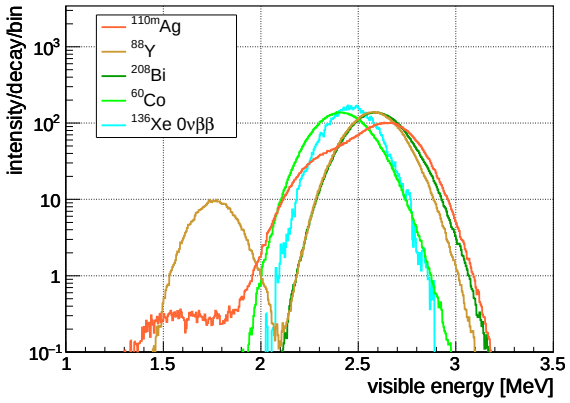

Figure 8.27.: Expected visible energy spectrum for potential backgrounds in Xe-LS (^{110m}Ag, ^{88}Y, ^{208}Bi, ^{60}Co) with $0\nu\beta\beta$ signal.

8.7.3. ^{208}Bi, ^{60}Co, ^{88}Y

Remaining candidate nuclei having 2.6 MeV peak namely ^{208}Bi, ^{60}Co, ^{88}Y are still taken into account as potential background, though they are undetected. Upper-limits obtained from spectrum fit with ^{110m}Ag are <7.1, <4.3 and <6.3 (ton·day)$^{-1}$ for ^{208}Bi, ^{60}Co and ^{88}Y, respectively. Every nucleus is disfavored compared to ^{110m}Ag. $0\nu\beta\beta$ decay search is performed in both cases that, only ^{110m}Ag contributes and that all four nuclei contribute.

As for ^{88}Y, it can be regarded as negligible considering the lifetime (τ = 154 day). Even if 10% of ^{110m}Ag was observed as ^{88}Y in Phase-I, expected events in Phase-II is less than 1 events in the whole volume. As discussed in Sec. 8.6. it can be produced

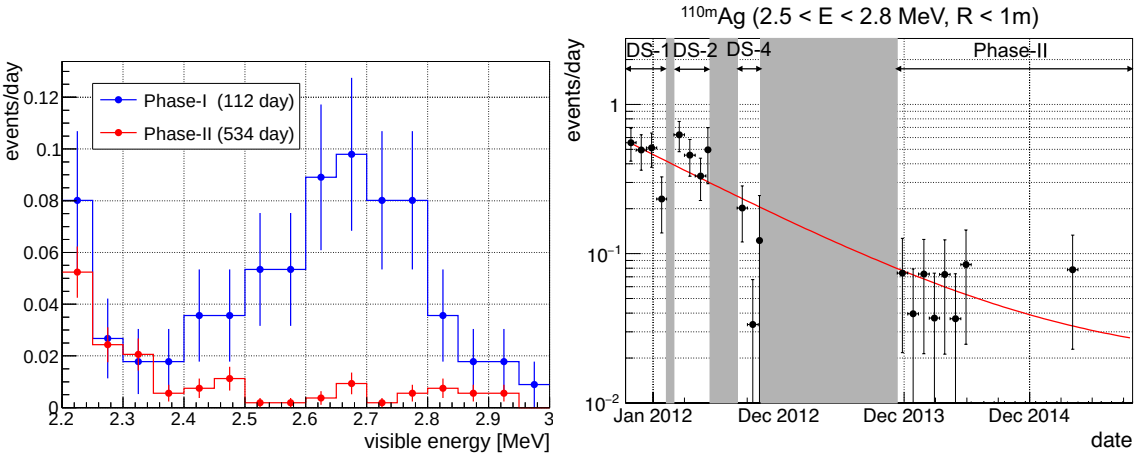

(a) Energy spectrum ($R < 1$ m) (b) Time variation

Figure 8.28.: Energy spectrum and time variation of ^{110m}Ag. (a) Comparison of energy spectrum between before(blue) and after(red) purification. (b) Time variation in ^{110m}Ag energy window ($2.5 < E < 2.8$ MeV). Additional volume cut is applied for DS-2 and DS-4 to avoid backgrounds from a stainless-steel inlet located at $z \sim$-1.2m. It makes their rate slightly high. For reference, ^{110m}Ag decay curve assuming initial rate as 0.55 events/day is drawn with a red line.

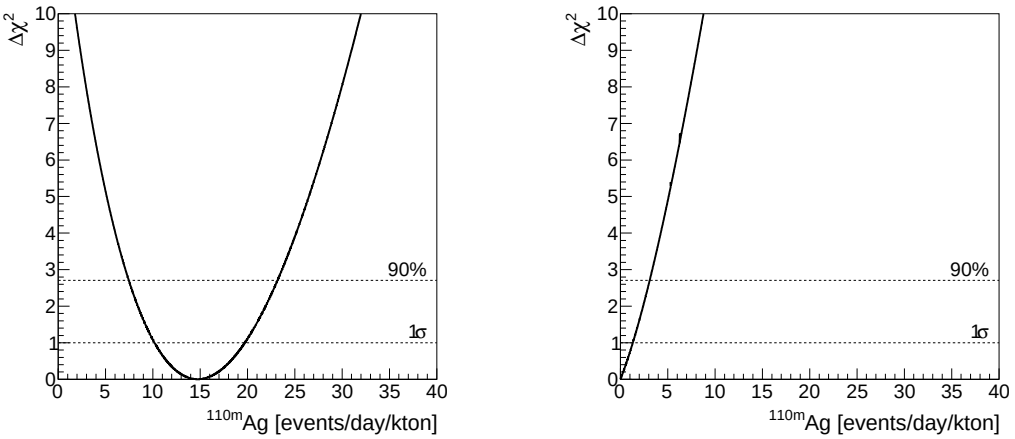

(a) Period-1 (b) Period-2

Figure 8.29.: $\Delta\chi^2$ distribution of ^{110m}Ag rate in Xe-LS. The best-fit rate is 15 ± 5 (kton·day)$^{-1}$ in Period-1, and 0 (kton·day)$^{-1}$ with upper limit < 3.1 (90% C.L.) in Period-2.

by muon spallation in the Xe-LS, but the contribution is much less than ^{10}C spallation background so far.

9. Double-Beta Decay Analysis

Contribution of signals are extracted by subtracting background contributions via spectral fit in optimized fiducial volumes. In this chapter, selection of fiducial volume and fitting procedure are described. (Procedure of $2\nu\beta\beta$ decay measurement is slightly different with $0\nu\beta\beta$ search.) And neutrino mass constraints based on half-life limit of $0\nu\beta\beta$ decay are discussed and compared with results from other experiments.

9.1. Fiducial Volume Selection

Signal and background events distributes uniformly in the Xe-LS, or along the 1.54-m-radius IB. In the further external region, connecting tube between the IB and the corrugated pipe located at $Z \sim 4.3$ m is strong background source. By taking account of these backgrounds, fiducial volume is optimized to maximize the sensitivity of $0\nu\beta\beta$ and $2\nu\beta\beta$, respectively.

9.1.1. Spherical Cut

Fig. 9.1 shows energy spectrum in each radius cut. Film backgrounds such as ^{137}Cs ^{134}Cs, ^{214}Bi, and ^{208}Tl dominates over the whole energy range in the external region, and the contribution in lower hemisphere is more than in upper hemisphere. ^{214}Bi from the IB is one of primary background in $0\nu\beta\beta$ energy window partitioned with dotted lines in Fig. 9.1. To evaluate the background tail in the internal region, whole Xe-LS region should be included. On the other hand, in $2\nu\beta\beta$ energy window below 2 MeV, systematic uncertainty originated from massive film backgrounds such as ^{134}Cs and ^{137}Cs overcomes statistics of $2\nu\beta\beta$. To reduce such large systematic uncertainties, the external region is rejected. Thus each radius cut is determined like below.

- $0\nu\beta\beta$ analysis : $R < 2$m, 16.68 ± 0.07 m^3 (Xe-LS)
- $2\nu\beta\beta$ analysis : $R < 1$m, 4.19 m^3

Total XeLS within the fiducial volume, 16.68 m^3 is measured amount of LS by a flowmeter when the IB was pulled out of the KamLAND detector after the end of Phase-II.

9.1.2. Fiducial Volume Uncertainty

$2\nu\beta\beta$ analysis uses a part of Xe-LS. Therefore, it needs to take account of the systematic uncertainty from vertex resolution and vertex reconstruction, which is calculated as count

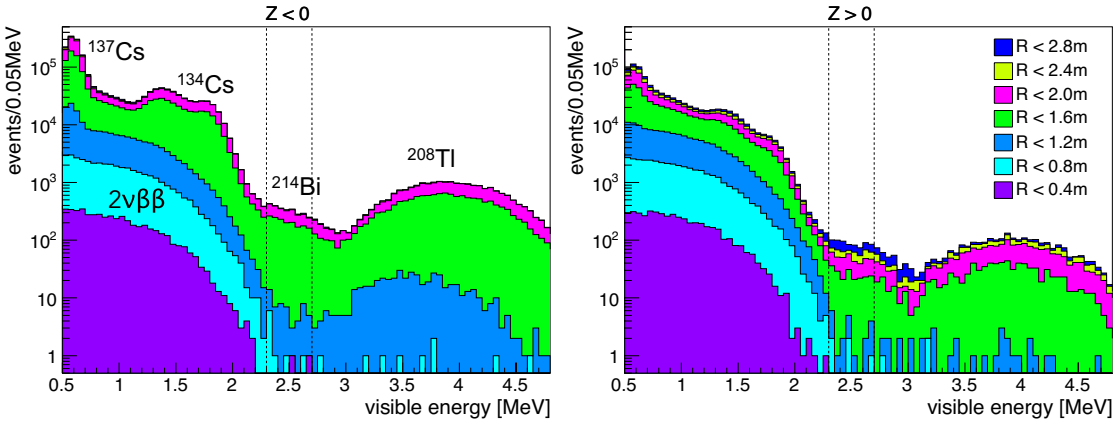

Figure 9.1.: Energy spectrum in each radius cut for (a) lower and (b) upper hemisphere. Backgrounds from the IB dominates around $R \sim$1.5 m.

ratio R_{count} defined as follows.

$$\begin{aligned} R_{\text{count}} &= \frac{\text{the number of } ^{214}\text{Bi events in } R < 1 \text{ m}}{\text{the number of } ^{214}\text{Bi events in } R < 4 \text{ m}} \\ &= 0.253 \pm 0.005(\text{stat}) \pm 0.001(\text{c, syst}) \end{aligned} \tag{9.1}$$

^{214}Bi event is uniformly distributed events in Xe-LS originated from initial ^{222}Rn contaminated on dissolving of Xe. They are tagged by the delayed coincidence method with 3 parameters: $0.4 < E_{\text{d}} < 1.2$ MeV, $\Delta R < 1$m, $5 < \Delta T < 1000$ us with additional cut (-4 $< Z <$ 2 m) to avoid backgrounds from connecting tube. 4-m-radius cut larger than total Xe-LS volume is to include all detected events in Xe-LS as possible. Thus systematic error of R_{count} denoted as (c, syst) is broken down into tagging efficiency and 4-m-radius cut inefficiency.

Measurement error of Xe-LS volume is also included as R_{volume}:

$$\begin{aligned} R_{\text{volume}} &= \frac{\text{1-m-radius spherical volume}}{\text{total Xe-LS volume by measurement}} \\ &= \frac{4.19}{16.68 \pm 0.17} \\ &= 0.251 \pm 0.0026(\text{v, syst}) \end{aligned} \tag{9.2}$$

According to equivalence between R_{count} and R_{volume}, total fiducial volume uncertainty is defined as the deviation of two values, resulting 3.0 %.

$$\begin{aligned} (\text{FV error}) &= \left| \frac{R_{\text{count}} - R_{\text{volume}}}{R_{\text{volume}}} \right| \\ &= \frac{(0.002 + 0.005(\text{stat})) \oplus 0.0026 \oplus (\text{v, syst}) 0.001 \oplus (\text{c, syst})}{0.251} \\ &= 0.030 \end{aligned} \tag{9.3}$$

Table 9.1.: Fiducial volume uncertainty for $2\nu\beta\beta$ analysis

Radius cut	$R < 1$ m
Volume ratio (R_{volume})	0.251 ± 0.003 (syst)
Event ratio (R_{count})	0.253 ± 0.005 (stat) ± 0.001 (syst)
FV uncertainty	3.0 %

In case of $0\nu\beta\beta$ analysis, the uncertainty is not dominative because of large statistical error more than 10 %. The error is conservatively same as $2\nu\beta\beta$, 3.0 %.

9.2. Number of Targets

Number of ^{136}Xe targets is estimated from mass of xenon dissolved in the LS and enrichment factor of ^{136}Xe.

9.2.1. Xe Mass

Xe dissolved in the Xe-LS is evaluated from "amount of dissolution" and "recovered amount".

from Dissolution Xe mass dissolved in Phase-II is given as subtraction of leftover amount from original mass before dissolving as listed below. Each value is measured by weight scale or gas chromatography.

- initial Xe mass : 411.5 ± 1.0 kg
- residual Xe amount : 28.7 ± 1.8 kg
  - in Xe system : 25.3 ± 1.5 kg
  - in cylinder bundle : 1.0 ± 1.0 kg
  - in LS tank area : 2.4 ± 0.4 kg
- → Xe mass in the IB : 382.8 ± 2.1 kg (dissolution)

from Extraction Dissolved Xe was degassed just after the end of Phase-II. The recovered amount is not necessarily equivalent to Xe mass in the IB, since it is possible to leak out during the data set. The potential loss is limited by the measurement of outer-LS sampled for Xe amount evaluation. Thus Xe mass from extraction is estimated as the summation of the recovered amount and potential wastage like bellow:

- extracted Xe amount : 377.9 ± 2.2 kg
  - in cylinder bundle : 368.3 ± 1.4 kg
  - in LS tank area : 7.0 ± 1.4 kg
  - in Xe system : 2.6 ± 1.0 kg

- potential loss amount : <0.5 kg
- → Xe mass in the IB : 378.4 ± 2.2 kg (extraction)

The mean value of Xe mass is derived as weighted average of above estimates. And its uncertainty is calculated as the root sum square of the error in extraction and deviation of mass in extraction from the average, namely $\sqrt{2.2^2 + (378.4 - 380.7)^2} = 3.2$ kg. Therefore, Xe mass dissolved in the Xe-LS is calculated to be $W_{\mathrm{Xe}} = (380.7 \pm 3.2)$ kg.

9.2.2. Xe Concentration

Mass concentration of Xe mass (W_{Xe}) in the Xe-LS is calculated using Xe-LS volume (16.75 m^3) and its density (780.13 $\mathrm{kg/m}^3$):

$$\begin{aligned} C_{\mathrm{Xe}} &= (\text{mass of Xe in total Xe-LS}) \ / \ (\text{mass of total Xe-LS}) \\ &= 380.7\ [\mathrm{kg}] \ / \ (16.75\ [\mathrm{m}^3] \cdot 780.13\ [\mathrm{kg/m}^3]) \\ &= (2.91 \pm 0.04)\ \% \end{aligned} \tag{9.4}$$

The 0.04 % error comes from error of xenon mass and total Xe-LS volume. 16.75 m^3 includes 0.07 m^3 of LS in the corrugated pipe, which is not used for analysis.

9.2.3. ^{136}Xe Abundance

Composition of enriched xenon gas is evaluated using a mass spectrometer calibrated with natural xenon gas. Isotopic abundances are measured to be $R_{^{136}\mathrm{Xe}} = (90.77 \pm 0.08)$ % for ^{136}Xe and (8.96 ± 0.02) % for ^{134}Xe, relative to natural abundance of 8.87 % for ^{136}Xe and 10.44 % for ^{134}Xe. Systematic uncertainty comes from database error and deviation of natural abundance between this measurement and referred values. The result gives relative atomic mass of enriched xenon gas ($\mathrm{RAM_{Xe}}$) as 135.716 u.

9.2.4. Number of ^{136}Xe

The number of target is calculated with Eq. 9.4, Avogadro constant N_A, $R_{^{136}\mathrm{Xe}}$ and $\mathrm{RAM_{Xe}}$ in the previous section:

$$\begin{aligned} \text{the number of } ^{136}\mathrm{Xe} &= (10^9[\mathrm{g}] \cdot C_{\mathrm{Xe}}\, R_{^{136}\mathrm{Xe}} \ / \ \mathrm{RAM_{Xe}}) \cdot N_A \\ &= (10^9 \cdot 0.0291 \cdot 0.9077/135.716) \cdot 6.022 \times 10^{23} \\ &= 1.17 \times 10^{29}\ (\text{kton of Xe-LS})^{-1} \end{aligned} \tag{9.5}$$

It indicates 344.1 kg of ^{136}Xe is contained in 13 tons of Xe-LS.

9.3. Spectral Fit

9.3.1. Fit Condition

Fit condition to evaluate signal and background rates is summarized as follows.

Table 9.2.: Summary of the Xe-LS information

Xe-LS density	780.13 kg/m^3
Xe-LS volume	(16.68 ± 0.17) m^3
Xe concentration	(2.91 ± 0.04) % by weight
isotopic abundance of ^{136}Xe	(90.77 ± 0.08) %
the number of ^{136}Xe	1.17×10^{29} kton^{-1}
uncertainty of Xe mass	0.8 %
uncertainty of ^{136}Xe abundance	0.04 %

- Run selection : the good runs and the half-bad runs
- $0\nu\beta\beta$ analysis :
  - Fiducial volume : 16.68 m^3 inside 2-m-radius (Xe-LS)
  - Energy range : $0.8 < E < 4.8$ MeV
- $2\nu\beta\beta$ analysis :
  - Fiducial volume : 4.19 m^3 inside 1-m-radius
  - Energy range : $0.5 < E < 4.8$ MeV

Data set

As shown in Fig. 9.2, remarkable background reduction of ^{110m}Ag is found in Phase-II, indicating variation of background in the $0\nu\beta\beta$ energy window, unlike Phase-I. Hence, Phase-II is divided into two-equal time periods, defined as Period-1 and Period-2. It is determined by taking account of ^{110m}Ag decay, and the length of each period is almost equal to its lifetime. The division allows not only a variable background model but also ^{110m}Ag standard decay. The $2\nu\beta\beta$ analysis uses a single data set because such variation is not found for the primary backgrounds. The condition of each data set is summarized in Table 9.3.

Table 9.3.: Summary of the Phase-II data. It is divided into Period-1 and Period-2 for the $0\nu\beta\beta$ decay analysis to deal with the irregular time variation of ^{110m}Ag background. For the $2\nu\beta\beta$ analysis, whole Phase-II is treated as a single period.

	Period-1	Period-2	Phase-II	
period		Dec. 11, 2013 - Nov. 17, 2014	Nov. 17, 2014 - Dec. 27, 2015	Dec. 11, 2013 - Dec. 27, 2015
livetime [days]		270.7	263.8	534.5
^{136}Xe exposure [kg-yr]	(all volume)	255.0	248.5	503.5
	($R < 1$m)	64.0	62.4	126.4

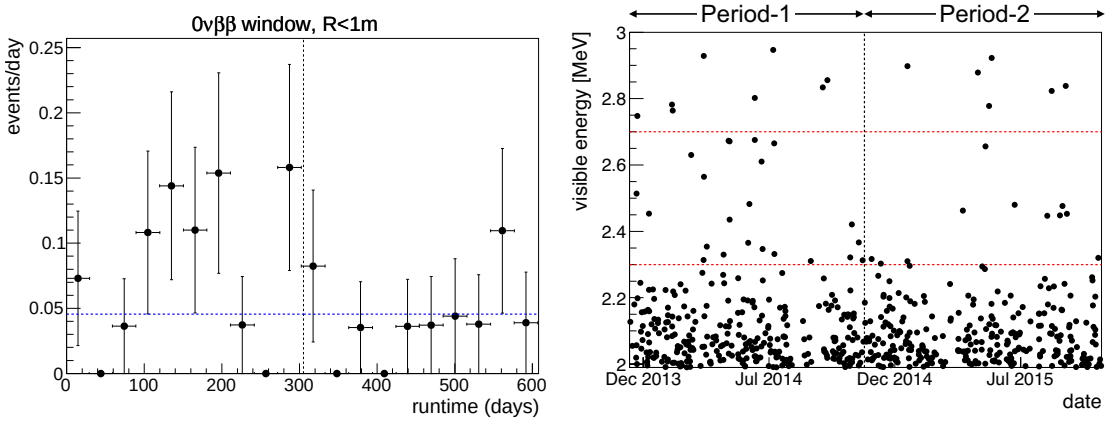

(a) (b)

Figure 9.2.: The time variation of event rate (a) and the energy dependence (b) of events in the $0\nu\beta\beta$ window in $R < 1$ m. The blue dotted line indicates background rate other than ^{110m}Ag (0.046 events/day in Period-1, 0.043 events/day in Period-2). The black dashed line is the border of two-periods. In the $0\nu\beta\beta$ window surrounded with the red dashed lines, 22 and 11 events are observed in Period-1 and Period-2, respectively.

9.3.2. Fit Method

Volume Bin

For the $0\nu\beta\beta$ analysis, both of the internal and external regions are used for the spectral fit. The former is sensitive to the $0\nu\beta\beta$ search, and the latter is useful to determine the ^{214}Bi film backgrounds correctly. These regions are separated into half spherical shells as shown in Fig. 9.9(b). Thus, a maximum likelihood fit is performed for the binned energy, radius and theta distributions. The vertical division into the upper and lower hemisphere allows non-uniformity of the IB film backgrounds as found in ^{214}Bi, ^{134}Cs and ^{208}Tl (see Sec. 8.3.1).

χ^2 Definition

Chi-square is defined for the binned spectra and constrained parameters, respectively.

$$\chi^2 = \chi^2_{\rm bin} + \chi^2_{\rm penalty} \tag{9.6}$$

Goodness of distribution models is tested using poisson chi-square like below.

$$\chi^2_{\rm bin} = \begin{cases} 2\sum_i \sum_j \sum_k \left[\nu_{ijk} - n_{ijk} + n_{ijk}\log(n_{ijk}/\nu_{ijk})\right] & (n_{ijk} \neq 0) \\ 2\sum_i \sum_j \sum_k \left[\nu_{ijk} - n_{ijk}\right] & (n_{ijk} = 0) \end{cases}$$

n_{ijk} and ν_{ijk} are observed and expected events for (i, j, k)-th bin identified by energy, radius and theta, respectively. Condition of each region is set as follows,

- energy bin: 0.05 MeV width
  - $0\nu\beta\beta$: $0.8 < E < 4.8$ MeV (i =1,2,..80)
  - $2\nu\beta\beta$: $0.5 < E < 4.8$ MeV (i =1,2,..86)
- radius bin:
  - $0\nu\beta\beta$: spherical shell divided into 20 equal-volume bins (j =1,2,..20)
  - $2\nu\beta\beta$: 1-m-radius sphere (j =1)
- theta bin:
  each radius bin are split into upper and lower region (k =1,2)

Part of the parameters are free but constrained by the evaluated values. The penalty Chi-square is described by using the n-th observed (O_n) and expected (E_n) value and its error (σ_n);

$$\chi^2_{\text{penalty}} = \sum_n \left(\frac{O_n - E_n}{\sigma_n} \right)^2 \tag{9.7}$$

The energy nonlinearity parameters (kB, R) for the internal and external region are exceptionally constrained by ^{214}Bi spectral shape and source calibration data.

Fit Parameters ($0\nu\beta\beta$)

The fit parameters for the $0\nu\beta\beta$ analysis are summarized in Table. 9.4 and detailed information is described below. Nondominant backgrounds are fixed at best-fit values by a exploratory fit including below 0.8 MeV.

- ^{136}Xe $0\nu\beta\beta$: Best-fit value is searched by scanning event rate at intervals of 0.05 (ton·day)$^{-1}$ and performing the spectral fit.
- ^{136}Xe $2\nu\beta\beta$: Event rate is freely varied in the fit.
- ^{238}U series : The contribution of ^{214}Pb and ^{214}Bi are included by assuming radiative equilibrium. Constraint on event rate in Xe-LS is estimated by tagged ^{214}Bi-^{214}Po sequential events inside 1.2-m-radius with 0.046 % tagging inefficiency. For the IB film distribution, non-uniform vertical model described in Sec. 8.3.1 is included. Furthermore, the contribution of the lower and upper IB film are freely floated as independent parameters. The rejection inefficiency of ^{214}Bi is fixed to 70 %.
- ^{210}Bi : ^{210}Pb-^{210}Bi-^{210}Po subchain of the ^{238}U series is out of equilibrium due to ^{210}Pb contamination, so the downstream nuclei; ^{210}Bi and ^{210}Po are treated independently. ^{210}Bi of Xe-LS, film and outer-LS in each period are fixed at best-fit values by the exploratory fit including below 0.8 MeV.

- ^{210}Po : The spectrum of the ^{210}Bi daughter is defined as gaussian with $\sigma = 0.03708$ and mean = 0.3068 MeV. The energy peak is significantly lower than the Q-value of ^{210}Po α decay (5.4 MeV) due to large energy loss. The event rate is fixed to 3.4×10^7 (kton·day)$^{-1}$ in both of the periods.

- ^{232}Th series : The contribution of ^{212}Bi and ^{208}Tl are included assuming radiative equilibrium. Rejection inefficiency of ^{212}Bi film by the delayed coincidence tag is fixed to 70 %. The evaluated nonuniform model is applied to ^{208}Tl IB film. Event rate in Xe-LS and film are fixed to best-fit values in a exploratory spectral fit.

- ^{40}K : Distributions from the four sources; Xe-LS, the lower and upper hemisphere of the IB film and outer-LS are included. Each event rate is fixed to best-fit values in the prior spectral fit.

- ^{85}Kr : Uniformly distributing ^{85}Kr in Xe-LS is assumed. Event rate is fixed to best-fit values in the prior spectral fit.

- ^{110m}Ag : Three components uniformly dispersed in Xe-LS and the lower and upper hemisphere of the IB film are freely varied independently.

- ^{137}Cs : Event rate in the lower and upper hemisphere of the IB film are fixed to best-fit values in the prior spectral fit.

- ^{134}Cs : Non-uniform z distribution model is included for the IB film. Event rate in the lower and upper hemisphere of the IB film are fixed to best-fit values in the prior spectral fit.

- ^{137}Xe : Event rate is floated but constrained to 3.9 $\pm$ 2.0 (kton·day)$^{-1}$, estimated from the production rate of spallation neutron and the capture cross sections of thermal neutron by the Xe-LS components.

- ^{11}C : Event rate is floated but constrained to 1106 $\pm$ 299 (kton·day)$^{-1}$ evaluated using non Xenon-loaded LS (S. Abe, Enomoto, et al., 2010 [53]). The error includes additional 22 % uncertainty of the flux of spallation neutron in Xe-LS.

- ^{10}C, ^{6}He, ^{12}B : Event rate of these spallation products are floated but constrained by the simultaneous fit of time and energy for shortlived light isotopes (Sec. 8.6.1). The expected rates are 10.1 $\pm$ 2.6, 0.7 $\pm$ 1.8 and 7.2 $\pm$ 2.1 (kton·day)$^{-1}$ for ^{10}C, ^{6}He and ^{12}B, respectively.

- Energy scale nonlinearity : It consists of scale factor (α), Birks constant (kB) and ratio of Cherenkov and scintillation contribution (R) defined in Sec. 6.3.2. They are independently evaluated for the internal and external regions separated at $R = 1.34$ m. Though visible energy is corrected to be $\alpha \sim 1$ in advance, it is fine-tuned by scanning the value from 0.986 to 1.006 during the spectral fit. kB and R have anti-correlated spectrum distortion effects. Best-fit values are searched in a reticular pattern for each α. Their combination is limited in a range where

delta-chi-square from the best fit evaluated by the source calibration data and ^{214}Bi spectrum from initial ^{222}Rn is less than 9.0.

Table 9.4.: Fit parameters for $0\nu\beta\beta$ analysis

	condition	material source			
^{136}Xe $0\nu\beta\beta$	scanned	Xe-LS	-	-	-
^{136}Xe $2\nu\beta\beta$	floated	Xe-LS	-	-	-
^{238}U series	constrained	Xe-LS	-	-	-
	floated	-	IB($z<0, z>0$)	-	-
^{232}Th series	fixed	Xe-LS	IB($z<0, z>0$)	-	-
^{40}K	fixed	Xe-LS	IB($z<0, z>0$)	Outer-LS	-
^{210}Bi	fixed	Xe-LS	IB	Outer-LS ($z<0, z>0$)	-
^{85}Kr	fixed	Xe-LS	-	-	-
^{110m}Ag	floated	Xe-LS	IB($z<0, z>0$)	-	-
^{137}Cs	fixed	-	IB($z<0, z>0$)	-	-
^{134}Cs	fixed	-	IB($z<0, z>0$)	-	-
^{137}Xe	constrained	-	-	-	cosmogenic
^{11}C	constrained	-	-	-	cosmogenic
^{10}C	constrained	-	-	-	cosmogenic
^{6}He	constrained	-	-	-	cosmogenic
^{12}B	constrained	-	-	-	cosmogenic
^{210}Po	fixed	-	-	-	uniform
energy scale nonlinearity	constrained	-	-	-	-

Fit Parameters ($2\nu\beta\beta$)

Difference from the $0\nu\beta\beta$ analysis is the dominant backgrounds in the $2\nu\beta\beta$ energy window are floated, namely ^{40}K, ^{210}Bi, ^{85}Kr, ^{137}Cs and ^{134}Cs. External backgrounds from the IB and outer-LS are constrained or fixed by the prior spectrum fit in $R < 2$ m. Expected event rates are summarized in Table. 9.5. Constraint to ^{11}C spallation product which is also a main background, is the same with that of the $0\nu\beta\beta$ analysis (1106 ± 299 events/day/kton). Energy scale parameters are also floated.

Table 9.5.: Expected rates for the dominant external backgrounds for $2\nu\beta\beta$. The values indicate event rates without volume cut. The IB backgrounds are constrained, and the outer-LS backgrounds are fixed to listed values.

	Expected rate	
	$Z < 0$	$Z > 0$
IB [events/day]		
^{238}U series	31.1 ± 3.2	23.6 ± 3.5
^{232}Th series	131.8 ± 13.0	109.7 ± 12.0
^{40}K	1249 ± 126	533 ± 54
^{137}Cs	4033 ± 403	438 ± 44
^{134}Cs	761 ± 76	695 ± 70
^{210}Bi	994 ± 103	
Outer-LS [events/day/kton]		
^{40}K	3851	
^{210}Bi	10538	50773

9.3.3. Best Fit Result

There are no $0\nu\beta\beta$ signal excess over the background expectation in both periods. The best-fit spectra of 40 equal-volume bins are drawn in Figs. 9.3, 9.4, 9.5 and 9.6, for which the spectra of Period-1 and Period-2 are summed after the fit. The Spectra in the low background region are shown in Fig. 9.7. The dominant background rates at the best-fit are summarized at Table. 9.6. Energy scale nonlinearity parameters in Xe-LS are $(\alpha,\ kB,\ R) = (0.997,\ 0.20,\ 0.035)$ in Period-1 and $(\alpha,\ kB,\ R) = (0.994,\ 0.26,\ 0.025)$ in Period-2, in comparison to estimation by ^{214}Bi and composite source; $(kB, R) = (0.34, 0.00)$. Though $0\nu\beta\beta$ favors negative rate, it is not so significant. According to extrapolation of the $\Delta\chi^2$ distribution, positive region are statistically allowed within 35 % (Period-1) and 14 % (Period-2) probability.

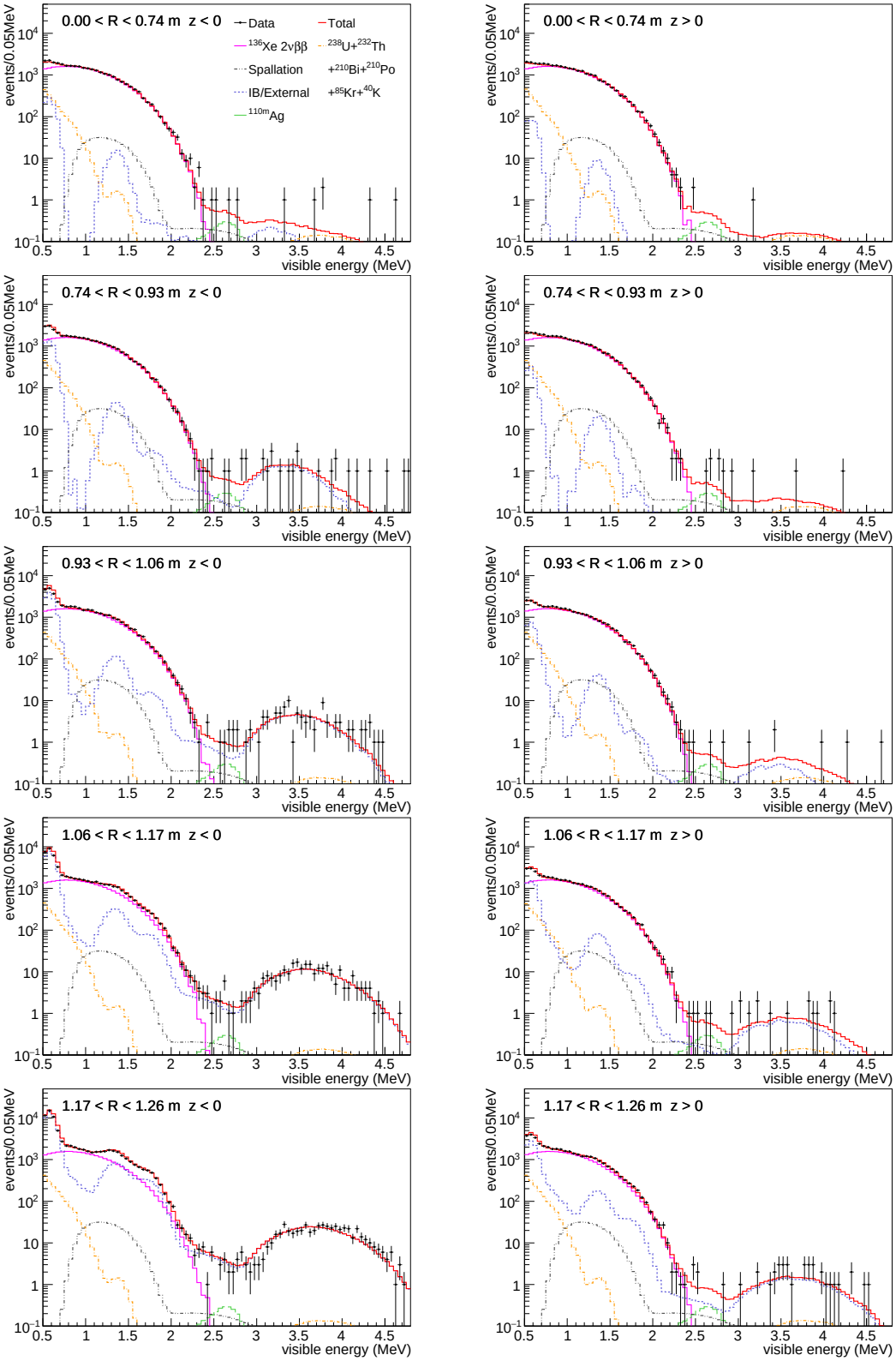

Figure 9.3.: Energy distributions of equal-volume bins ($0 < R < 1.26$ m) for combination of Period-1 and Period-2 after the fit. Each line shows the best-fit MC expectation.

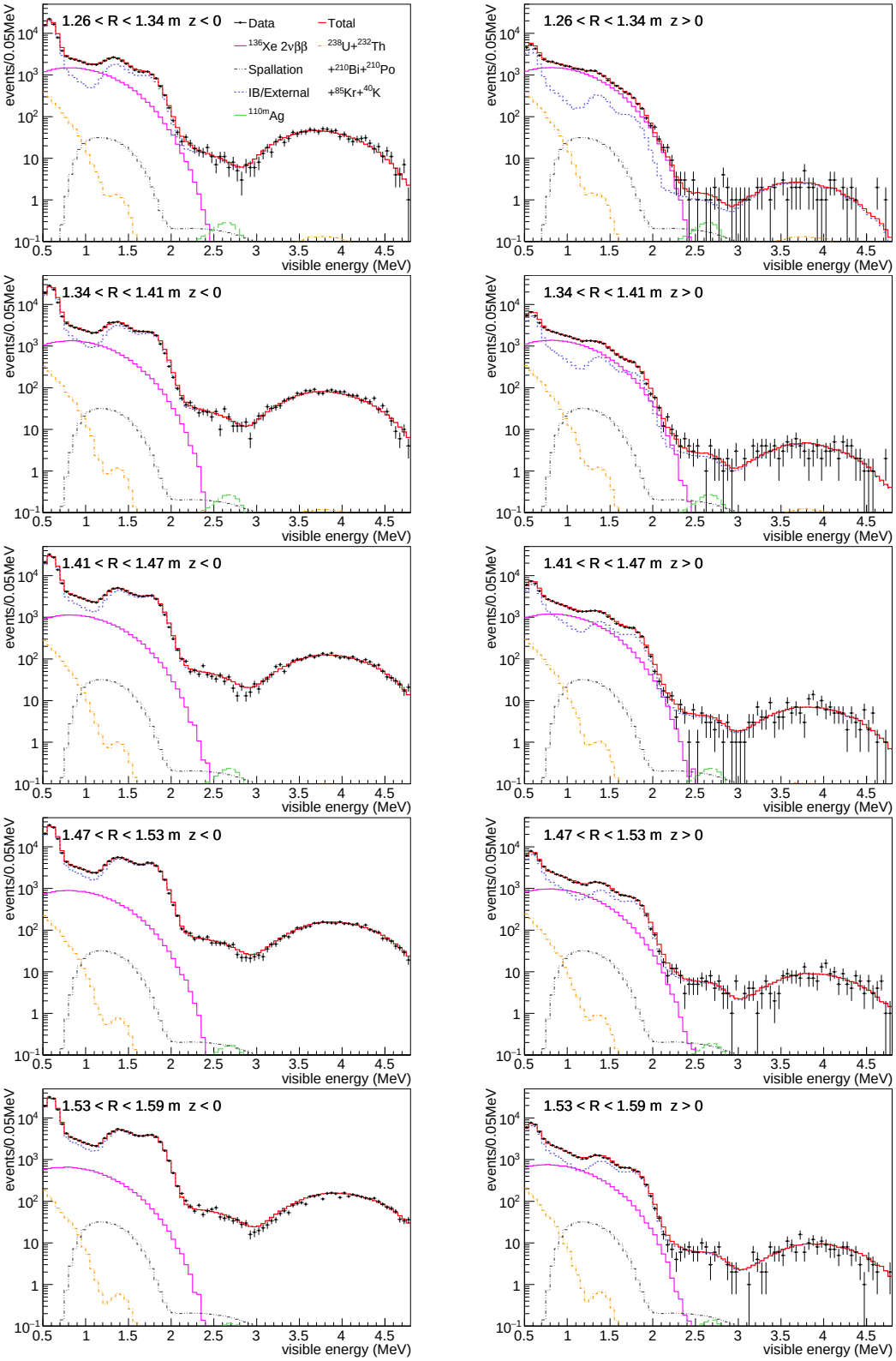

Figure 9.4.: Energy distributions of equal-volume bins ($1.26 < R < 1.59$ m)

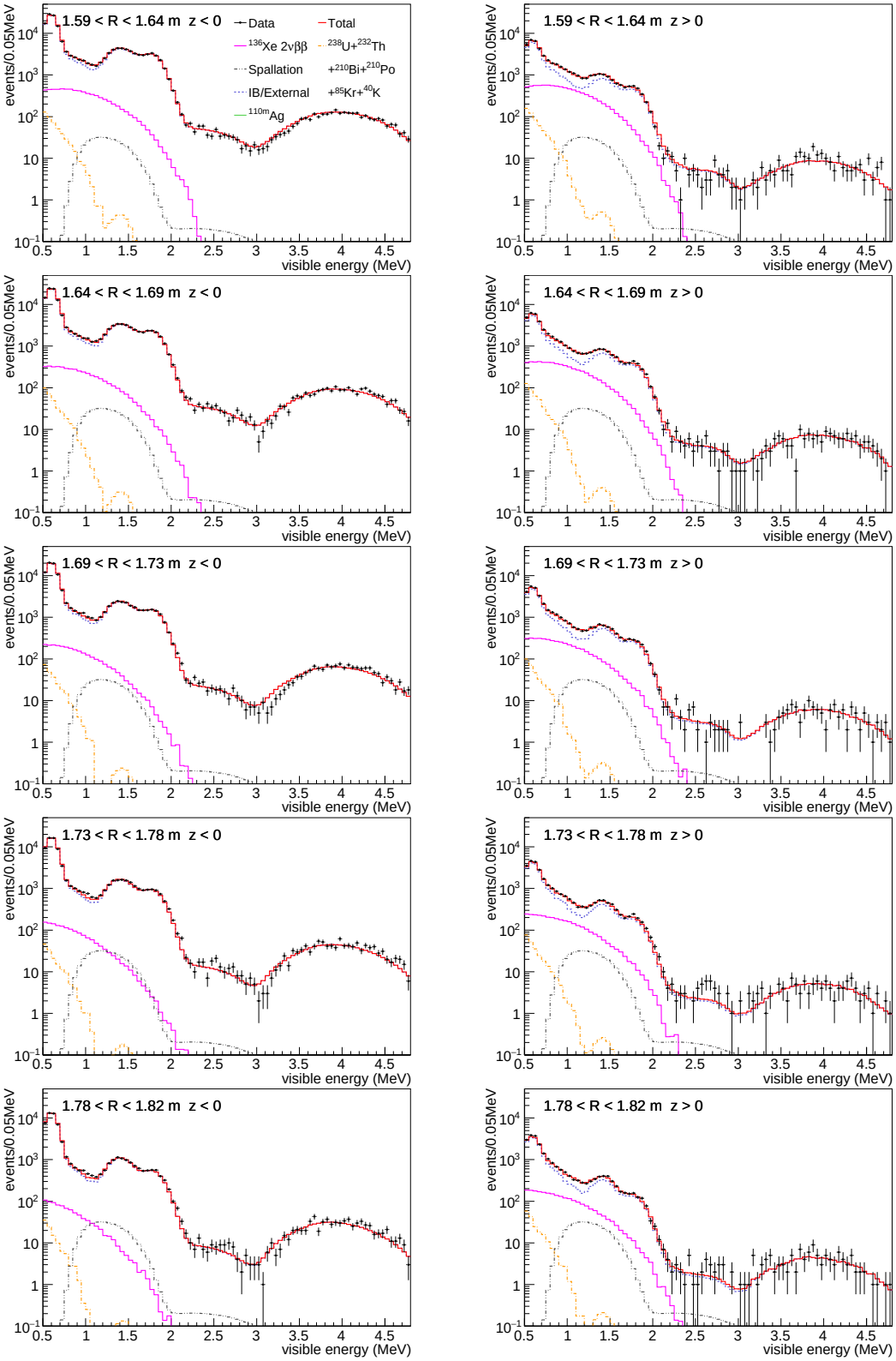

Figure 9.5.: Energy distributions of equal-volume bins ($1.59 < R < 1.82$ m)

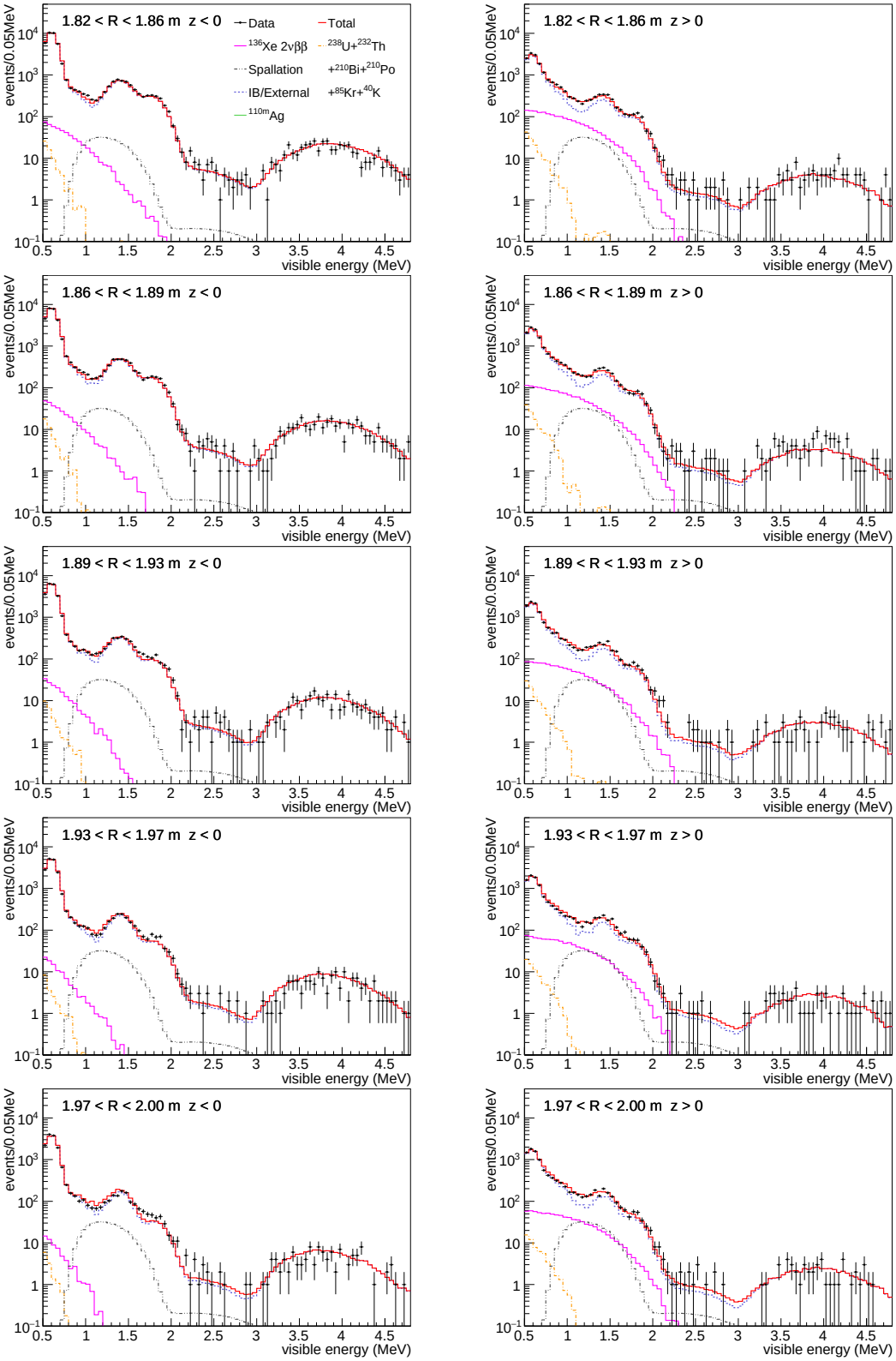

Figure 9.6.: Energy distributions of equal-volume bins ($1.82 < R < 2.00$ m)

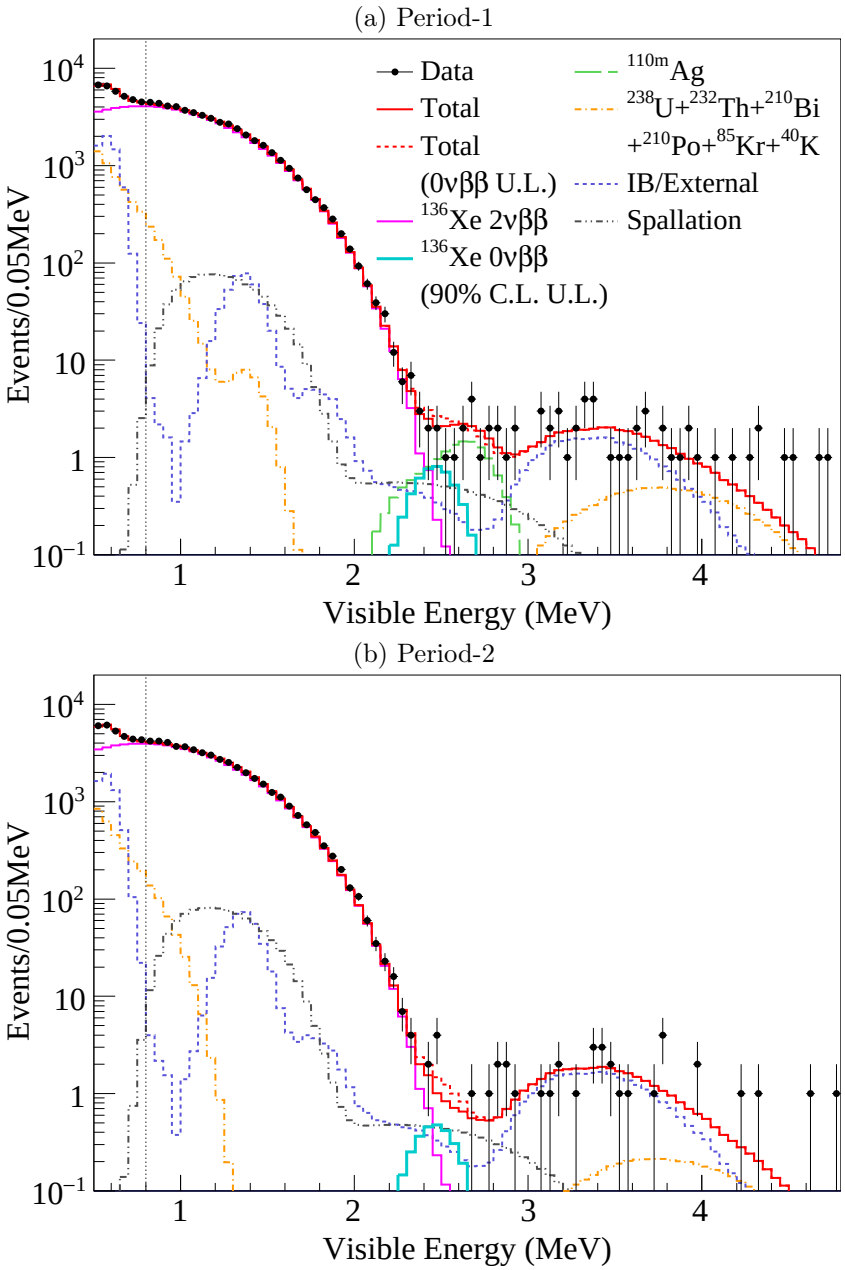

Figure 9.7.: Energy spectra with best-fit backgrounds inside 1-m-radius in (a) Period-1 and (b) Period-2. The cyan lines are $0\nu\beta\beta$ decay spectra at 90 % C.L. upper limits. The dotted line is the lower edge of the fit range (0.8 MeV).

Table 9.6.: Summary of the dominant backgrounds at $0\nu\beta\beta$ best-fit. The units of the event rate are [events/day/kton] for Xe-LS, outer-LS and spallation products, and [events/day] for IB. Number of total expected events in $2.3 < E < 2.7$ MeV inside 1-m-radius are well consistent with observed events.

		Period-1 (270.7 days)		Period-2 (263.8 days)	
		rate	events in $0\nu\beta\beta$ window	rate	events in $0\nu\beta\beta$ window
Xe-LS					
^{136}Xe $2\nu\beta\beta$		1.00×10^5	5.48	0.99×10^5	5.29
^{238}U series (^{214}Bi)		24.1×10^2	0.25	2.8×10^2	0.03
^{232}Th series (^{208}Tl)		32.9	0.001	14.7	0.001
^{110m}Ag		15.6	8.5	0.0	0.0
IB Film					
^{238}U series	lower	17.4	2.37	17.4	2.27
	upper	2.3	0.19	2.4	0.18
^{232}Th series	lower	41.7	0.017	43.9	0.023
	upper	3.7	0.002	3.7	0.002
^{110m}Ag	lower	0.0	0.0	0.0	0.0
	upper	0.3	0.003	0.2	0.002
Spallation Products					
^{10}C		12.3	3.3	11	2.8
^{137}Xe		4.3	0.5	3.8	0.4
^{12}B		7.9	0.16	7.7	0.15
^{6}He		0.83	0.08	0.81	0.08
total expected		-	20.8	-	11.3
observed		-	22	-	11
χ^2/ n.d.f		4211 / 3177		4030 / 3177	

^{110m}Ag Contribution

The sensitivity for the $0\nu\beta\beta$ search has strong correlation with ^{110m}Ag. Table. 9.7 shows background dependences of $0\nu\beta\beta$ upper limit, which shows that accurate estimation of ^{110m}Ag quantity is required. According to Chi-square scanning in multidimensional parameter space by $0\nu\beta\beta$ and ^{110m}Ag, the best-fit in Period-1 ($0\nu\beta\beta$, ^{110m}Ag) = (0.0, 15.2) events/day/kton strongly supports existence of ^{110m}Ag. And in Period-2, ^{110m}Ag decreases significantly as shown in Fig. 9.8. These are consistent with the results in Chi-square scanning in 1D parameter space of $0\nu\beta\beta$, shown in Table. 9.6.

Table 9.7.: Background dependence of $0\nu\beta\beta$ limit. Each value indicates deviation [%] of upper limit between the case when all below backgrounds are free, and that when one background rate is fixed with mean value $+1\sigma$ or -1σ error. A negative value means more strict limit than the best-fit limit. ^{110m}Ag has the largest influence in Period-1 with smaller contribution from ^{214}Bi in the upper IB. In Period-2 after the decrease of ^{110m}Ag, estimation of spallation backgrounds gains importance.

		Period-1		Period-2	
		-1σ	$+1\sigma$	-1σ	$+1\sigma$
Xe-LS					
^{136}Xe $2\nu\beta\beta$		0.7	1.1	-0.9	-0.9
^{238}U-series		0.4	0.4	-0.9	-0.9
^{110m}Ag		30	-37	-0.9	-12
IB film					
^{214}Bi	($z < 0$)	2.2	-2.2	2.7	-5.1
	($z > 0$)	6.4	-4.6	1.5	-3.3
^{110m}Ag	($z < 0$)	0.4	1.8	0.3	-3.3
	($z > 0$)	-6.2	5.8	-0.9	-0.9
Spallation products					
^{137}Xe		0	0.4	5.7	-6.9
^{10}C		1.1	-1.1	11	-12
^{6}He		0.4	0	0.3	-3.3
^{12}B		0.4	0.7	-0.3	-1.5

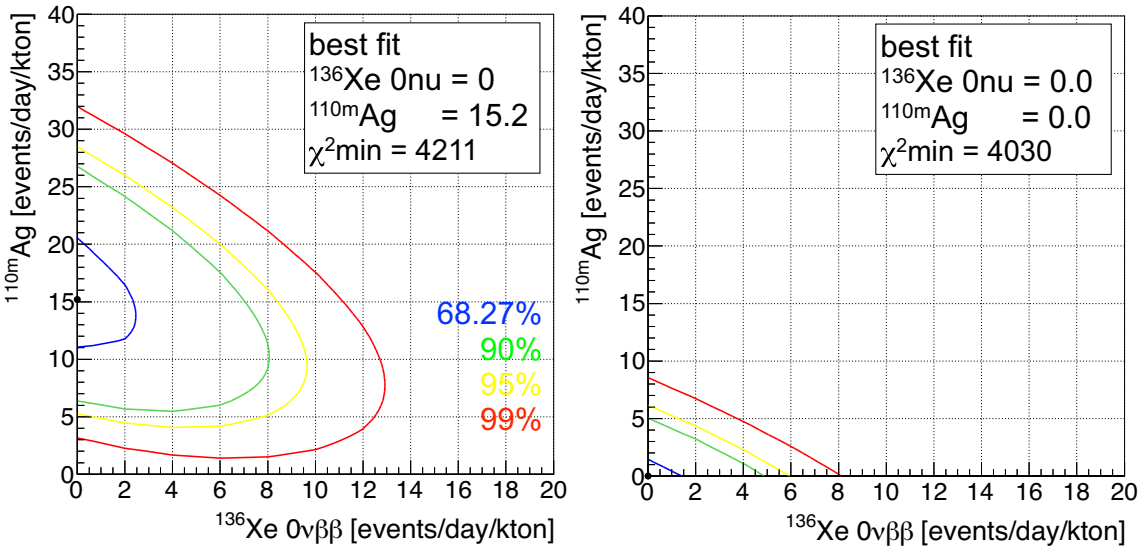

(a) Period-1 (b) Period-2

Figure 9.8.: Correlation between $0\nu\beta\beta$ and ^{110m}Ag background rate in each period. Their best-fit are derived by implementing spectral fit at each fixed combination of $0\nu\beta\beta$ and ^{110m}Ag. It ensures the ^{110m}Ag contribution in Period-1, and the significant reduction in Period-2.

^{214}Bi Vertex Distribution

^{214}Bi dominates 99 % of the IB film backgrounds in the $0\nu\beta\beta$ window, and contributes even in the internal region. Therefore, spacial distribution of ^{214}Bi has to be reproduced accurately for correct background estimation. Quality of MC simulation is tested with tagged ^{214}Bi-Po events from the earliest high Rn data. Fig. 9.9(a) shows that the simulated attenuation is consistent with data by ∼3 order of magnitude. The reproduction quality for the vertical non-uniformity is confirmed by comparing vertex distribution of single events with that of normalized ^{214}Bi MC (Fig. 9.9(b)).

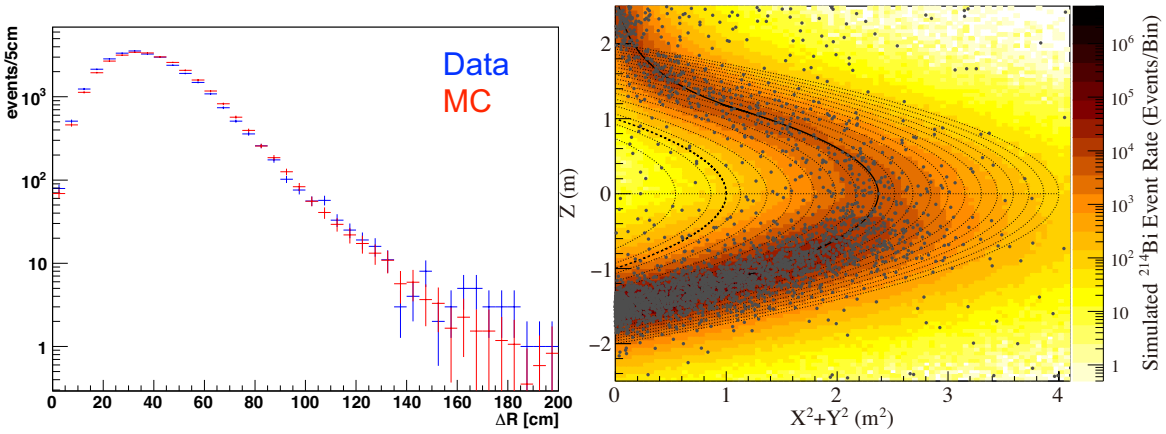

(a) Distance between ^{214}Bi and ^{214}Po (b) ^{214}Bi MC vertex with events in $0\nu\beta\beta$ window

Figure 9.9.: Vertex distribution of ^{214}Bi events with expectation. (a) Distance between tagged ^{214}Bi and ^{214}Po from the earliest high Rn period in Xe-LS. It shows ^{214}Bi MC vertex distribution (red) reproduces its position dependent attenuation by ∼3 order of magnitude. (b) Vertex distribution of ^{214}Bi MC (colored histogram) with single events in $2.3 < E < 2.7$ MeV (black points). The normalization of ^{214}Bi MC is arbitrary. The solid and thick dashed lines indicate the shape of the IB and the 1-m-radius spherical volume, respectively. The thin dashed lines are the border of equal-volume half spherical shells used in the spectral fit.

9.4. Half-Life of ^{136}Xe $2\nu\beta\beta$ Decay

In the fiducial volume of $R < 1$ m, contribution of external backgrounds causing large uncertainty is significantly lower than $2\nu\beta\beta$ events, as shown in Fig. 9.10. From scanning of chi-square distribution by spectral fit in $R < 1$ m divided into the vertical half-shells, $2\nu\beta\beta$ decay rate is estimated to be 100.5 ± 1.0 (ton·day)$^{-1}$, with best fit backgrounds shown in Table. 9.8. ^{40}K, ^{210}Bi and ^{85}Kr are the most contributing backgrounds in Xe-LS, but their quantity cannot be confirmed independently due to dominant $2\nu\beta\beta$ events. Especially, $2\nu\beta\beta$ rate strongly depends on ^{40}K if it has a finite value, so validity of the estimation is confirmed by checking correlation with $2\nu\beta\beta$ spectrum. Other backgrounds distributing in Xe-LS such as ^{214}Pb in ^{238}U series, ^{212}Bi in ^{232}Th series and ^{11}C spallation product is well determined by estimation of their daughter nucleus, or constrained by the past estimation.

In order to check the possibility of Xe leak from the IB, rate stability is confirmed. Time variation of event rate in $2\nu\beta\beta$ energy window ($1.2 < E < 2.0$ MeV) within 1-m-radius is stable within 5 % from average (Fig. 9.11). From the spectral fit in divided periods, $2\nu\beta\beta$ decay rates in Period-1 $(100.1^{+1.1}_{-1.8})$ (ton·day)$^{-1}$ and in Period-2 $(100.0^{+1.0}_{-0.9})$ (ton·day)$^{-1}$ are well consistent within the statistical uncertainties. Smaller

error in Period-2 is brought by decrease of ^{134}Cs radiative decay.

Thus, half-life of ^{136}Xe $2\nu\beta\beta$ decay is measured as follows;

$$T^{2\nu}_{1/2} = 2.21 \pm 0.02(\text{stat}) \pm 0.07(\text{syst}) \times 10^{21}\ \text{yr} \tag{9.8}$$

Systematic uncertainties are summarized at Table. 9.9. Uncertainty related to Xe amount is described in Sec. 9.2. Detection efficiency is calculated from the event selection. Detector energy scale (0.3 %) indicates uncertainty caused by energy scale parameters (α, kB, R). Fiducial volume error (3.0 %) dominates the total uncertainty, which will be improved by its enlargement. Background reduction by swap of the IB for cleaner one will enable it at the next phase. Obtained result agrees with both of results in Phase-I; 2.38 $\pm$ 0.02(stat) $\pm$ 0.14(syst)$\times 10^{21}$ yr (A. Gando et al., 2012 [68]), 2.30 $\pm$ 0.02(stat) $\pm$ 0.12(syst)$\times 10^{21}$ yr (A. Gando et al., 2012 [42]), and results measured by the EXO-200 experiment; 2.11 $\pm$ 0.04(stat) $\pm$ 0.21(syst)$\times 10^{21}$ yr (Ackerman et al., 2011 [69]), 2.23 $\pm$ 0.017(stat) $\pm$ 0.22(syst)$\times 10^{21}$ yr (Auger et al., 2012 [43]), 2.165 $\pm$ 0.016(stat) $\pm$ 0.059(syst)$\times 10^{21}$ yr (Albert, Auger, et al., 2014 [22]), as shown in Fig. 9.12.

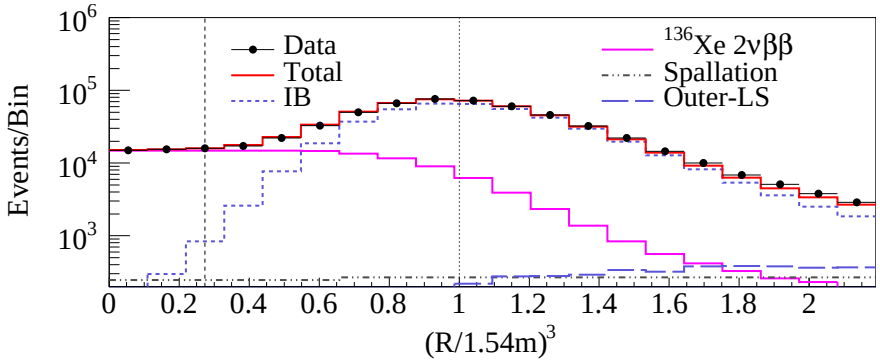

Figure 9.10.: R^3 distribution in $2\nu\beta\beta$ region ($1.2 < E < 2.0$ MeV). ^{40}K dominates 80 % of the IB film backgrounds. And 99 % of spallation backgrounds is originated from ^{11}C. The dashed and dotted lines indicate $R = 1$ m and the IB radius ($R = 1.54$ m), respectively.

Table 9.8.: Best-fit background rate contributing to $2\nu\beta\beta$ measurement. ^{210}Bi and ^{85}Kr are the most contributing backgrounds in Xe-LS. ^{214}Pb rate in ^{238}U series is constrained by counting daughter nucleus, ^{214}Bi tagged by delayed coincidence. ^{11}C spallation product is constrained. ^{212}Bi rate in ^{232}Th series is determined by the estimation of daughter nuclei, ^{208}Tl.

	Best fit [events/day/kton]
^{238}U series	1203
^{232}Th series	27.3
^{40}K	0.0
^{210}Bi	2.59×10^{4}
^{85}Kr	1.35×10^{4}
^{11}C	688.4

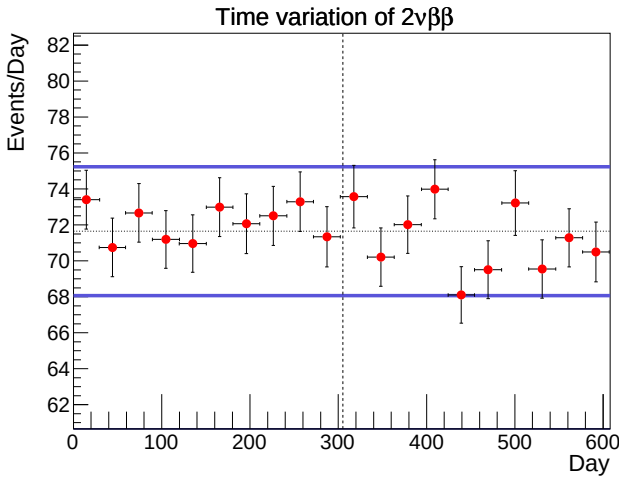

Figure 9.11.: Event time variation in $2\nu\beta\beta$ energy window ($1.2 < E < 2.0$ MeV) within 1-m-radius. Event rate is stable within 5 % from the average.

Table 9.9.: Systematic uncertainties for measurement of $2\nu\beta\beta$ half-life

Source	Systematic uncertainty [%]
Fiducial volume	3.0
Enrichment factor of ^{136}Xe	0.09
Xenon amount	0.8
Detector energy scale	0.3
Detection efficiency	0.2
Total	3.1

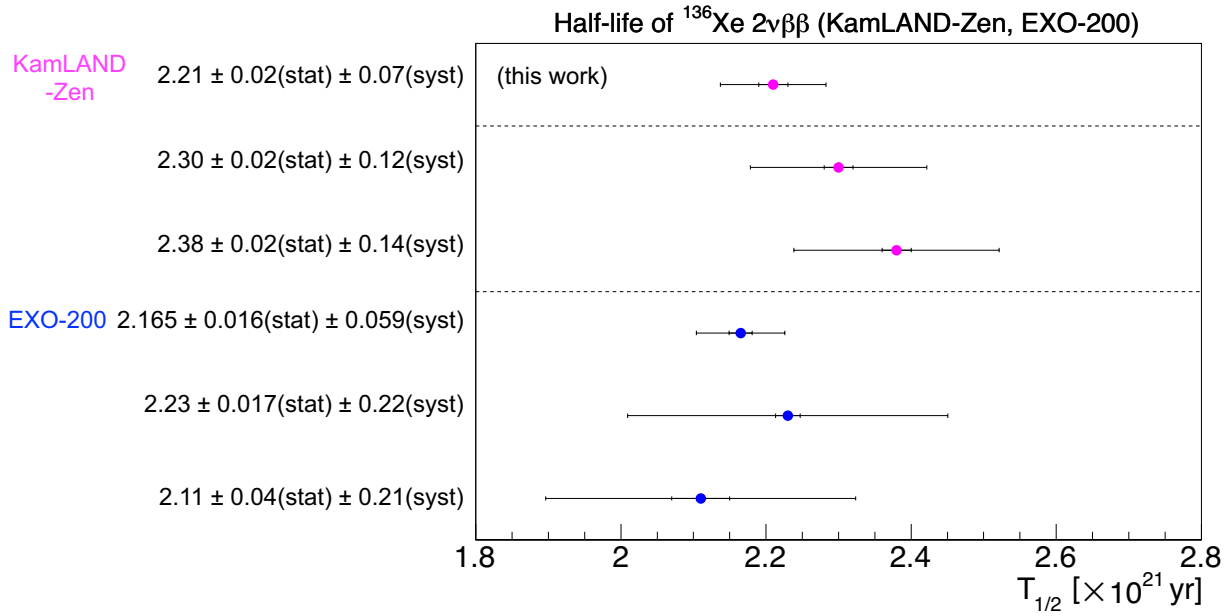

Figure 9.12.: Comparison of ^{136}Xe $2\nu\beta\beta$ decay half-life. Result of this work (2.21 ± 0.02(stat) $\pm$ 0.07(syst) $\times$ 10^{21} yr) is in agreement with the previous measurements in KamLAND-Zen (A. Gando et al., 2012 [68]); (A. Gando et al., 2012 [42]) and results from the EXO-200 experiment (Ackerman et al., 2011 [69]); (Auger et al., 2012 [43]); (Albert, Auger, et al., 2014 [22]).

9.5. Limits on ^{136}Xe $0\nu\beta\beta$ Decay

9.5.1. Decay Rate and Half-Life Limits

90% C.L. upper limit of $0\nu\beta\beta$ decay is given from a χ^2 test as shown in Fig. 9.13. It results < 5.5 (kton·day)$^{-1}$ in Period-1 and < 3.4 (kton·day)$^{-1}$ in Period-2 (Table. 9.10). Combining the results of both periods, the upper limit < 2.4 (kton·day)$^{-1}$ (90% C.L.) is obtained. It corresponds to half-life limit:

$$T^{0\nu}_{1/2}\ (\text{Phase-II}) \ > \ 9.2 \times 10^{25}\ \text{yr} \quad (90\ \%\ \text{C.L.}) \tag{9.9}$$

^{110m}Ag dominates even if potential backgrounds ^{208}Bi and ^{60}Co and ^{88}Y are included in the fit. The rate of ^{110m}Ag is given to be 7.9 (kton·day)$^{-1}$ in Period-1, which is almost half of the result on a fit with only ^{110m}Ag, 16 (kton·day)$^{-1}$. The residual is allocated to ^{208}Bi 4.2 (kton·day)$^{-1}$, ^{88}Y 2.8 (kton·day)$^{-1}$ and ^{60}Co 1.0 (kton·day)$^{-1}$, respectively at the best-fit. The difference does not have large impact on the limits, resulting < 5.95 (kton·day)$^{-1}$ for Period-1, < 3.35 (kton·day)$^{-1}$ for Period-2, and < 2.45 (kton·day)$^{-1}$ for combined period at 90% C.L., though the limit in Period-1 is slightly worse.

The half-life limit in Phase-II is also combined with the result of Phase-I, $T^{0\nu}_{1/2} > 1.9 \times 10^{25}$ yr (90% C.L.) with ^{136}Xe exposure 89.5 kg-yr, and is calculated to be:

$$T^{0\nu}_{1/2}\ (\text{Phase-I+II}) \ > \ 1.07 \times 10^{26}\ \text{yr} \quad (90\ \%\ \text{C.L.}), \tag{9.10}$$

which is almost sixfold improvement from Phase-I. It demonstrates reduction power of the purification and the background rejection. Obtained $\Delta\chi^2$ curves are summarized in Fig. 9.14 with the result of ^{136}Xe $0\nu\beta\beta$ decay experiment, EXO-200 (Albert, Auty, et al., 2014 [32]).

Table 9.10.: ^{136}Xe $0\nu\beta\beta$ decay limits in Phase-II with their sensitivities.

	Period-1	Period-2	Combined
decay rate limit (kton·day)$^{-1}$	< 5.5	< 3.4	< 2.4
$T^{0\nu}_{1/2}$ limit (yr)	$> 4.0\times10^{25}$	$> 6.5\times10^{25}$	$> 9.2\times10^{25}$
sensitivity (yr)	$> 2.4\times10^{25}$	$> 4.4\times10^{25}$	$> 5.6\times10^{25}$

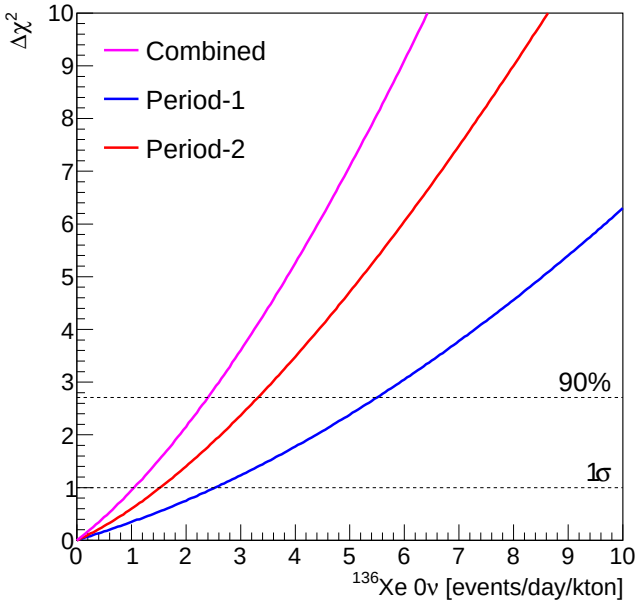

Figure 9.13.: $\Delta\chi^2$ distribution for $0\nu\beta\beta$ decay rate. The scan interval is 0.05 $(\text{kton}\cdot\text{day})^{-1}$. Zero consistent rates are favored, and their upper limits at 90 % C.L. are < 5.5 $(\text{kton}\cdot\text{day})^{-1}$ in Period-1 and < 3.4 $(\text{kton}\cdot\text{day})^{-1}$ in Period-2. These combination results < 2.4 $(\text{kton}\cdot\text{day})^{-1}$.

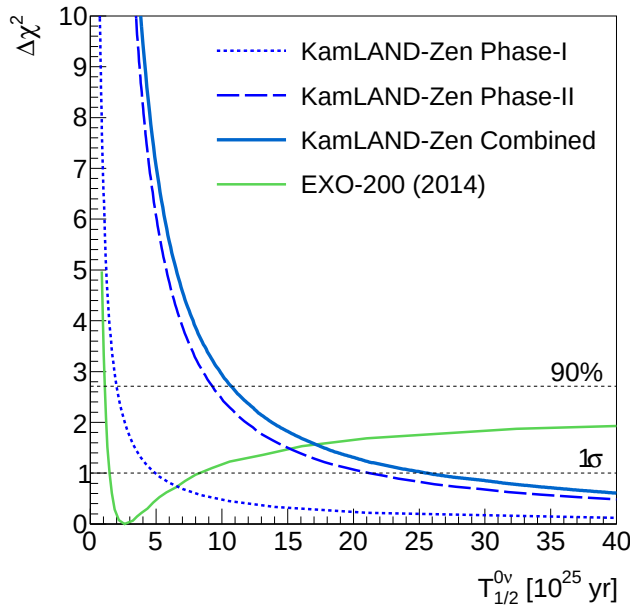

Figure 9.14.: $\Delta\chi^2$ distribution of $0\nu\beta\beta$ half-life. Combination of half-life limit at 90 % C.L. between this work ($T^{0\nu}_{1/2} > 9.2\times10^{25}$ yr) and Phase-I ($T^{0\nu}_{1/2} > 1.9\times10^{25}$ yr), gives $T^{0\nu}_{1/2} > 1.07\times10^{26}$ yr. The result of EXO-200 experiment ($T^{0\nu}_{1/2} > 1.1\times10^{25}$ yr) is also drawn (Albert, Auty, et al., 2014 [32]).

9.5.2. Rate Analysis

The validity of the limit can be tested by a rate analysis with a single volume which is optimized against ^{214}Bi on the IB having strong radial dependence. Fig. 9.15 shows radial distributions of observed events with estimated backgrounds at the best-fit, in $0\nu\beta\beta$ window. By considering the ^{214}Bi contribution, $R < 1.06$ m in $z < 0$ and $R < 1.26$ m in $z > 0$ regions are expected to be sensitive to $0\nu\beta\beta$ search. This region corresponds to 8 equal-volume bins and the volume is 6.7 m^3.

Fig. 9.16 is energy spectrum in the vertically asymmetric volume. In Period-2, the number of observed and expected background events in the $0\nu\beta\beta$ energy window are 16 and 21.0 events in the vertically asymmetric volume. Upper limit of the number of $0\nu\beta\beta$ events at 90% C.L. is derived < 4.48 events from the method (Feldman and Cousins, 1998 [70]), after correction of 88.3 % energy cut efficiency for $0\nu\beta\beta$. Corresponding decay rate limit < 3.25 (kton·day)$^{-1}$ is almost consistent with the result of the multi-volume analysis; < 3.4 (kton·day)$^{-1}$.

9.5.3. Sensitivity

The $0\nu\beta\beta$ decay limits are also confirmed by a simulation. It calculates "sensitivity" defined as an average limit, given by analysis of MC data in the same fit procedure as the real data. For the MC data, each background event is generated according to a poisson statistics based on an estimation with the real data. On the data construction, $0\nu\beta\beta$ decay rate is fixed to zero, and ^{208}Bi, ^{88}Y and ^{60}Co potential backgrounds other than ^{110m}Ag are neglected. A $0\nu\beta\beta$ decay limit is calculated by the spectral fit of the MC data in the same way as described above. The repetition makes a probability distribution of $0\nu\beta\beta$ limit, and the average is the sensitivity.

The sensitivity of half-life limit results in $T^{0\nu}_{1/2} > 5.6 \times 10^{25}$ yr at 90 % C.L. for combination of Period-1 and Period-2, which is indicated by a black dotted line in Fig. 9.17. Comparing with the measurement $T^{0\nu}_{1/2} > 9.2 \times 10^{25}$ (blue line), probability to get such a better limit is calculated to be 12 %. The sensitivity in each period is listed in Table. 9.10.

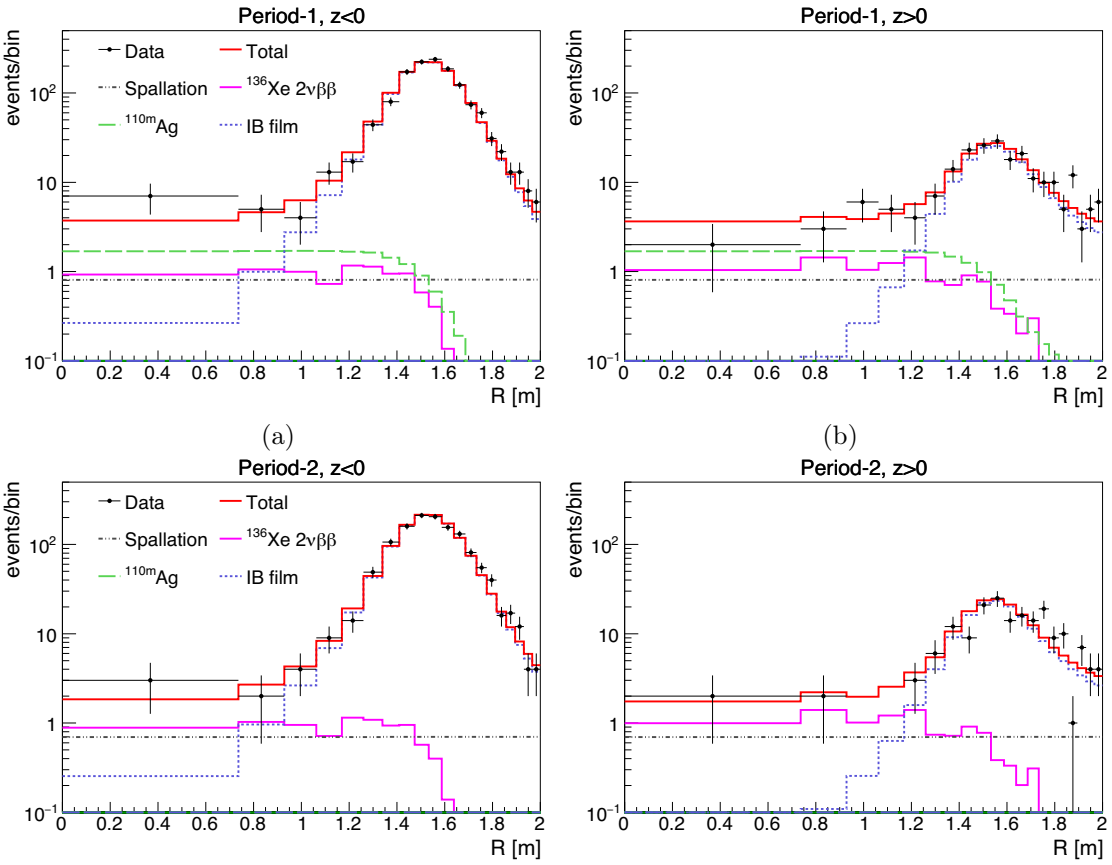

Figure 9.15.: Radial distribution in the $0\nu\beta\beta$ window ($2.3 < E < 2.7$ MeV) with best-fit backgrounds, in Period-1 ((a)$z < 0$, (b)$z > 0$) and in Period-2 ((c)$z < 0$, (d)$z > 0$). Each bin corresponds to a radial division used in the multi-volume analysis. ^{214}Bi is a dominator of the IB background and there is small contribution of ^{110m}Ag and ^{208}Tl. By considering the IB film contribution, $R < 1.06$ m in $z < 0$ and $R < 1.26$ m in $z > 0$ regions are expected to be sensitive to $0\nu\beta\beta$ search. The expected number of events in this region is 21.0 events compared to 16 observed events for Period-2.

(a) Period-1

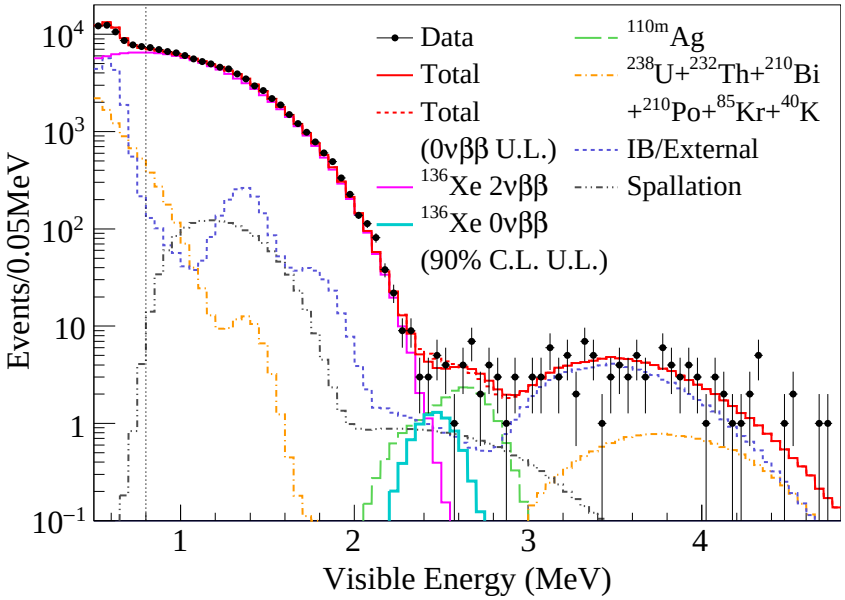

(b) Period-2

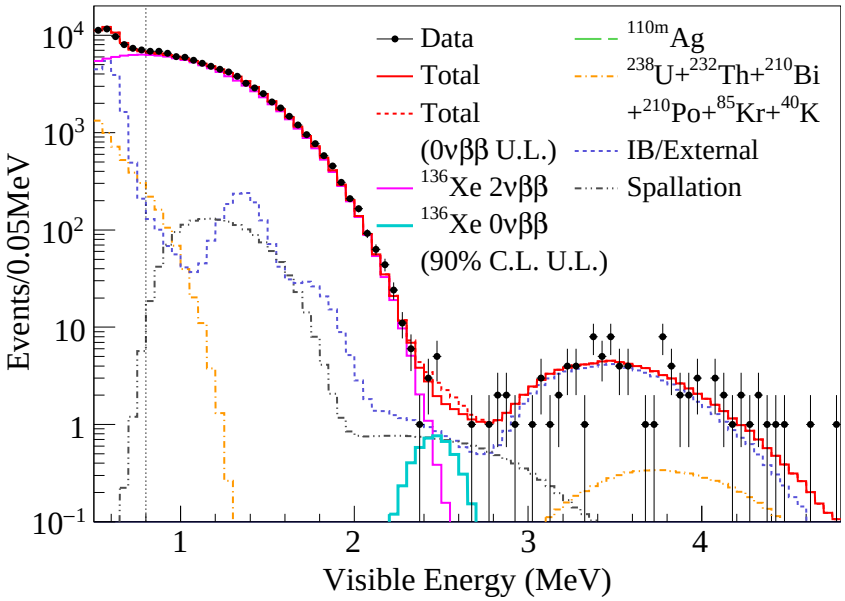

Figure 9.16.: Energy spectra with best-fit backgrounds and $0\nu\beta\beta$ spectra at 90% C.L. upper limit in (a) Period-1 and in (b) Period-2. 8 equal-volume bins ($R <$ 1.06 m in $z < 0$ and $R <$ 1.26 m in $z > 0$) are selected from 40 bins as sensitive to $0\nu\beta\beta$ decay search.

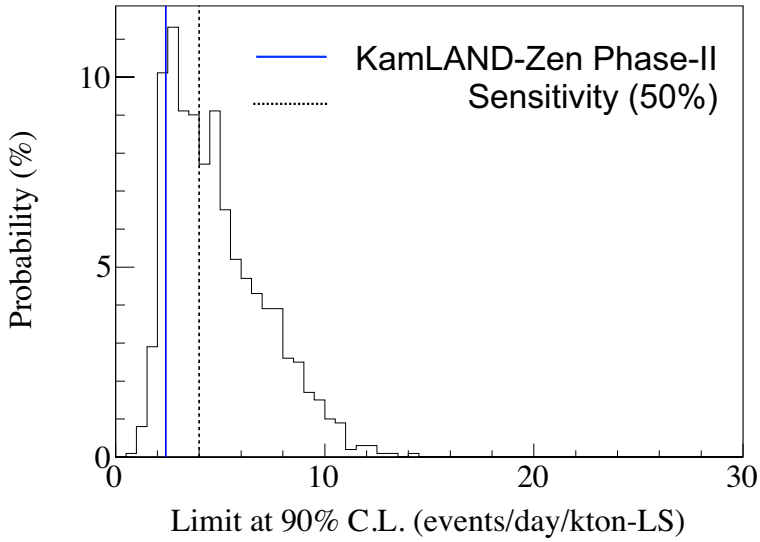

Figure 9.17.: Probability distribution of $0\nu\beta\beta$ decay rate limit at 90 % C.L. in Phase-II. The dotted line indicates a mean limit expected at 50%. The probability obtaining the data limit (blue line) is 12 %.

9.6. Discussion on the Neutrino Mass

9.6.1. Effective Majorana Neutrino Mass

As described in Chap. 2, the effective Majorana neutrino mass $\langle m_{\beta\beta}\rangle$ can be calculated from $0\nu\beta\beta$ decay half-life $T^{0\nu}_{1/2}$, where the process mediated by exchange of light left-handed neutrino is assumed;

$$(T^{0\nu}_{1/2})^{-1} = G^{0\nu}\left(\frac{g_{A,\mathrm{eff}}}{g_A}\right)^4 |M^{0\nu}|^2\langle m_{\beta\beta}\rangle^2 \tag{9.11}$$

The phase space factor (PSF) $G^{0\nu}$ and the nuclear matrix elements (NME) $M^{0\nu}$ are nucleus-specific given by numerical calculation. PSF is defined as densities of states available per unit energy, which can be calculated precisely by solving Dirac equation. The recent study (Kotila and Iachello, 2012 [71]) implemented rigorous numerical calculation with exacter electron wave function including electron screening effect and finite nuclear size. The improvement caused significant difference especially for heavier nuclei compared with older calculation. Besides, Ref. (Mirea, Pahomi, and Stoica, 2014 [27]) updated Coulomb potential introducing realistic proton density distribution in the daughter/parent nucleus. The study introduces redefined PSF $G'_{0\nu}(^{136}\mathrm{Xe}) = 14.54\times10^{-15}$ yr^{-1} which satisfies $G^{0\nu} = G'^{0\nu}g_A^4/m_e^2$. Using measured axial-vector coupling constant for free nucleon $g_A \simeq 1.27$, $G^{0\nu}$ is calculated to be 1.444 $\times10^{-25}$ yr^{-1}eV^{-2}. NME is calculated based on a wave function of nucleus. It is strongly depends on nucleus models and causes large uncertainty. Applying the value for each NME listed in Table. 9.11, following mass

limit is obtained from our limit (Eq. 9.10);

$$\langle m_{\beta\beta} \rangle < (61 - 165) \text{ meV} \quad (90 \text{ \% C.L.}) \tag{9.12}$$

This assumes not quenched axial-vector coupling constant, that is $g_{A,\text{eff}}/g_A = 1$. It is a first constraint below 100 meV of all nuclei and reaches the bottom of the quasi-degenerate neutrino mass region as shown in Fig. 9.18. And the result is the most stringent limit of all double-beta decay nuclei as listed in Table. 9.13.

Table 9.11.: Nuclear matrix elements for ^{136}Xe $0\nu\beta\beta$ decay

model	$M^{0\nu}$	Ref.
EDF	4.20	(Rodríguez and Martínez-Pinedo, 2010 [72])
ISM	1.77	(Menéndez et al., 2009 [73])
IBM-2	3.05	(Barea, Kotila, and Iachello, 2015 [74])
pnQRPA	2.91	(Hyvarinen and Suhonen, 2015 [75])
SRQRPA-B	2.95	(Meroni, Petcov, and Šimkovic, 2013 [76])
SRQRPA-A	2.29	(Meroni, Petcov, and Šimkovic, 2013 [76])
QRPA-B	2.460	(Šimkovic et al., 2013 [77])
QRPA-A	2.177	(Šimkovic et al., 2013 [77])
SkM-HFB-QRPA	1.55	(Mustonen and Engel, 2013 [28])

Interplay with Cosmology

Current cosmological data provides tight upper bounds on $\sum m_i$ as $\sim$ 0.1 - 0.2 eV. Taken at face value, it would slightly disfavors the IH case, which requires $\sum m_i$ values larger than $\sim$0.1 eV. This indication is consistent with a possible slight preference for the NH from the global 3ν analysis. However it is hard to exclude the IH only with the cosmological data, unless there will be a great improvement on the knowledge of $\sum m_i$. Combination with $\langle m_{\beta\beta} \rangle$ allows to improve significantly the exclusion region.

On the other hand, if $\sum m_i$ is measured, the next generation of double-beta decay experiments also have possibilities to detect a signal of $0\nu\beta\beta$, which requires ton scale of $\beta\beta$ source. Both measurements will enable to diminish the theoretical uncertainties of double-beta measurements and conclude the quenching effect of the axial coupling constant. If the signal is not found in the region of cosmological claim, it would disprove some assumptions of the present cosmological models, or suggest that a different mechanism other than that the light neutrino exchange mediates the transition.

9.6.2. Lightest Neutrino Mass

The obtained effective Majorana mass limit can be translated into the neutrino mass limit owing to knowledge of oscillation parameters. they are expressed with the masses m_i and the elements of the mixing matrix U_{ei} associating the flavor eigenstates with the mass eigenstates: $|\nu_e\rangle = \sum_{i=1}^{3} U_{ei}^{*}|\nu_i\rangle$.

$$\langle m_{\beta\beta}\rangle \equiv \left|\sum_{i=1}^{3} U_{ei}^{2} m_i\right| = \left|e^{i\alpha_1}|U_{e1}^{2}|m_1 + e^{i\alpha_2}|U_{e2}^{2}|m_2 + |U_{e3}^{2}|m_3\right| \tag{9.13}$$

$\alpha_{1,2}$ are Majorana CP-violating phases. The extremes are calculated by floating unconstrained parameters $\alpha_{1,2}$ freely (Dell'Oro, Marcocci, and Vissani, 2014 [78]):

$$\langle m_{\beta\beta}\rangle^{\max} = \sum_{i=1}^{3} |U_{ei}^{2}|m_i \tag{9.14}$$

$$\langle m_{\beta\beta}\rangle^{\min} = \max\{2|U_{ei}^{2}|m_i - \langle m_{\beta\beta}\rangle^{\max}, 0\} \quad i = 1, 2, 3 \tag{9.15}$$

Furthermore, it is expressed as a function of the lightest neutrino mass m_l, for two neutrino mass spectra: normal hierarchy (NH) and inverted hierarchy (IH).

- NH ($m_l = m_1$)

$$\langle m_{\beta\beta}\rangle^{\max} = |U_{e1}^{2}|m_l + |U_{e2}^{2}|(m_l^2 + \delta m^2)^{\frac{1}{2}} + |U_{e3}^{2}|\left(m_l^2 + \Delta m^2 + \delta m^2/2\right)^{\frac{1}{2}} \tag{9.16}$$

- IH ($m_l = m_3$)

$$\langle m_{\beta\beta}\rangle^{\max} = |U_{e1}^{2}|\left(m_l^2 + \Delta m^2 - \delta m^2/2\right)^{\frac{1}{2}} + |U_{e2}^{2}|\left(m_l^2 + \Delta m^2 + \delta m^2/2\right)^{\frac{1}{2}} + |U_{e3}^{2}|m_l \tag{9.17}$$

Where, two squared mass gaps δm^2, Δm^2 are defined as follows:

$$\begin{aligned} \delta m^2 &= m_2^2 - m_1^2 \\ \Delta m^2 &= m_3^2 - (m_1^2 + m_2^2)/2 \end{aligned} \tag{9.18}$$

$\langle m_{\beta\beta}\rangle^{\min}$ is expanded as well. Fig. 9.18 shows the allowed ranges of $\langle m_{\beta\beta}\rangle$ for NH and IH respectively as a function of m_l (denoted m_{lightest}), obtained by applying result of the global 3ν oscillation analysis listed in Table. 9.12 to Eqs. 9.16 and 9.17. By utilizing the relation and the uncertainties from the oscillation parameters, the KamLAND-Zen result gives the strongest constraint on the light neutrino mass,

$$m_{\text{lightest}} < (180 - 480)\ \text{meV} \quad (90\%\ \text{C.L.}) \tag{9.19}$$

Table 9.12.: Neutrino mass-mixing parameters by the global 3ν oscillation analysis for two hierarchies (Capozzi, Fogli, et al., 2014 [79]). $\Delta m^2 = m_3^2 - (m_1^2 + m_2^2)/2$ is defined as $+\Delta m^2$ for NH and as $-\Delta m^2$ for IH herein. As for δm^2 and $\sin\theta_{12}$, common values are used in both hierarchies because of tiny differences.

parameter	NH		IH	
	best fit	3σ range	best fit	3σ range
$\delta m^2/10^{-5}\text{eV}^2$	7.54	6.99 - 8.18	7.54	6.99 - 8.18
$\Delta m^2/10^{-3}\text{eV}^2$	2.43	2.23 - 2.61	2.38	2.19 - 2.56
$\sin\theta_{12}/10^{-1}$	3.08	2.59 - 3.59	3.08	2.59 - 3.59
$\sin\theta_{13}/10^{-2}$	2.34	1.76 - 2.95	2.40	1.78 - 2.98

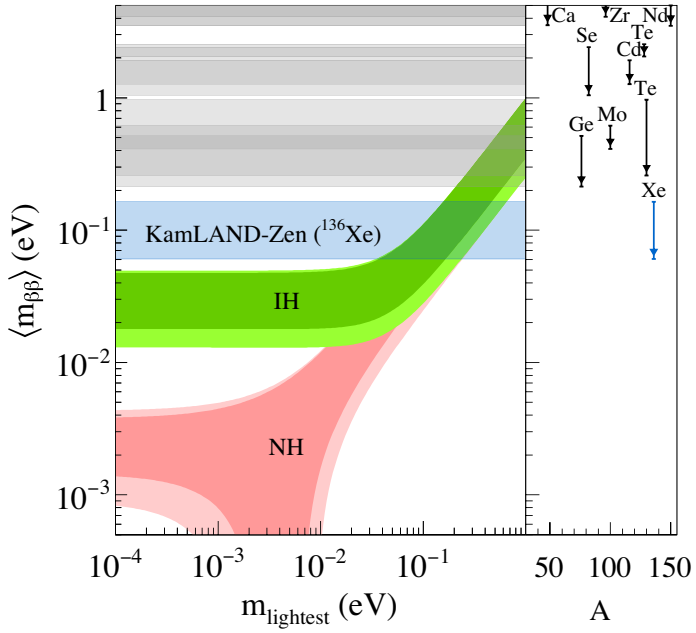

Figure 9.18.: Effective Majorana neutrino mass $\langle m_{\beta\beta} \rangle$ as a function of the lightest neutrino mass m_{lightest}, with a band of KamLAND-Zen limit (Eq. 9.12) and that of other experiments listed in Table. 9.13. The dark shaded regions are the predictions based on best-fit values of neutrino oscillation parameters for the NH and the IH. And the light shaded regions indicate the 3σ ranges calculated from the oscillation parameter uncertainties.

Table 9.13.: Summary of $0\nu\beta\beta$ decay half-life and effective Majorana neutrino mass limits at 90 % C.L. (A S Barabash, 2011 [80]); (Agostini, Allardt, Andreotti, et al., 2013 [33]); (Alfonso et al., 2015 [35]); (Arnold, Augier, J. D. Baker, A. S. Barabash, Basharina-Freshville, Blondel, Blot, Bongrand, V. Brudanin, Busto, Caffrey, Calvez, Cerna, et al., 2015 [81]). Same NME and PSF models introduced in Sec. 9.6.1 are applied for all nuclei.

Isotope	$Q^{\beta\beta}$ [MeV]	$T^{0\nu}_{1/2}$ [yr]	$\langle m_{\beta\beta}\rangle$ [eV]
^{136}Xe	2.458	$> 1.07 \times 10^{26}$	< 0.061 - 0.165
^{76}Ge	2.039	$> 3.0 \times 10^{25}$	< 0.213 - 0.517
^{100}Mo	3.034	$> 1.1 \times 10^{24}$	< 0.411 - 0.616
^{130}Te	2.527	$> 4.0 \times 10^{24}$	< 0.259 - 0.970
^{128}Te	0.867	$> 1.6 \times 10^{24}$	< 2.05 - 2.54
^{116}Cd	2.814	$> 1.7 \times 10^{23}$	< 1.26 - 1.92
^{82}Se	2.995	$> 3.6 \times 10^{23}$	< 1.04 - 2.40
^{150}Nd	3.371	$> 1.8 \times 10^{22}$	< 3.50 - 5.55
^{48}Ca	4.272	$> 5.8 \times 10^{22}$	< 3.54 - 15.5
^{96}Zr	3.350	$> 9.2 \times 10^{21}$	< 4.09 - 8.50

9.7. Future Prospects

In this work, search for Majorana neutrinos in quasi-degenerate neutrino mass was almost completed. The enhancement of sensitivity in a relatively short period is owing to detector scalability and intensive background reduction. It justifies improvement by increase of target mass for search in inverted mass hierarchy region.

The next phase, "KamLAND-Zen 800" will start in 2016, in which ∼750 kg of Xe will be installed with new inner-balloon. The exchange of IB will significantly improve background situation. ^{110m}Ag will be negligible because it will be removed by Xe purification system. ^{214}Bi from the IB film is unavoidable background, and cannot be reduced after the IB installation, therefore it will be important in the next phase. However, the contribution will further decrease compared to Phase-II, by fabrication of new balloon in much low-impurity environment. We can expect $10^{-1} - 10^{-2}$ of reduction for uranium concentration. Rejection method of ^{10}C spallation background is to be improved by optimization of event selection or improvement of trigger just after highly energetic muon. This phase will be able to start exploration of the inverted mass hierarchy region, and will cover half of the region.

10. Summary

In KamLAND-Zen (KamLAND ZEro Neutrino double-beta decay) Phase-I data period, unexpected ^{110m}Ag background covering ^{136}Xe $0\nu\beta\beta$ energy region was found. In order to reduce it by more than hundredth, Xe and LS purification was performed.

Unfortunately, inner-balloon (IB) was contaminated by a trouble during the operation, which trebled ^{214}Bi rate. It narrowed low background region sensitive to $0\nu\beta\beta$. On the other hand, effect of purification was seen in the target of reduction, ^{110m}Ag. In former part of Phase-II after the purification, the time variation was consistent with standard radioactive decay, but the events much decreased in the latter period. The reason of discrepancy is considered that some dust sank to the bottom of the IB. Accordingly, reduction factor of ^{110m}Ag is estimated as $< 1/10$.

This work first introduced three-fold coincidence method and modified pileup rejection, developed to remove bismuth and ^{10}C spallation background contributing to $0\nu\beta\beta$ energy region. The former tags muon, spallation neutron and spallation products, which achieved (64 ± 4) % rejection efficiency for ^{10}C, but it was suppressed by loss of neutrons just after highly energetic muons. The latter improved pulse discrimination capability, which increased rejection efficiency of ^{212}Bi $\sim$40 % from the previous method.

In order to extract $0\nu\beta\beta$ contribution, background rates were estimated via simultaneous spectral fit using full volume broken down into 40 equal-volume spherical half-shell regions. It was enabled owing to precise vertex estimation of ^{214}Bi on the IB. As a result, lower limit of $0\nu\beta\beta$ decay half-life obtained in Phase-II was $T^{0\nu}_{1/2} > 9.2 \times 10^{25}$ yr (at 90 % C.L.). Combining with Phase-I result, the limit resulted in $T^{0\nu}_{1/2} > 1.07 \times 10^{26}$ yr. Assuming exchange of light majorana neutrinos, it corresponds to limit of the effective Majorana neutrino mass: $\langle m_{\beta\beta} \rangle < (61 - 165)$ meV, or the lightest neutrino mass: $m_{\text{lightest}} < (180 - 480)$ meV. These are the most stringent limit of all double-beta decay experiments. The limits reaches near the bottom of the quasi-degenerate neutrino mass region.

A. Level Diagrams

A.1. Natural Radionuclides

A.1.1. ^{208}Tl

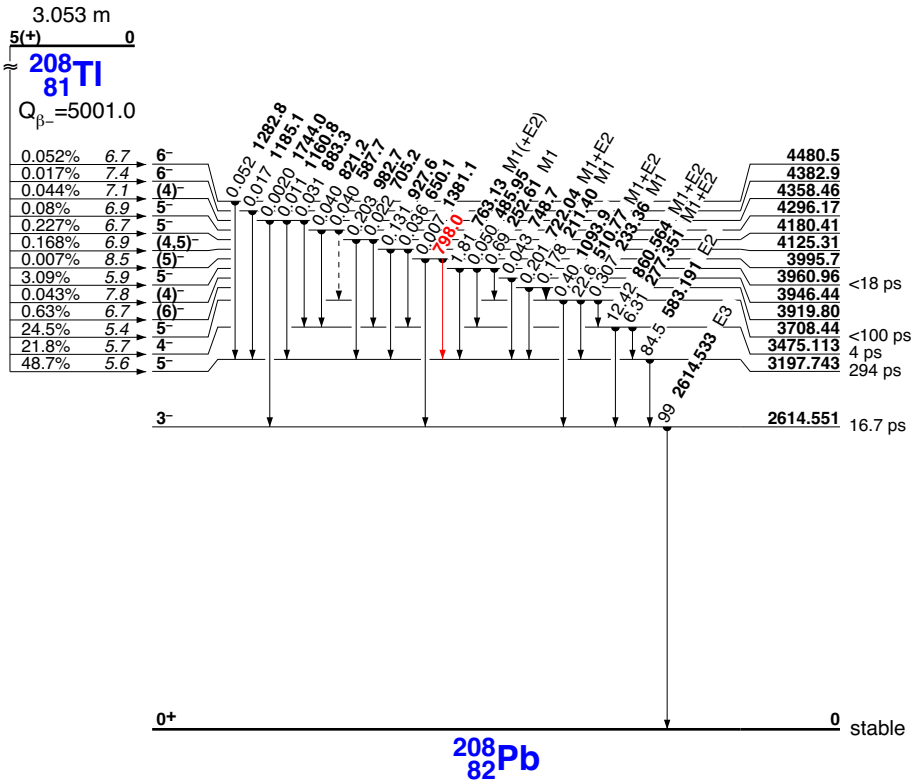

Figure A.1.: Level diagram for ^{208}Tl (Firestone et al., 1997 [82])

A.1.2. ^{214}Bi

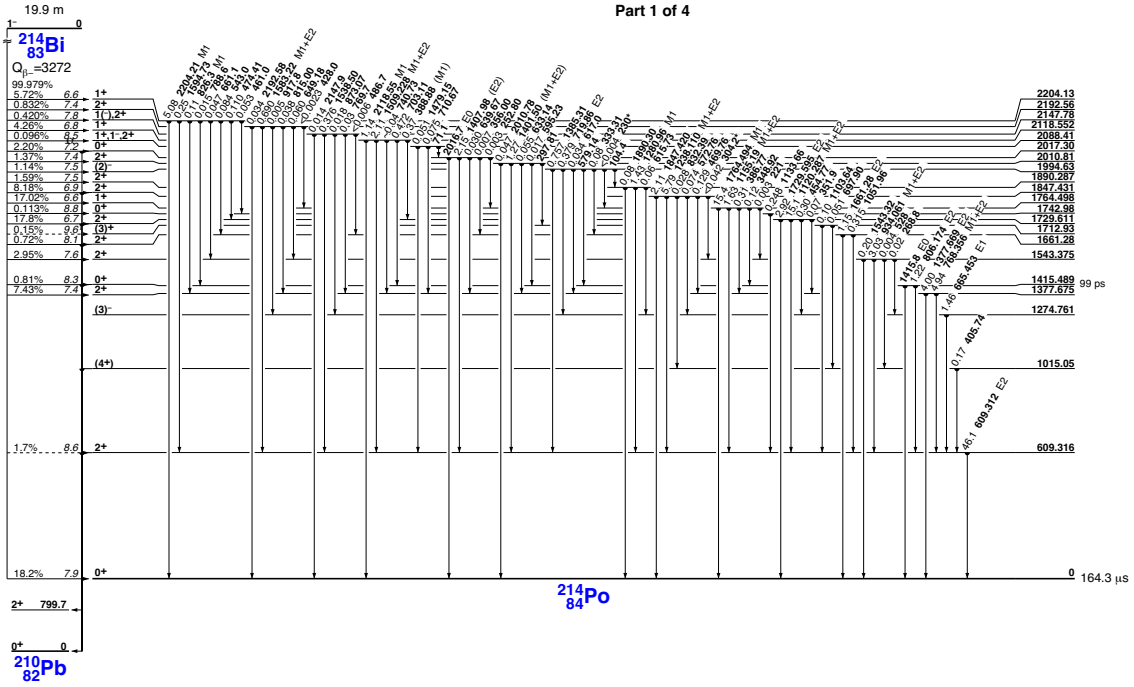

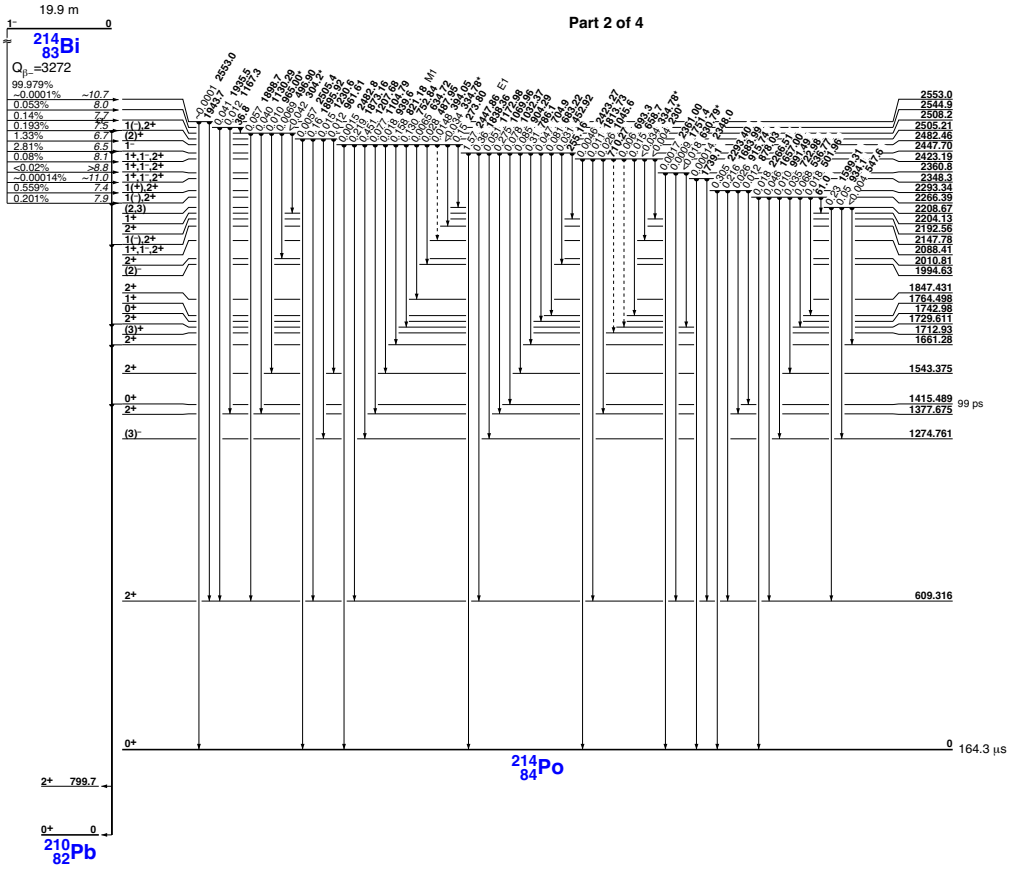
Part 2 of 4
19.9 m
214 83 Bi
Qβ-=3272
214 84 Po
164.3 µs
99 ps
210 82 Pb
2+ 799.7
0+ 0

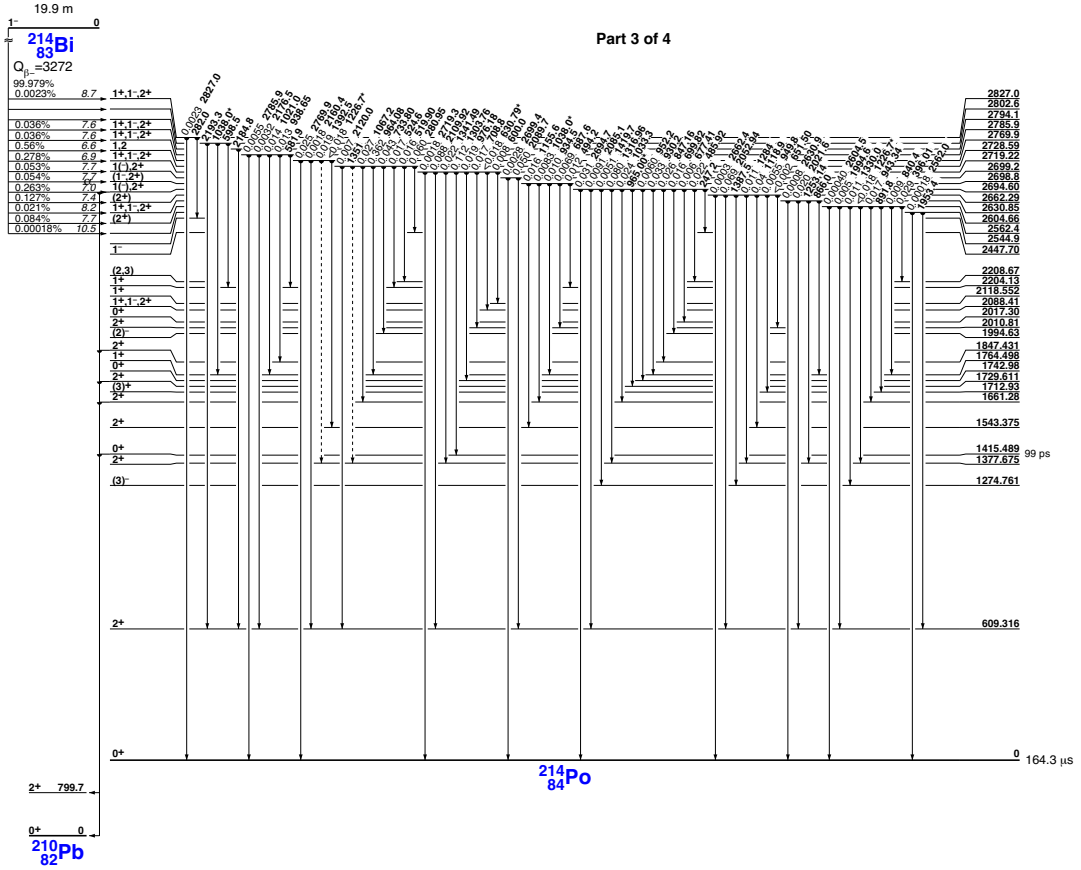
Part 3 of 4
19.9 m
214 83 Bi
Q β− =3272
99.979%
0.0023%
1+,1−,2+
0.036%
1+,1−,2+
0.036%
1+,1−,2+
0.56%
1,2
0.278%
1+,1−,2+
0.053%
1(−,2+)
0.054%
1(−,2+)
0.263%
1(−),2+
0.127%
(2+)
0.021%
1+,1−,2+
0.084%
(2+)
0.00018%
1−
(2,3)
1+
1+
1+,1−,2+
0+
2+
(2)−
2+
1+
0+
2+
(3)+
2+
2+
0+
2+
(3)−
2+
0+
214 84 Po
2+ 799.7
0+ 0
210 82 Pb
99 ps
164.3 µs

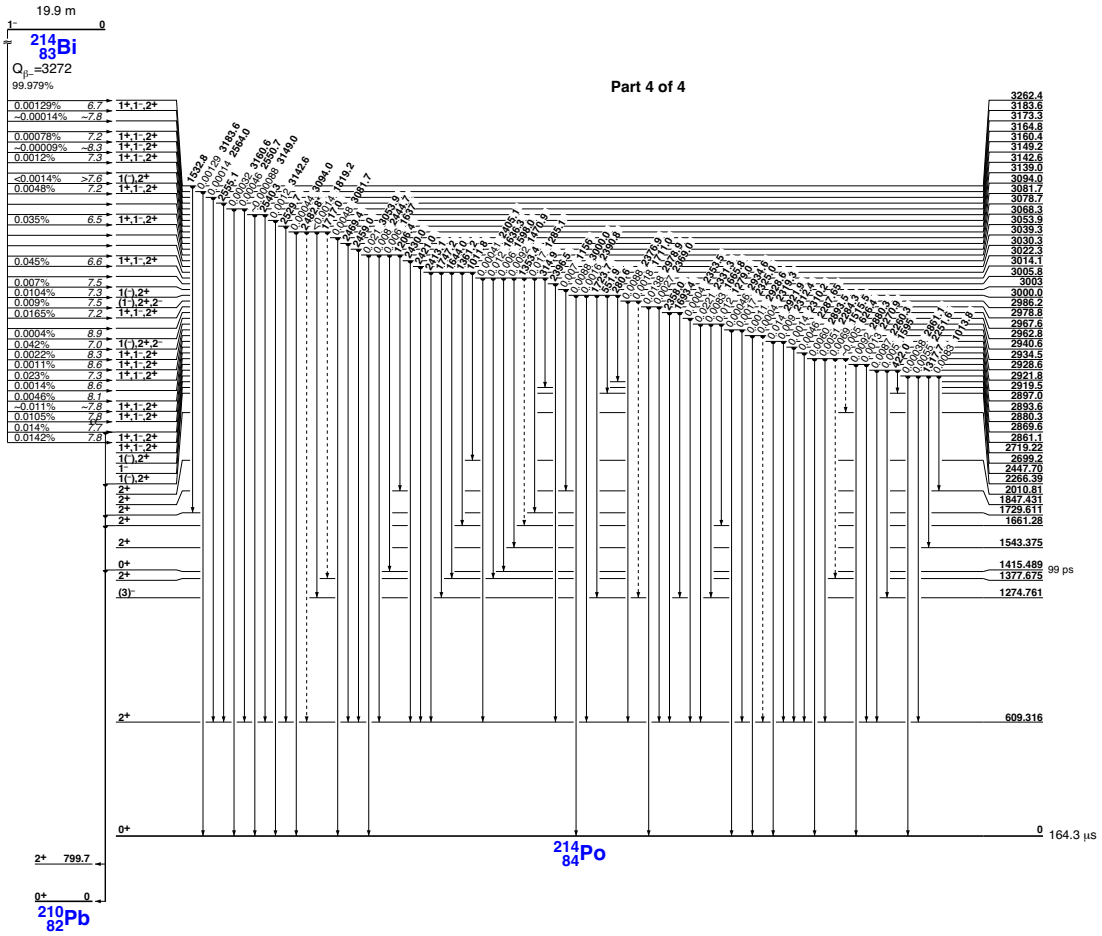

Figure A.2.: Level diagram for ^{214}Bi (Firestone et al., 1997 [82])

A.1.3. ^{212}Bi

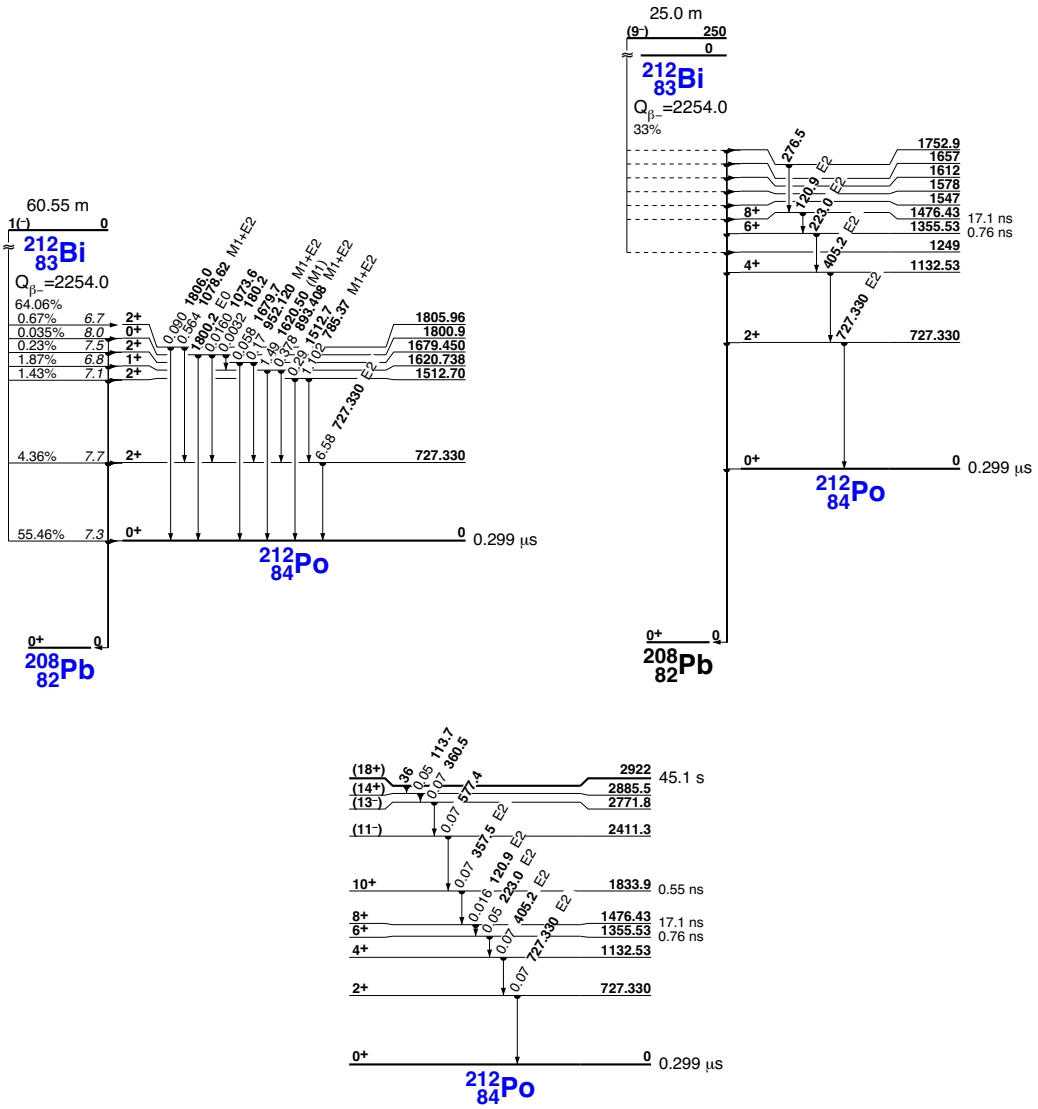

Figure A.3.: Level diagram for ^{212}Bi (Firestone et al., 1997 [82])

A.2. Spallation Products

A.2.1. Light Isotopes

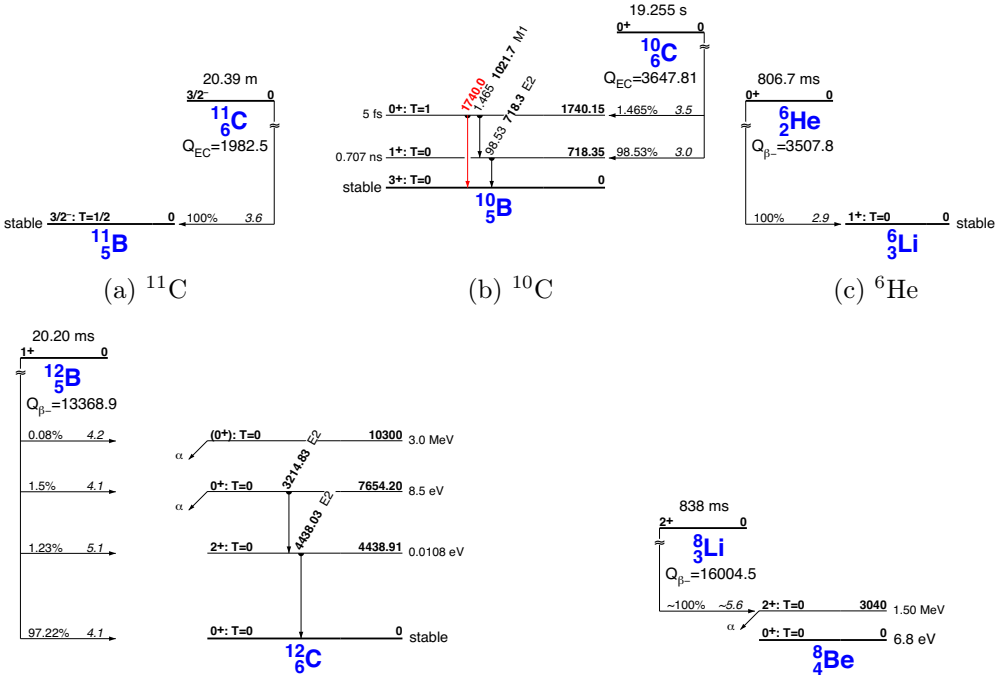

(a) ^{11}C (b) ^{10}C (c) ^{6}He

(d) ^{12}B (e) ^{8}Li

Figure A.4.: Level diagram for light isotopes (Firestone et al., 1997 [82])

A.2.2. Heavy Isotopes

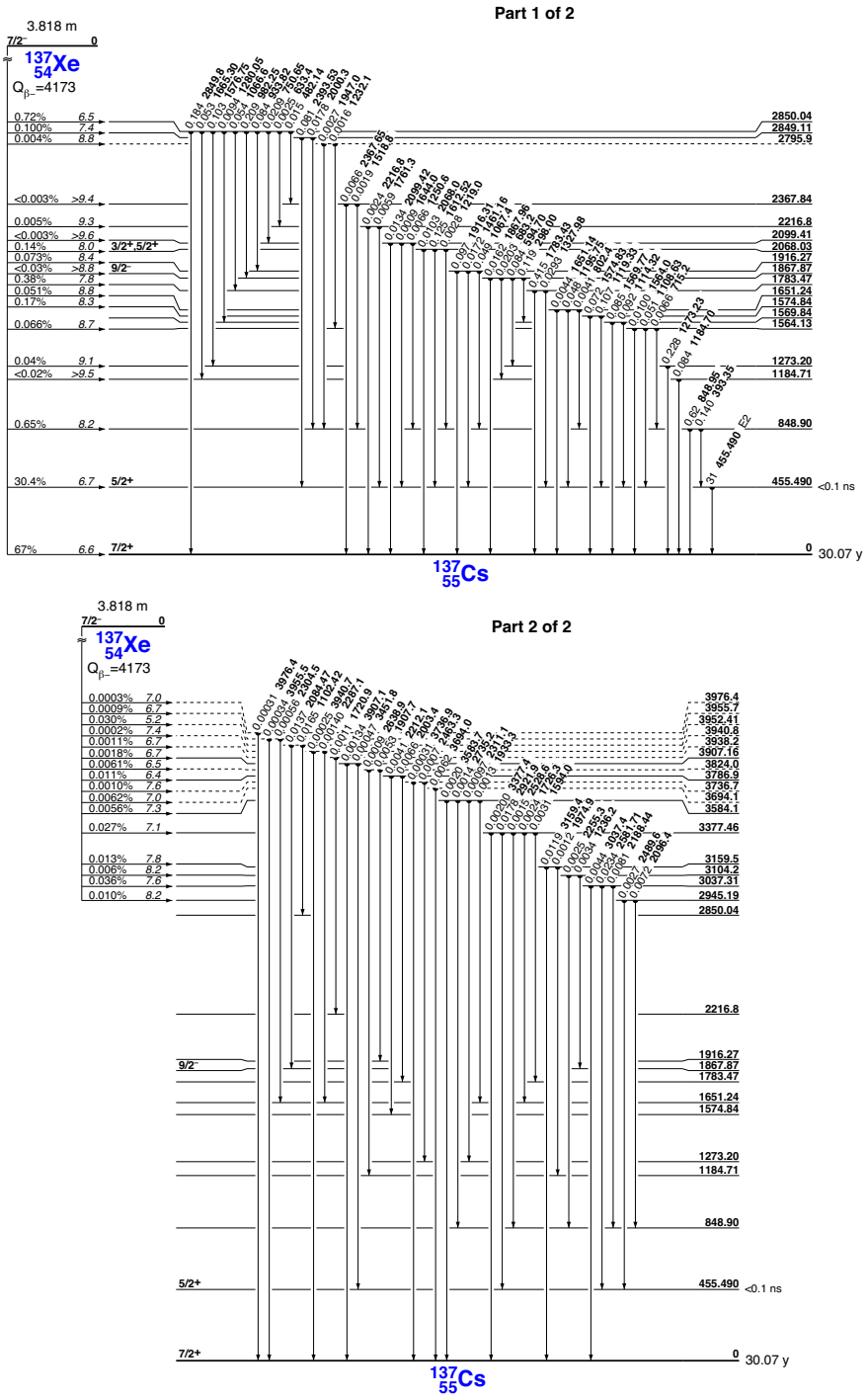

Figure A.5.: Level diagram for ^{137}Xe (Firestone et al., 1997 [82])

A.3. Potential Backgrounds

A.3.1. ^{208}Ag

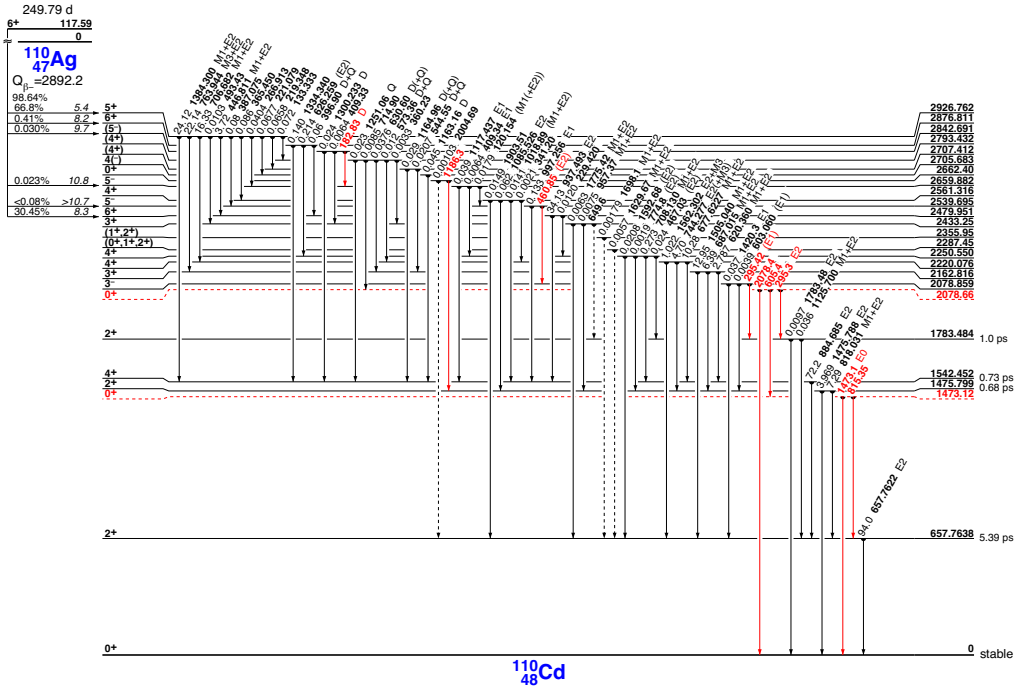

Figure A.6.: Level diagram for ^{110m}Ag (Firestone et al., 1997 [82])

A.3.2. ^{88}Y

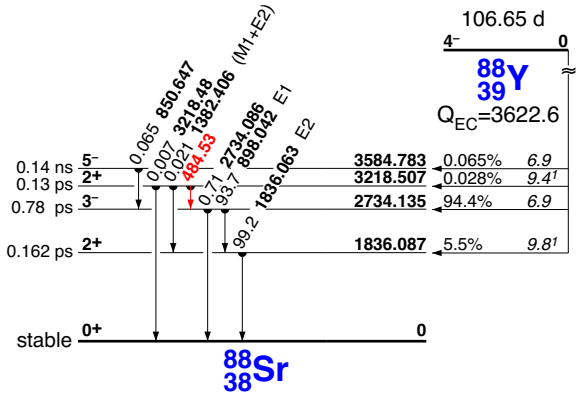

Figure A.7.: Level diagram for ^{88}Y (Firestone et al., 1997 [82])

A.3.3. ^{208}Bi

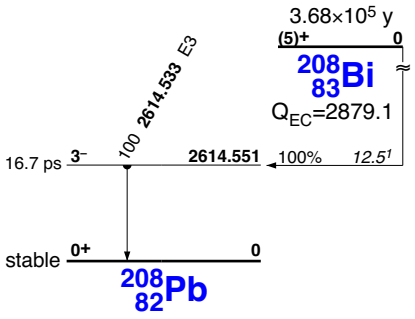

Figure A.8.: Level diagram for ^{208}Bi (Firestone et al., 1997 [82])

A.3.4. ^{60}Co

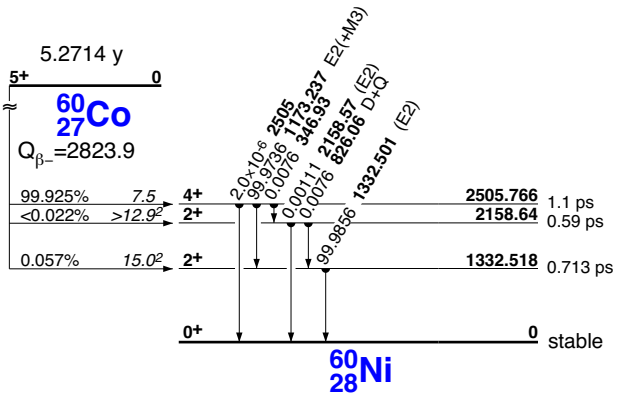

Figure A.9.: Level diagram for ^{60}Co (Firestone et al., 1997 [82])

Bibliography

[1] A. Gando, Y Gando, et al. "Search for Majorana Neutrinos Near the Inverted Mass Hierarchy Region with KamLAND-Zen". *Phys. Rev. Lett.* 117.8 (Aug. 2016), p. 082503. DOI: 10.1103/PhysRevLett.117.082503. arXiv: arXiv:1605.02889v2. URL: http://link.aps.org/doi/10.1103/PhysRevLett.117.082503.

[2] H. V. KLAPDOR-KLEINGROTHAUS and I. V. KRIVOSHEINA. "THE EVIDENCE FOR THE OBSERVATION OF $0\nu\beta\beta$ DECAY: THE IDENTIFICATION OF $0\nu\beta\beta$ EVENTS FROM THE FULL SPECTRA". *Mod. Phys. Lett. A* 21.20 (June 2006), pp. 1547–1566. DOI: 10.1142/S0217732306020937. URL: http://www.worldscientific.com/doi/abs/10.1142/S0217732306020937.

[3] K. Iwamoto. *Recent Results from T2K and Future Prospects*. URL: http://indico.cern.ch/event/432527/contributions/2143636/.

[4] F. Capozzi, E. Lisi, et al. "Neutrino masses and mixings: Status of known and unknown 3ν parameters". *Nucl. Phys. B* 908 (July 2016), pp. 218–234. DOI: 10.1016/j.nuclphysb.2016.02.016. arXiv: 1601.07777. URL: http://linkinghub.elsevier.com/retrieve/pii/S0550321316000602.

[5] S. Abe, T. Ebihara, et al. "Precision measurement of neutrino oscillation parameters with KamLAND". *Phys. Rev. Lett.* 100.22 (2008), pp. 1–5. DOI: 10.1103/PhysRevLett.100.221803. arXiv: 0801.4589.

[6] Stephen F King and Christoph Luhn. "Neutrino mass and mixing with discrete symmetry." *Rep. Prog. Phys.* 76.5 (2013), p. 056201. DOI: 10.1088/0034-4885/76/5/056201. arXiv: 1301.1340. URL: http://arxiv.org/abs/1301.1340.

[7] V. N. Aseev et al. "Upper limit on the electron antineutrino mass from the Troitsk experiment". *Phys. Rev. D - Part. Fields, Gravit. Cosmol.* 84.11 (2011). DOI: 10.1103/PhysRevD.84.112003. arXiv: 1108.5034.

[8] Ch Kraus et al. "Final results from phase II of the Mainz neutrino mass search in tritium β decay". *Eur. Phys. J. C* 40.4 (2005), pp. 447–468. DOI: 10.1140/epjc/s2005-02139-7. arXiv: 0412056 [hep-ex].

[9] G. Drexlin et al. "Current direct neutrino mass experiments". *Adv. High Energy Phys.* 2013.i (2013). DOI: 10.1155/2013/293986. arXiv: 1307.0101.

[10] Planck Collaboration et al. "Planck 2015 results". *Astron. Astrophys.* 594 (2016), A13. DOI: 10.1051/0004-6361/201525830. URL: http://dx.doi.org/10.1051/0004-6361/201525830.

[11] Nathalie Palanque-Delabrouille et al. "Constraint on neutrino masses from SDSS-III/BOSS Lyα forest and other cosmological probes". *J. Cosmol. Astropart. Phys.* 2015.02 (2015), pp. 045–045. DOI: 10.1088/1475-7516/2015/02/045. arXiv: 1410.7244. URL: http://arxiv.org/abs/1410.7244.

[12] Alessandro Strumia. "Neutrino masses and mixings..." (2007). arXiv: hep-ph/0606054 [hep-ph].

[13] A. S. Barabash. "Precise half-life values for two-neutrino double-β decay". *Phys. Rev. C* 81.3 (Mar. 2010), p. 035501. DOI: 10.1103/PhysRevC.81.035501. URL: http://link.aps.org/doi/10.1103/PhysRevC.81.035501.

[14] M. F. Kidd et al. "Two-neutrino double-β decay of ^{150}Nd to excited final states in ^{150}Sm". *Phys. Rev. C* 90.5 (Nov. 2014), p. 055501. DOI: 10.1103/PhysRevC.90.055501. URL: http://link.aps.org/doi/10.1103/PhysRevC.90.055501.

[15] R. Arnold, C. Augier, A. M. Bakalyarov, et al. "Measurement of the double-beta decay half-life and search for the neutrinoless double-beta decay of ^{48}Ca with the NEMO-3 detector". *Phys. Rev. D* 93.11 (June 2016), p. 112008. DOI: 10.1103/PhysRevD.93.112008. arXiv: 1011.1669v3. URL: http://link.aps.org/doi/10.1103/PhysRevD.93.112008.

[16] M. Agostini, M. Allardt, A. M. Bakalyarov, et al. "Results on $\beta\beta$ decay with emission of two neutrinos or Majorons in ^{76}Ge from GERDA Phase I". *Eur. Phys. J. C* 75.9 (Sept. 2015), p. 416. DOI: 10.1140/epjc/s10052-015-3627-y. URL: http://link.springer.com/10.1140/epjc/s10052-015-3627-y.

[17] R. Arnold, C. Augier, J. Baker, A. Barabash, et al. "First results of the search for neutrinoless double-beta decay with the NEMO 3 detector". *Phys. Rev. Lett.* 95.18 (2005), pp. 3–6. DOI: 10.1103/PhysRevLett.95.182302.

[18] J. Argyriades et al. "Measurement of the two neutrino double beta decay half-life of Zr-96 with the NEMO-3 detector". *Nucl. Phys. A* 847.3-4 (Dec. 2010), pp. 168–179. DOI: 10.1016/j.nuclphysa.2010.07.009. URL: http://linkinghub.elsevier.com/retrieve/pii/S0375947410006238.

[19] R. Arnold, C. Augier, J. D. Baker, and A. S. Barabash. "Results of the search for neutrinoless double-β decay in ^{100}Mo with the NEMO-3 experiment". *Phys. Rev. D* 92.7 (Oct. 2015), p. 072011. DOI: 10.1103/PhysRevD.92.072011. URL: http://link.aps.org/doi/10.1103/PhysRevD.92.072011.

[20] A. S. Barabash and V. B. Brudanin. "Investigation of double-beta decay with the NEMO-3 detector". *Phys. At. Nucl.* 74.2 (Feb. 2011), pp. 312–317. DOI: 10.1134/S1063778811020062. URL: http://link.springer.com/10.1134/S1063778811020062.

[21] R. Arnold, C. Augier, J. Baker, A. S. Barabash, et al. "Measurement of the $\beta\beta$ Decay Half-Life of ^{130}Te with the NEMO-3 Detector". *Phys. Rev. Lett.* 107.6 (Aug. 2011), p. 062504. DOI: 10.1103/PhysRevLett.107.062504. URL: http://link.aps.org/doi/10.1103/PhysRevLett.107.062504.

[22] J. B. Albert, M. Auger, et al. "Improved measurement of the $2\nu\beta\beta$ half-life of ^{136}Xe with the EXO-200 detector". *Phys. Rev. C* 89.1 (Jan. 2014), p. 015502. DOI: 10.1103/PhysRevC.89.015502. URL: http://link.aps.org/doi/10.1103/PhysRevC.89.015502.

[23] R. Arnold, C. Augier, J. D. Baker, A. S. Barabash, A. Basharina-Freshville, S. Blondel, S. Blot, M. Bongrand, V. Brudanin, J. Busto, A. J. Caffrey, S. Calvez, M. Cascella, et al. "Measurement of the $2\nu\beta\beta$ decay half-life of ^{150}Nd and a search for $0\nu\beta\beta$ decay processes with the full exposure from the NEMO-3 detector". *Phys. Rev. D* 94 (7 Oct. 2016), p. 072003. DOI: 10.1103/PhysRevD.94.072003. URL: http://link.aps.org/doi/10.1103/PhysRevD.94.072003.

[24] F. Šimkovic et al. "Possibility of measuring the CP Majorana phases in $0\nu\beta\beta$ decay". *Phys. Rev. D* 87.7 (Apr. 2013), p. 073002. DOI: 10.1103/PhysRevD.87.073002. URL: http://link.aps.org/doi/10.1103/PhysRevD.87.073002.

[25] O. Haug et al. "Neutrino oscillations and R-parity violating supersymmetry". *Nucl. Phys. B* 565.1-2 (Jan. 2000), pp. 38–48. DOI: 10.1016/S0550-3213(99)00695-1. URL: http://linkinghub.elsevier.com/retrieve/pii/S0550321399006951.

[26] M. Hirsch and J. W F Valle. "Supersymmetric origin of neutrino mass". *New J. Phys.* 6 (July 2004), pp. 76–76. DOI: 10.1088/1367-2630/6/1/076. arXiv: 0405015 [hep-ph]. URL: http://stacks.iop.org/1367-2630/6/i=1/a=076?key=crossref.a7bc66febc1cd9fb97725fbd599c40f7.

[27] M. Mirea, T. Pahomi, and S. Stoica. "Phase Space Factors for Double Beta Decay: an up-date". 2.1 (Nov. 2014), pp. 1–10. arXiv: 1411.5506. URL: http://arxiv.org/abs/1411.5506.

[28] M. T. Mustonen and J. Engel. "Large-scale calculations of the double-β decay of ^{76}**Ge**, ^{130}**Te**, ^{136}**Xe**, and ^{150}**Nd** in the deformed self-consistent Skyrme quasiparticle random-phase approximation". *Phys. Rev. C* 87.6 (June 2013), p. 064302. DOI: 10.1103/PhysRevC.87.064302. URL: http://link.aps.org/doi/10.1103/PhysRevC.87.064302.

[29] J. Barea, J. Kotila, and F. Iachello. "Nuclear matrix elements for double-β decay". *Phys. Rev. C - Nucl. Phys.* 87.1 (2013), pp. 1–20. DOI: 10.1103/PhysRevC.87.014315. arXiv: 1301.4203.

[30] R. G. H. ROBERTSON. "EMPIRICAL SURVEY OF NEUTRINOLESS DOUBLE BETA DECAY MATRIX ELEMENTS". *Mod. Phys. Lett. A* 28.08 (Mar. 2013), p. 1350021. DOI: 10.1142/S0217732313500211. URL: http://www.worldscientific.com/doi/abs/10.1142/S0217732313500211.

[31] Andrea Giuliani and Alfredo Poves. "Neutrinoless Double-Beta Decay". *Adv. High Energy Phys.* 2012 (2012), pp. 1–38. DOI: 10.1155/2012/857016. URL: http://www.hindawi.com/journals/ahep/2012/857016/.

[32] J. B. Albert, D. J. Auty, et al. "Search for Majorana neutrinos with the first two years of EXO-200 data". *Nature* 510.7504 (June 2014), pp. 229–234. DOI: 10.1038/nature13432. arXiv: arXiv:1402.6956. URL: http://www.nature.com/doifinder/10.1038/nature13432.

[33] M. Agostini, M. Allardt, E. Andreotti, et al. "Results on Neutrinoless Double-β Decay of ^{76}Ge from Phase I of the GERDA Experiment". *Phys. Rev. Lett.* 111.12 (Sept. 2013), p. 122503. DOI: 10.1103/PhysRevLett.111.122503. URL: http://link.aps.org/doi/10.1103/PhysRevLett.111.122503.

[34] GERDA Collaboration. *First results from GERDA Phase II*. 2016. URL: https://www.mpi-hd.mpg.de/gerda/public/2016/t16_neutrino_gerda_ma.pdf.

[35] K. Alfonso et al. "Search for Neutrinoless Double-Beta Decay of ^{130}Te with CUORE-0". *Phys. Rev. Lett.* 115.10 (2015), pp. 1–7. DOI: 10.1103/PhysRevLett.115.102502. arXiv: 1504.02454.

[36] Osamu Tajima. "Measurement of Electron Anti-Neutrino Oscillation Parameters with a Large Volume Liquid Scintillator Detector". Ph.D. thesis. Tohoku University, 2003. URL: http://hdl.handle.net/10097/26184.

[37] Kyohei Nakajima. "First Results from ^{7}Be Solar Neutrino Observation with KamLAND". Ph.D. thesis. Tohoku University, 2010. URL: http://hdl.handle.net/10097/50853.

[38] W.C. Haxton and G.J. Stephenson. "Double beta decay". *Prog. Part. Nucl. Phys.* 12 (1984), pp. 409–479. DOI: 10.1016/0146-6410(84)90006-1. URL: http://linkinghub.elsevier.com/retrieve/pii/0146641084900061.

[39] H. Yoshida. "Limit on Majorana Neutrino Mass with Neutrinoless Double Beta Decay from KamLAND-Zen". Ph.D. thesis. Tohoku University, 2014. URL: http://hdl.handle.net/10097/58802.

[40] A. Gando. "First Results of Neutrinoless Double Beta Decay Search with KamLAND-Zen". Ph.D. thesis. Tohoku University, 2012. URL: http://hdl.handle.net/10097/55602.

[41] K. Abe et al. "Distillation of liquid xenon to remove krypton". *Astropart. Phys.* 31.4 (2009), pp. 290–296. DOI: 10.1016/j.astropartphys.2009.02.006. URL: http://linkinghub.elsevier.com/retrieve/pii/S092765050900036X.

[42] A. Gando et al. "Limits on Majoron-emitting double-β decays of ^{136}Xe in the KamLAND-Zen experiment". *Phys. Rev. C - Nucl. Phys.* 86.2 (2012), pp. 8–11. DOI: 10.1103/PhysRevC.86.021601. arXiv: arXiv:1307.2929.

[43] M. Auger et al. "Search for Neutrinoless Double-Beta Decay in ^{136}Xe with EXO-200". *Phys. Rev. Lett.* 109.3 (July 2012), p. 032505. DOI: 10.1103/PhysRevLett.109.032505. arXiv: 1205.5608. URL: http://link.aps.org/doi/10.1103/PhysRevLett.109.032505.

[44] A. Gando, Y. Gando, H. Hanakago, H. Ikeda, K. Inoue, K. Ishidoshiro, R. Kato, et al. "Limit on neutrinoless $\beta\beta$ decay of ^{136}Xe from the first phase of KamLAND-Zen and comparison with the positive claim in ^{76}Ge". *Phys. Rev. Lett.* 110.6 (2013), pp. 1–5. DOI: 10.1103/PhysRevLett.110.062502. arXiv: arXiv:1211.3863v2.

[45] K. Asakura et al. "Search for double-beta decay of ^{136}Xe to excited states of ^{136}Ba with the KamLAND-Zen experiment". *Nucl. Phys. A* 946 (Sept. 2016), pp. 171–181. DOI: 10.1016/j.nuclphysa.2015.11.011. arXiv: 1509.03724. URL: http://dx.doi.org/10.1016/j.nuclphysa.2015.11.011.

[46] A. Oki. "^{10}C background rejection by new trigger in KamLAND-Zen". Master thesis. Tohoku University, 2013.

[47] William H. Press et al. *Numerical Recipes 3rd Edition: The Art of Scientific Computing*. 3rd ed. Cambridge University Press, 2007, p. 456. ISBN: 0521880688, 9780521880688.

[48] T. I. Banks et al. "A compact ultra-clean system for deploying radioactive sources inside the KamLAND detector". *Nucl. Instruments Methods Phys. Res. Sect. A Accel. Spectrometers, Detect. Assoc. Equip.* 769 (2015), pp. 88–96. DOI: 10.1016/j.nima.2014.09.068. arXiv: 1407.0413.

[49] Raymond Tsang, Andreas Piepke, and Jerry Busenitz. *Fabrication of the KamLAND Composite Source*. Tech. rep. University of Alabama, 2015, pp. 1–6.

[50] T. Hachiya. "Study on Background Reduction Using Waveform Information in KamLAND-Zen". Master thesis. Tohoku University, 2016.

[51] S. Enomoto. "Neutrino Geophysics and Observation of Geo-Neutrinos at KamLAND". Ph.D. thesis. Tohoku University, 2005, p. 233. URL: http://hdl.handle.net/10097/39197.

[52] H. Watanabe. "Comprehensive Study of Anti-neutrino Signals at KamLAND". Ph.D. thesis. Tohoku University, 2015. URL: http://hdl.handle.net/10097/54040.

[53] S. Abe, S. Enomoto, et al. "Production of radioactive isotopes through cosmic muon spallation in KamLAND". *Phys. Rev. C - Nucl. Phys.* 81.2 (Feb. 2010), p. 025807. DOI: 10.1103/PhysRevC.81.025807. arXiv: arXiv:0907.0066v2. URL: http://link.aps.org/doi/10.1103/PhysRevC.81.025807.

[54] S. Agostinelli et al. "GEANT4 - A simulation toolkit". *Nucl. Instruments Methods Phys. Res. Sect. A Accel. Spectrometers, Detect. Assoc. Equip.* 506.3 (2003), pp. 250–303. DOI: 10.1016/S0168-9002(03)01368-8. arXiv: 1005.0727v1.

[55] J. Allison et al. "Geant4 developments and applications". *IEEE Trans. Nucl. Sci.* 53.1 (Feb. 2006), pp. 270–278. DOI: 10.1109/TNS.2006.869826. URL: http://ieeexplore.ieee.org/lpdocs/epic03/wrapper.htm?arnumber=1610988.

[56] A. Gando, Y. Gando, H. Hanakago, H. Ikeda, K. Inoue, K. Ishidoshiro, H. Ishikawa, et al. "^{7}Be solar neutrino measurement with KamLAND". *Phys. Rev. C* 92.5 (2015), p. 055808. DOI: 10.1103/PhysRevC.92.055808. arXiv: 1405.6190. URL: http://link.aps.org/doi/10.1103/PhysRevC.92.055808.

[57] Wataru Nitta et al. "Atmospheric ^{85}Kr and ^{133}Xe activity concentrations at locations across Japan following the Fukushima Dai-ichi Nuclear Power Plant accident". *J. Nucl. Sci. Technol.* 51.5 (2014), pp. 712–719. DOI: 10.1080/00223131.2014.888960. URL: http://www.tandfonline.com/doi/abs/10.1080/00223131.2014.888960.

[58] TAKAHIRO WATANABE et al. "Distribution of artificial radionuclides (^{110m}Ag, ^{129m}Te, ^{134}Cs, ^{137}Cs) in surface soils from Miyagi Prefecture, northeast Japan, following the 2011 Fukushima Dai-ichi nuclear power plant accident". *Geochem. J.* 46.4 (2012), pp. 279–285. DOI: 10.2343/geochemj.2.0205. URL: http://jlc.jst.go.jp/DN/JST.JSTAGE/geochemj/2.0205?lang=en&from=CrossRef&type=abstract.

[59] Michio Aoyama et al. "^{134}Cs and ^{137}Cs in the North Pacific Ocean derived from the March 2011 TEPCO Fukushima Dai-ichi Nuclear Power Plant accident, Japan. Part one: surface pathway and vertical distributions". *J. Oceanogr.* 72.1 (Feb. 2016), pp. 53–65. DOI: 10.1007/s10872-015-0335-z. URL: http://link.springer.com/10.1007/s10872-015-0335-z.

[60] Cristiano Galbiati et al. "Cosmogenic ^{11}C production and sensitivity of organic scintillator detectors to *pep* and CNO neutrinos". *Phys. Rev. C - Nucl. Phys.* 71.5 (May 2005), p. 055805. DOI: 10.1103/PhysRevC.71.055805. arXiv: hep-ph/0411002 [hep-ph]. URL: http://link.aps.org/doi/10.1103/PhysRevC.71.055805.

[61] J. B. Albert, S. J. Daugherty, et al. "Measurement of neutron capture on ^{136}Xe". *Phys. Rev. C* 94 (3 Sept. 2016), p. 034617. DOI: 10.1103/PhysRevC.94.034617. URL: http://link.aps.org/doi/10.1103/PhysRevC.94.034617.

[62] G. Battistoni et al. "The FLUKA code: description and benchmarking". *AIP Conf. Proc.* Vol. 896. AIP, 2007, pp. 31–49. DOI: 10.1063/1.2720455. URL: http://scitation.aip.org/content/aip/proceeding/aipcp/10.1063/1.2720455.

[63] A. Ferrari et al. *FLUKA: a multi-particle transport code*. Tech. rep. October. 2005. URL: http://cds.cern.ch/record/898301.

[64] P. Antonioli et al. "A three-dimensional code for muon propagation through the rock: MUSIC". *Astropart. Phys.* 7.4 (Oct. 1997), pp. 357–368. DOI: 10.1016/S0927-6505(97)00035-2. URL: http://linkinghub.elsevier.com/retrieve/pii/S0927650597000352.

[65] Said F Mughabghab. *Atlas of Neutron Resonances: Resonance Parameters and Thermal Cross Sections. Z=1-100; 5th ed.* Elsevier, 2006. URL: https://cds.cern.ch/record/1086969.

[66] Keiichi Shibata et al. "JENDL-4.0: A New Library for Nuclear Science and Engineering". *J. Nucl. Sci. Technol.* 48.1 (Jan. 2011), pp. 1–30. DOI: 10.1080/18811248.2011.9711675. URL: http://www.tandfonline.com/doi/abs/10.1080/18811248.2011.9711675.

[67] *ENSDF, the Evaluated Nuclear Structure Data File*. URL: http://www.nndc.bnl.gov/ensdf/.

[68] A. Gando et al. "Measurement of the double-β decay half-life of ^{136}Xe with the KamLAND-Zen experiment". *Phys. Rev. C - Nucl. Phys.* 85.4 (2012), pp. 1–6. DOI: 10.1103/PhysRevC.85.045504. arXiv: 1201.4664.

[69] N. Ackerman et al. "Observation of Two-Neutrino Double-Beta Decay in ^{136}Xe with the EXO-200 Detector". *Phys. Rev. Lett.* 107.21 (Nov. 2011), p. 212501. DOI: 10.1103/PhysRevLett.107.212501. URL: http://link.aps.org/doi/10.1103/PhysRevLett.107.212501.

[70] Gary J Feldman and Robert D Cousins. "A Unified Approach to the Classical Statistical Analysis of Small Signals". *Phys. Rev.* D57.7 (1998), pp. 3873–3889. DOI: 10.1103/PhysRevD.57.3873. arXiv: physics/9711021 [physics]. URL: http://journals.aps.org/prd/abstract/10.1103/PhysRevD.57.3873.

[71] J. Kotila and F. Iachello. "Phase-space factors for double-β decay". *Phys. Rev. C* 85.3 (Mar. 2012), p. 034316. DOI: 10.1103/PhysRevC.85.034316. arXiv: arXiv:1209.5722v1. URL: http://link.aps.org/doi/10.1103/PhysRevC.85.034316.

[72] Tomás R. Rodríguez and Gabriel Martínez-Pinedo. "Energy density functional study of nuclear matrix elements for neutrinoless $\beta\beta$ decay". *Phys. Rev. Lett.* 105.25 (2010), pp. 1–4. DOI: 10.1103/PhysRevLett.105.252503.

[73] J. Menéndez et al. "Disassembling the nuclear matrix elements of the neutrinoless $\beta\beta$ decay". *Nucl. Phys. A* 818.3-4 (Mar. 2009), pp. 139–151. DOI: 10.1016/j.nuclphysa.2008.12.005. URL: http://linkinghub.elsevier.com/retrieve/pii/S0375947408008233.

[74] J. Barea, J. Kotila, and F. Iachello. "$0\nu\beta\beta$ and $2\nu\beta\beta$ nuclear matrix elements in the interacting boson model with isospin restoration". *Phys. Rev. C* 91.3 (2015), p. 034304. DOI: 10.1103/PhysRevC.91.034304. URL: http://link.aps.org/doi/10.1103/PhysRevC.91.034304.

[75] Juhani Hyvarinen and Jouni Suhonen. "Nuclear matrix elements for $0\nu\beta\beta$ decays with light or heavy Majorana-neutrino exchange". *Phys. Rev. C - Nucl. Phys.* 91.2 (2015), pp. 1–12. DOI: 10.1103/PhysRevC.91.024613.

[76] A. Meroni, S. T. Petcov, and F. Šimkovic. "Multiple CP non-conserving mechanisms of $(\beta\beta)_{0\nu}$ -decay and nuclei with largely different nuclear matrix elements (article) Author". *J. High Energy Phys.* 2013.2 (2013). DOI: 10.1007/JHEP02(2013)025.

[77] Fedor Šimkovic et al. "$0\nu\beta\beta$ and $2\nu\beta\beta$ nuclear matrix elements, quasiparticle random-phase approximation, and isospin symmetry restoration". *Phys. Rev. C - Nucl. Phys.* 87.4 (2013), pp. 1–9. DOI: 10.1103/PhysRevC.87.045501. URL: http://link.aps.org/doi/10.1103/PhysRevC.87.045501.

[78] Stefano Dell'Oro, Simone Marcocci, and Francesco Vissani. "New expectations and uncertainties on neutrinoless double beta decay". *Phys. Rev. D* 90.3 (Aug. 2014), p. 033005. DOI: 10.1103/PhysRevD.90.033005. arXiv: arXiv:1404.2616v2. URL: http://link.aps.org/doi/10.1103/PhysRevD.90.033005.

[79] F. Capozzi, G. L. Fogli, et al. "Status of three-neutrino oscillation parameters, circa 2013". *Phys. Rev. D* 89.9 (May 2014), p. 093018. DOI: 10.1103/PhysRevD.89.093018. arXiv: 1312.2878. URL: http://link.aps.org/doi/10.1103/PhysRevD.89.093018.

[80] A S Barabash. "Double Beta Decay : Historical Review of 75 Years of Research". 74.4 (2011), pp. 603–613. DOI: 10.1134/S1063778811030070.

[81] R. Arnold, C. Augier, J. D. Baker, A. S. Barabash, A. Basharina-Freshville, S. Blondel, S. Blot, M. Bongrand, V. Brudanin, J. Busto, A. J. Caffrey, S. Calvez, C. Cerna, et al. "Results of the search for neutrinoless double- β decay in Mo 100 with the NEMO-3 experiment". *Phys. Rev. D - Part. Fields, Gravit. Cosmol.* 92.7 (2015), pp. 1–23. DOI: 10.1103/PhysRevD.92.072011. arXiv: 1506.05825.

[82] R.B. Firestone et al. "The 8th edition of the Table of Isotopes". English (1997). URL: http://inis.iaea.org/Search/search.aspx?orig_q=RN:29029102.